# A Study of the $^{9}Be(^{10}B)$ Reaction

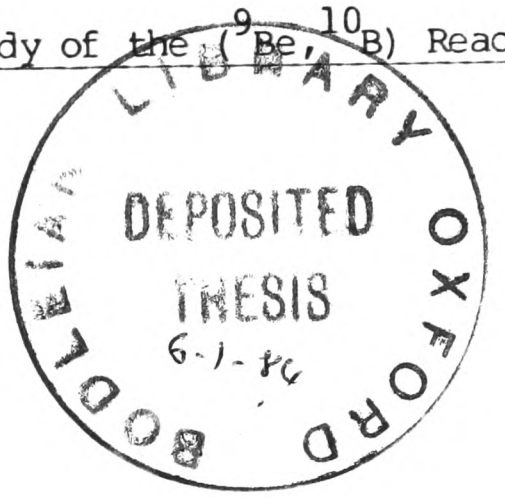


John Stuart Winfield

New College

Oxford

A thesis submitted for the degree of

Doctor of Philosophy in the

University of Oxford

Trinity Term 1983

La vraisemblance n'est pas

toujours du côté de la vérité

Pierre Bayle

(1647-1706)

# A Study of the ($^{9}$Be,$^{10}$B) Reaction.

John Stuart Winfield,

New College,
Oxford.

Abstract of thesis submitted for the degree of Doctor of Philosophy

Trinity Term 1983.

## ABSTRACT

Angular distributions have been measured for the ($^{9}$Be,$^{10}$B$_{0,1}$) reactions on $^{63}$Cu, $^{54}$Fe, $^{26,24}$Mg and $^{16}$O at 43 MeV and on $^{40}$Ca at 45 and 30 MeV. Several of these experiments were performed with the Oxford MDM-2 spectrometer and the design and testing of its 30 cm focal plane detector, which is of the "hybrid" type, is described. Despite the size of the counter, in particular the large cathode to Frisch-grid separation, the resolution of the ionization signals is comparable with that of smaller counters. The position resolution is < 0.6 mm.

Optical potentials have been obtained from the measured elastic scattering of $^{9}$Be from $^{16}$O, $^{26}$Mg and $^{40}$Ca, and $^{10}$B from $^{25}$Mg and $^{39}$K. The exact finite-range DWBA calculations have generally well reproduced the shape of the experimental reaction cross-sections. However, inconsistencies of up to 50% between the extracted spectroscopic factors for $^{10}$B$_{0}$ and $^{10}$B$_{1}$ have been found. This anomaly was found insensitive to changes in either optical potential or bound state parameters.

A new method of form factor calculation is described that uses a shell model potential in conjunction with a surface-peaked potential, the depth of which is adjusted to give the correct asymptotic form to the wavefunctions. Whilst this form factor showed some success, it did not account for the $^{10}$B$_{0}$/$^{10}$B$_{1}$ anomaly.

Collective model DWBA analyses of the inelastic excitation of the first $2^{+}$ state in $^{26}$Mg and $3^{-}$ state in $^{40}$Ca have given values for deformation parameters in reasonable agreement with light-ion work. A CCBA analysis of the $^{26}$Mg $2^{+}$ state was carried out to estimate the effect of the coupling.

Calculations performed for a two-step reaction process through inelastic excitation of a strongly coupled $5/2^{-}$ state in the projectile showed that this indirect route is important, but it could not solve the $^{10}$B$_{0}$/$^{10}$B$_{1}$ problem alone. The conclusion is that other routes (projectile or target excitation) must be included.

# C O N T E N T S

## Acknowledgements.

It is a pleasure to thank the many people who have helped me in the work described here. I would particularly like to express my gratitude to the following:

Professor K.W.Allen and Professor D.H.Perkins for allowing me to use the excellent facilities of the Oxford Nuclear Physics Laboratory.

Dr. N.A.Jelley, my supervisor, for his encouragement and interest in my work, also for his valuable guidance during the writing of this thesis.

The other members of the NAJ group - Dr. C.L.Woods, Mr. P.A.Le Bas and Mrs. O.L.Avila-Aguirre - for their willing assistance on the scattering chamber experiments, and (CLW) for teaching me the rudiments of DWBA calculations.

Mr. D.M.Pringle, Dr. W.N.Catford, and Mr. D.G.Lewis who helped at all stages in the focal plane detector work and provided a comradely spirit even during the worst moments. Dr. E.F.Garman and Ms. S.K.B.Hesmondhalgh who, along with the afore-mentioned trio, spent many a happy hour manning "Blue Bertha". Dr. Catford kindly read through the chapter on the detector.

Dr. W.D.M.Rae for many useful discussions and suggestions, in particular about the form factor description, and for patiently explaining the intricacies of SESIME to me. I would also like to thank Dr. Rae and Dr. R.K.Bhowmik for helpful suggestions for the focal plane detector.

Other members of, and visitors to, the laboratory with whom I have had useful discussions, particularly Dr. J.R.Rook, Professors M.Kawai and K.-I.Kubo, Dr. B.A.Brown and Dr. R.Lindsay. Also, Dr. D.Sinclair and Dr. L.K.Fifield, who helped with early designs for the counter.

Mr. H.R.McK.Hyder, the Machine group and the accelerator operators - Messrs. A.Aitken, J.Early, R.Hole, R.Hopkins, F.Kelly and N.Walters - for ion beams and cheerful company.

The "lads" from the main workshop who devoted themselves to the building of the spectrometer and focal plane detector, making a couple of spare items for good measure. The members of the OEG workshop who made some smaller, but no less vital, detector parts.

The members of the OEG Techniques group for providing a wide variety of targets, the OEG Computer Group for expert assistance with software and the Central Electronics Group for various electrical bits and pieces.

Miss D.J.Pollard for cheerful help with the word processor program and the printing out the final copy of this thesis.

Ms. L.R.Binstock for some grammatical advice and, together with Mr. H.A.Klein, Mr. D.G.Vaughan and Ms. A.L.Burrows, for proof reading sections of this manuscript.

Financial support from the Science and Engineering Research Council is gratefully acknowledged.

Finally, I would like to give my special thanks to my parents for their continuing support and encouragement.

# CHAPTER 1

## INTRODUCTION

Over the last decade there has been considerable interest in heavy-ion transfer reactions. One of the questions was whether heavy-ion reactions would be as successful a probe of nuclear structure as light-ion reactions had proved over the preceding years. The spectroscopic utility of transfer reactions depends to a large extent on the accuracy of the commonest method of analysis: the Distorted Wave Born Approximation (DWBA). This method has been shown to describe light-ion reactions well (see, for example, the compilation of spectroscopic factors by Endt [End77]). When first applied to the more complex processes of heavy-ion reactions, it was soon realized that the finite extent of the projectile would have to be treated properly and that the "zero-range" or even the "no-recoil finite-range" approximations for the interaction matrix were often inadequate [Hod78]. With the advent of "exact", or full-recoil, finite-range computer codes, remarkable success was achieved in several heavy-ion DWBA analyses. An example that is frequently quoted is the study by Ford et al. [For74] of all four single-nucleon transfer reactions resulting from the bombardment of $^{208}Pb$ by 72.2 MeV $^{11}B$ ions. All but one of these reactions were kinematically well-matched, and on the whole, the spectroscopic factors deduced in this study were very similar to light-ion ones. Yet in many heavy-ion reactions some inadequacy of the DWBA method was apparent: on occasions, especially when there was a

large angular momentum mismatch, it proved necessary to make arbitrary adjustments to the optical potential parameters in order to achieve a satisfactory fit to the data (Kovar [Kov74] and Tamura et al. [Tam80] review these problems). Sometimes it has also been difficult to extract reliable spectroscopic factors: differences of up to a factor of two have been reported from analyses of the same reaction (see, for example, Woods et al. [Woo80]). This problem may be a reflection on the ambiguities present in optical potentials derived from heavy-ion elastic scattering data or on the uncertainties in the description of the bound state wavefunctions: these points are discussed in Chapters 4 and 5.

Intermediate-mass ions (A=6-10) have not received as much attention as heavier mass projectiles such as $^{12}C$ and $^{16}O$. Lithium and beryllium, in particular, are interesting in the light of Satchler and Love's discovery that $^{6}Li$ and $^{9}Be$ elastic scattering is anomalous in the sense that the double-folding model potentials must be reduced by a factor of approximately 0.6 if the calculated cross-sections are to fit the data [Sat79]. The cause behind the failure of the double-folding model in these cases has been suggested as the ease of breakup of the projectile in the field of the target nucleus (both $^{6}Li$ and $^{9}Be$ are weakly bound). One would like to know whether this phenomenon will also cause problems in DWBA analyses involving such projectiles. The $(^{6}Li,^{7}Be)$ reaction has now been studied in some detail with respect to this ([Woo80],[Woo81]), and the DWBA appears to be accurate in the description of the $^{26}Mg(^{6}Li,^{7}Be)^{25}Na$ reaction, providing that shallow, large-radius optical potentials are used. The corresponding $^{9}Be$ induced single-proton pickup reaction is $(^{9}Be,^{10}B)$. This has not been studied previously (to the author's knowledge), probably because (i) $^{9}Be$ beams have been difficult

to obtain until recently and are still of rather low intensity, and (ii) because the ejectile nucleus, $^{10}B$, has many low-lying bound states which make the reaction unsuitable for a detailed spectroscopic study of the target. We are satisfied here, however, with the analysis of a few states, since the aim is to test our understanding of the reaction mechanism, rather than to learn about the structure of the target nuclei. Moreover, transfer to both $^{10}B$ ground and first excited state is observed, and, as discussed in Chapter 5, this can help prevent uncertainties in the bound state description and optical potential ambiguities from masking a failure in the DWBA.

All experiments reported here were performed with $^{9}Be$ beams from the Oxford Folded Tandem accelerator which gave a maximum beam energy of 43 to 45 MeV. At this energy, and for targets with $Z < 30$, the scattering is well above the Coulomb barrier, so that the dominant processes are expected to be elastic scattering, inelastic scattering and direct transfer reactions. As will be shown in Chapter 5, the kinematic conditions of Brink [Bri72] are fulfilled for the reaction at this energy, but the Q-values are generally several MeV away from optimum. The observed cross-section magnitudes are quite reasonable: they peak at the order of 1 mb/sr. DWBA analyses of single-nucleon transfer reactions are expected to be more reliable if optical potentials that describe the elastic scattering in the entrance and exit channel are used - this is discussed in Appendix A. It was therefore important to find appropriate potentials by analysing the elastic scattering data for several $^{9}Be$ and $^{10}B$ channels and this is described in Chapter 4.

In order to provide a good test of the DWBA, it is necessary to obtain reaction angular distributions covering a large range and with good statistical accuracy on each datum point. The use of magnetic spectrometers represents a considerable improvement in data-taking power compared with the usual alternative of silicon surface-barrier detector telescopes. Other advantages include better resolution and "cleaner" particle identification through the focal plane detector. The recently completed heavy-ion spectrometer at Oxford has greatly facilitated the experimental work described in this thesis. A "hybrid" type detector for this spectrometer has been developed and has performed very successfully for various ($^{9}$Be,$^{10}$B) reactions. Chapter 3 contains a detailed description of this detector.

The choice of targets has been governed by the following criteria:

(i) the residual nucleus should not possess too many low-lying excited states,

(ii) the target and residual nuclei should not be too deformed - or else coupled-channels type problems may be expected,

(iii) they should be low enough in atomic number such that the reaction is well above the Coulomb barrier,

(iv) the target material should have no elements present that would interfere with the extraction of the data for the nucleus of interest.

Since this work has been undertaken in the spirit of a test of the DWBA, we should be aware of the nature of the approximations involved. The theoretical basis of the DWBA as applied to transfer reactions is discussed in Appendix A, where it is seen that there are two basic approximations made. One of these involves the replacement of the exact wavefunction which describes the two-body system by the distorted waves

generated by an optical potential. This will be a good approximation if the reaction cross-section is small in relation to that of the elastic scattering. The other approximation involved is the neglect of terms higher than first-order in the transition matrix. We may distinguish between two sorts of second-order processes: those that proceed via an excited state of one of the interacting nuclei and those that proceed via an intermediate state which has a different mass partition: these latter are termed "coupled reaction channels", or CRC, processes. The CRC processes are unlikely to be important for single nucleon transfer reactions unless the direct process is strongly inhibited. Processes of the other type may be neglected if the inelastic excitation probability is small or if the transfer from the excited state is inhibited. The Born Approximation is expected to be accurate when the perturbation is weak and, more generally, when the centre-of-mass energy is high [Lan77]. The energies used in the ($^{9}$Be,$^{10}$B) experiments reported here are rather lower than the criterion suggested by MacMillan and Redish [Mac82], so that success or failure of the DWBA in this case will depend on the relative strengths of the indirect processes. These processes are discussed in Chapter 6, where an assessment of the DWBA for the ($^{9}$Be,$^{10}$B) is given.

# CHAPTER 2

# EXPERIMENTAL METHOD & SPECTRA

## 2.1 Introduction.

The principal aim of the experiments was to obtain differential cross-section angular distributions for the reactions $^{63}Cu, ^{54}Fe, ^{26,24}Mg, ^{16}O(^{9}Be, ^{10}B)$ at 43 MeV and for the $^{40}Ca(^{9}Be, ^{10}B)$ reaction at 45 and 30 MeV. In addition, for certain cases the appropriate entrance and exit channel elastic scattering was measured and angular distributions have been extracted for the two strong inelastic excitations of the $2^+$, 1.81 MeV level in $^{26}Mg$ and the $3^-$, 3.74 MeV state in $^{40}Ca$.

The elastic scattering data were taken in order that optical model potentials could be determined for use in the DWBA analysis of the reaction (see Chapter 4). The entrance channel elastic scattering could be recorded simultaneously with the reaction data when solid state detector telescopes were used: this was done for the initial three experiments with the $^{26}Mg$, $^{16}O$ and $^{40}Ca$ targets. Separate elastic scattering experiments were performed with $^{10}B$ beams in order to obtain optical model potentials for the exit channels of these reactions. By this means it was hoped to provide a good test of the DWBA through the extraction of spectroscopic information.

A further series of experiments was then carried out with the Oxford MDM-2 spectrometer. These concerned the reaction on $^{63}Cu$, $^{54}Fe$ and $^{24}Mg$ targets with an incident $^{9}Be$ energy of 43 MeV and a $^{40}Ca$ target with a $^{9}Be$ energy of 30 MeV. The emphasis of the second series of experiments was slightly different: they were a further investigation of an anomaly found in the analysis of the earlier experiments. This anomaly, which will be described in Chapter 5, was found to be independent of the optical potentials used, so that there was no need for further elastic scattering data.

The statistical accuracy and angular intervals of the data were, in so far as time permitted, fine enough to reveal oscillations in many cases, and thus a quite detailed comparison with the DWBA predictions was possible. This was particularly true of the reaction data for the $^{63}Cu$, $^{54}Fe$ and $^{24}Mg$ targets, for which the large solid angle of the magnetic spectrometer was utilised.

The required energy resolution varied from target to target. The most demanding case occurred for the $^{26}Mg(^{9}Be,^{10}B)^{25}Na$ reaction where the separation of the ground and first excited state is only 90 keV. This energy difference was beyond the resolution capabilities of the experiment performed with solid state detectors and so the resulting angular distribution was for both states summed. However, a light-ion experiment had shown that that spectroscopic factor for the $3/2^{+}$ first excited state was only one eighth of that for the $5/2^{+}$ ground state [Jän73]. Thus a DWBA analysis which assumed 100% pickup of a $d_{5/2}$ proton was expected to be sufficiently accurate. The relative strengths of these two states as populated by $(^{9}Be,^{10}B)$ was subsequently measured by the use of a thin target and the high resolving power of the Oxford

spectrometer (this is discussed at the end of section 2.6).

In most reaction studies the superior resolution of a magnetic spectrometer would be an advantage† in that more states would be resolved and there would be less interference from "contaminant" peaks in the spectra (i.e. peaks arising from reactions off contaminants in the target such as oxygen and carbon). Resolution also limits the forward angle elastic scattering data accuracy, since the peaks due to all the various elements in the target converge with decreasing angle. For the $^{16}O(^{9}Be,^{9}Be)^{16}O$ data in particular, the errors on the forward angle points are largely attributable to the uncertainties in fitting the poorly resolved peaks.

## 2.2 Experimental Arrangement with Solid State Detector Telescopes.

The large scattering chamber on line "A3" of the Oxford folded tandem Van de Graaff was used for the $^{9}Be$ experiments performed with silicon surface barrier detector telescopes. The beryllium beam intensity was typically 70 nA on target. Beryllium does not readily form negative ions and was therefore extracted from the sputter source in the form of $BeH^{-}$. This difficulty somewhat limits the resultant beam intensity. The $^{39}K(^{10}B,^{10}B)^{39}K$ experiment was carried out using the same line and scattering chamber, but the $^{25}Mg(^{10}B,^{10}B)^{25}Mg$ experiment was at sufficiently low incident energy for beams from the Oxford EN tandem to be used. In the latter case, the small scattering chamber on line "B4" was used; however, the experimental arrangement was very similar to that on line "A3", the boron beam intensity being typically

---

† other advantages are discussed in section 2.3.

130 nA. The set-up was basically the same as that described in detail by Woods [Woo81], therefore only a summary will be given here.

In general, three DE-E solid state detector telescopes were used. These were separated by 5° intervals on the rotatable base plate of the scattering chamber. Each telescope consisted of a single transmission DE detector (thickness typically 16 μm) and a single E detector which was at least 300 μm thick - this meant that the elastically scattered particles were stopped well within the depletion depth of the E-detectors. The base plate of the scattering chamber was rotated by a stepping motor drive controlled remotely by the on-line computer. A new angle setting was always approached from the same direction to avoid backlash errors in the angle readout. For the first experiments ($^{26}Mg$ and $^{16}O$ targets), the detector angles were read from the resistance of a potentiometer connected to the drive mechanism; this was limited to an accuracy of 0.2°. Later an angle encoder was installed in the chamber which enabled relative angles to be determined to 0.02° . Slit collimators in front of each telescope were used to reduce the kinematic broadening and mask the edges of the detectors. The angle in the reaction plane subtended by each collimator was always less than 0.5°. The solid angle subtended by the collimators was typically 0.2 msr: less for the most forward angle detector, more for the most backward angle detector to help offset the falling cross-section.

A fixed monitor detector was mounted on the opposite side of the beam to the detector telescopes. The elastic scattering counts recorded in this detector in conjunction with the integrated beam current from the Faraday cup were used to check for degradation of the target or shifts in the beam position. The Faraday cup was sufficiently long

(1.2 m) for suppression to be unnecessary. This assumption was confirmed during one experiment by putting various negative voltages (down to -750 V) on a short section of insulated pipe just before the cup: the ratio of the integrated current to monitor elastic counts was constant to within 4%. The monitor elastic counts were used to normalize telescope data for a given beam energy. This was done by finding the average ratio of monitor elastic counts per beam current and then constructing effective integrated currents for each run from the monitor counts recorded.

The target thickness and collection geometries of the telescopes were determined during the course of an experiment by obtaining Rutherford scattering data for several angles at incident energies in the range 12 to 18 MeV, depending on the target atomic number. Since the Rutherford cross-section is well known, this method should be accurate and eliminate any systematic error produced by the current integrator. The only error introduced would be if the position of the beam changed across a non-uniform target surface. The thickness of the $^{26}Mg$ target was measured off-line with an alpha source and the values obtained differed by less than 8%.

Centre-of-mass (c.m.) cross-sections were then calculated according to:

$$\frac{d\sigma}{d\Omega}(\theta) = \frac{Y(\theta)}{nN\Delta\Omega} = 265.7 \times \frac{Y(\theta) C \times M}{\Delta\Omega \times Q \times t} \quad mb/sr$$

where $\Delta\Omega$ = c.m. solid angle subtended (msr),

Y = number of reaction counts recorded at the c.m. angle $\theta$,

n = number of incident particles per second,

N = number of scattering centres per $m^2$ of target,

C = charge state of the beam (this was found from [Mar68]),

M = Mass of target nucleus in amu,

Q = integrated beam current in $10^{-9}$ C,

t = target thickness in $\mu g\ cm^{-2}$.

The targets were manufactured by the OEG techniques group. A list of some of the forms and measured thicknesses of the targets is given in table 2.1. Also listed in table 2.1 is the isotopic enrichment of the element; this is the specified value from the manufacturers (UKAEA Harwell). The iron targets were made from material for which records no longer existed. This was not important, as the main interest in this target was the extraction of relative spectroscopic factors for $^{54}Fe(^{9}Be,^{10}B_{0,1})^{53}Mn$. Absolute spectroscopic factors could be determined for this target, given the total thickness of iron, by measuring the ratio of yields from $^{54}Fe$ and $^{56}Fe$ since these are the only significant isotopes present.

A detailed description of the electronics used has been given in [Woo81]; a summary will suffice here. Slow coincidences were required between signals from the E and DE detectors in each telescope. The E and DE signals were recorded on magnetic tape along with a "routing" signal that labelled the telescope in which the event had occurred. The dead time of the CAMAC and on-line computer was measured by means of a pulser signal periodically sent to the preamplifiers of each telescope in turn. The dead time was typically less than 3%, but for forward angle runs, steps were taken to avoid values in excess of 10% (by reducing the beam intensity or by raising low-level discriminators in the electronics to reject elastic scattering events) so that pileup of consecutive events in the amplifiers was always negligible. In order to

Table 2.1

Target Details

| | | enrichment | thickness ($\mu g/cm^2$) |
|---|---|---|---|
| $^{26}Mg$ | self supporting foil | 98.7% | 100 |
| $^{25}Mg$ | " " " | 95.7% | 140 |
| $SiO_2$ | " " " | - | 150 ($SiO_2$) |
| $^{40}Ca$ | evaporated on 20$\mu g/cm^2$ carbon | 98% | 80 (Ca) |
| $^{39}KI$ | " " 15$\mu g/cm^2$ " | 99% | 150 (KI) |
| $^{63}Cu$ | self supporting foil | 99% | 100 |
| $^{54}Fe$ | " " " | 50%† | 180 |
| $^{24}Mg$ | " " " | 99% | 150 |
| $^{26}Mg$ | evaporated on 20$\mu g/cm^2$ carbon | 98.7% | 20 (Mg)* |

†) empirically determined (see text)

*) for high resolution experiment on spectrometer

achieve a good particle identification (PI) signal, the gains of the E and DE amplifiers needed to be accurately matched. This was done by sending pulses from a precision pulse generator through a charge terminator into both preamplifiers of a given telescope in turn. The amplifier gains were adjusted such that equal amounts of deposited charge in the detectors produced signals of equal amplitude.

The PI signal was generated within the on-line PDP-11/60 computer. The algorithm used was the one described in ref. [Woo80]. This has the form:

$$PI = \frac{(E_T^k - E^k)}{[1 + c.E/(b.E + \Delta E)]}$$

where $E_T = E + \Delta E$, the sum of the energies deposited in the residual energy and energy loss detectors. The value of the constants k, b and c depend on the thickness of the DE detector; typical values are k = 1.8, b = 4 and c = 1. The resulting PI signal is approximately independent of the particle's energy, providing the particle deposits more than 1 MeV in the E detector [Woo81]. Spectra of the total energy, $E_T$, were gated by the particle type of interest (i.e. $^{9}Be$ or $^{10}B$). Fig. 2.1 shows a PI spectrum obtained for $^{9}Be$ particles incident on a $^{26}Mg$ target. It is seen that the peaks corresponding to $^{10}B$ and $^{11}B$ are not completely separated (note that $^{9}B$ is particle unbound). Therefore on playback, the PI gates had to be set carefully to make sure that all the $^{10}B$ particles were accepted whilst excluding as many $^{11}B$'s as possible. Fortunately the Q-value of the ($^{9}Be$,$^{11}B$) reaction is quite different from that of ($^{9}Be$,$^{10}B$) for $^{26}Mg$ and $^{40}Ca$, so that in the energy region of interest a small continuum background occurs rather than additional discrete peaks. The spectra were compared with those gated on all the

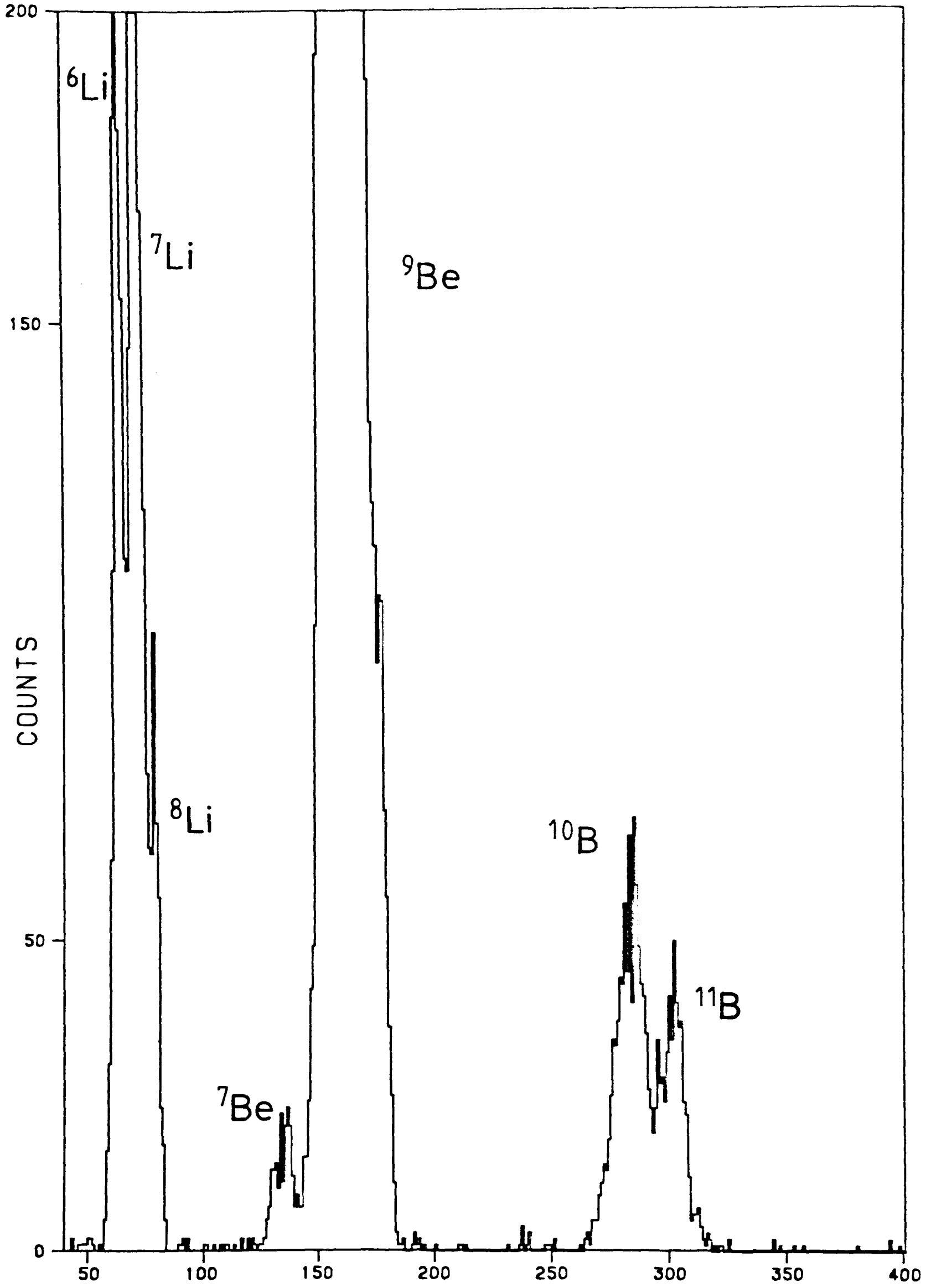


Fig. 2.1 PI spectrum for 43 MeV $^{9}$Be incident on $^{26}$Mg. $\theta_{lab}$ = 23°.

borons to check that no significant number of $^{10}B$ events were lost. Typical $^{10}B$-gated spectra are shown in figs. 2.7 to 2.10.

## 2.3 Experimental Procedure with the Oxford Spectrometer.

Use of the Oxford MDM-2 magnetic spectrometer and its associated gas-filled detector had four main advantages over the solid-state detector telescope system for the ($^{9}Be$,$^{10}B$) reactions studied:

(1) the large entrance aperture (~5 msr compared with ~0.2 msr for the solid state telescopes);

(2) the particle identification ($^{10}B$ and $^{11}B$ are cleanly separated);

(3) the elastically scattered $^{9}Be$ are deflected away from the focal plane detector when $^{10}B^{5+}$ are detected - thus the counting rate remains reasonably low ( < 1 kHz) even at very forward angles;

(4) the high resolution of the spectrometer.

Point (3) is also partly a disadvantage as it means that a separate experiment is needed if elastic scattering data is required. In any case, a large angular bite may be unsuitable if the angular distribution to be measured has very pronounced oscillations, although these could be extracted if the angle of incidence was measured.

The spectrometer entrance slit settings for the ($^{9}Be$,$^{10}B$) experiments were ±0.65" horizontally and ±0.65" vertically. This was nearly the maximum allowable by the slit box position and design then in use. It had been verified that all particles passing through this aperture (and having the correct rigidity) would also pass through the 6 cm high window opening to the focal plane detector. This was done by checking that the counting rate scaled with aperture size down to a very

small setting. The horizontal slit setting corresponded to an angular acceptance of ±2.0° (in the laboratory frame). Thus each data point in the resulting angular distribution represents an average over this range.

The dipole magnet was set to bring $^{10}B$ ions in their $5^+$ charge state onto the focal plane. At even the lowest $^{10}B$ energy considered, that for $^{40}Ca(^{9}Be,^{10}B)$ at $E(^{9}Be)$ = 30 MeV, $\theta_{lab}$ = 37°, the charge state probability for $^{10}B^{5+}$ is greater than 98% [Mar68]. The pressure within the spectrometer was less than $5\times10^{-6}$ mbar. For vacuums as good as this, charge-exchange for the in-flight ions by collision with residual gas atoms is believed to be negligible; Chait [Cha76] presents some calculations for $^{16}O$ ions at similar pressures.

The hybrid focal plane detector for the spectrometer is described in detail in the next chapter including an account of the electronics used and method of data analysis. It is therefore sufficient here to list some parameters used specifically for the $(^{9}Be,^{10}B)$ experiments. The gas pressures required to stop the $^{10}B$ particles in the region between the second proportional wire and the end of the counter varied from 90 to 35 torr of isobutane, depending on the reaction Q-value and scattering angle. A 12.5 $\mu$m Mylar window was used to contain the gas at the entrance to the counter.

A contour representation of a $\Delta E$ versus E two-dimensional spectrum obtained from the gas detector is given in fig. 3.10. Windows on spectra such as these were used to project-out position spectra for $^{10}B$ ions. Fig. 3.10 shows that the separation of $^{10}B$ from its nearest contaminant, $^{11}B$, is almost complete. Total separation of these two

ions could be achieved by setting a window around the boron group in the ΔE-E spectrum and using this to construct a sorted position versus E spectrum (see fig. 3.11).

Three points should be noted about the arrangement in the spectrometer's scattering chamber. First, the small Faraday cup within the chamber needed to be suppressed before a true reading of the integrated beam current was obtained. This was realized by placing a ring of metal, held at a potential of -500 V, immediately in front of the cup. This voltage was ascertained to be sufficient by variation. Secondly, the angle that the target ladder presented to the beam was adjusted whenever the spectrometer angle was changed, so that the combination of energy-loss straggling by the $^{9}Be$ entering and the $^{10}B$ leaving the target was roughly minimised. This was done by setting the angle between the target and the normal to the beam to be one half of the spectrometer angle. This does not, of course, completely optimize the effects of energy-loss straggling since that from the $^{10}B$ is greater than $^{9}Be$, but the error is small. The third point about the arrangement in the scattering chamber is that a surface barrier detector was mounted at an angle of 25° to the beam in order to monitor the target. As for experiments on line A3, data points at different angles were normalized with respect to the number of elastic scattering counts in this detector.

## 2.4 Energy Resolution.

There will be contributions to the energy resolution from various effects caused by the finite target thickness, noise in the detector and electronics, and because the beam is not perfectly monoenergetic or parallel. For the solid state detector telescope experiments, there will also be an important contribution from kinematic broadening. It is therefore convenient to discuss the expected resolution for the spectrometer experiments separately.

The accelerator beam quality should be approximately independent of the particular beamline in use (the additional 90° magnet in the spectrometer beamline does not further analyse the beam). The energy resolution of the beams used in these experiments is discussed in appendix C. The divergence of the beams is calculated from the emittance, which is estimated as $9\pi/\sqrt{E_b}$ (mm mrad $\sqrt{}$MeV), where $E_b$ is the beam energy in MeV [Pri83].

### 2.4.1 Energy Resolution in the Detector Telescope Experiments.

We consider specifically the case of the $^{26}Mg(^{9}Be,^{10}B)^{25}Na$ reaction at an incident energy of 43 MeV and a detection angle of $13^{\circ}_{lab}$. The target was a self-supporting 100 $\mu g/cm^2$ magnesium foil.

There will be contributions from kinematic broadening caused by the finite beam size at the target (assumed to be equal to that of the 3 mm diameter beam collimator in the target chamber, the divergence making negligible difference), the finite horizontal collimation in front of the detectors and the divergence of the beam. For the experiment considered, the beam spot on the target subtended an angle of 0.9° at

the detector collimator and the detector collimator subtended 0.4° at the target. Given that the change in energy of the outgoing $^{10}B$ nucleus with angle is 117 keV/degree, the spread in energy from these two sources is calculated as 110 keV and 51 keV respectively. That from the estimated 0.08° divergence of the beam is 9 keV.

The largest contribution to the resolution from the target is that caused by the difference in rate of energy-loss between $^{9}Be$ and $^{10}B$, and thus the dependence on total energy-loss upon the position of the interaction within the target (the large negative Q-value of the $^{26}Mg(^{9}Be,^{10}B)^{25}Na$ reaction exaggerates this effect). The maximum energy spread in keV is given by

$$\left( \text{S.P.(eject.)} \times \frac{1}{\cos(\theta-\theta_t)} - \text{S.P.(proj.)} \times \frac{1}{\cos\theta_t} \right) t \qquad (2.1)$$

where S.P. is the stopping power in keV/$\mu$g/cm$^2$, t is the absolute target thickness in $\mu$g/cm$^2$, $\theta$ is the scattering angle and $\theta_t$ is the target angle. For the case under consideration, this works out to be 108 keV. Equation 2.1 shows that this energy spread will become greater as the angle of detection increases, especially if the target is maintained perpendicular to the beam. However, this helps reduce the effective beam spot size at backward angles.

The energy-loss straggling has been calculated by use of a program written by Clarkson and Jarmie [Cla71] that takes a Vavilov distribution. Assuming that the interaction takes place in the middle of the target and adding in quadrature the fwhm energy spreads for $^{9}Be$ and $^{10}B$ gives a total energy-loss straggling of 30 keV fwhm. An alternative approach that takes the average of the energy spreads for

$^{9}Be$ and $^{10}B$ passing through the whole thickness of target gives 31 keV fwhm.

Any variation in target thickness will result in corresponding differences in energy lost by the traversing ions. A 15% variation, which is probably a generous estimate of this, gives an energy spread of 22 keV. Finally, multiple scattering in the target has been estimated from the formulae given by Marion and Young [Mar68] to produce an angular spread of 0.2° fwhm. This is converted by kinematic broadening to an energy spread of 22 keV.

The energy resolution of the thick solid state detector used was measured by the use of an alpha source to be ~~25~~ 60 keV. The contribution of the electronics (mainly the preamplifier) for one detector is also estimated to be small: from the observed width of the pulser peak it is 50 keV.

All these contributions are listed in table 2.2, where it is seen that kinematic broadening and target effects dominate. It is concluded that the resolution could only be significantly be improved at the cost of a lower count-rate. The experimentally observed fwhm energy resolution was 220 keV (fig. 2.7). This is in reasonable agreement with the result of adding all the theoretical contributions in quadrature (190 keV).

### 2.4.2 Energy Resolution in the Experiments with the Spectrometer.

With the exception of the finite angle of acceptance, for which the spectrometer is kinematically compensated, the sources of energy spread for the experiments performed with the spectrometer are basically the

Table 2.2

Contributions to Energy Resolution in Detector Telescope Experiments

| Source of energy spread | Spread (keV) |
|---|---|
| Beam energy variation | 15 |
| Beam divergence | 9 |
| Finite Beam spot | 110 |
| Finite collimator size | 51 |
| Difference in energy-loss $^{9}Be, ^{10}B$ | 108 |
| Energy-loss straggling | 30 |
| Target non-uniformity (15%) | 22 |
| Multiple scattering in target | 22 |
| Detectors and electronics (×2) | 79 |

same as those considered in the previous section. The relative importance of each contribution is rather different, however, since kinematic broadening is now removed. For example, the effect of the beam collimator width, which dominated table 2.2, is felt here merely through the spectrometer's horizontal magnification (M = 0.42) and is almost negligible.

To illustrate the change in importance with angle and target of the various components in the total energy spread, four cases are listed in table 2.3. Some explanation is required of the estimations before the table can be discussed. As in the previous section, an effect which causes a scatter in angle of the emerging particles must be converted into a corresponding scatter in energy at the detection instrument. When the discussion concerns magnetic spectrometers, it is conventional to define a kinematic factor, $k = -(1/p)(dp/d\theta)$, where p is the particle's momentum and $\theta$ the scattering angle. Then a spread in angle of magnitude $\Delta\theta$ is converted to a spread in energy $\Delta E$ through

$$\Delta E/E = |2k\Delta\theta|.$$

The values of k for each case are also given in table 2.3.

The effects of target thickness have been calculated as before, except that the target angle, $\theta_t$ in equation 2.1, is not 90°. The beam divergence is estimated to have been greater for these experiments since a narrower beam collimator was used (1 mm as opposed to 3 mm). The spectrometer and focal plane detector together are known to have an intrinsic energy resolution of better than 1 part in 3000 (see Chapter 3) and this figure was assumed as an upper limit for the present purposes.

Table 2.3 shows that, whilst at forward angles the difference in energy-loss of the $^{9}Be$ and $^{10}B$ particles is dominant, at more backward angles effects due to the divergence of the beam and multiple small angle scattering in the target become progressively more important. This is simply a reflection of the increase of the kinematic factor with angle. The reaction on the $^{63}Cu$ target has the lowest k-value and also the most positive Q-value, so that the emerging $^{10}B$ particles are at higher energies compared to the experiments with the magnesium targets (other things being equal). This results in the contributions to broadening for the $^{63}Cu$ target being the smallest.

The results of the contributions to energy broadening have been added in quadrature and compared with the experimentally observed (fwhm) peak widths. The agreement is fair considering that this summing procedure is rather dubious in view of the expected shape of the individual energy spread distributions.

## 2.5 Sources of Error.

### 2.5.1 Random Errors.

Statistical fluctuations in the number of counts in a peak are obviously more important when count rates are low, i.e. at backward angles or for low cross-section reactions. This error is usually the dominant one in such cases.

A second type of statistical error enters the analysis through the method of normalization of each data point at different angles since the number of counts in the monitor spectrum elastic scattering peak will

Table 2.3

Contributions to Energy Resolution for some ($^{9}Be$,$^{10}B$) Experiments Performed on the Oxford Spectrometer.

| Target | $^{24}Mg$ | $^{24}Mg$ | $^{63}Cu$ | $^{26}Mg$ | |
|---|---|---|---|---|---|
| $\theta_{lab}$ | 9° | 27° | 31° | 35° | |
| kinematic factor, k | 0.07 | 0.20 | 0.08 | 0.25 | |
| Outgoing $^{10}B$ energy (MeV) | 37 | 34 | 41.6 | 31.3 | |
| Target thickness ($\mu g/cm^2$) | 150 | 150 | 100 | 100 | |
| 1) Energy-loss straggling | 40 | 41 | 32 | 31 | |
| 2) 15% Target non-uniformity | 33 | 36 | 17 | 22 | |
| 3) Difference in energy-loss | 125 | 145 | 64 | 104 | |
| 4) Target multiple scattering | 22 | 69 | 29 | 71 | |
| 5) Beam divergence (4.4 mrad) | 26 | 75 | 30 | 94 | |
| 6) Beam energy spread | 15 | 15 | 15 | 15 | |
| 7) Spectrometer object size | 10 | 10 | 10 | 10 | |
| 8) Spectrometer + f.p. detector | 12 | 11 | 14 | 10 | |
| Added in quadrature | 141 | 171 | 88 | 163 | keV |
| Observed fwhm | 132 | 157 | 90 | 145 | keV |

also show statistical fluctuations. However, during the experiment this was ensured always to be a large number (>5000, say) so that the associated random error is small.

In some cases, particularly for forward-angle elastic scattering data when composite targets were used, it was necesary to use a double or triple Gaussian fit to obtain estimates of the number of counts in the peaks. There is then an error caused by the inaccuracy of the fit to the data, especially if the peaks are not strictly of the Gaussian shape.

The error bars on the points in the angular distributions presented in this thesis include all the above uncertainties. There are, however, some other small sources of random error which have not been included.

The dead time monitoring introduces a second-order error - second-order since it is an error in a quantity that is a correction applied to the data. An estimate of the uncertainty in the dead time measurement is obtained through the comparison of two different methods. For the experiments with the spectrometer the dead time was measured both by the pulser method described in section 2.2 and by comparing the number of strobes sent to CAMAC with the total integrated number of counts for a given ADC, including channel zero. These two methods always agreed to within 4%, and since the actual size of the dead time correction was less than 10%, the resulting uncertainty in the data after the correction is applied may be safely assumed to be negligible.

There was a random error in the angle settings from data point to data point. This is expected to be more important for the elastic scattering experiments where other (statistical) errors are small and

the angular distributions are more oscillatory. The accuracy of the angle readout on the scattering chamber A3 has been mentioned in section 2.2. Several points on an elastic scattering distribution were always repeated during an experiment, partly to check telescope relative normalizations. This also reduces the angular uncertainty on the combined data points for these cases. The spectrometer angle setting could be read to within 0.1° and in view of the nature of the smoothly varying reaction cross-sections studied and the 4° horizontal acceptance used, the error involved may be neglected.

Particles which lose an anomalously large or small amount of energy in the DE detector (or under the ΔE plate of the spectrometer's focal plane detector) may give a PI signal that falls outside the window used to gate the total energy spectra. It is difficult to estimate the size of this error but the lack of counts around the peaks in the PI spectra (see figs. 2.1 and 3.10) suggests that it will be small. The number of counts in a given elastic scattering peak differed by <1% whether the spectra were gated by the beryllium group or not.

2.5.2 Systematic Errors.

For the experiments performed on line A3 there was an uncertainty of approximately 0.2° in the 0° and 180° angle settings determined by lining up detector collimators through a telescope. There is also a possible systematic angle error if the beam does not pass straight through the geometric axis of the chamber, but this could not have been more than 0.4° from the maximum observed displacement of the beam spot. Upper limits on these errors could be estimated by comparing the position of various identified peaks in the spectra against the

calibrations for different angle hypotheses. By this method the "true" angle for a given run could be determined to within ±0.15°. No systematic error greater than 0.1° was observed in any experiment.

The zero angle on the spectrometer has been determined to within 0.1° by fitting Rutherford scattering of 43 MeV $^{9}$Be from a gold target (this included data taken for angles on either side of the beam). During the reaction experiments, the beam may have entered at a small angle to the zero but evidence from the position of the beam spot suggests this would be <0.3° for all cases. This would make negligible difference to the reaction cross-section normalization.

The target thicknesses and collection geometries for the solid state detector telescope experiments were determined together through the Coulomb elastic scattering data, as explained in section 2.2. The accuracy of the overall normalization of the angular distributions obtained in these experiments is estimated as 8%.

The normalization of the data from the spectrometer is less certain since it was determined through the spectrometer's geometric solid angle of acceptance, the integrated current from the Faraday cup and the target thickness. The target thickness was estimated from the elastic scattering count-rate in the monitor spectrum - this is accurate provided that the cross-section is well-known. The thickness of the $^{63}$Cu target was also measured off-line with an alpha source and this result agreed to within 15% with the value deduced by the above method. The systematic error on the normalizations for the $^{24}$Mg, $^{63}$Cu and 30 MeV $^{40}$Ca experiments is therefore estimated as 15%. The $^{54}$Fe reaction data normalization has an additional uncertainty caused by the presence of a

significant amount of $^{56}Fe$ in the target.

## 2.6 Examples of Spectra Obtained.

The energy spectrum for the elastic scattering of $^{9}Be$ on $^{26}Mg$ at 27.7° is shown in fig. 2.2. The spectrum is dominated by the $^{26}Mg$ elastic scattering peak. Peaks on the high energy side of this correspond to scattering on tantalum and other heavy element contaminants present in small quantities from the target manufacture. Peaks are labelled that arise from elastic and inelastic scattering on $^{26}Mg$, $^{16}O$ (present from the oxidation of the target) and $^{12}C$ (deposited on the surface of the target during the course of bombardment). The ground state of $^{26}Mg$ is deformed and the first $2^+$ state at 1.809 MeV is quite strongly coupled to it (see, for example, Blair and Naqib [Bla70] who found $\beta_2 = 0.29$). In fig. 2.2 the second $2^+$ state at 2.938 MeV (which is the ground state of the $K^\pi = 2^+$ rotational band) is seen to be less strongly excited. Some strength to the triplets of levels at 4.3 and 4.9 MeV is also observed. At certain more forward angles the elastic scattering peaks from the $^{12}C$ and $^{16}O$ contaminants in the target cross through the $^{26}Mg_{1.81}$ peak, making analysis impossible. No peaks corresponding to projectile excitation are observed because all excited states in $^{9}Be$ are unbound.

Sample energy spectra for the elastic scattering of $^{9}Be$ on the $SiO_2$ and $^{40}Ca$ target are shown in figs. 2.3 and 2.4 respectively. The important peaks have been labelled (note that the $^{40}Ca$ target had a carbon backing which accounts for the relatively large peak from that nucleus in the spectrum).

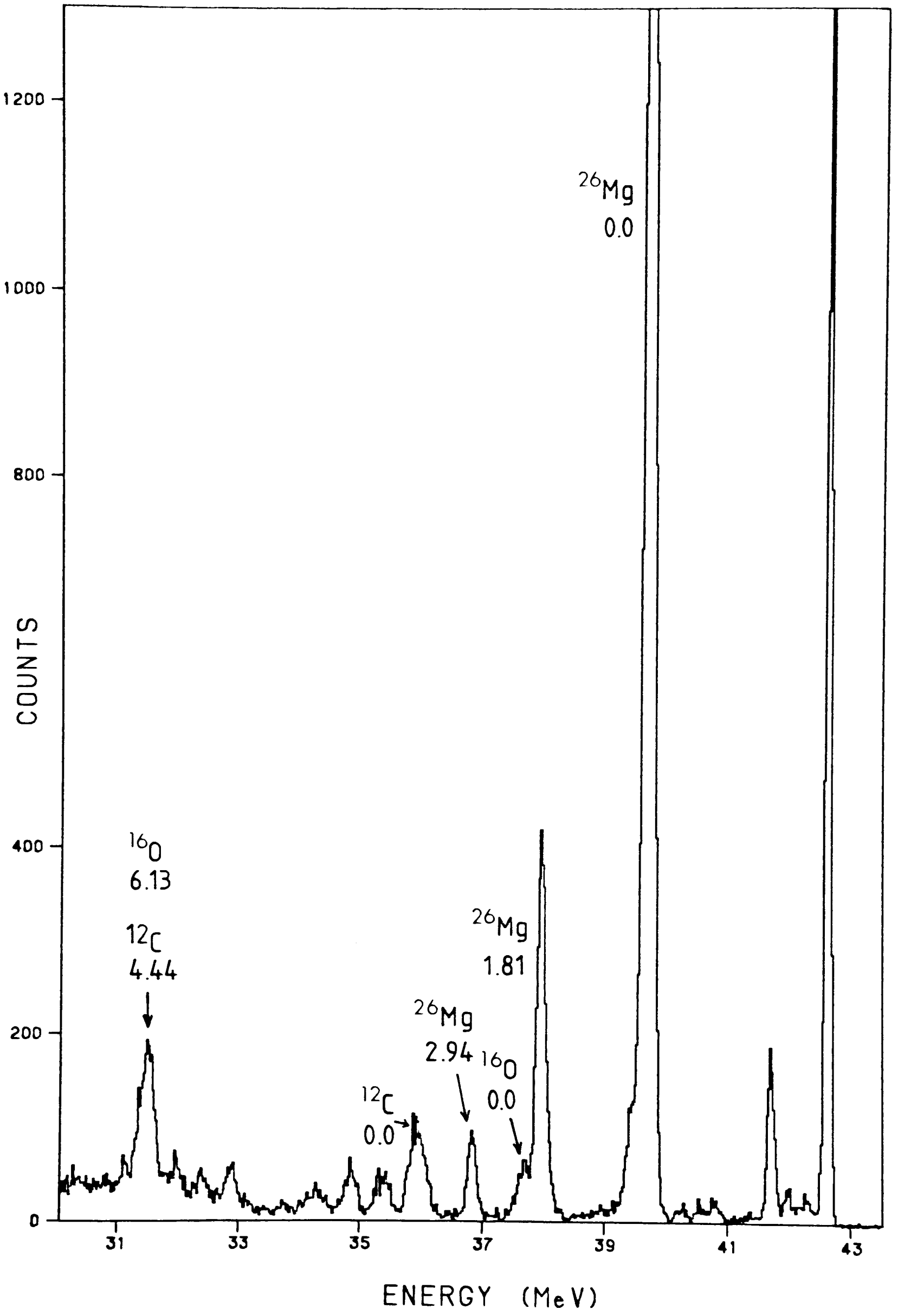


Fig. 2.2 Ungated energy spectrum obtained at $\theta_{lab} = 28°$ for 43 MeV $^{9}$Be incident on a $^{26}$Mg target. Peaks of interest are labelled.

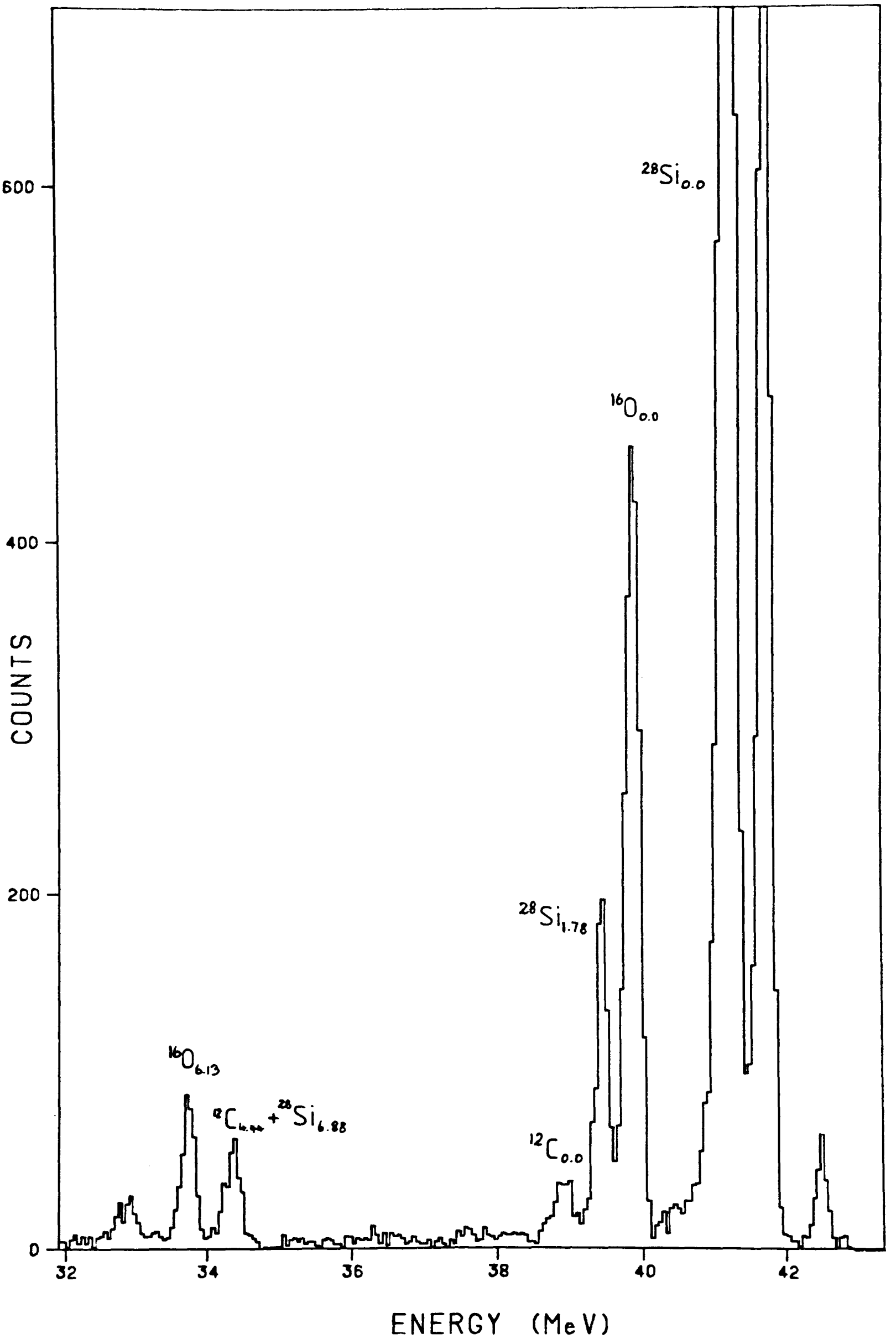


Fig. 2.3 Beryllium-gated energy spectrum for $^{9}$Be elastic and inelastic scattering on a $SiO_2$ target. $\theta_{lab} = 21°$.

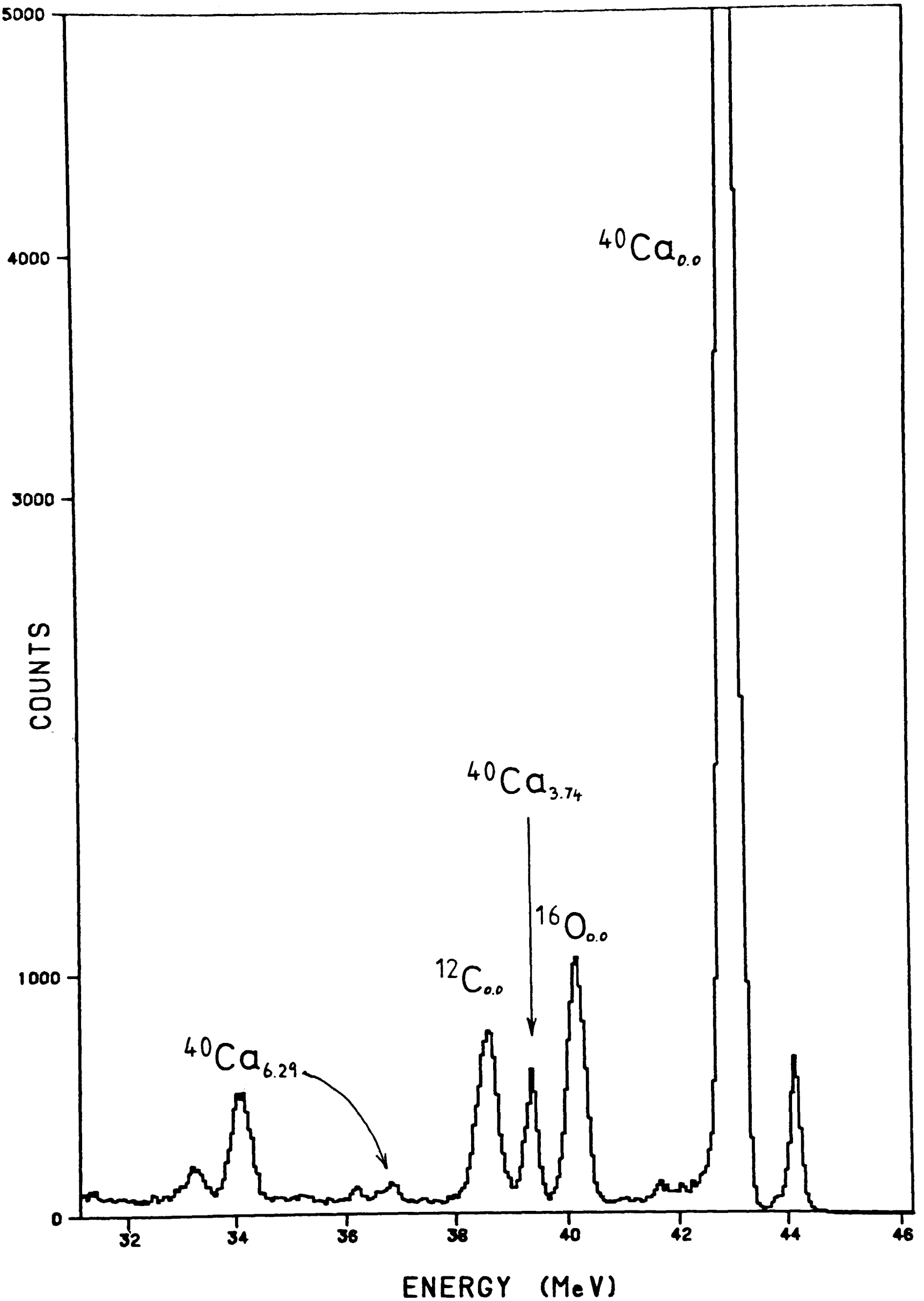


Fig. 2.4 Spectrum for $\theta_{lab} = 26°$ elastic and inelastic scattering of 45 MeV $^{9}Be$ on a $^{40}Ca$ target.

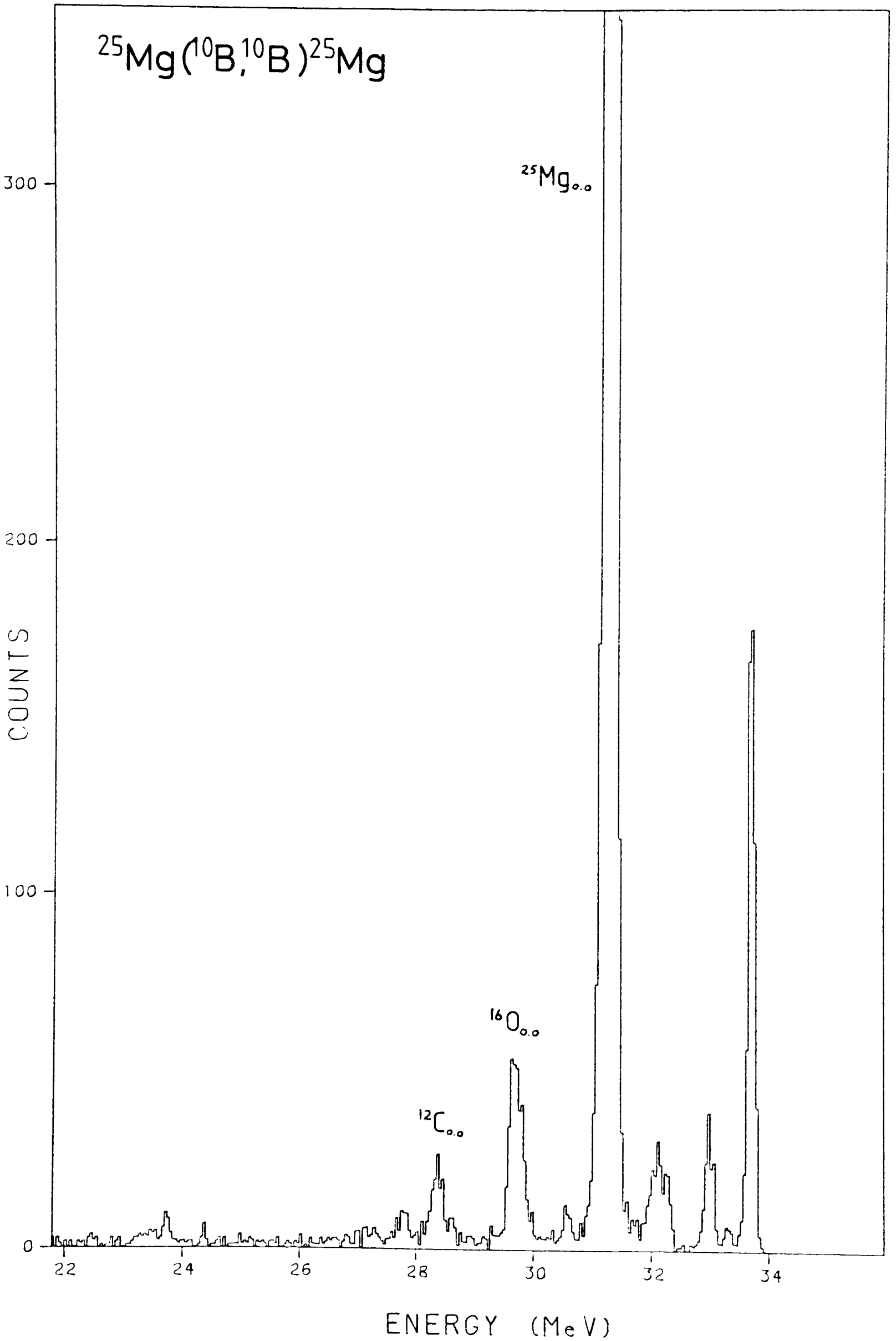


Fig. 2.5 Elastic scattering energy spectrum for 33.9 MeV $^{10}B$ on a $^{25}Mg$ target with $\theta_{lab} = 26°$.

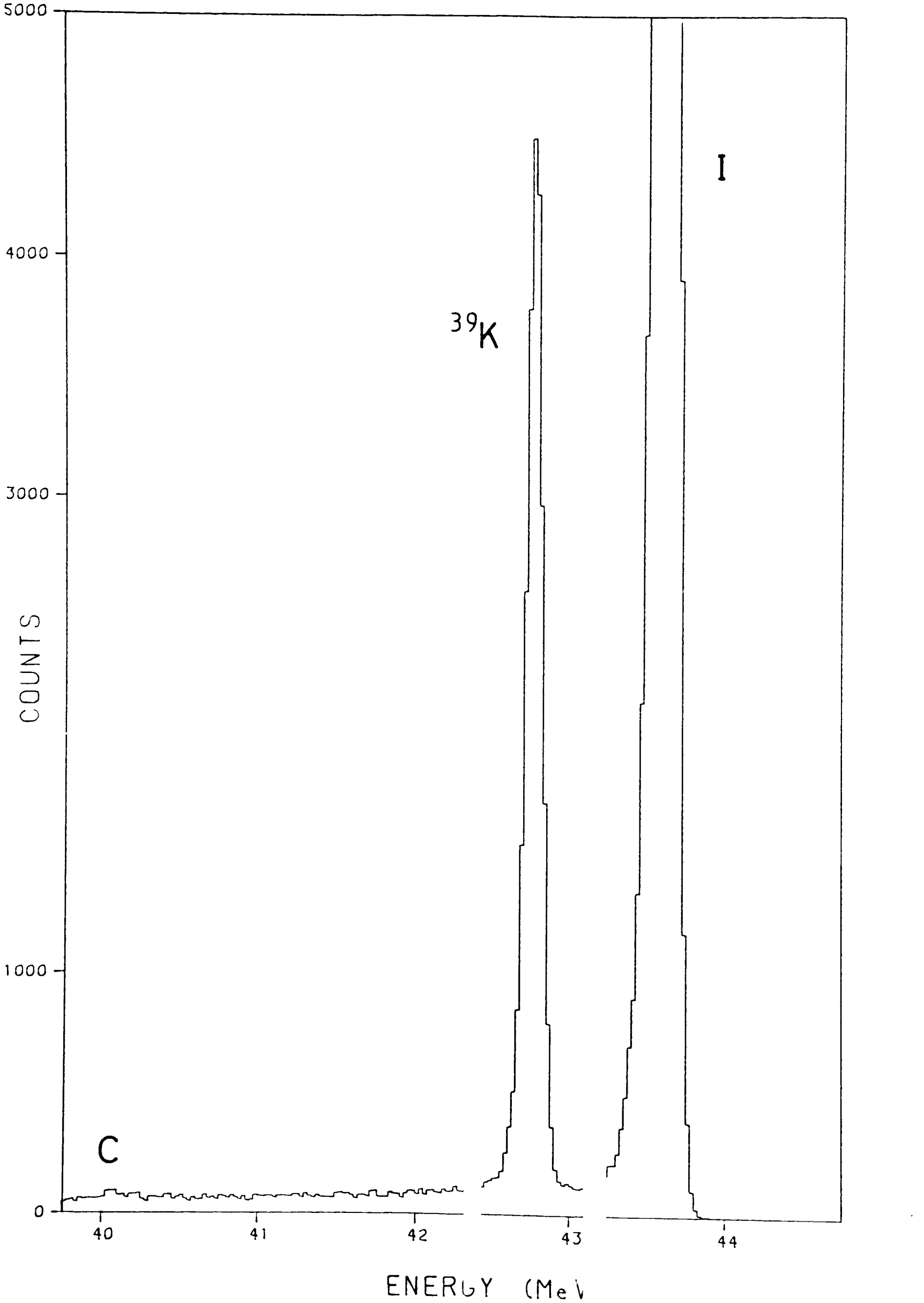


Fig. 2.6 Elastic scattering energy spectrum fo 43.96 MeV $^{10}B$ on a $^{39}KI$ target. $\theta_{lab} = 19°$.

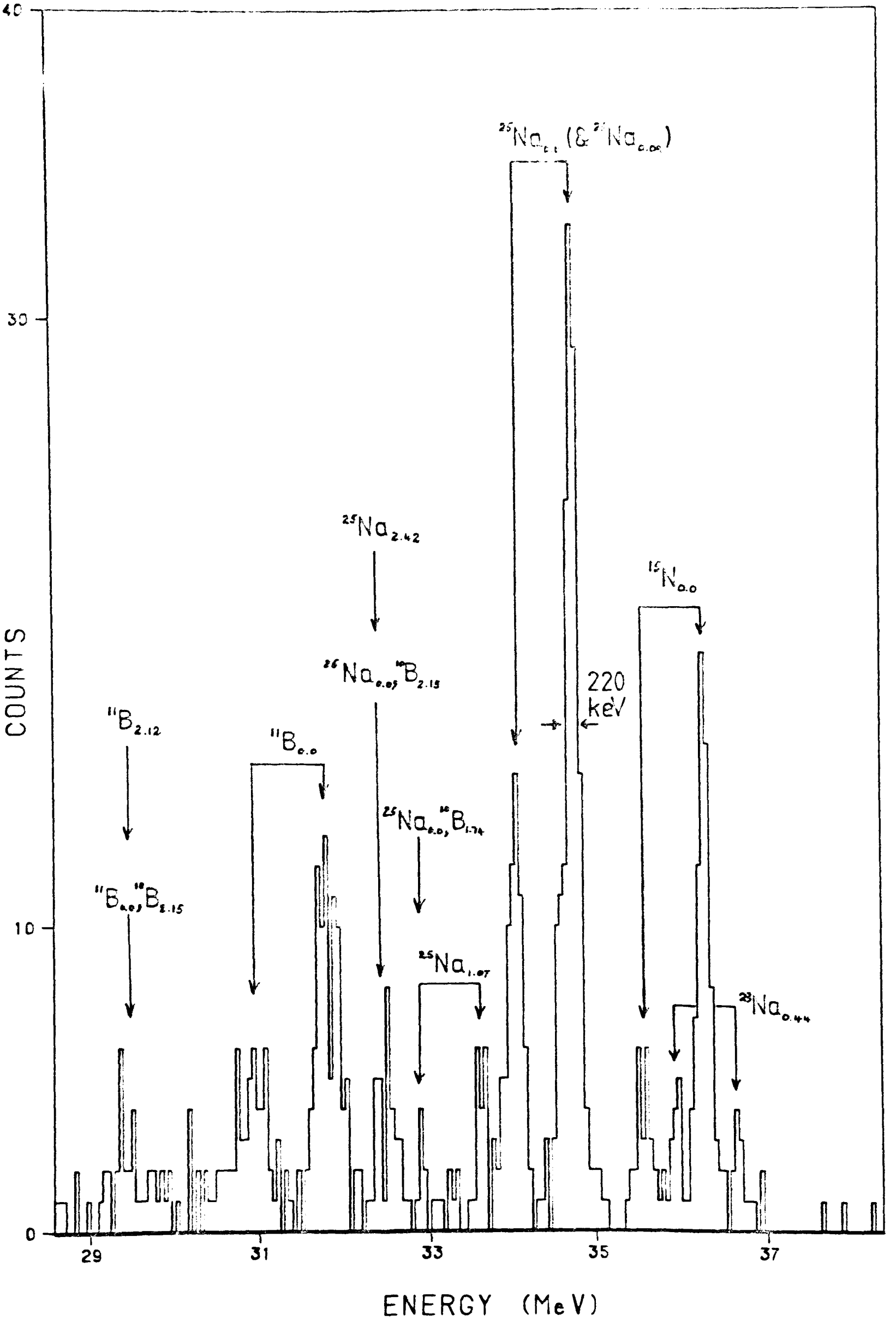


Fig. 2.7 $^{10}$B-gated energy spectrum at $\theta_{lab}$ = 13° for 43 MeV $^{9}$Be incident on a $^{26}$Mg target. The double arrows indicate population of the 0.0 and 0.72 MeV states in $^{10}$B. The labels refer to states in the residual nuclei.

The elastic scattering spectrum of $^{10}B$ on $^{25}Mg$ at 26° is shown in fig. 2.5 and that for $^{10}B$ on $^{39}K$ at 19° in fig. 2.6. The latter spectrum has a very large peak from the iodine in the target. The $^{39}K$ peak is well separated from this, however, and analysis was straightforward.

The $^{10}B$-gated energy spectrum for $^{9}Be$ + $^{26}Mg$ at 13° is shown in fig. 2.7. Reaction peaks are observed for $^{26}Mg$, the contaminants $^{16}O$ and $^{12}C$ and also for the small amount of isotopic impurity, $^{24}Mg$, in the target. The spectrum is complicated by the relatively high number of bound states in the ejectile, so that for every residual nucleus state there are up to six possible peaks in the spectrum. Fig. 2.8 shows the low-lying energy levels as given by Lederer and Shirley [Led78]. Fortunately for the purposes of analysis, only the ground and

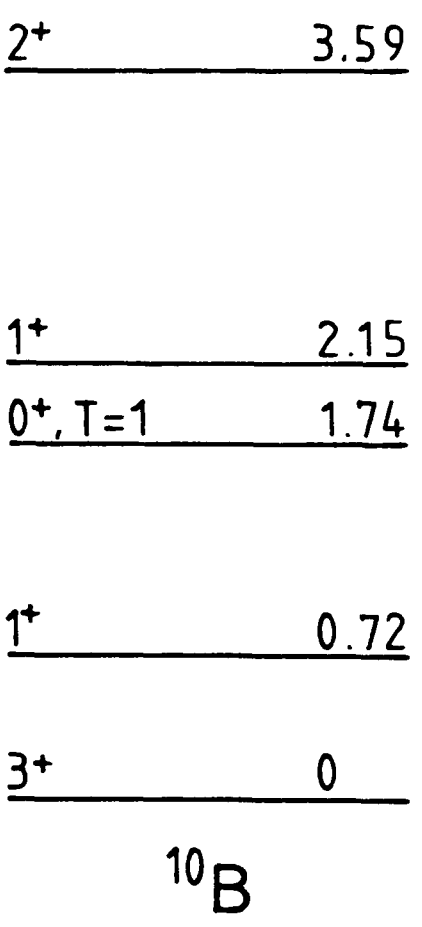


Fig. 2.8

first excited states are strongly populated (the lower excitations are

preferred because of the kinematic matching of the reactions, as will be explained in Chapter 5, and also because the $1^+$, 1.74 MeV and the $2^+$, 3.59 MeV states in $^{10}B$ have small spectroscopic factors [Coh67]). Thus for every state of the residual nucleus ($^{25}Na$, $^{15}N$, $^{11}B$, etc.) we see in fig. 2.7 doublets corresponding to the 0.0 and 0.718 MeV states in $^{10}B$. The largest doublet observed is that for the $^{26}Mg(^{9}Be,^{10}B_{0,1})^{25}Na_{0,1}$. The ground state and first excited state of $^{25}Na$ are not resolved in this experiment as has already been mentioned. A weak doublet corresponding to $^{25}Na$ in its second (1.07 MeV) excited state is also observed. The peaks arising from the $^{16}O$ contaminant are a slight problem in this reaction since as the scattering angle is increased they "move" through the peaks of interest and extraction of the data is difficult. At more backward angles the resolution deteriorates because the effect of kinematic broadening is greater.

The $^{10}B$-gated spectrum for the $SiO_2$ target is shown in fig. 2.9. At many angles with this target various members of the low-lying states in $^{27}Al$ give rise to peaks below the $^{15}N$ ones of interest. However, the spectroscopic factors to the 0.844, 1.014, 2.734, 2.98 and 3.68 MeV levels in $^{27}Al$ are all one-fifth or less of that to the ground state [End77] (other transitions to low-lying states were too weak to be measured), and the ground state transition is fairly small compared to $^{16}O(^{9}Be,^{10}B)^{15}N_0$. The transitions to the first two excited states of $^{27}Al$ are confirmed to be small in this spectrum and at more backward angles other states are seen with very low cross-section. For angles less than $12°_{lab}$, it was not possible to obtain reliable data for $^{15}N$ from this target, since the non-negligible doublet from $^{27}Al_0$ begins to interfere. Three data points for the angular distribution have instead

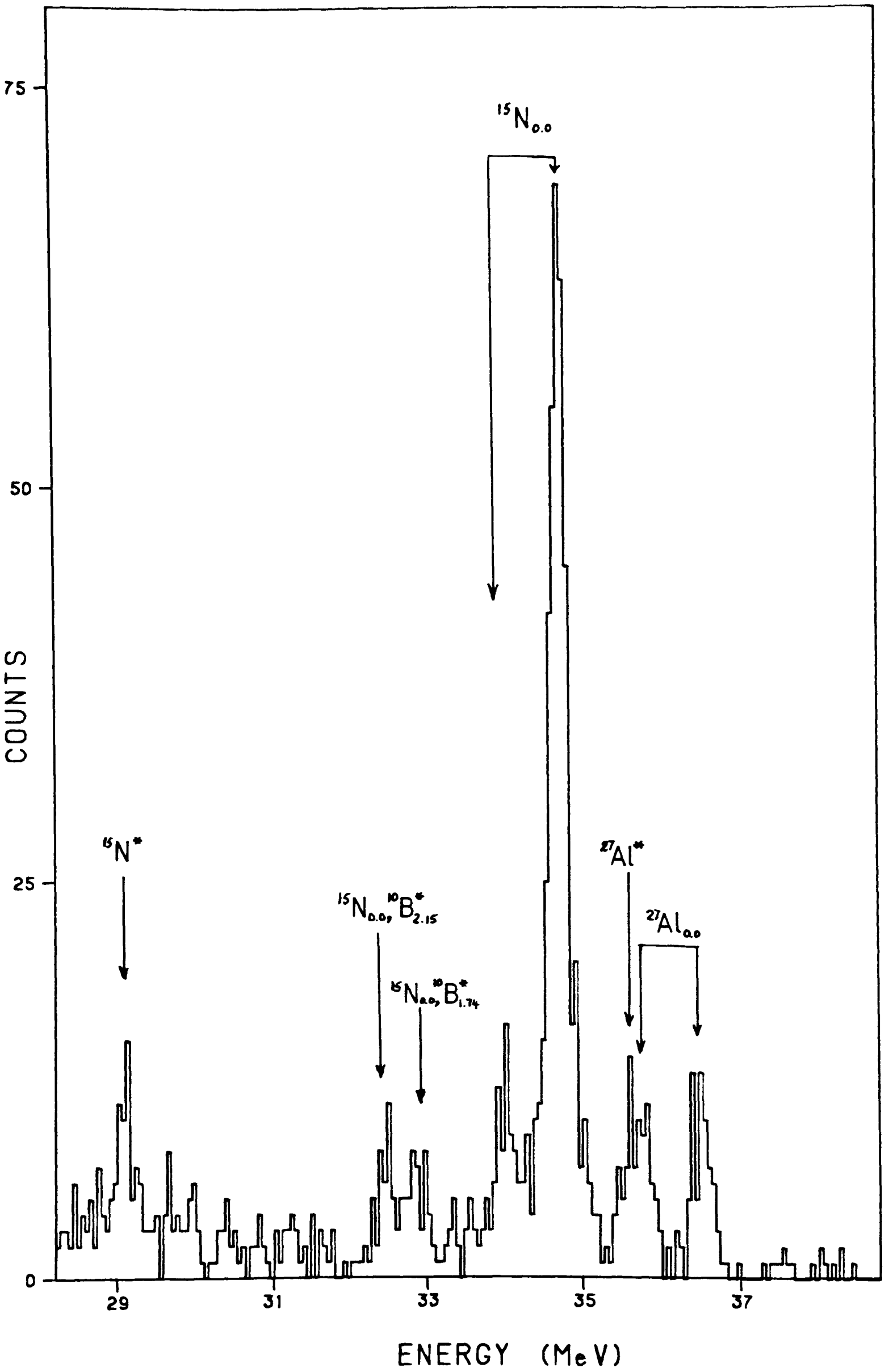


Fig. 2.9 Boron-gated spectrum obtained at $\theta_{lab} = 19°$ for 43 MeV $^{9}Be$ on a $SiO_2$ target (see caption to fig. 2.7). The arrow labelled "$^{27}Al^{*}$" indicates the expected position of the 0.844 and 1.014 MeV excited states of that nucleus.

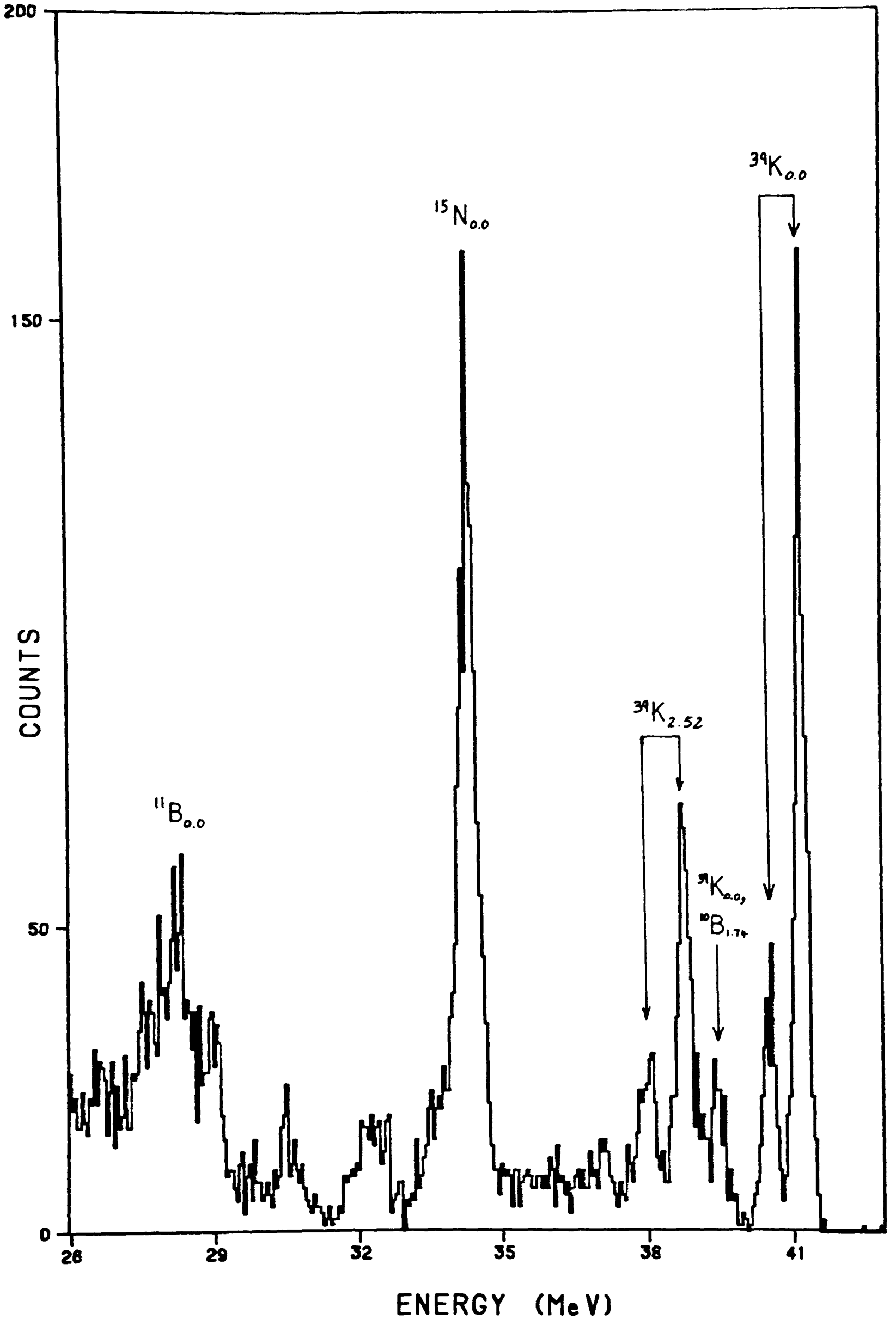


Fig. 2.10 $^{10}$B-gated energy spectrum at $\theta_{lab}$ = 26° for 45 MeV $^{9}$Be on a $^{40}$Ca target (see caption to fig. 2.7).

been extracted from analysis of the $^{16}O$ contaminant in the $^{26}Mg$ target. These points were normalized to the $SiO_2$ data by comparison of the $^{16}O$ elastic scattering yields.

The $^{10}B$-gated spectrum for $^{9}Be + ^{40}Ca$ is displayed in fig. 2.10. In this case, the small negative Q-value of the $^{40}Ca(^{9}Be,^{10}B)^{39}K$ reaction keeps the peaks of interest well away from contaminant peaks and from the $^{12}C(^{9}Be,^{10}B)^{11}B$ doublet due to the carbon backing of the target.

Sample position spectra taken with the Oxford spectrometer are shown for $^{63}Cu, ^{54}Fe, ^{40}Ca, ^{24}Mg(^{9}Be,^{10}B)$ in figs. 2.11, 2.12, 2.14 and 2.13 respectively. Fig. 2.13 shows spectra for a range of angles as a good illustration of how the lighter $^{16}O$ contaminant doublet progresses across the $^{24}Mg$ doublets as the scattering angle is increased. One can also see that the peaks arising from the $^{16}O$ are not focussed by the spectrometer since the position of the focal plane changes with the kinematic factor, k (see Chapter 3, section 3.2).

The spectrum for the iron target shows peaks for excited states in $^{53}Mn$ and $^{55}Mn$. The $7/2^-$ state in $^{53}Mn$ at 0.0 MeV and the corresponding one in $^{55}Mn$ at 0.126 MeV are expected to be much more strongly populated than the other low-lying states [New68], so that although the $^{55}Mn(0.126)$ peak lies on top of the $^{53}Mn(3/2^-,1.289)$ peak, the contribution of the latter is insignificant.

Finally a $^{10}B$-gated position spectrum for the experiment with the thin $^{26}Mg$ target is shown in fig. 2.15. This was taken in order that an estimate of the $^{25}Na_0$:$^{25}Na_1$ population could be made. The Gaussian fit laid over the spectrum gave a value of 5.9:1 for this ratio. The

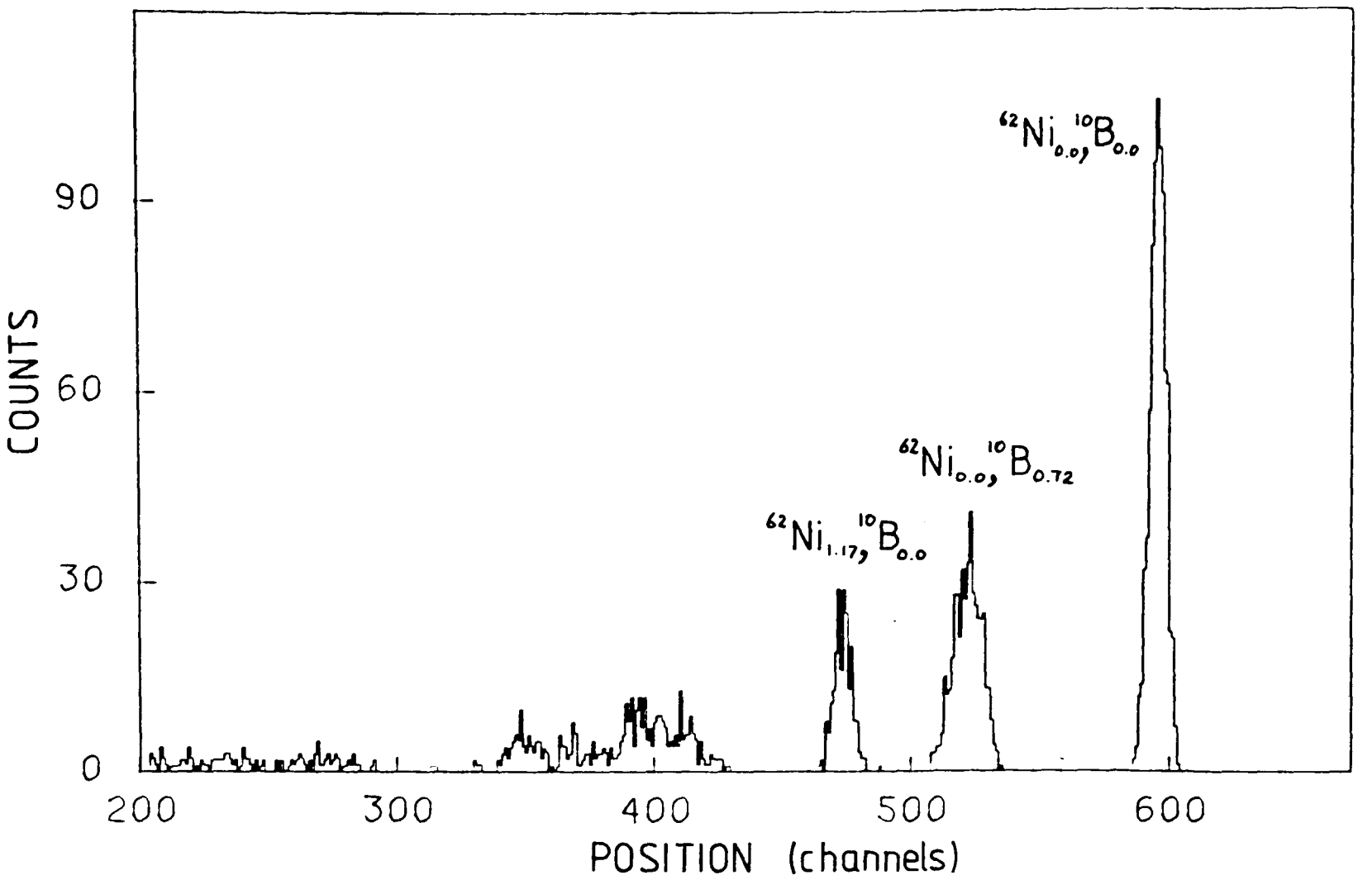


Fig. 2.11 Position spectrum for $^{63}Cu(^{9}Be, ^{10}B)^{62}Ni$ taken with the Oxford spectrometer and focal plane detector. The spectrometer angle was 18°. Note the lack of background around the lower excited states.

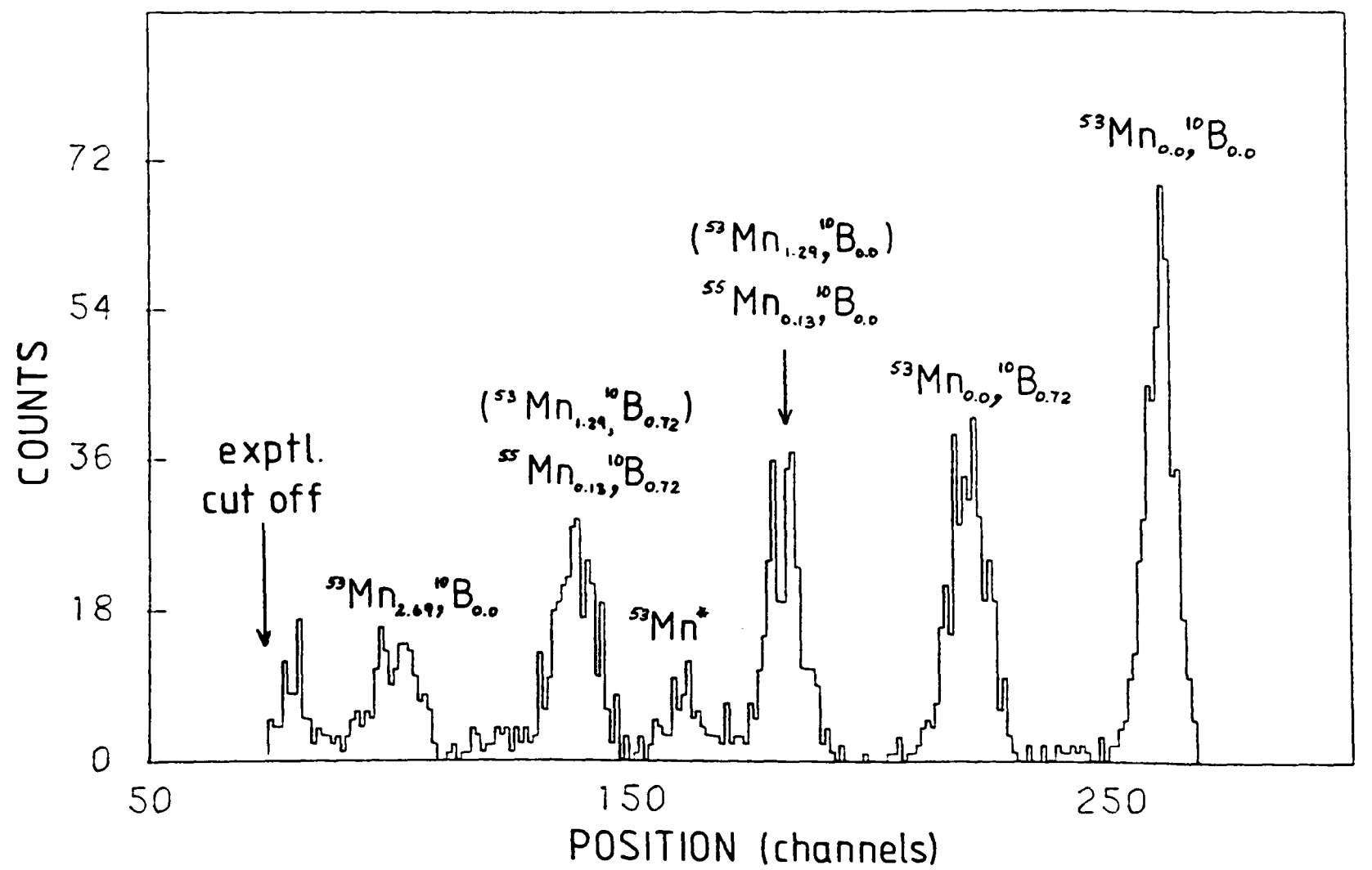


Fig. 2.12 $^{10}B$-gated position spectrum for 43 MeV $^{9}Be$ incident on an iron target. States in the residual nuclei and ejectile are indicated. Most of the contribution to the peak labelled $^{53}Mn^{*}$ is probably $(^{53}Mn_{0.0}, ^{10}B_{1.74})$. $\theta_{lab} = 24°$

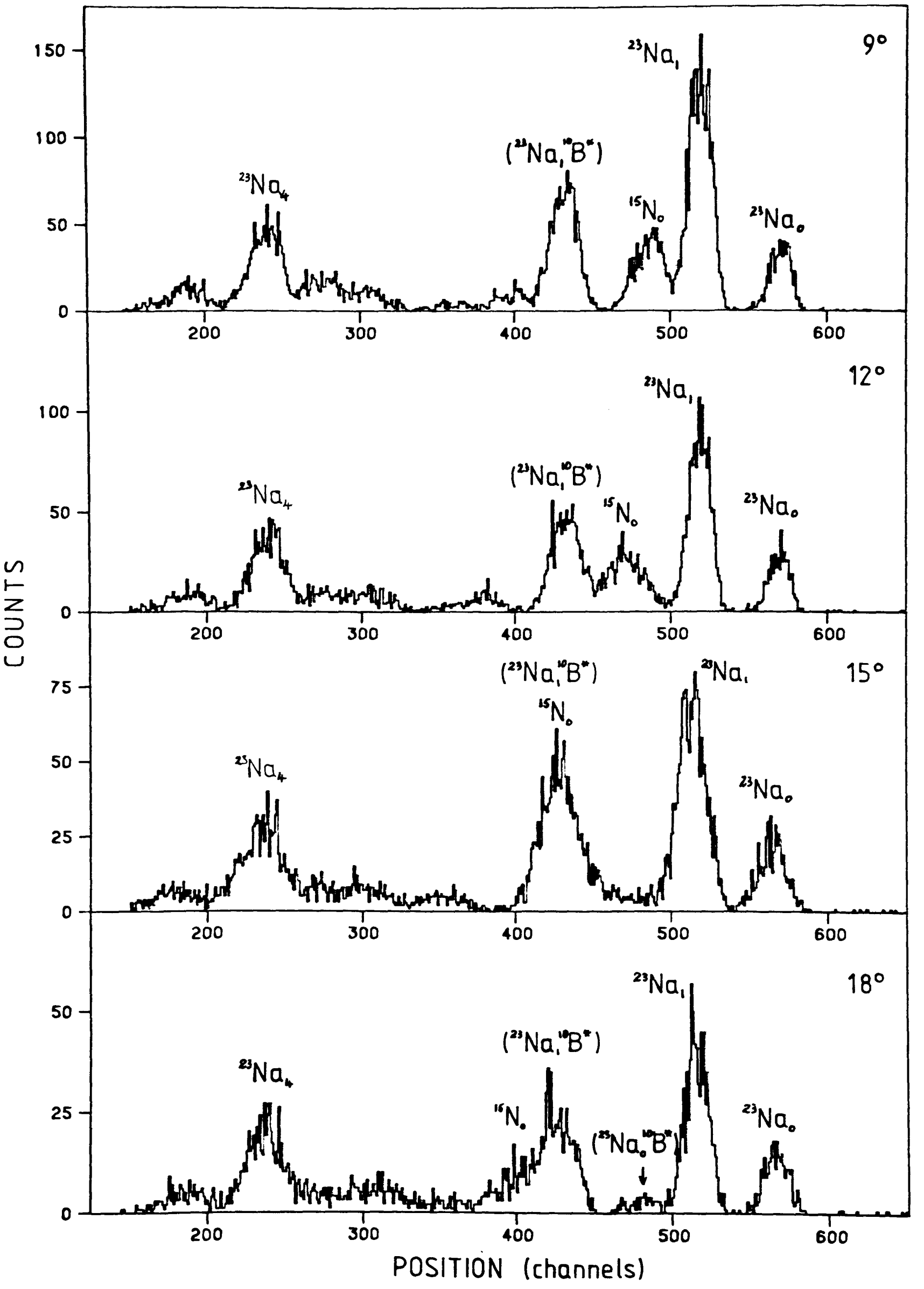


Fig. 2.13 Position spectra for 43 MeV $^{9}Be$ incident on a $^{24}Mg$ target. The subscripts on the residual nuclei refer to excited states. The label $^{10}B^*$ indicates the 0.72 MeV excitation of the ejectile.

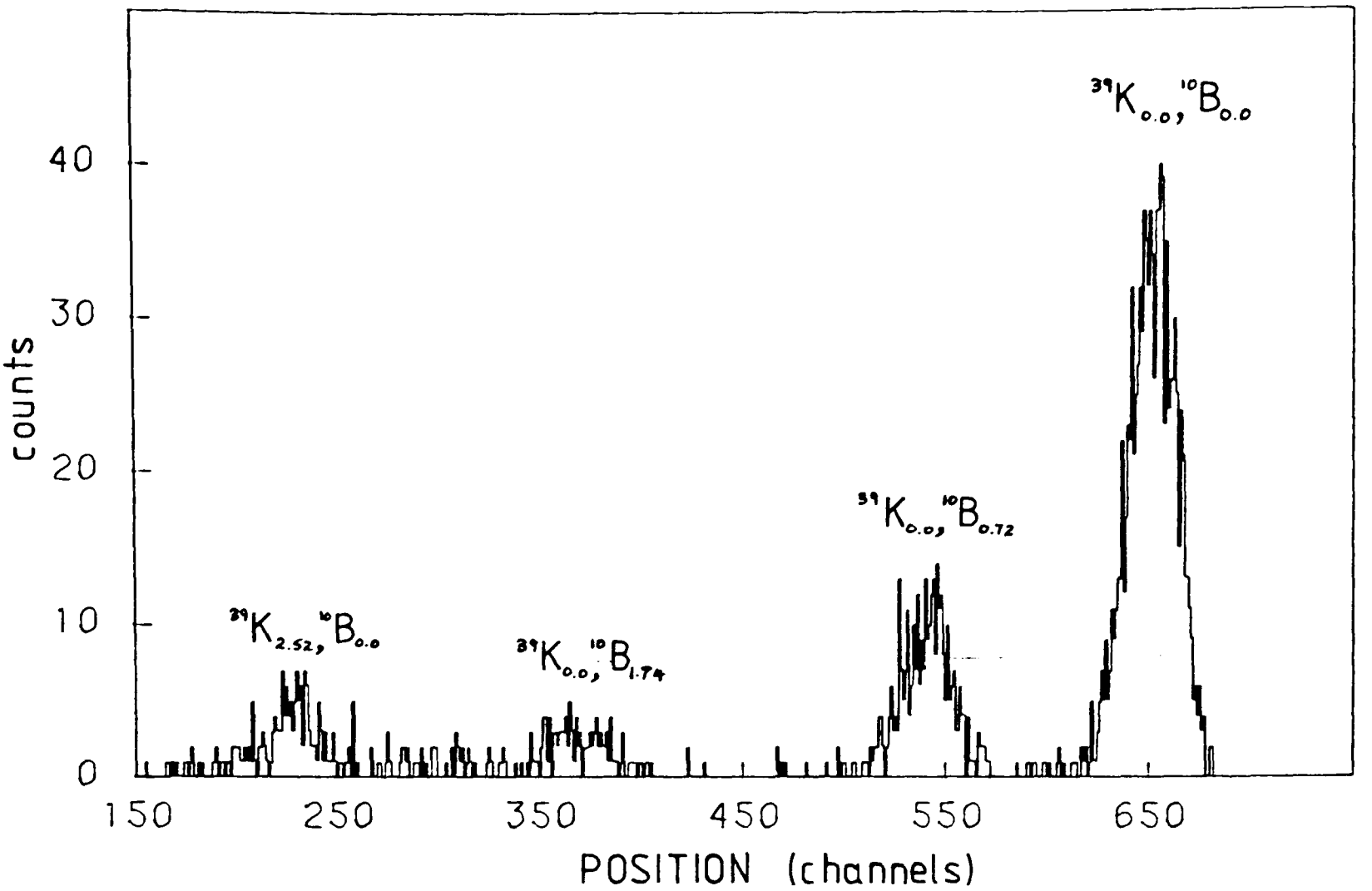


Fig. 2.14 Position spectrum for $^{40}Ca(^{9}Be,^{10}B)^{39}K$ at 30 MeV. The spectrometer angle was 31°.

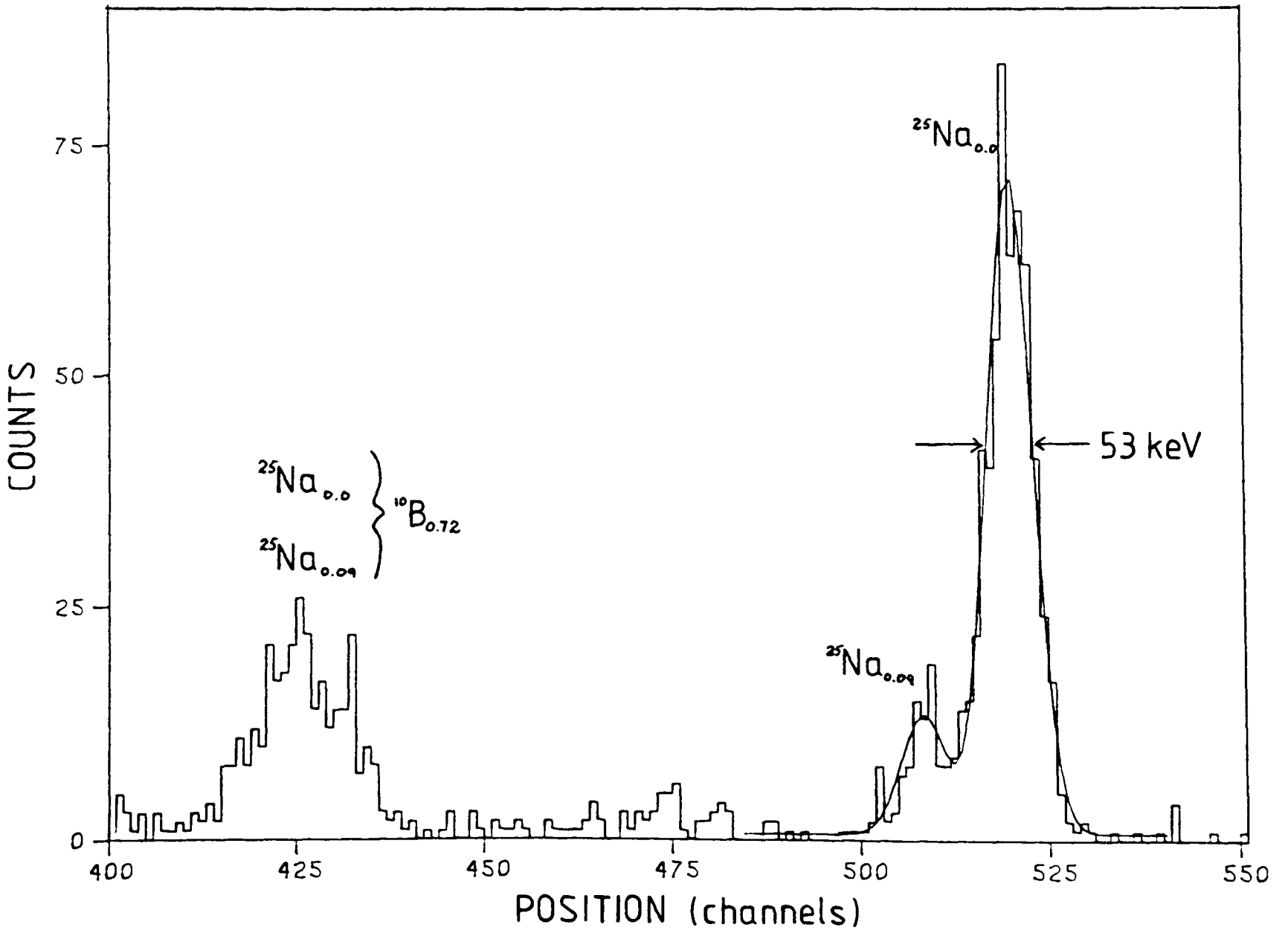


Fig. 2.15 Position spectrum for $^{26}Mg(^{9}Be,^{10}B)^{25}Na$ at 43 MeV and 15°. The target was 20 $\mu g/cm^2$ $^{26}Mg$ on a 20 $\mu g/cm^2$ carbon backing. The resolution of the peaks where $^{10}B$ is in its ground state are limited by target and beam effects.

resolution of the two peaks is 59 keV fwhm. It can be seen that the $^{10}B_1$ peak is much broader than this (103 keV fwhm), so that the $^{25}Na_{0,1}$ is not resolved. This is because the excited $^{10}B$ nucleus decays in flight long before it reaches the focal plane and is detected (the flight time is ~250 ns, the lifetime of the state is 0.71 ns [Led78]). The $^{10}B$ nucleus recoils with a range of energies depending on the direction of emission of the gamma ray. A simple calculation shows that this range is

$$\frac{(mv \pm E_\gamma/c)^2}{2m} \approx (\tfrac{1}{2}mv^2 \pm v.E_\gamma/c)$$

where mv is the momentum of the ejectile and $E_\gamma$ is the energy of the gamma emission. For the case above, this gives a maximum spread in energy of 123 keV.

# CHAPTER 3

# FOCAL PLANE DETECTOR

## 3.1 Introduction.

The study of heavy-ion reactions with magnetic spectrometers requires a focal plane detector with better discrimination than the nuclear emulsions [Ers79] or gas proportional counters [For79] which are commonly used in light-ion work. In heavy-ion studies it is important to be able to distinguish between a wide range of ion species which have relatively small differences in their mass and energy-loss characteristics. One may be interested in the observation of a reaction channel that differs only by one mass or atomic number unit from the ion-type that corresponds to inelastic scattering - perhaps several orders of magnitude more intense than the wanted species.

A focal plane detector must be capable of measuring the incident particle's position along the focal plane with a resolution that does not compromise the $B\rho$ resolution of the magnetic spectrometer itself. Furthermore, it must be compatible with the large solid angle that magnetic spectrometers admit. These two features, excellent momentum resolution and ample solid angle acceptance, together with the possibility of deflecting intense elastically scattered ions away from the detector, make spectrometers very desirable and sometimes essential compared with alternative systems such as the $\Delta E$-E silicon surface-barrier detector described in Chapter 2. When using a spectrometer in conjunction with heavy-ion beams, the energy resolution

should be limited primarily by target effects and the quality of the incident beam rather than by the detection instrument. The solid angle of the $\Delta$E-E telescope is limited mainly by considerations of kinematic broadening: this is not important in a spectrometer.

One of the most significant advances over the last decade in focal plane detectors for heavy-ions has been the development of so-called hybrid counters ([Sha75], [Ers76], [Ful79a]). These consist of a gridded ionization chamber with a segmented anode that has position-sensitive proportional counters (PSPC's) embedded in it. The cathode and grid assembly provide the total energy, $E_T$, and the anode plates provide the energy-loss, $\Delta$E, signals. Two PSPC's are used to determine the particle's crossing-point along the focal plane and the angle of incidence.

Measured resolution figures of 1 mm in 40 cm for position, 1% for E and 4% for $\Delta$E illustrate the capabilities of these counters [Ful79a]. Complete separation of atomic number and mass for ions up to A = 40 has been achieved [Sha75] and versions of these counters have been constructed at many nuclear physics facilities, including Oxford, where a small prototype of the design presented here has been tested [Sin80].

The characteristics of the new magnetic spectrometer at Oxford, particularly the vertical extent of the image at the focal plane, has necessitated a larger counter than hitherto attempted. The design goal was to maintain the excellent performance of the smaller counters despite the anticipated problems with field distortions around the edges of the ionization chamber. Some knowledge of the Oxford magnet design is needed before the requirements imposed on the focal plane detector

may be fully appreciated, and a brief description of this follows in the next section. Afterwards the counter itself will be described, beginning with a review of the operational principles of ionization chambers and PSPC's. The chapter concludes with a discussion of the present counter's performance and of future developments.

## 3.2 Overview of the Oxford MDM-2 Magnetic Spectrometer.

The installation of a new magnetic spectrometer at Oxford for the study of charged-particle reactions received financial approval in 1977. A joint design team from Oxford and Rutherford Laboratory was formed and was soon attracted by the great simplifications to the design optimisation and usage if a single dipole element were employed with additional focussing provided by external multipoles. The Berkeley spectrometer [Hen74] which possessed these features was chosen as the basis for the design. The design requirements were:

(i) large solid angle of acceptance,

(ii) moderately high resolution even at full solid angle,

(iii) a large momentum bite (±7%) but with small dispersion in order that the detector need not be excessively long,

(iv) normal incidence of particles to the focal plane,

The radial acceptance was made larger than the Berkeley design; this increased the maximum solid angle from 2 msr to 8 msr whilst improving the energy range covered at a given field setting.

It was considered essential to have the focal plane normal to the incident particle paths: this ensured that the best use was made of the detector's position resolution, minimised energy-loss dependence on

entrance angle in the detector and also kept the detector length small. Other common types of magnetic spectrometers currently used in nuclear physics, such as the "Q3D" or "Split-Pole" (see [Eng79] for a review of spectrometer designs), possess focal planes at 45° to the mean particle trajectory and thus restrict the performance of the focal plane detector - especially if heavy ions are incident. In the Oxford design normal incidence is achieved by means of the dipole's concave exit boundary (as per Berkeley) together with sextupole and octupole fields in the exit multipole.

The coordinate system used in this chapter to describe particle trajectories in ion-optical systems is the one defined by Enge in ref. [Eng79]; namely x and y as horizontal and vertical distances away from the "Non-Real-Central-Ray" (an imaginary path through the geometric centre of all magnetic elements in the system), z as the distance along that ray, and $\theta$ and $\phi$ as the horizontal and vertical angles of the particle upon entry to the system. Transfer coefficients, which are the coefficients of a Taylor expansion of the exit coordinates in terms of the entrance coordinates and momentum, will also be denoted following the same reference: eg. the first-order coefficients $x/x$ and $\theta/\theta$ are the horizontal magnification and the horizontal angular magnification, respectively. The most important second- and third-order terms are the aberration terms $x/\theta^2$, $x/\phi^2$, $x/\theta^3$, $x/\theta\phi^2$, etc. because they blur the image formed of the object (i.e. target beam spot) by particles of identical momentum. Fourth- and higher-order terms are not so critical, neither is the extent of the image in the vertical direction - the only considerations in this respect being to ensure that no rays strike the walls of the containing vessel and to produce an image height that is

accepted by the focal plane detector.

Let us now turn to the Oxford design, the layout of which is shown in fig. 3.1. Particular emphasis is given here to the image shape (a more comprehensive and detailed description will be found in [Pri83]). The system is a modular one: Multipole-Dipole-Multipole.

Entry Quadrupole and Sextupole. The quadrupole is vertically focussing and has additional, fixed proportions of sextupole, octupole, decapole and duodecapole fields obtained by shaping the profile of the pole pieces. Immediately pre a smaller adjustable sextupole. This may be varied as required: either to minimize both $x/\theta^2$ and $x/\phi^2$ errors or to make $x/\phi^2$ zero (at the expense of relatively large $x/\theta^2$) if ray reconstruction through the focal plane detector is being employed. The sextupole also partially determines the height of the image near the horizontal focus.

Analysing Magnet. The convex entry face to the dipole magnet helps reduce $x/\theta^2$ aberrations and, in addition to the sextupole term, is shaped to provide octupole and decapole field components. These latter, in conjunction with the external multipole fields, correct the third order aberrations $x/\theta^3$ and $x/\theta\phi^2$. The main dipole has a radial magnetic field gradient with

$$n = \frac{-r}{H}\frac{dH}{dr} = 0.19$$

This provides some additional vertical focussing and also increases the dispersion by a factor of $(1-n)^{-1}$. In addition, the gradient field helps offset the large negative $x/\theta^2$ error introduced by the concave exit face.

Fig. 3.1 **Oxford MDM-2 heavy ion magnetic spectrometer**

Multipole-dipole-multipole

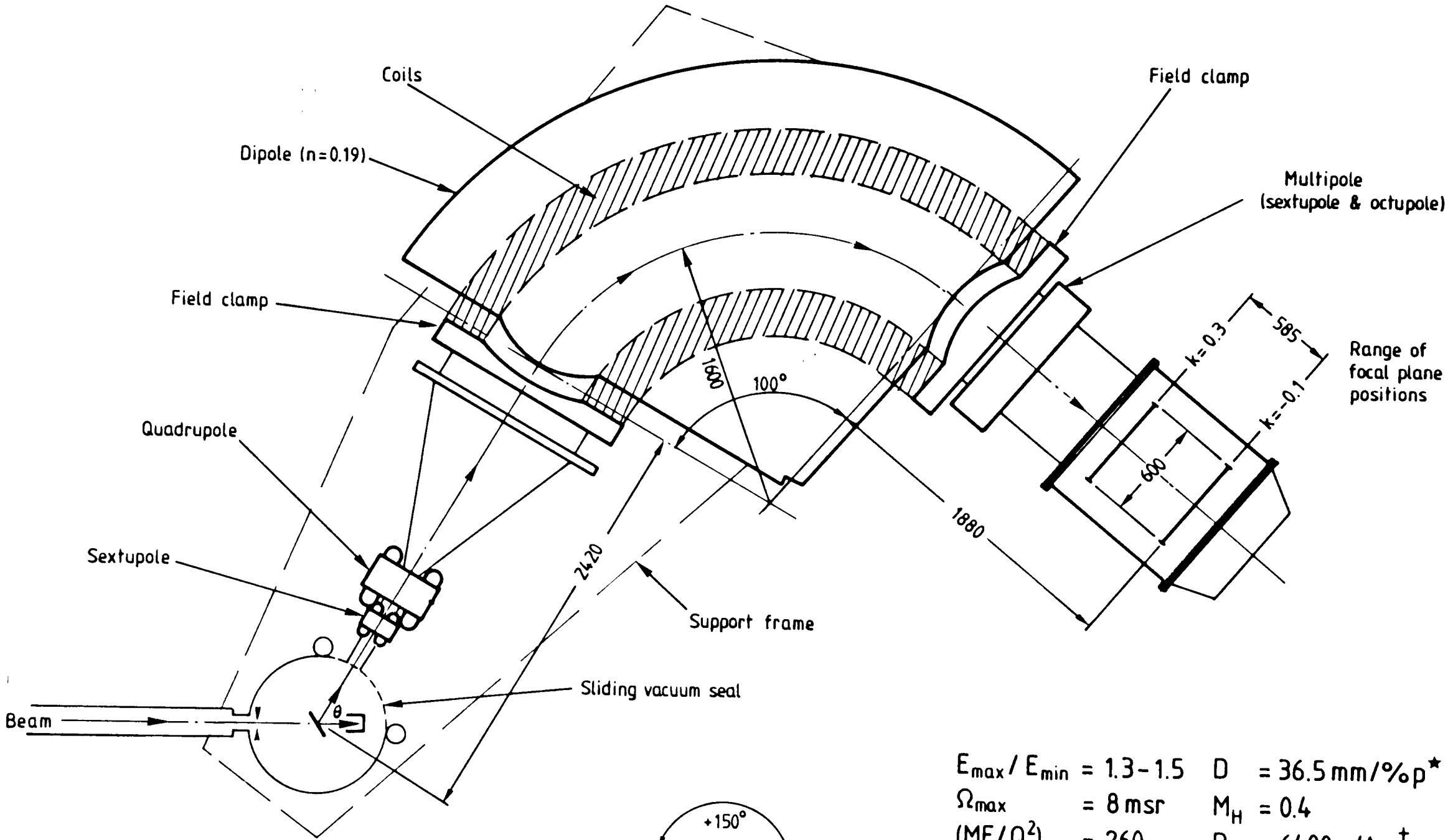


Dimensions in mm

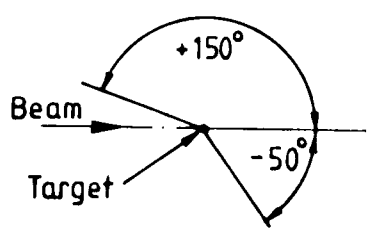


ANGULAR RANGE

$E_{max}/E_{min}$ = 1.3-1.5 D = 36.5 mm/%p★

$\Omega_{max}$ = 8 msr $M_H$ = 0.4

$(ME/Q^2)_{max}$ = 260 $R_{ab} \simeq 6400\,p/\Delta p$ †

★ Dispersion at centre of focal plane for k = 0.1

† Approximate aberration limited resolving power

Table 3.1

Spectrometer Specifications

| | |
|---|---|
| Horizontal Acceptance, $2\theta$ | 80 mrad |
| Vertical Acceptance, $2\phi$ | 100 mrad |
| Maximum Solid Angle, $\Omega$ | 8 msr |
| $E_{max}/E_{min}$ for $\Omega$ = 1 msr | 1.52 |
| $E_{max}/E_{min}$ for $\Omega$ = 8 msr | 1.31 |
| Mean Dispersion, D | 3.8 cm/% |
| Horizontal Magnification, X/X | -0.42 |
| Vertical Magnification, Y/Y | -5.02 |
| Horizontal Angular Magn., $\theta/\theta$ | -2.45 |
| Vertical Angular Magn., $\phi/\phi$ | -0.21 |
| Resolving Power ($E/\delta E$) | >3000 |
| Radius at central ray | 1.6 m |
| Mass Energy Product (max.) | 250 amu MeV |
| Mean Flight Path (target-detector) | ~6.5 m |

Exit Multipole. This provides variable sextupole and octupole fields that may be used to rotate and straighten the focal plane. The dipole exit pole face has been arranged such that no further correction need be made when focussing particles with a kinematic factor, k, of 0.1 $rad^{-1}$, where k is defined as:

$$k = -(1/p).(dp/d\theta) \qquad (3.1)$$

where p is the momentum of the ion. For kinematic factors not equal to 0.1, the multipole is powered to values calculated for a perpendicular, flat focal plane.

The position of the focal plane moves "upstream" with increasing k. It is 172 cm from the dipole exit boundary for k=0.0 and has moved 42 cm towards the magnet for k=0.3. In order to allow for reactions within this range of k-values (which encompasses most heavy-ion work feasible at Oxford), the detector needs to be mounted on a moveable table within the vacuum vessel.

The major parameters of the Oxford spectrometer design are listed in table 3.1.

## 3.3 Principles of Operation of Hybrid Focal Plane Detectors.

The two basic constituents of a "hybrid" counter, the ionization part and the proportional counters, are distinguished by the size of the "reduced field", X/p (where X is the electrical field strength and p is the gas pressure), within the region. In an ionization chamber, the field should be sufficient that all electrons and positive ions liberated by the incident particle are collected at the electrodes, but

not so strong that the electrons may acquire enough energy as they drift between collisions for secondary ionization to take place. Proportional counters are operated with higher reduced fields such that an avalanche of secondary electrons is formed close to the anode wire. The size of the signal rises more or less exponentially with increased field but it still should be proportional to the amount of primary ionization until the "Geiger" region is reached, where the positive-ion space charge limits the avalanche size.

### 3.3.1 The Ionization Chamber.

The purpose of the ionization chamber in a hybrid detector is to extract information about the incident particle's energy and rate of energy loss. The basic principle is, of course, the reaction between the charged particle and the atomic electrons of the counter gas. If an ionizing particle is stopped within the counter and if the amount of energy which the particle loses on average to form one ion pair, W, remains constant over the whole track of the particle, then the total ionization may be taken as a direct measurement of the energy. W is actually remarkably independent of the charge and mass of the particle [Seg65] and the variation of W with energy gives rise to a sufficiently small (less than 1%) departure from linearity of pulse height (see ref. [Wil50], p19) that it may be generally ignored.

Taking as a rough guide the 27 eV needed to produce one ion pair in isobutane, the average number of electrons liberated by a particle that loses 10 MeV in the chamber is 370 000 (equivalent to $5\times10^{-14}$ C). If the particle is stopped within the detector, the ionization straggling is negligible: the Poisson distribution of ion pairs formed shows a

variance equal to the average number multiplied by the Fano factor, for which a typical value of 0.3 may be used. Then in the above case, the Poisson distribution is very close to a Gaussian form with full width half maximum of 0.1%. On the other hand, if the particle is not stopped within the detector, energy loss straggling may be very important (as is also the case for the $\Delta E$ signals in the hybrid counter).

A good energy signal will only be obtained if all the primary electrons are collected. This requires a high enough field such that recombination effects are minimised ($X/p >> 0.2$ V/cm/torr is typical) and the absence of electronegative molecules, such as oxygen, which would capture electrons to form slow-moving ions. The drift velocity of electrons under the influence of fields commonly used in ionization chambers has been measured as between 3 to $6\times10^6$ cm/s [Ful79b] whereas the positive ions drift about 1000 times slower than this.

The other quantities of immediate interest are the rate of energy loss and the particle's range - the latter obviously governs if (and where) the ion is stopped within the counter. These quantities may be estimated from Bethe's well-known stopping power formula for a particle of charge Ze traversing matter of atomic number z and containing n atoms/cm$^3$,

$$-\frac{dE}{dx} = \frac{4\pi z^2 e^4 nz}{mv^2}\left[\log \frac{2mv^2}{I(1-\beta^2)} - \beta^2\right] \qquad (3.2)$$

where E is the particle energy, v is its velocity, m the electron mass, $\beta = v/c$ and I represents a kind of average excitation energy of the atom (see, eg., [Seg65], [Wil50]). This is not accurate for the case of slow heavy ions, which continuously change their charge state as they move

through the gas so that an "effective charge state" or $Z_{eff}$ should be used in (3.2). Since all ions of a particular species will have similar $Z_{eff}$ (assuming that the range of incident energies is not too great), the dE/dx signal will still distinguish between different elements. For particles with Z less than about 20 and with E greater than about 5 MeV/amu, dE/dx is proportional to $Z^2$.

Signal Generation in Ionization Chambers.

Wilkinson [Wil50] discusses in detail the mechanism of pulse formation which will be summarised here. We consider first a two-electrode ionization chamber. When an ion pair is created within the chamber the electron and positive ion immediately begin to move apart because of the applied field and by induction signal current flows from the positive to the negative electrode.

At the instant of formation of the ion pair the positive and negative charges induce equal and opposite charges on the electrodes. Because the electron moves very much more rapidly than the positive ion, the initial signal is due to the changing distance of the electron from the anode until it is collected at some time $t_1$ after the instant of formation. The potential of the collecting electrode at this time is still less than the final value of -e/C (where C is its capacity) because the positive ion has scarcely moved, and the influence of the positive ion persists until it reaches the cathode at time $t_2$. Since the time $t_1$ is typically one microsecond compared to values of milliseconds for $t_2$, only that part of the signal due to the electron motion is seen in practical fast-pulse spectroscopy and the positive-ion effect may be regarded as constant within the integration times of

amplifiers.

It can be shown [Wil50] that the effective charge induced on a given electrode as an electron moves through a potential difference $\Delta V$ inside the chamber is:

$$q = e\Delta V/V, \qquad (3.3)$$

where V is the potential difference between the two electrodes. The total charge ultimately transported to the electrode by an ion pair is e, but as long as the positive ion remains within the chamber the part transported by the electron may range from zero to e, depending on the point of creation (next to the anode or next to the cathode, respectively). This is because the charge induced by the positive ion is of opposite sign to that induced by the electron. With such a chamber pulse heights will depend on the vertical position of the track, which is undesirable in general.

The above problem can be avoided by screening the collecting electrode from the volume in which the particle tracks are formed. This is usually done by inserting a Frisch grid as a third electrode in the chamber (fig. 3.2).

Consider a grid of parallel wires of spacing d, wire radius r, placed a distance b' from the collecting electrode B and a distance a' from the other electrode A. The ionization electrons now induce little charge on the anode until they approach and pass through the grid since most of their lines of

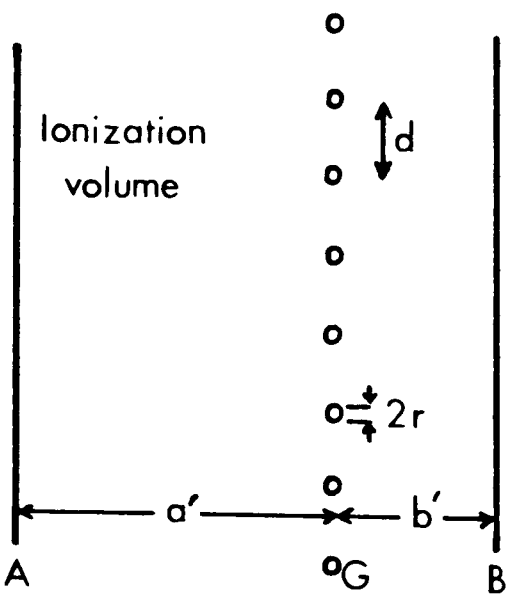


Fig. 3.2 Gridded ionization chamber.

force finish on the grid instead of the electrode B. Bunemann et al. [Bun49] have derived a formula for the effectiveness of this grid in the parallel plate case. The inefficiency in shielding is given by

$$\sigma = \ell/(b' + \ell) ,$$

where $\ell = \frac{d}{2\pi}(\rho^2/4 - \log\rho)$ ,

and $\rho = 2\pi r/d$ .

In the desired limit of small $\sigma$ ($\ell << b'$) and for small values of $\rho$ ($\rho^2 << \log\rho$), this becomes:

$$\sigma = (d/2\pi b')\log(d/2\pi r) . \qquad (3.4)$$

Insertion of some values into this formula (in fact the ones for the Oxford counter) shows that very nearly complete shielding is readily obtained: a grid made of 100 μm diameter wires spaced 1.5 mm apart at 1.5 cm from the collecting electrode will have a $\sigma$ of less than 3%. Thus pulses of very uniform height can be obtained from randomly orientated ionization tracks within the chamber. The rise-time of the pulse is also improved by the insertion of a grid, since no signal is seen until the electrons have reached the grid.

There remains the important question of the transparency of the grid, that is the fraction of the electrons collected onto the grid instead of B (and so lost as far as pulse production is concerned). If this were a small constant fraction, there would be no problem. But this fraction may depend on the orientation of the ionization track if this is near to the grid, so it is desirable in all cases to ensure that virtually all the field lines close to where an ion pair may be formed terminate on the collector, B. This is achieved [Wil50] when the ratio of the field between grid and collecting electrode to that in the main

body of the chamber, satisfies

$$\frac{V_B - V_G}{V_G - V_A} \times \frac{a'}{b'} > \frac{1 + 2\pi/d}{1 - 2\pi/d} \qquad (3.5)$$

This condition is met for the example given above by making the field between grid and anode twice that in the main chamber.

Let us now consider in detail the signals seen from the three electrodes of the gridded chamber. Fig. 3.3 illustrates the signal development with time: the origin is taken to be the instant of passage of the ionizing particle. As the electrons drift upwards, more and more charge is induced on the cathode and grid, but in equal and opposite amounts so that the summed signal is zero. The anode sees no charge if the screening is perfect. At the moment when the electrons pass through the grid the cathode signal has reached its greatest magnitude of $E_T(H-h)/H$ (compare eq. 3.3). The grid signal, however, continues to change as the electrons drift towards the anode. Finally, when all the electrons have been collected, either the anode or the summed cathode and grid signal provides a measure of the total ionization independent of h.

### 3.3.2 Position Sensitive Proportional Counters.

The proportional counter is still amongst the principal instruments used for research in nuclear physics. Its continued usage owes much to the very accurate determination of the position at which incident radiation passes. For the purposes of the present discussion, only a basic knowledge of pulse development within proportional counters is needed; more extensive reviews are given by Curran [Cur58] and

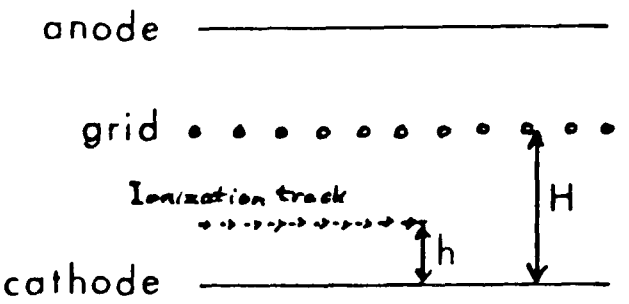


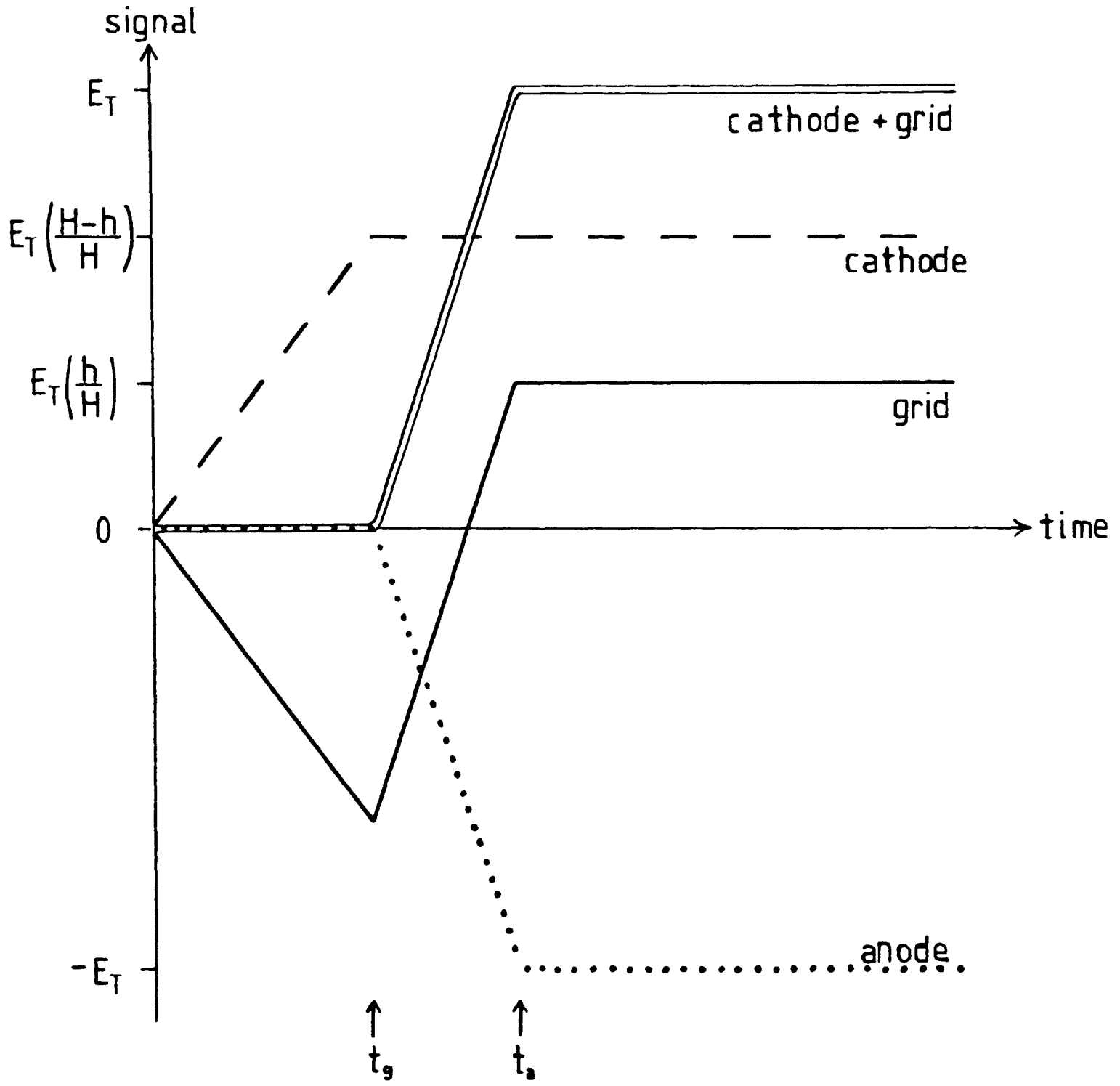


Fig. 3.3 Signal development in a gridded ionization chamber.

$t_g$: time at which electrons pass through grid,

$t_a$: time at which electrons are collected at anode.

Wilkinson [Wil50].

Proportional counters are generally operated with field strengths close to the onset of the Geiger region in order to maximise the signal-to-noise ratio. A maximum avalanche size of about $5 \times 10^7$ electrons is possible before instabilities leading to non-proportionality develop [Ric74].

The distributed nature of both the resistance of the anode wire and the capacitance between the anode and cathode, make the proportional counter essentially a distributed delay line. In the case of the hybrid counter configuration, electrons that have drifted upwards from an ionization track in the main body of the detector produce an avalanche that injects a charge impulse to the proportional counter wire. Both the amplitudes and rise-times of the current pulses observed at each end of the counter are dependent on the position along the wire at which the electron avalanche occurs. This is the basis of the two techniques commonly used for position determination: charge division and rise-time measurement. A discussion of the charge division method is given first.

The amplitudes of the pulses from the ends of the PSPC wire differ because the currents flowing from the charge collection point are inversely proportional to the respective resistances encountered. Thus, for times larger than the counter's relaxation time RC, the charges collected at ends A and B are:

$$Q_A = (1 - P/L)Q$$

$$Q_B = (P/L)Q$$

where P is the position of the event from end A, L is the length of the wire and Q is the total charge collected. The ratio $Q_B/(Q_A + Q_B)$ is

therefore directly related to the position of the event. It should also be noted that the position measurement is independent of the total deposited charge. Fig. 3.4 illustrates the technique; the analogue divider is now usually replaced by software division.

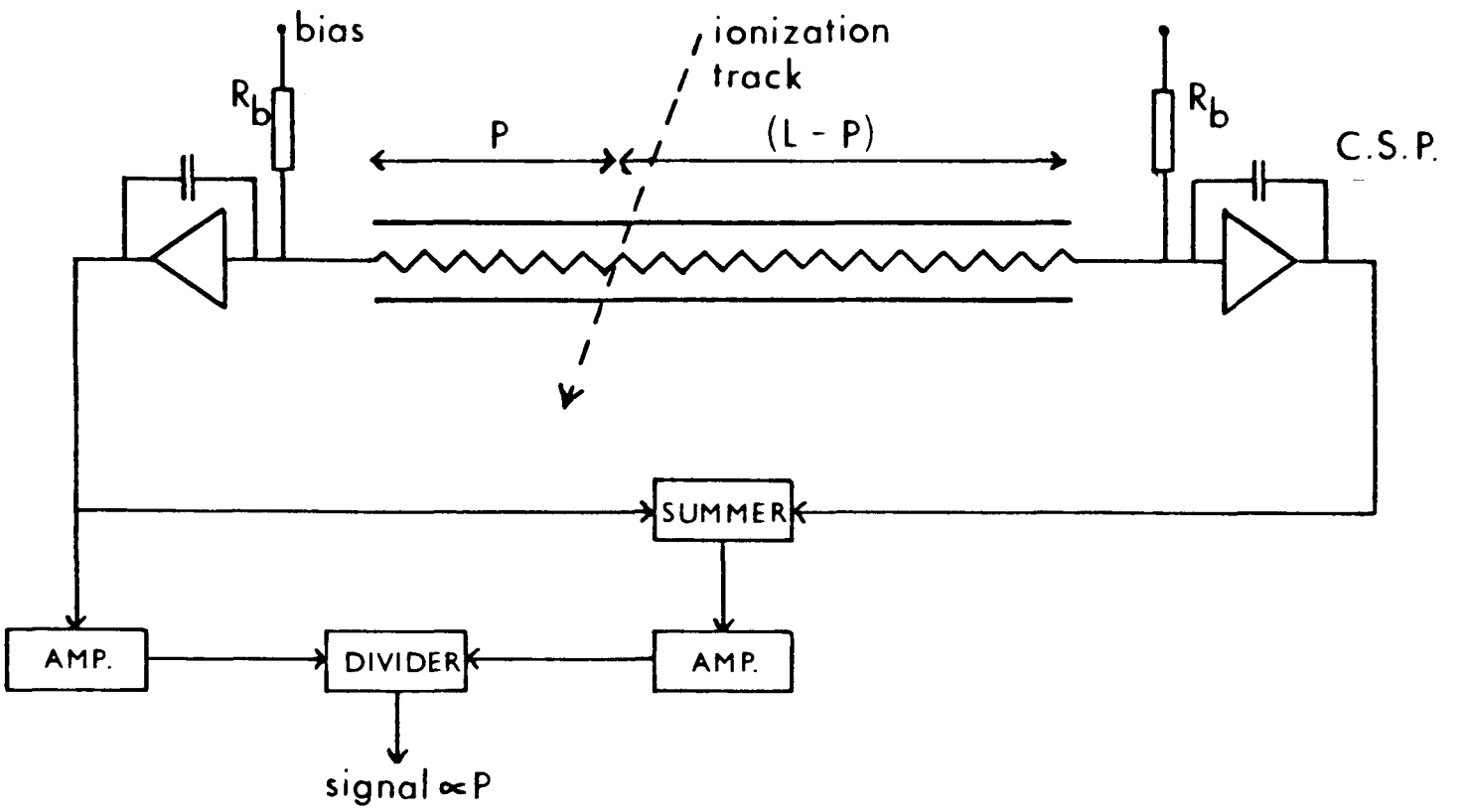


Fig. 3.4 Charge division technique for position determination.
(c.s.p. = charge sensitive preamplifier.)

In fig. 3.4, $R_b$ represents the preamplifier bias resistor. Taking this into account, we obtain

$$\frac{Q_B}{Q_A + Q_B} = \frac{(P/L)R_0L + R_b}{R_0L + 2R_b}$$

where $R_0$ is the resistance per unit length of the anode. $R_0$ is often chosen to be large compared to $R_b$ in order that the spatial sensitivity is high, and $R_b$ itself must be large since the electronic noise is inversely proportional to its value.

The major noise sources in a PSPC may be represented by a parallel component, which is mainly Johnson noise in the resistive wire, and a series component arising from the input FET within the preamplifier. For the wire resistances used when the charge division method of position readout is used, Johnson noise is the dominant contribution. Radeka [Rad74] estimates the thermal-noise limited position resolution by consideration of the input signal modified by amplifiers whose shaping time is set to be 80% of the counter's natural time constant. His result is

$$\frac{\delta X}{L} \simeq \frac{2.54}{Q}(kTC_0L)^{\frac{1}{2}} , \qquad (3.6)$$

where $C_0$ is the capacitance per unit length, k is Boltzmann's constant and T is the absolute temperature. For example, $C_0$ is usually of the order of $10^{-14}$ Farads $mm^{-1}$, Q may be $10^{-12}$ C, say, so for a 500 mm long counter, $\delta X$ would be about 0.2 mm. In the context of the Oxford spectrometer, it is useful to bear in mind that a position resolution of 1 mm at the centre of the focal plane corresponds to a resolution in momentum of $p/\delta p = 3600$ (or $E/\delta E = 1800$) using the $k = 0.1$ dispersion value of 3.6 cm/%. Experience with PSPC's in this laboratory [Sin80] has shown that position resolutions better than 0.5 mm can be achieved with 46 cm long counters.

The alternative method of obtaining a position signal utilises the rise-time dependence of the pulse on position. For a discussion of this method see, for example, Borkowski and Kopp [Bor68]. In order to give sufficient dispersion of the signal, wire resitivities for the rise time method are usually from 1000 to 8000 $\Omega mm^{-1}$ whereas the charge division method requires only 8 to 20 $\Omega mm^{-1}$. The increase in resistivity results

in a longer natural time constant which demands longer shaping times in the main amplifiers if non-linearities are to be avoided. For very long counters (> 1 m, say) this can be a problem if high counting rates are to be expected.

In the case of the Oxford counter, both methods of position determination can be made to give sufficiently good resolution for the spectrometer's requirements; the choice was largely a matter of convenience. If the rise-time technique had been employed, the preamplifiers almost certainly would have had to be mounted immediately next to the ends of the counter in order to keep the load capacitance small (or else one faces the same counting-rate problem mentioned above). The preamplifiers are then located within the vacuum box of the spectrometer - the worst place to be if a preamplifier should fail. Using the charge division method, the preamplifiers could be mounted outside the vacuum vessel since the additional capacitance of the cabling does not unacceptably degrade the position resolution.

## 3.4 Design and Construction of the Oxford Hybrid Detector.

### 3.4.1 General Description.

The detector is basically a gridded ionization chamber with a split anode plane that incorporates position sensitive proportional counters. A cross-section of the counter is shown in fig. 3.5.

The incident ions enter through a thin Mylar window and are stopped within the central part of the counter, ionizing the gas along their path. An electric field causes the electrons to drift upwards towards

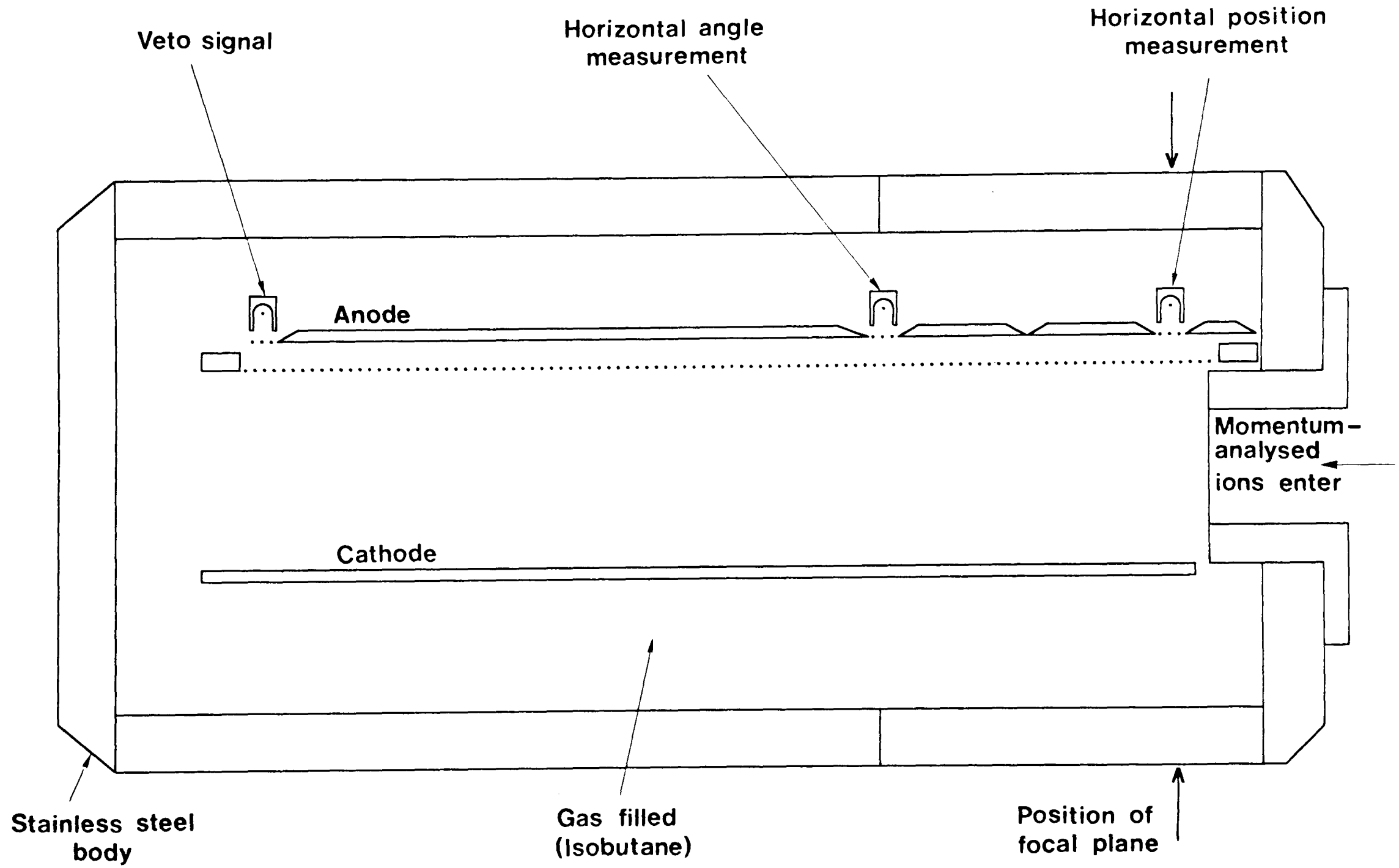


OXFORD HYBRID DETECTOR - SIDE VIEW

Fig. 3.5 Schematic side section of the Oxford hybrid counter.

the grid and anode structure where the total energy signal is taken as the summed cathode plus grid and two energy-loss ($\Delta E$) signals are taken from separate anode elements. Electrons that are initially liberated directly beneath a PSPC will finally arrive in the high-field region close to the thin counter wire. Since the PSPC wires are held at a high positive potential, an avalanche of secondary ionization results and the position of the event may be deduced by the charge division technique outlined in the previous section.

The wire labelled "position" in fig. 3.5 is arranged to lie along the focal plane of the spectrometer. A second wire (labelled "angle" in fig 3.5), which is 15 cm from the first, is used to measure the position of the track a second time and thus enable the angle of incidence to be determined. Additionally there is a third proportional counter at the extreme end of the assembly ("veto" in fig. 3.5). This is not used to give a position signal but merely records particles that do not stop within the 51 cm depth of the counter. These particles may then either be rejected if the wanted particle types are known to be stopped for the gas pressure used or, conversely, counted as "good" events if they are known not to stop. In the latter case, the counter is said to be operated in "light-ion" mode.

### 3.4.2 Overall Design.

The dimensions and detailed arrangement of the elements are shown in fig. 3.6. The counter is surrounded by a vacuum-tight box that contains the gas. This gas cell is made from 35 mm thick stainless steel plates welded to form an open-ended box, with front and back plates detachable. It is wide enough (70 cm interior width) to

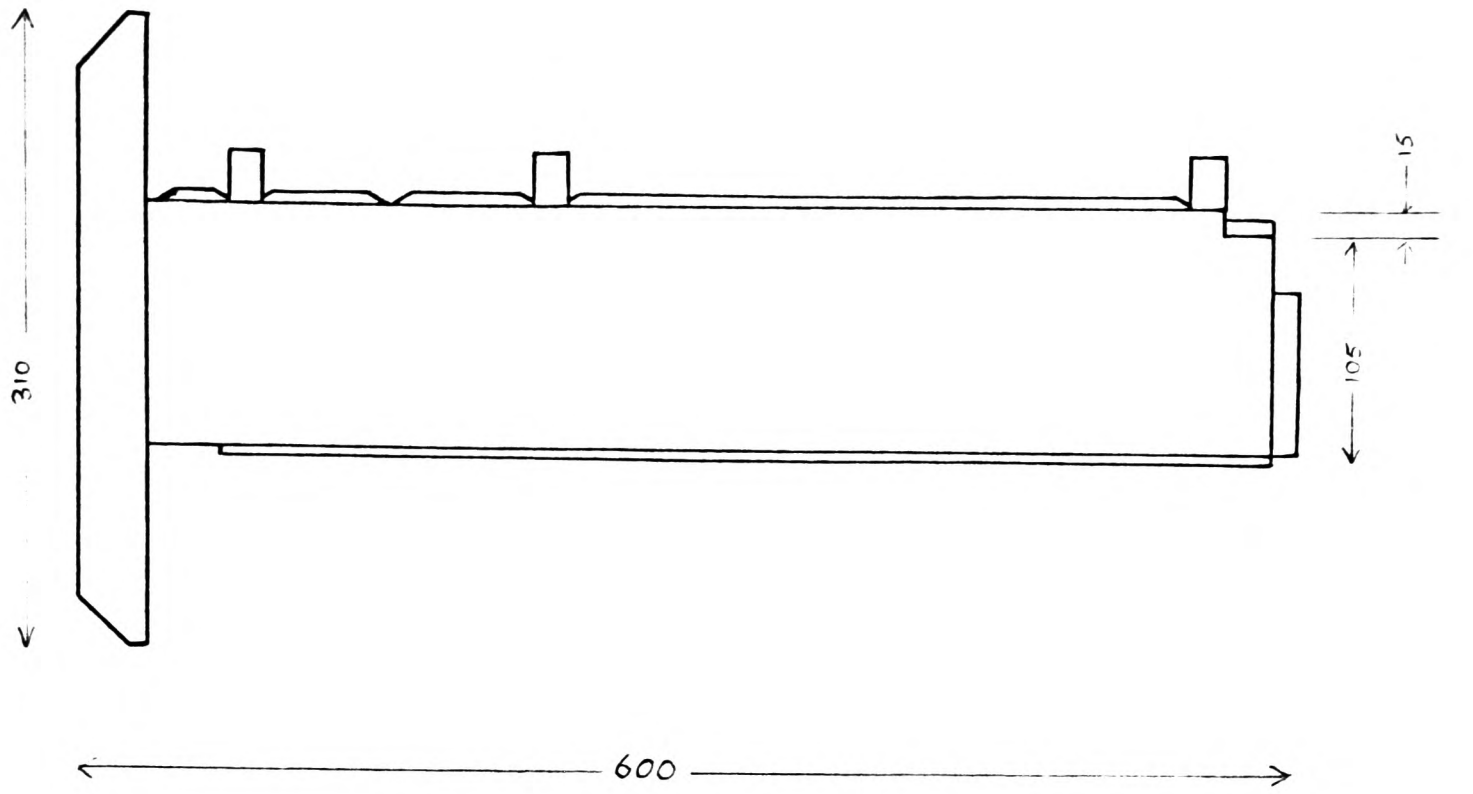


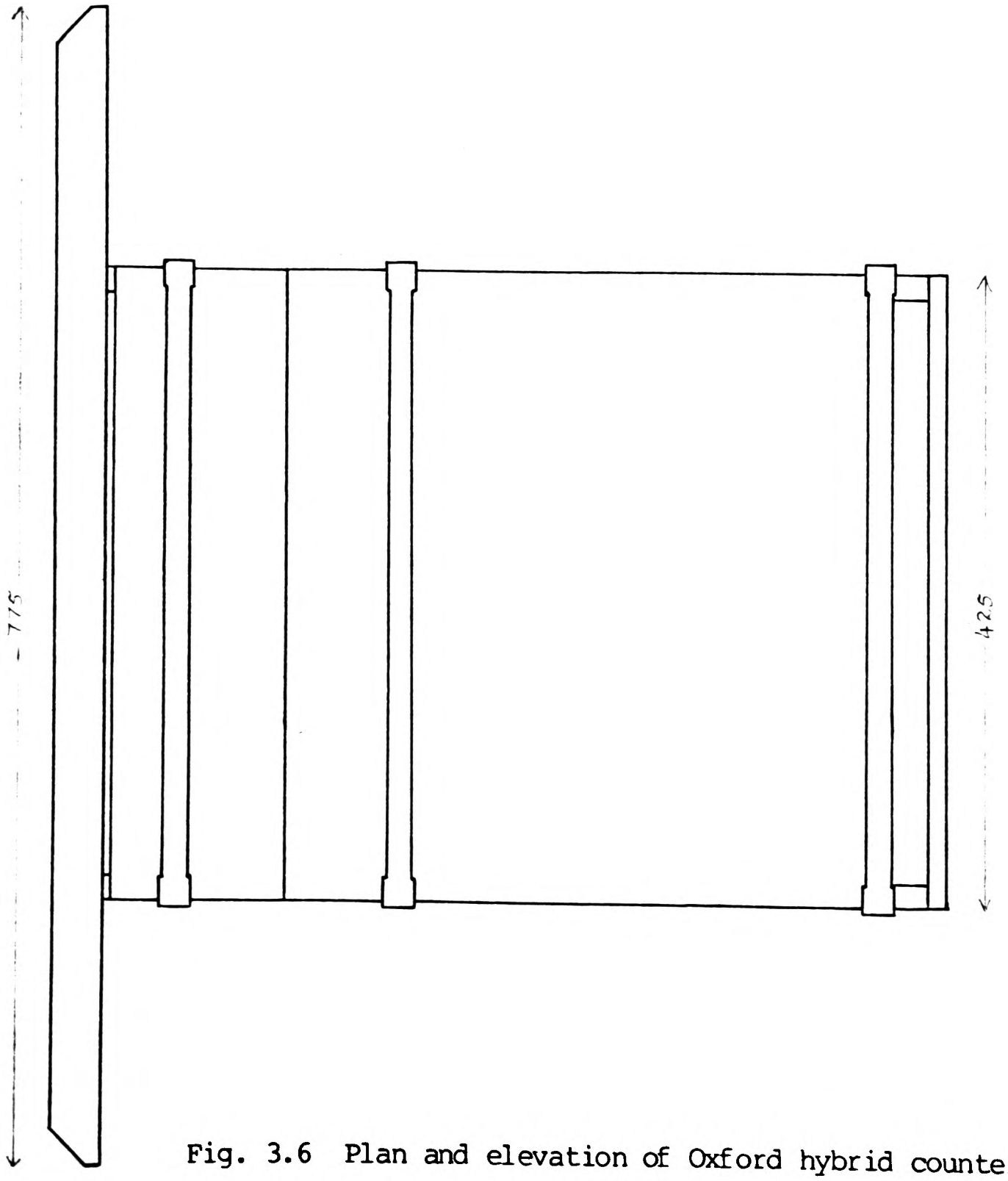


Fig. 3.6 Plan and elevation of Oxford hybrid counter.

(Dimensions in mm.)

accommodate a detector spanning the entire 60 cm focal plane; a new front plate will be required to extend the present 30 cm wide window aperture but the remainder of the gas cell would be unchanged. The window aperture in this initial focal plane detector for the Oxford spectrometer was restricted to $6 \times 30$ cm$^2$ because that already represented a considerable increase in scale compared with previous hybrid detectors. The 30 cm wide window only compromises experiments where an excitation energy range $E_{max}/E_{min}$ in excess of 1.2 is required, in which case two "exposures" at different field settings would have to be taken for every one if the full focal plane were available.

The gas cell is sufficiently large that that stray capacitance between the electrodes and the (earthed) walls is kept reasonably small despite the large size of these electrodes. Noise arising from a large capacitance between the cathode and containing vessel contributed significantly to the total energy ($E_T$) resolution obtainable with a counter built at Argonne Laboratories [Ers76]. Since the $E_T$ signal is also derived from the Frisch grid, it is equally important to keep <u>its</u> capacitance small - a point which is often not mentioned.

The feature that distinguishes this hybrid counter is its large vertical dimension. No counter with a cathode to Frisch grid separation as great as 10.5 cm has been reported previously (the largest in this respect known to the author was a counter constructed at GSI Darmstadt [Püh79] with a 7 cm cathode-grid separation). The large vertical magnification and acceptance (±50 mrad) of the Oxford spectrometer, together with the fact that there is no vertical focus at the (horizontal) focal plane, necessitated a 6 cm high window to the focal plane detector. Since it was desirable to have a re-entrant window (see

next section) the cathode to grid spacing had to accommodate the thickness of the window mounting as well. The resulting 10.5 cm height ensures that incident particles do not strike the cathode or pass through the grid, since the spectrometer's vertical angular magnification is only 0.2. Even with a generous allowance for multiple scattering (15 mrad for 50 MeV $^{16}O$ ions through 40 torr isobutane), the maximum additional spread in the vertical direction is only 1 cm.

The last dimension to consider is the depth. This determines the "dynamic range" of the counter, i.e. the ratio of maximum to minimum track lengths that can be stopped within the counter. The shortest "useful" track (in the sense of giving particle identification signals) is one that just reaches wire 2 (if an ionization track stops short of this an anomalous $\Delta E$ signal will be recorded). The longest useful track is one that stops just before the end of the counter so that a good $E_T$ signal is obtained. The Oxford counter's dimensions provide for a dynamic range of 3.0, which is a significant improvement on the Argonne and Rochester counters (values of 2.3 and 2.5 respectively). Also the greater depth itself means that the counter can be operated with lower gas pressures and this has obvious advantages.

The first proportional counter should be as close to the entrance window as possible, in order that the position resolution is least affected by multiple scattering of the incident ions in the foil and intervening gas. What prevents the counter being located immediately after the window is the detrimental effect of field non-uniformities in this region. Hence it is crucial to keep these to a minimum. This is discussed in the following section (3.4.3).

The separation between the first two PSPC's has been chosen as 15 cm. This partly determines the angular resolution obtainable since the intrinsic resolution of each wire contributes less and less to the uncertainty in the angle measurement as the separation is increased. Other contributions to the angular resolution, in particular that from the multiple scattering of the incident ion in the entrance window and the gas, will eventually dominate. Estimates of the size of multiple scattering using the expressions and values of Sigmund and Winterbon as given by Ford [For79] together with calculations done using the formulae from Marion and Young [Mar68], have shown that 15 cm is roughly the optimum separation.

All the detector elements (electrodes, PSPC's and grid assemblies) are firmly bolted to two blocks of Delrin plastic. This frame is mounted off the front plate of the gas cell, through which all electrical and gas connections are made. Thus the entire body of the detector can be taken out from the gas cell without disconnecting any internal cables and easy access is then provided to all parts of the counter.

Reports on other hybrid counters ([Ers76] and [Sha75]) had mentioned trouble with microphonic noise on the ionization signals arising from rotary vacuum pumps on their spectrometers. Despite the cantilever mounting of this detector, microphonic noise was not a problem: some low frequency (~30 Hz) noise that was associated with one rotary pump was observable on the output of the preamplifier connected to the cathode, but this was entirely filtered out by the main amplifiers (Tennelec TC205A or Ortec 440A).

### 3.4.3 Electrostatic Field Calculations.

Shapira et al. [Sha80] have shown the importance of taking steps to correct non-uniformities in the electric field distribution which arise around the edges of the counter when the vertical distance between the cathode and grid is significant compared with the other dimensions. In their case the separation was 6.5 cm; for the Oxford counter it is 10.5 cm, so it is clear that corrections will be even more necessary. Non-uniformities in the field render useless that part of the counter affected, due to the decrease in the energy, energy-loss and position resolution and linearity. The ionization signals suffer because electrons may be swept away towards the insulating support structure or the cell walls. At the front of the counter, the efficiency of the proportional counter might be greatly reduced and an unwanted dependence of the position signal on the particle's height, y, might be introduced.

Figure 3.7 shows the electric field lines and equipotentials calculated for various possible configurations at the front of the counter by a computer program FISH [All80] that solves the two-dimensional Laplace equation. In these simulations the grid was approximated by a simple line electrode and the gas cell front plate was taken into account. Diagram 3.7a illustrates the case where no corrections are attempted: a simple metallised window held at an intermediate potential results in severe distortion of the field underneath the position wire. The other diagrams illustrate three ways of correcting the field: 3.7b is an idea suggested by Shapira et al. [Sha80], 3.7c is an extension of this used by Naulin et al. [Nau81] and 3.7d utilises two guard plate on the vacuum side of the (non-metallised) window. The window strips in 3.7b and 3.7c and the

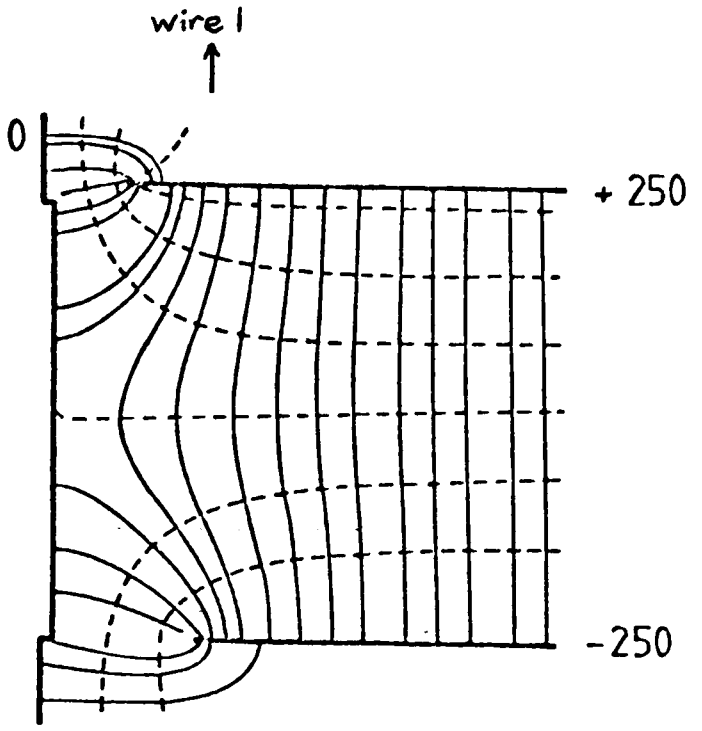


3.7 a

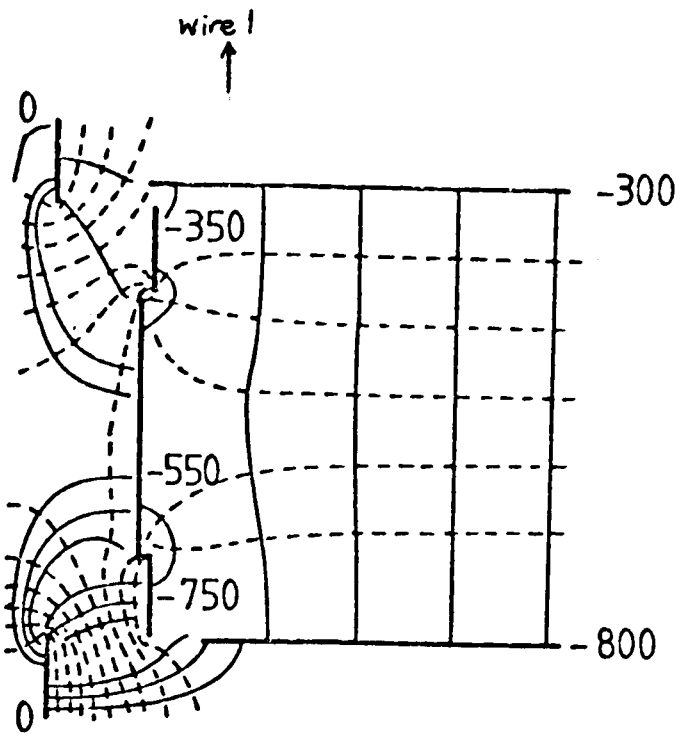


3.7 b

Fig. 3.7 Results of electrostatic calulations for various entrance window configurations (see text). In all cases the window is to the left of the picture. Electrode voltages are labelled.

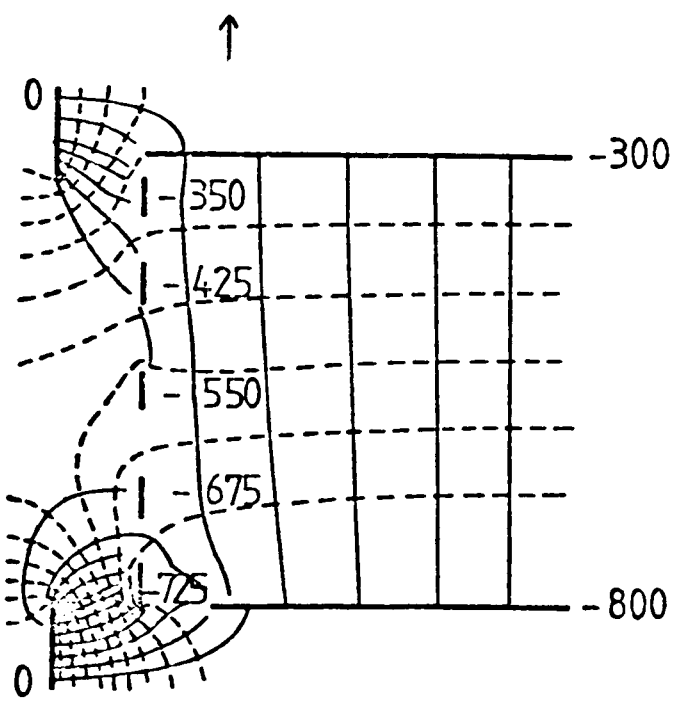


3.7 c

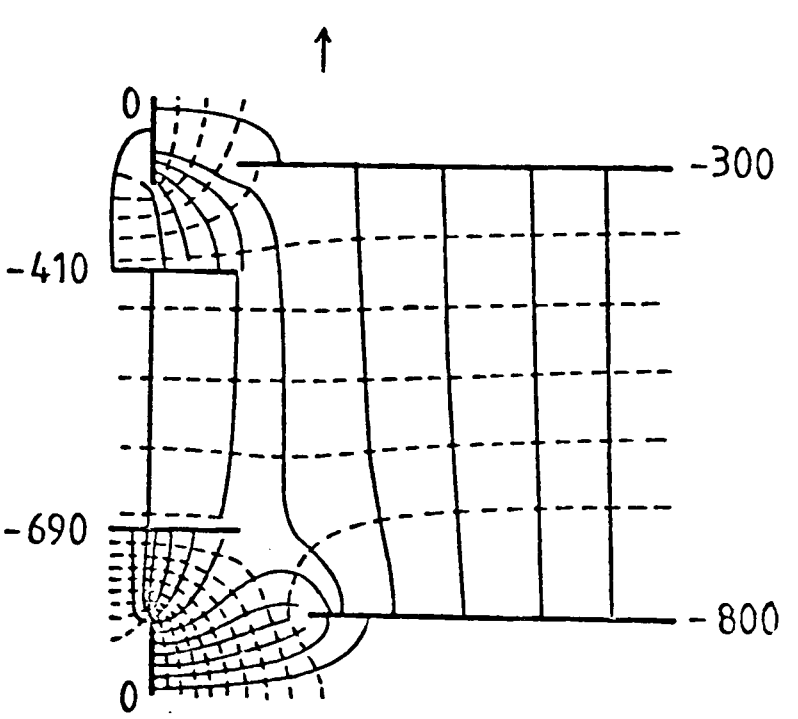


3.7 d

5cm

Electrode
Field line
Equipotential

guard plates in 3.7d would in practice be held at intermediate potentials by bias chains. In all three cases the window mount is re-entrant which has the advantage that less gas is traversed by the particle before the position signal is recorded (2 cm in these simulations). The "three strip" window does not work as well as the more elaborate scheme of Naulin et al. (where the window is aluminised Mylar foil with aluminium removed in 3 mm horizontal strips every 6 mm).

It was decided that a clear Mylar window with external guard plates attached to an insulating window mount would be the easier to construct than the "striped window". Subsequent tests with the completed detector have shown that whilst the appropriate biassing of the guard electrodes does have a significantly favourable effect, the electric field beneath position wire 1 and the first ΔE plate is still distorted. Without the guard electrodes biassed the pulses from the first proportional counter (PC1) were a factor of 20 smaller than those from the second counter (PC2) with equal voltages on both wires. This could be remedied by setting the upper and lower guard plates to potentials approximately equal to the Frisch grid and cathode, respectively. However, there remained significant timing discrepancies between signals from PC1 and PC2 (PC1 was up to 2 μs later than PC2) and also between those from the two ΔE plates. Furthermore, the resolution of the ΔE1 signal was worse than that from ΔE2. Some of these problems could be alleviated by varying the applied guard electrode voltages but the corrections appeared to change as the tests progressed, especially when the accelerator beam was stopped or the counter gas was flushed through.

It is thought that the charging-up of the window material as particles ionize the gas may have been the cause of the residual non-uniformities. An immediate solution to this problem has been the insertion of a double bank of horizontal potential-defining wires at 7 mm spacing. This is perhaps not as neat as the graded potential window of Naulin et al., but it does allow for easy replacement of window foils. No further problems have been experienced with signal timing.

In order to prevent field non-uniformities around the sides and back of the counter, a single bank of potential-defining wires were installed. As in the case of the two rows at the front, the wires were spaced at 7 mm intervals.

### 3.4.4 Entrance Window.

The window foil mount is a composite structure of a 13 mm thick 42×18 $cm^2$ steel flange incorporating the window aperture together with a glass-fibre re-entrant section. The glass-fibre part was machined out of a single block of material and fits snugly within the opening in the front plate of the gas cell. The window foil is thus brought to within 2 cm of the line of position wire 1 (see fig. 3.5).

The glass-fibre section is permanently bolted to the flange and sealed by an O-ring (initially, sealing by Araldite epoxy resin was tried but proved troublesome). The complete window assembly can easily be dismounted from the front plate of the counter, being secured by twelve bolts and vacuum sealed by another O-ring. Two window assemblies have been made so that a spare window (possibly of different thickness) can be always ready-mounted during an experiment. The window foils are

simply glued to the smoothed surface of the glass-fibre surround (also with Araldite epoxy resin).

Two different thicknesses of Mylar have been used in experiments to date: 12 μm (which withstands some 200 torr gas pressure for foils of this area) and 25 μm (which withstands some 500 torr). For very heavy ions ($z > 20$, say) it would be important to use the minimum foil thickness that will bear the counter gas pressure because multiple scattering in the entrance foil would then be very significant. Fortunately a wide range of foil thicknesses are commercially available.

### 3.4.5 Electrode Voltages.

The ratio of the voltages between cathode, grid and anode structure were set by means of a potential divider circuit (see fig. 3.8) such that the drifting electrons encounter an approximately doubled electric field after passing through a grid, as suggested by eq. 3.5. Before this biassing circuit was installed, the sufficient ratio of fields above and below the Frisch grid was verified to be roughly 2:1 by comparing $E_T$ resolutions for several settings.

The original design for the counter was a double-gridded ionization chamber in common with most other hybrid counters described in the literature. The upper grid in these cases serves to shield the Faraday cage from the large number of ions generated in the proportional counters. The second grid had to be abandoned for the Oxford counter, however, because it added an unacceptably large stray capacitance to the $E_T$ circuit due to the large capacitance between the two grids (area $40 \times 53$ cm$^2$, separation 1 cm). As a sequel to the removal of the second grid, the shielding of the PSPC's was improved by raising them 6 mm

above the anode plane whilst maintaining a short section of grid underneath each individual counter (this is the final design shown in fig. 3.5). About +200 V is required on the proportional counter body to ensure that the electric field just above the shielding grid is greater than that just below.

The electrode voltages for a given gas pressure (or, more precisely, the reduced electric field X/p) affects the drift velocity of the electrons. Bohrmann et al. [Boh74] have measured electron drift velocities in isobutane and found that about 7 V/cm/torr is required before the electron drift velocity reaches its maximum of ~6 cm/μsec. However, it is still as great as 3 cm/μsec at a reduced field of only 1 V/cm/torr. Tests with the hybrid counter where the magnitude and resolution of the $E_T$ signal was measured as a function of cathode voltage gave the following results. The signal reached its maximum at 0.7 V/cm/torr, indicating that all primary electrons were passing through the grid, whilst the resolution did not improve significantly after 0.8 V/cm/torr had been achieved (the amplifier shaping time was 4 μsec). During subsequent heavy-ion experiments the reduced field in the main body of the counter ranged from 0.8 to 1.2 V/cm/torr, which is considerably lower than the values used by Erskine et al. [Ers76] in their 1.9 cm high chamber (2 to 9 V/cm/torr).

When the counter has been operated in "light-ion" mode the fields have been necessarily even lower (because of the high pressures used and limiting voltage withstandable by the cables and preamplifiers), although in this case the cathode-grid signal is no longer a measure of $E_T$ but one of $\Delta E$ and thus a small loss in signal resolution is acceptable.

### 3.4.6 Grids.

The grids were made from beryllium-copper wire, 100 μm in diameter. A centre-to-centre spacing of 1.5 mm was used for the Frisch grid (thus $\sigma$ = 2.4% from eq. 3.4) whilst the small grids under the proportional counters had a finer spacing of 1 mm.

Several attempts were made to construct a rectangular grid frame that was sufficiently strong so as to keep the grid wires taut without any external support besides the fixing screws at each corner. Eventually a frame made out of glass-fibre board that could later be tensioned in the middle by means of jacking bolts was used. Strips of copper-coated printed circuit board were glued along the edges of the frame before winding commenced. During the winding (which was done by hand) the wire was anchored to the frame by epoxy resin and occasional pauses were made to solder the wire to the p.c. board.

The grids tend to be easily damaged because of the soft nature of the beryllium-copper wire. In this respect, Nichrome wire as used by Shapira et al. may be superior.

### 3.4.7 Position Sensitive Proportional Counters.

The proportional counter bodies (cathodes) are made from aluminium bars with U-shaped cross-section. The width of the slot is 10 mm and the anode wire lies along the axis of a cylindrical groove of radius 5 mm which is 9 mm from the open slot.

At first, persistent trouble was experienced with wire breakages during counter operation. This almost always occurred when volts were being put on the wire and it appears significant that no wire breakages

were recorded during several heavy-ion experiments when high voltages were not required (because the position resolution was limited by target effects rather than by counter resolution). It seems likely therefore that a spark or large corona discharge caused the breakage. Since no preamplifier FET's were destroyed at the same time, the discharges must have been small (Ophel and Johnston [Oph78] report that their preamplifiers FET's were often damaged by sparking). As a trial a 25 μm diameter wire has been mounted in the rear (veto) proportional counter. This wire has not broken to date.

Care must be taken with the routing of cables in order to avoid possible cross-talk between the large proportional counter signals and the small ionization ones. All signal cables are shielded where possible and individual BNC bulkhead feedthroughs are used. After the proportional counters were first raised up above the anode plane, some fast interference was observed between their signals and the neighbouring ΔE plate. This took the form of a decrease in ΔE signal size as the PSPC wire voltage was increased until eventually the ΔE signal polarity was reversed. That this was a cross-talk problem rather than a positive-ion problem was clear from the observation of delayed pulses some 300 μs later that were attributable to positive ions. Ophel [Oph82] reports the same two distinct problems with counters built at ANU. The remedies for the cross-talk problem were (i) to connect 5 nF capacitors between the PSPCs' bodies and earth, and (ii) to surround all the PSPCs by earthed copper shields.

### 3.4.8 Electrode Construction.

The anode elements were machined from 3 mm thick aluminium plate. Abutting edges are tapered to reduce capacitive coupling between electrodes. No signals are taken from the pre-anode or large rear plate which serve merely to define the electric field and collect ionization electrons. The ΔE electrodes are connected to charge-sensitive preamplifiers (Ortec 125) situated in vacuum just outside the front plate of the gas cell.

The cathode is also made of 3 mm thick aluminium. The edges are smoothly rounded where appropriate in order to reduce the risk of electrical breakdown.

### 3.4.9 Gas.

Many other workers (eg. Shapira et al. [Sha75], Erskine et al., Oed et al. [Oed83]) have shown that isobutane has two important advantages over argon-methane mixtures for hybrid counter use. At a given pressure the stopping power of isobutane is about 2.8 times greater than that of argon-methane, which means that the counter can be run with a lower gas pressure and thus a thinner entrance window. Secondly, because of the lower average nuclear charge of isobutane, multiple scattering is smaller than that in argon-methane for the same energy loss.

Isobutane (C.P. grade from BOC: 95% isobutane, 4% propane, 1% other) has been used for all experiments with the Oxford counter. Since the gas is sensitive to the presence of electronegative impurities such as oxygen, care has been taken to avoid materials within the detector

which may out-gas, in particular nylon. All preamplifiers are mounted outside the gas cell; the penalty one pays for this is slightly noisier ionization signals owing to the longer cables. Signals within the counter are carried by PTFE coated cables and in general trapped volumes have been avoided wherever possible.

After the counter has been open to the atmosphere it is pumped for at least one hour before gas is admitted. To improve the pumping speed of the counter a 4 cm diameter solenoid valve was installed in the back plate of the gas cell. This is set open (by energising the solenoid) before evacuating the detector and spectrometer focal plane box in unison. The large diffusion pump of the spectrometer box then pumps the detector interior with very little impedence. Before isobutane is admitted, the valve is closed remotely by switching off the current to the solenoid.

With these precautions it is possible to operate the detector without the need to flow the gas. A fresh "charge" of isobutane lasts typically 10 hours before the ionization signals unacceptably deteriorate. Nevertheless, for very heavy ion experiments, where very good particle identification is needed, flow-through may be necessary. The gas-handling system has been designed to allow for both continuous flow-through and for a future implementation of a closed, circulatory system with purification. In flow-through operation (or whenever changing the gas), isobutane enters the counter through a stainless steel flexible hose attached to one side of the gas cell's front plate and leaves through a similar pipe whose outlet is on the other side of the front plate (the hoses are flexible so that the counter may be moved for kinematic correction). Large holes of 5 cm diameter have been

drilled in the delrin side frames of the detector to facilitate circulation of the gas within the ionization volume.

## 3.5 Signal and Data Processing.

### 3.5.1 Counter Electronics.

The essential electronics of the hybrid counter are displayed in fig. 3.8. Charge-sensitive Ortec 125 preamplifiers were connected to each ΔE plate and an Ortec 142B preamplifier was connected to the AC-coupled grid and cathode (unless separate cathode and grid signals were required, in which case the coupling capacitor was removed and two Ortec 142B preamplifiers were used). Each end of the first two anode wires and one end of the rear anode wire were connected to charge-sensitive preamplifiers outside the vacuum chamber. Both Ortec 109A and Nuclear Enterprises 5287A types have been used and have given similar performance.

The bias chain for the cathode, the fifteen potential defining wires and the grid has RC filter networks incorporated in order to reduce noise pickup. The bias voltage for the proportional counters is applied through the preamplifiers which have filter networks built in. The counter with its gas cell has been electrically isolated from the spectrometer in order to avoid ground loops.

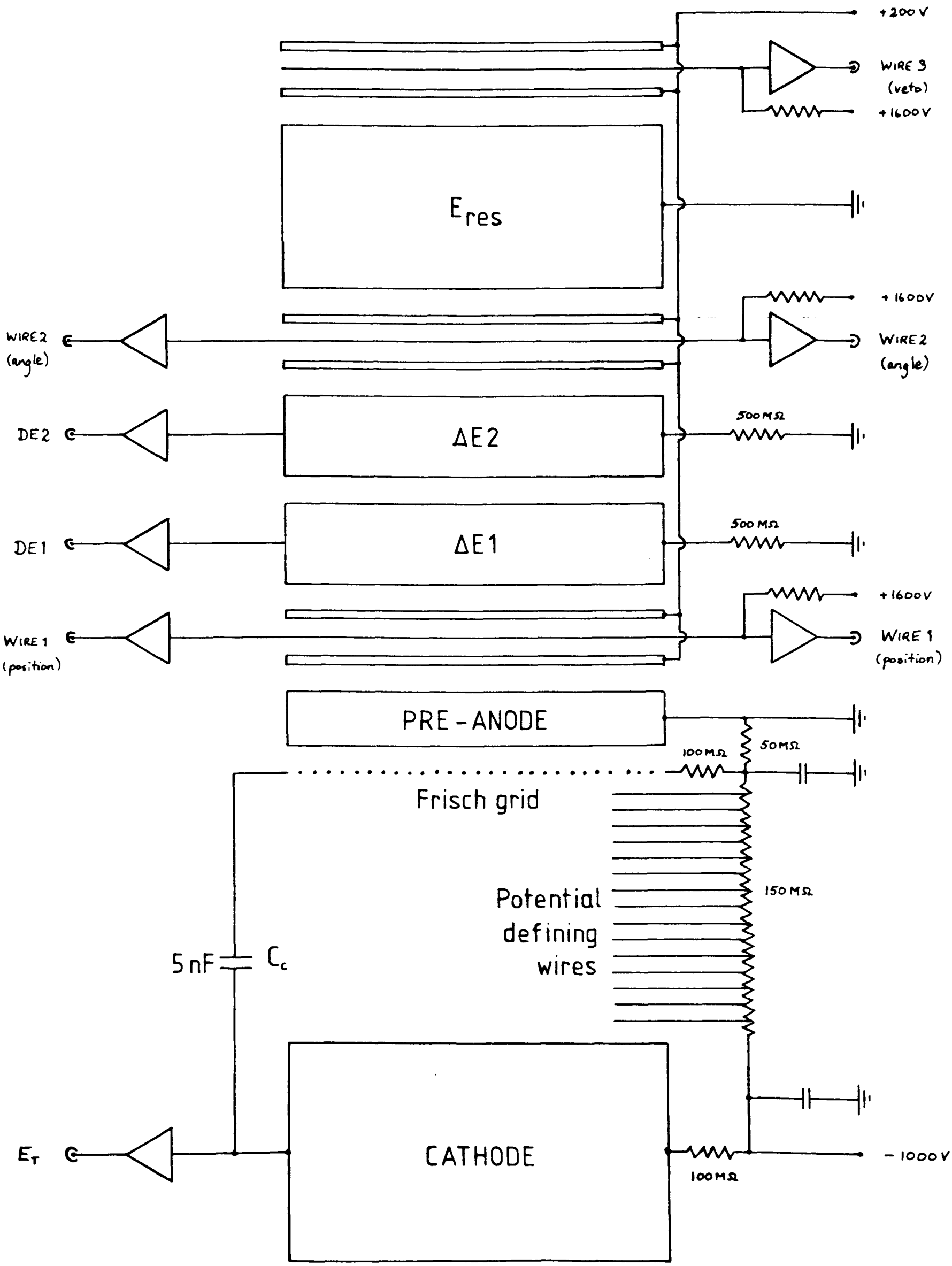


Fig. 3.8 Biassing and signal circuits in the hybrid counter.

### 3.5.2 External Electronics.

Fig. 3.9 shows a typical arrangement of the electronics for a heavy-ion experiment where a vertical position signal (Y.E) was generated by taking separate cathode and grid signals (see section 3.6.8). Most of the signal processing in this system is done by the computer software, namely (i) the division of the signal from one end of the PSPC by the sum of the signals from both ends; (ii) the use of a veto signal to reject events that have not stopped in the counter; (iii) division of the cathode signal by the total energy signal to obtain an energy-independent Y parameter; (iv) generation of an angle signal; and (v) generation of particle identification (PI) parameters if required.

Points (i) to (iv) above could be done relatively easily by analogue and logic circuits in the electronics. The advantage with not processing the signals before they are written to magnetic tape is flexibility: the tape can be replayed off-line with or without a requirement for a veto signal, for example, and inspection of the raw input is of great help if unexpected or possibly spurious effects are seen.

The strobe for the ADC could in principle be generated from all but the PC3 signal. If lightly-ionizing particles were to be detected it was convenient to use a signal from PC1 (both ends summed so that there was no dependence on position). Then the pulses of interest were well above the noise level. The various signals were arranged to reach their peak value during the 4 μs period in which the ADC was enabled after the reception of a strobe signal.

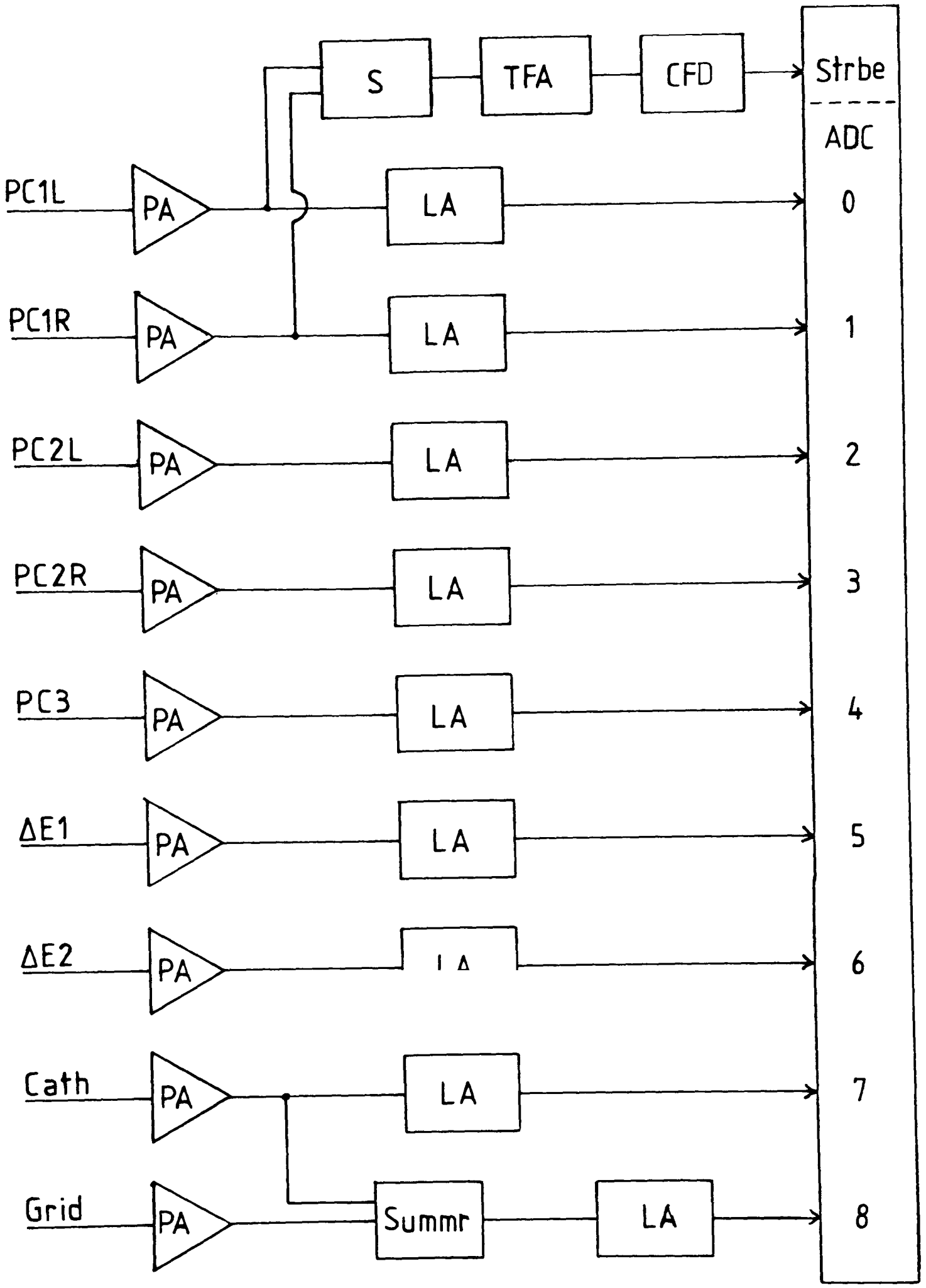


Fig. 3.9 Block diagram of electronics.

PA = preamplifier; LA = linear amplifier and filter;

S = summer; TFA = timing filter amplifier; CFD = constant fraction discriminator.

### 3.5.3 Computer Reduction of Data.

The desired end is the transformation of the input data into position spectra for each reaction product of interest, i.e. for given Z and M values of the detected particle. Examples of such gated position spectra have been given in Chapter 2.

If the first PSPC wire lies above the focal plane, then the position determination is straightforward. The rigidity $\rho$ is found from the measured value of the dipole field, B, and the calibration of the spectrometer once the position is known (this is readily done with the help of a kinematics program written specifically for the Oxford spectrometer, "MAGKIN").

The angle of incidence is determined by the difference of position signals 1 and 2. Fulbright and Erskine [Ful79a] review uses of the angle signal. For the Oxford spectrometer, whose focal plane is perpendicular to the mean angle of incidence, it is not necessary to correct the $\Delta E$ and $E_T$ signals for angle of incidence.

The atomic number Z and mass M are determined on the basis of the approximate relations:

$$\Delta E \propto MZ^2/E \ , \qquad (3.7)$$

with E the energy of the ion where $\Delta E$ is measured, and

$$(B\rho)^2/E = M/q^2 \ . \qquad (3.8)$$

The relation (3.7) is derived from the stopping power equation (3.2) in section 3.3.2, where it was noted that Z is strictly only equal to the nuclear charge if the energy per mass number is high enough.

Two approaches to the problem of particle identification (PI) are followed and these are discussed in detail by eg. Fulbright and Erskine [Ful79a]. Since two-dimensional displays were available for the on-line PDP11/60 computer at Oxford, the method that uses two-dimensional spectra was followed in general, although the alternative technique of using the relations (3.7) and (3.8) to generate PI parameters has been tested off-line on the VAX11/780.

Fig. 3.10a, which is a contour plot of $\Delta E$ against $E_T$ illustrates the first method. For the lighter heavy-ions ($Z < 6$, say), the range of different M for a given Z is restricted and, furthermore, the range of E values should be different as a consequence of the momentum selection of the spectrometer. This means that both Z and M can usually be separated for $Z < 6$ (following from relation (3.7)) and no further PI is then necessary. The selection is done by setting a two-dimensional gate on the group of interest, either by tracing out a window with a light-pen or, in the case of rectangular windows, projecting suitable one-dimensional gates onto the axes.

For heavier particles (or indeed for low energy light ions) the situation is more complicated, especially since particles of the same Z and M may have travelled round the analysing magnet in one of several possible charge states, q. Then relation (3.8) is used to find the mass M. The procedure is to select Z as above and construct a position (i.e. $B\rho$) versus $E_T$ display for particles satisfying this Z gate. The counts are usually seen lying clustered around sections of parabolic curves, one curve for each value of $q^2/M$ (see fig. 3.11 for an example). The light-pen is then used to set gates specifying the mass of interest.

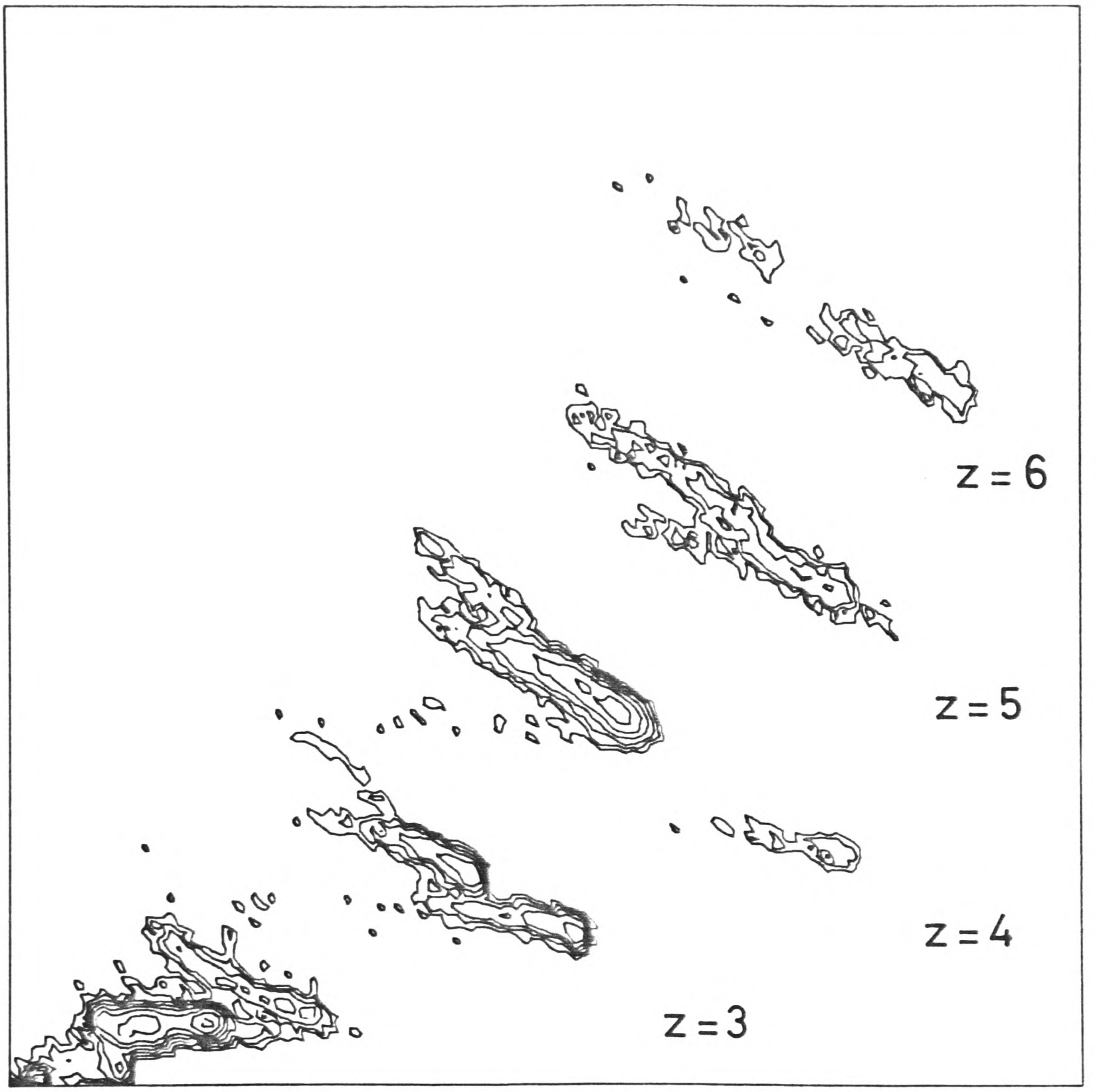


Fig. 3.10a Typical contour plot of $\Delta E$ vs. $E_T$ for ions stopped within the focal plane detector. This spectrum was obtained with 43 MeV $^{9}Be$ incident on a $^{26}Mg$ target. Only events that gave a PC2 signal were accepted. Hyperbolae of constant atomic number are indicated. Mass separation is also evident.

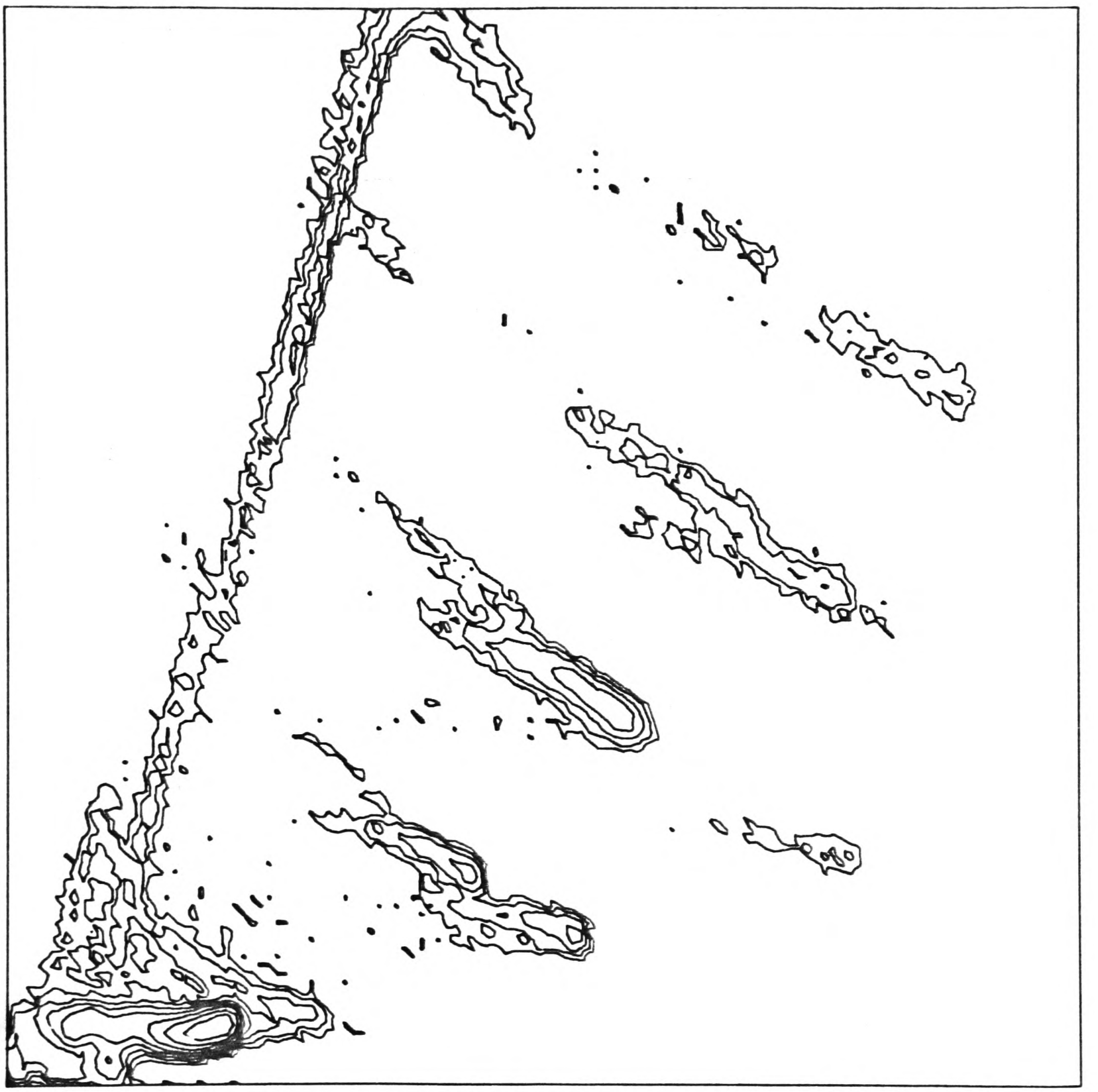


Fig. 3.10b As for fig. 3.10a except that all events were accepted. The low-energy tail that has appeared on the groups is due to heavy-ions that stop beneath the $\Delta E$ plate and thus give an anomalous $\Delta E$ signal.

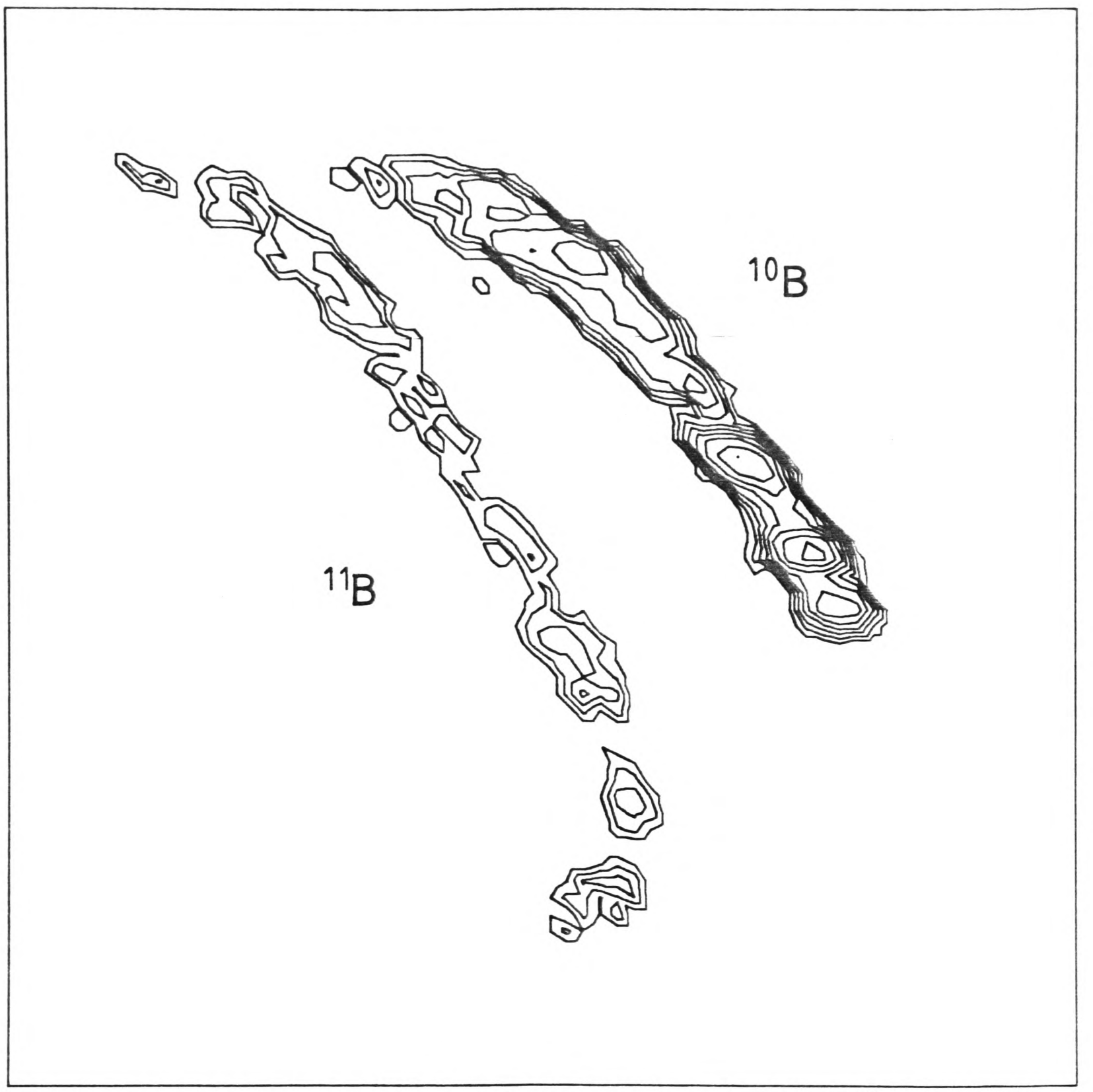


OXFORD

Fig. 3.11 Typical contour plot of position (or Bρ) against $E_T$ for boron ions, which was obtained by setting a 2-D window around the boron group in a ΔE vs. $E_T$ spectrum similar to fig. 3.10a. This case was for 43 MeV $^{9}$Be incident on a $^{24}$Mg target. The lowest drawn contour corresponds to the 1-count level. Clean separation of $^{10}$B and $^{11}$B is observed.

The $\Delta E$ versus $E_T$ spectrum shown in fig. 3.10a was generated by only accepting those events with a non-zero signal from the second proportional counter (PC2). This excludes particles that may have stopped beneath the $\Delta E$ plate and given an anomalously low $\Delta E$ signal. If this requirement is not imposed low energy tails appear on the particle groups as shown in fig. 3.10b. The gas pressure should thus be set such that the particles of interest stop between PC2 and the end of the counter. This is conveniently calculated using a small computer program HYBRID [Bho82] which has stopping power parameters for ions in isobutane derived from Northcliffe and Schilling [Nor70] together with the dimensions of the Oxford counter. Energy losses under all anode elements are also given by this program and losses in the entrance window may be included.

## 3.6 Measurement of Individual Particle Parameters.

Initial testing of the focal plane detector was done on the bench with an alpha source mounted inside the gas cell. Although this was convenient during the early stages, the ionization chamber signals are better investigated with more heavily ionizing particles since the signal-to-noise ratio is otherwise rather low. The performance of the proportional counters can readily be measured with an alpha source, however, since gas amplification overcomes the signal-to-noise problem.

### 3.6.1 Resolution Tests with an Alpha Source.

These tests were performed with the normal re-entrant window replaced by a blanking flange, to the centre of which were fixed the source and its collimation. A "three-line" source was used with strongest emissions at 5.168, 5.486 and 5.808 MeV. The counter was filled with 40 torr of isobutane after being evacuated to about 0.1 torr by absorption pumps. It was observed that the ionization signal strengths gradually deteriorated over a period of several hours if the gas was not changed, probably because the detector could not be adequately pumped out initially. Therefore the gas was flowed at a rate of about 1 atmospheric litre $min^{-1}$.

A comparison of the signals seen from the two $\Delta E$ plates showed that the uniformity of the electric field near the front of the counter was strongly distorted by the presence of the blanking flange[†]. This made it impossible to determine the true intrinsic resolutions of the $\Delta E$ and $E_T$ signals: these are better determined by tests with scattered beams from the spectrometer as described in section 3.6.6.

The position resolution of PC2 was investigated using double-slit collimation on the alpha source. Two sets of double slits, 0.5 mm wide at 2.5 mm separation, were mounted: one directly in front of the source and the other 14 mm towards PC2. The position signal from PC2, which was obtained by use of an analogue divider, was recorded for different bias voltages on the wire. The resolution improved from 1.6 mm at 700 V bias to a best value of 0.6 mm at 1000 V bias (fig. 3.12). This is consistent with the geometrical broadening of the object at a distance

---

[†] The first $\Delta E$ signal (DE1) was less than one half the size of the second (DE2) and had a fwhm resolution nearly three times worse.

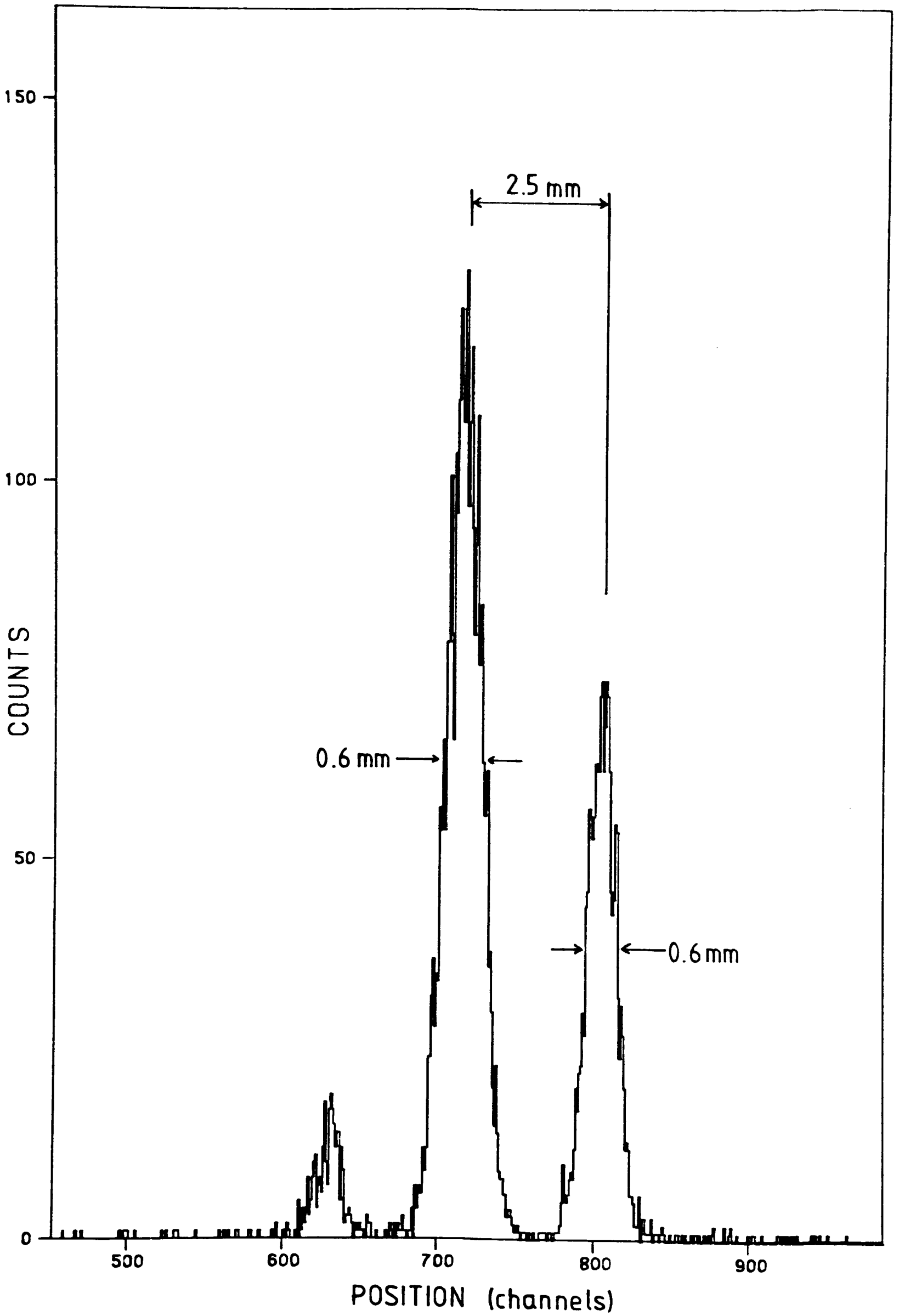


Fig. 3.12 Position spectrum obtained with pairs of double slits in front of an alpha source. (The small peak to the left corresponds to particles crossing from one half of the first collimator to

equal to that of the separation between the slits and PC2, so one may infer that the wire resolution is less than 0.6 mm.

### 3.6.2 Linearity Tests of the Proportional Counters.

It is not of overriding importance that the PSPCs should be linear in their position response: so long as the non-linearities are known corrections can be made in the software. However it is more satisfactory if they are, both in terms of simplicity and the assurance that no large field non-uniformities are present.

Linearity tests were conducted after the field correcting wires were inserted around the ionization chamber walls as described in section 3.4.3. A collimated alpha source was moved by means of a stepping motor and worm drive across the window of the hybrid counter whilst it was in the evacuated focal plane box of the spectrometer. The gas pressure in the counter was 30 torr in order that signals could be taken from PC1 and PC2 simultaneously. Before tests began the amplifiers connected to either end of a given PSPC were carefully gain-matched by sending pulses from a generator through a charge-terminator tee-ed to both the input of the preamplifier and the PSPC output, for each end in turn.

Fig. 3.13 is a plot of peak channel against position of the source. The first order fits to the points show less than 1% deviation from linearity except at the extreme end (last 8 mm) of PC1. PC2 shows less than 0.5% deviation from linearity over 28 cm of its length, which compares very favourably with PSPCs constructed at other laboratories (see Ford [For79] for a review).

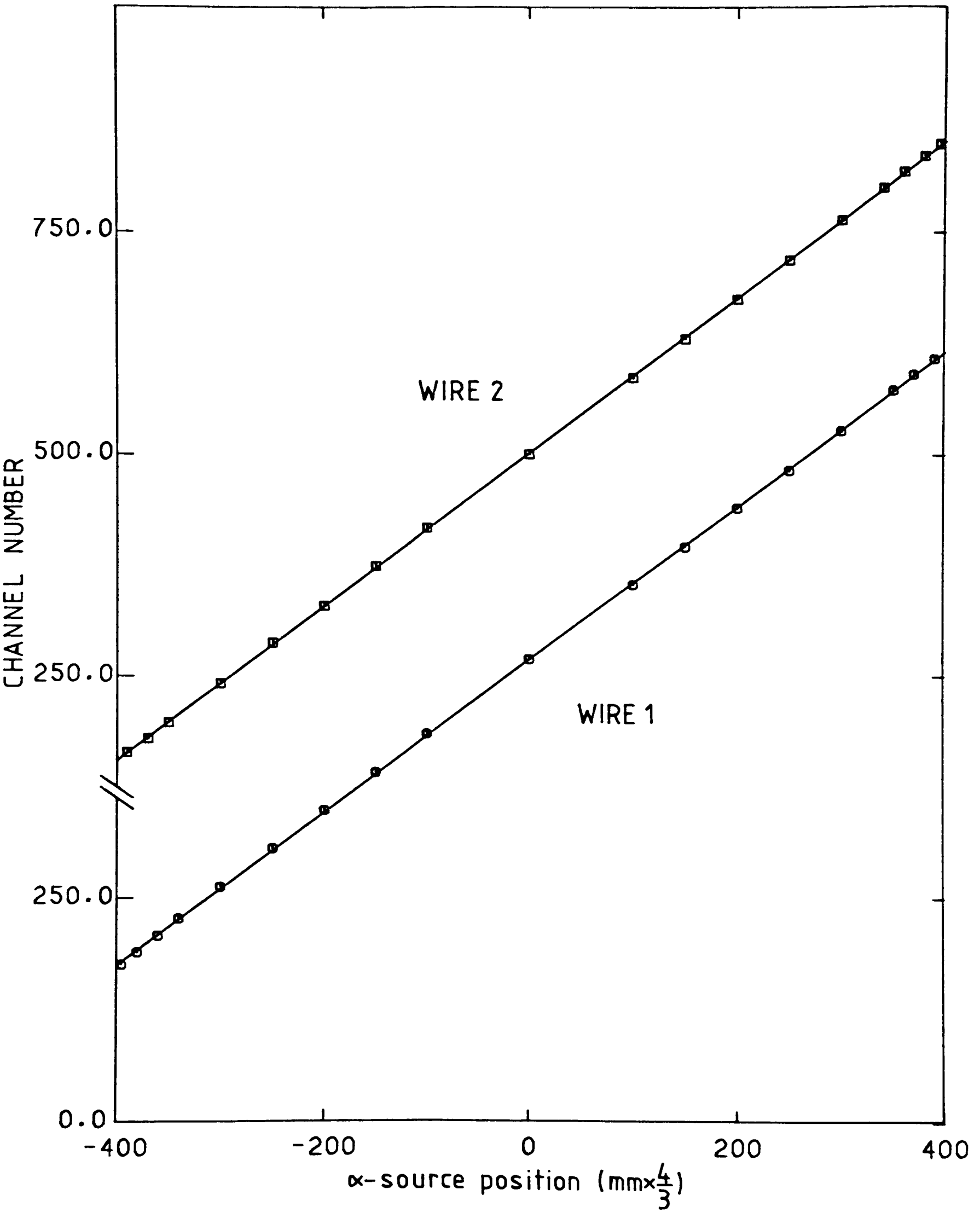


Fig. 3.13 Linearity tests of the proportional counters.

### 3.6.3 Positive Ion Problem.

Considerable effort was expended trying to stop the large numbers of positive ions generated in the PSPCs from reaching the ionization chamber region and giving spurious pulses on the $E_T$ or $\Delta E$ signal. The effect of the positive ions was accentuated when the counter was undergoing tests with alpha particles since (i) the low ionization meant that the $E_T$ and $\Delta E$ signals were especially small, and (ii) the initial bench tests were carried out with long amplifier shaping times of 8 μs to filter out radio-frequency pickup. The symptoms were a loss of resolution together with a shift in peak channel when the PSPCs were operated at high voltage. The positive ions appeared on the $E_T$ preamplifier as a slowly-rising pulse some 300 μs after the proportional counter signal (see fig. 3.14).

In an attempt to cure this problem the following measures were taken. First, a fine grid of wires was inserted beneath the counters. This was of some help in that 25% larger pulses could be obtained from PC2 before the $E_T$ resolution began to deteriorate. Note that the positive ions only have to emerge below the shielding grid for a spurious signal to be induced on the Frisch grid - it is not necessary for them to penetrate the Faraday cage. At this point, when the detector was in the focal plane box of the spectrometer and hence shielded, it was discovered that the positive ion pulses could be filtered out by the main amplifiers when the time constants were reduced: at $\tau_s$ = 4μs the pulses had almost disappeared from the output of the Ortec 440A amplifiers whilst at $\tau_s$ = 2μs the effect was completely negligible without seriously compromising the signal-to-noise ratio.

A further step was taken to reduce the number of positive ions escaping through the shielding grid. As described in section 3.4.5, this entailed raising the proportional counters above the anode plane, a measure suggested in part by apparently similar troubles encountered by Tassan-Got et al. [Tas82]. Whilst the proportional counter was on the anode plane, the shielding grid and counter body had to be at the same potential (in practice, ground potential). Then the field just above the grid was restricted to that produced by the anode wire 9 mm away (compare fig. 3.15a). When the counter was raised, the field above the grid could be increased by raising the voltage of the wire and body together - without danger of breakdown (fig. 3.15b). The field just above the shielding grid could then be made to be at least twice that between the Frisch grid and anode plane in order that the grid became less transparent to positive ions moving downwards but more transparent to electrons moving upwards (eq. 3.5). In practice it was found that although the efficiency of electron collection by the proportional counter was more than doubled by this means, the size of the positive ion pulse on the $E_T$ preamplifier output was only reduced by about 20% (for equivalent charge generation at the wires). The time delay between the PSPC signal and the start of the positive ion pulse on the ionization signal varied considerably with the voltage applied to the PSPC body: at 500 V it was 0.3 ms,but at 100 V it was 1.4 ms (the drift velocity of the ions is roughly proportional to the applied field [Wil50]).

It would therefore appear rather difficult to completely catch the positive ions, at least by using a single shielding grid. Instead, one must use appropriate filters and baseline restoration after the

Fig. 3.14 Representation of preamplifier signals. Top: PSPC signal, bottom: delayed pulse on $E_T$ signal due to positive ions.

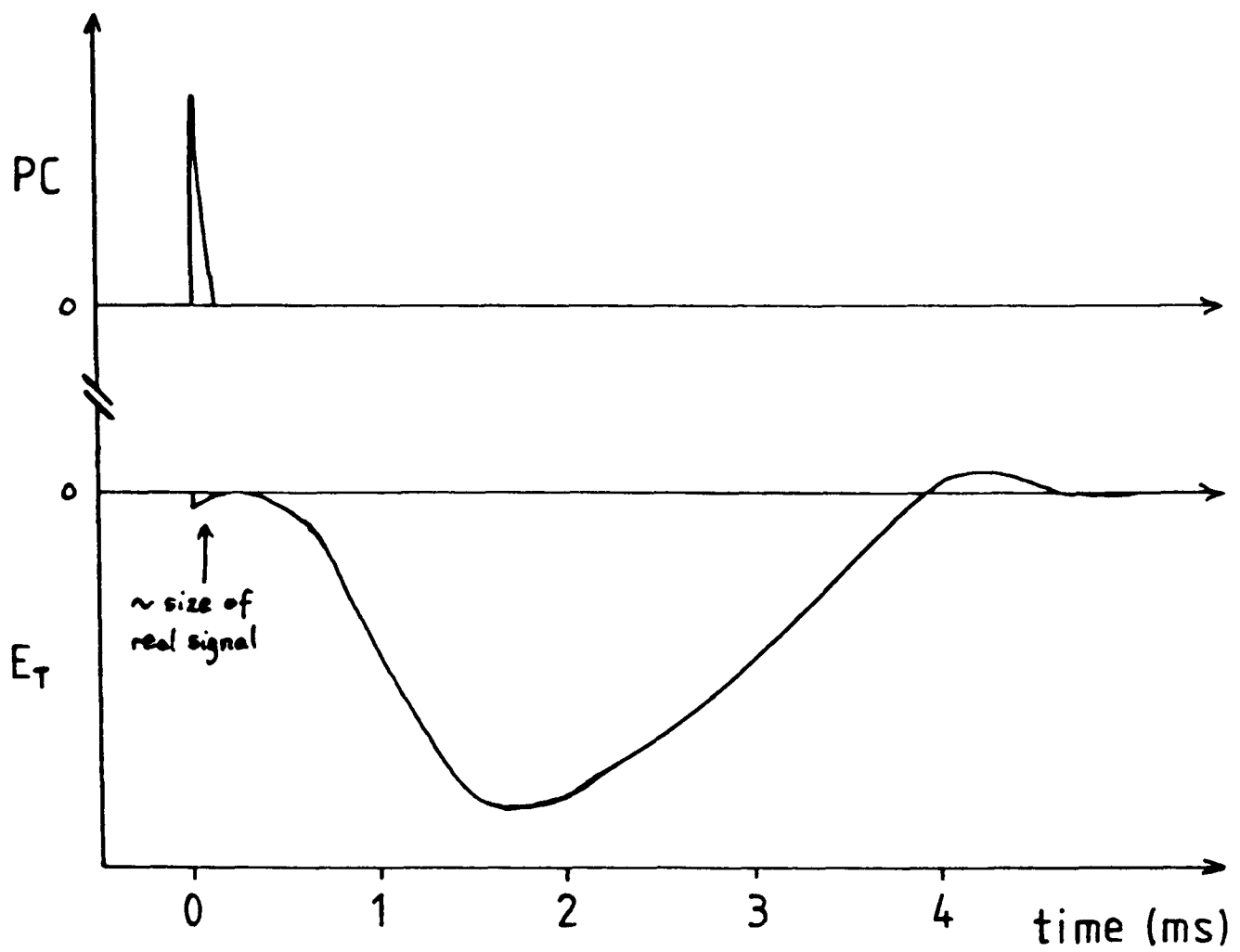


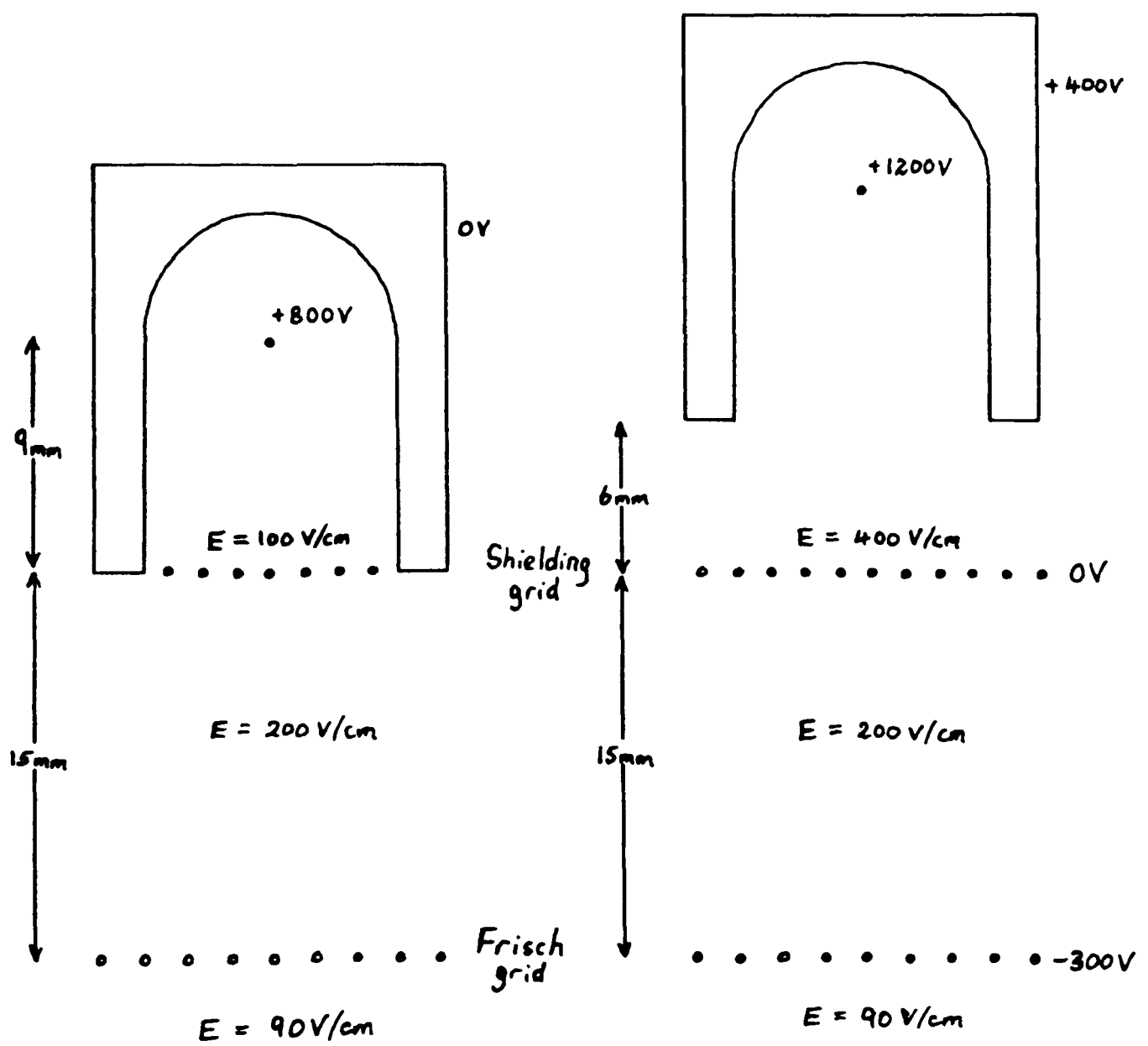

preamplifiers to deal with the effects (it was later found that Ophel [Oph82] had come to a similar conclusion with a small detector at the Australian National University). Subsequent tests with heavy-ion beams where the main amplifier shaping times have been set at 2 μs have shown no change in $E_T$ and ΔE resolution or peak channel whether the proportional counters were operating or not.

### 3.6.4 Position Resolution.

The position resolution observed with heavy-ion scattering is almost always limited by target effects. This was certainly true for the ($^{9}$Be,$^{10}$B) reaction data described in Chapter 2. On the other hand, the resolution observed with proton or deuteron scattering has been found to be limited by the size of signal from the PSPC, which is itself limited by the low ionization beneath the proportional counter. The voltage applied to the wire cannot be increased indefinitely (before instabilities or breakdown occur) so that the size of the avalanche is restricted and thus the noise level remains significant (see eq. 3.6). It is not then surprising that the best resolution seen with the spectrometer has been for the case of 27 MeV elastically scattered helium particles from a thin gold target (5 μg/cm$^2$) with a thin carbon backing (also 5 μg/cm$^2$). This resolution was $E/\delta E = 3030$ (fig. 3.16) which corresponds to 0.6 mm at the k = 0.0 dispersion of 3.80 cm/% δp/p. For this case the number of electrons liberated was calculated to be $2\times10^7$ from the size of the preamplifier signals (260 torr isobutane, wire voltage of 1690 V). Then the thermal noise contribution to the resolution is estimated from eq. 3.6 to be 0.09 mm. There are obviously other contributions to the resolution from the detector, such as multiple scattering in the entrance window and the diffusion of the

electrons as they drift upwards to the PSPC. In fact the diffusion effect is thought to be negligible when averaged over the $10^7$ electrons collected by the PSPC [Ric74]. Since the particles arrive at normal incidence, fluctuations in the centroid of the deposited charge are also insignificant [For79]. The major contribution to the spread in the position signal due to effects in the detector is from multiple scattering in the mylar foil, which for this case was 25 μm thick. This is estimated to contribute 0.38 mm to the resolution.

Table 3.2 lists estimates of contributions to the position resolution for the above case from beam, target and spectrometer effects. The effect of spectrometer aberrations and dipole power supply instabilities are not included but may be significant at this level. The most important contribution listed is that due to the spectrometer object size (i.e. from the beam collimator width of 1 mm). Unfortunately this cannot be added in quadrature with the other contributions, since it is unlikely that the image shape would have a Gaussian distribution.

Thus it is not clear from this measurement what the ultimate limiting resolution of the detector is, except that it is certainly better than 0.6 mm. This is consistent with the results of the bench tests described in section 3.6.1. In fact it is a more stringent test than the earlier one, since that did not include the effects of multiple scattering in the Mylar entrance foil.

Table 3.2

Contributions to position resolution from the effects of beam, target & spectrometer for 27 MeV $^{4}He$ scattered from $^{197}Au$ at 15°

| Source | FWHM Contribution (keV) |
|---|---|
| Beam energy spread[a)] | 3 |
| Beam divergence[b)] | 0 |
| $\delta\Delta E$ 5μg/cm2 carbon | 1 |
| $\delta\Delta E$ 5μg/cm2 gold | 1 |
| 20% target non-uniformity | 0.3 |
| Target multiple scattering | <0.1 |
| Spectrometer object size | 6 |

a) see notes in Appendix C

b) no effect for k = 0.0

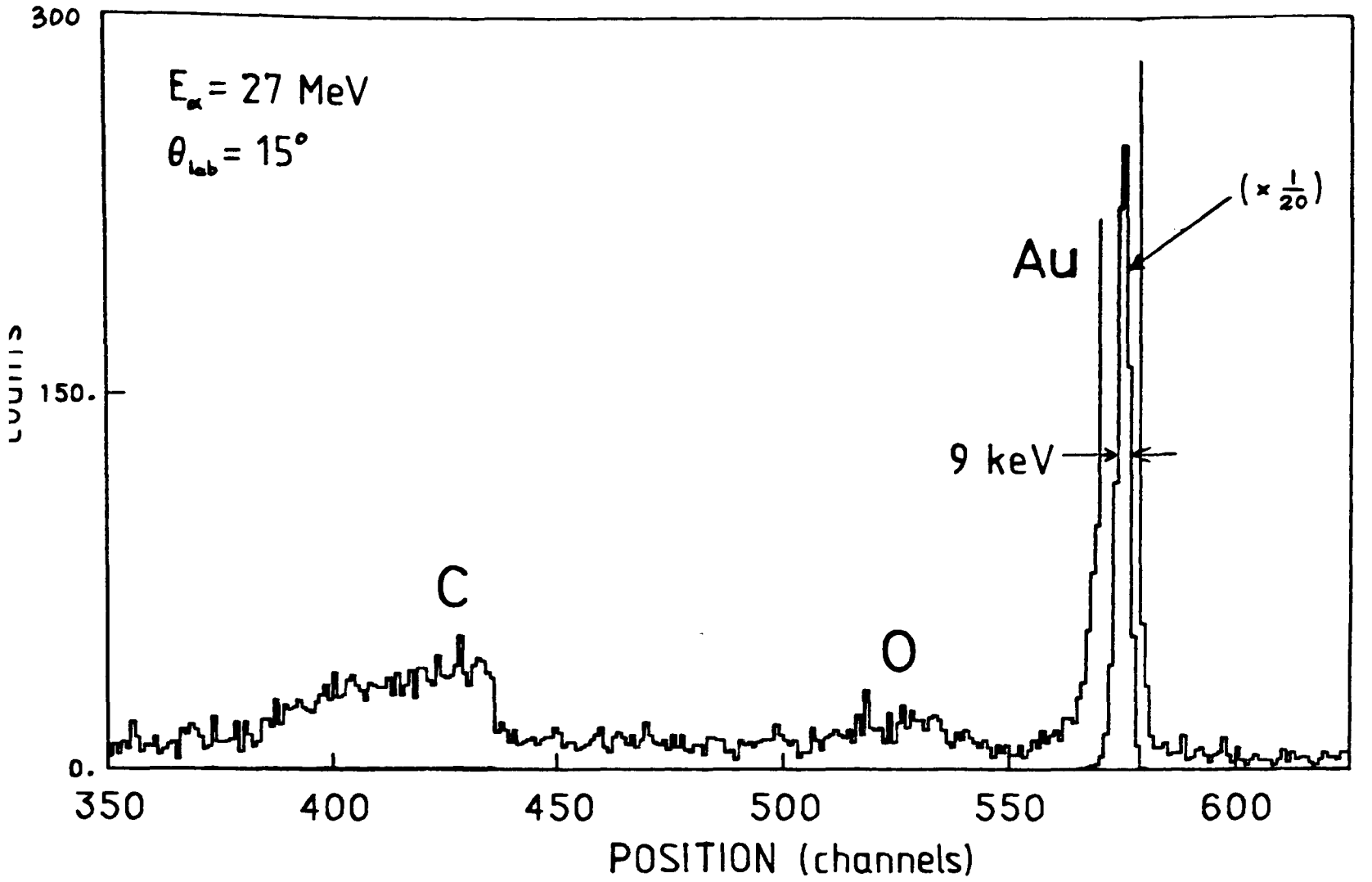


Fig. 3.16 Position spectrum obtained with 27 MeV alpha particles scattered off a thin gold target. The resolution was measured to be 1 in 3030. Kinematically-defocussed peaks for $^{16}O$ and $^{12}C$ in the target are also observed.

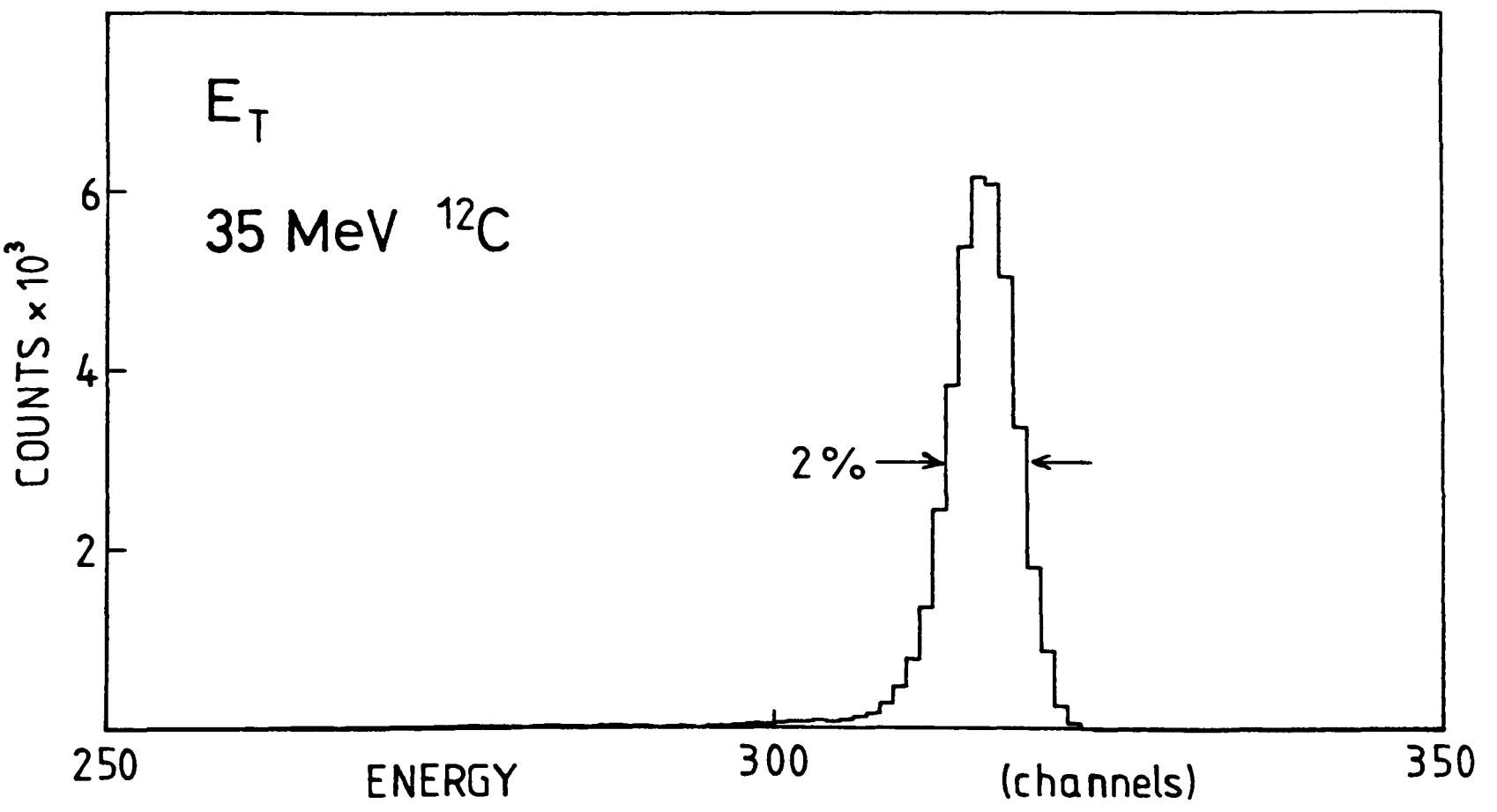


Fig. 3.17 Total energy spectrum obtained with 35 MeV $^{12}C$ ions scattered from a gold target.

### 3.6.5 Total Energy Resolution.

The best $E_T$ resolution obtained with the counter has been 0.9% (fwhm) or 570 keV for the case of 63 MeV $^{12}C$ ions elastically scattered from a gold target. The largest contribution to this resolution is probably from losses of induced charge from the sides and window of the ionization chamber (see section 3.6.7). For the above case, the contribution from the measured stray capacitance to ground of the cathode and grid together (measured with a bridge circuit to be 480 pF) is 150 keV or 0.24% and that arising from the energy straggling in the 12.5 μm window used is estimated as 174 keV or 0.28%. The bowing of the entrance window under pressure results in two small contributions which tend to cancel: the largest energy loss in the mylar is where the window is most curved, i.e. at the edges, but it is at the centre of the window that ions have to travel through more isobutane. Another contribution to the resolution comes from the capture or recombination of electrons by positive ions or electronegative impurities.

More typically, for lighter ions or less energetic $^{12}C$ ions, resolutions of between 1.5% to 2.5% have been observed. A total energy spectrum for the case of $^{12}C$ at 35 MeV is shown in fig. 3.17.

### 3.6.6 Energy Loss Signal.

An example of a ΔE spectrum is shown in fig. 3.18, where the resolution is 7.0%. Statistical fluctuations in the ionization dominate the ΔE resolution since the variation in path length due to the spread in incident angle of arrival is small for perpendicular focal planes (in contrast to 45° focal plane inclination, where this is the dominant effect). For the case of 43 MeV $^{9}Be$ ions in 100 torr of isobutane,

energy-loss straggling has been calculated as 6.3%, using the formula given by Fulbright [Ful58] multiplied by a factor of 1.6 in order to include an approximate correction for the effects of charge-exchange straggling, as suggested by Erskine et al. [Ers76]. Electronic noise contributes only 0.8% for this case. Other possible contributions to the resolution are inadequate grid shielding, bowing of the field lines and poisoning of the gas.

### 3.6.7 Loss of Energy Signal Amplitude at Sides of Counter.

Tests where an elastically scattered group of particles were systematically stepped across the detector showed that the energy signal began to drop in amplitude at some 8 cm away from the centre. At 12 cm from the centre the peak height was about 5% lower than the value at the centre and by 15 cm (i.e. near the edge of the window) it had further fallen to 10% down. Furthermore, the resolution of the energy signal started to noticeably deteriorate when the particles were detected more than 12 cm off centre. Both effects were less pronounced when the spectrometer's horizontal acceptance slits were closed in, as would be expected for a problem associated with particles that travel close to the sides of the counter.

Since it would appear from the proportional counter linearity tests that the electrostatic field at the sides of the counter is quite uniform, it seems that this loss in energy signal arises because the Faraday cage is not complete. No signals are taken from the potential defining wires around the sides of the counter and the positive ions left in the chamber as the electrons pass through the grid will induce charge on them to an extent that varies with distance. The solution is

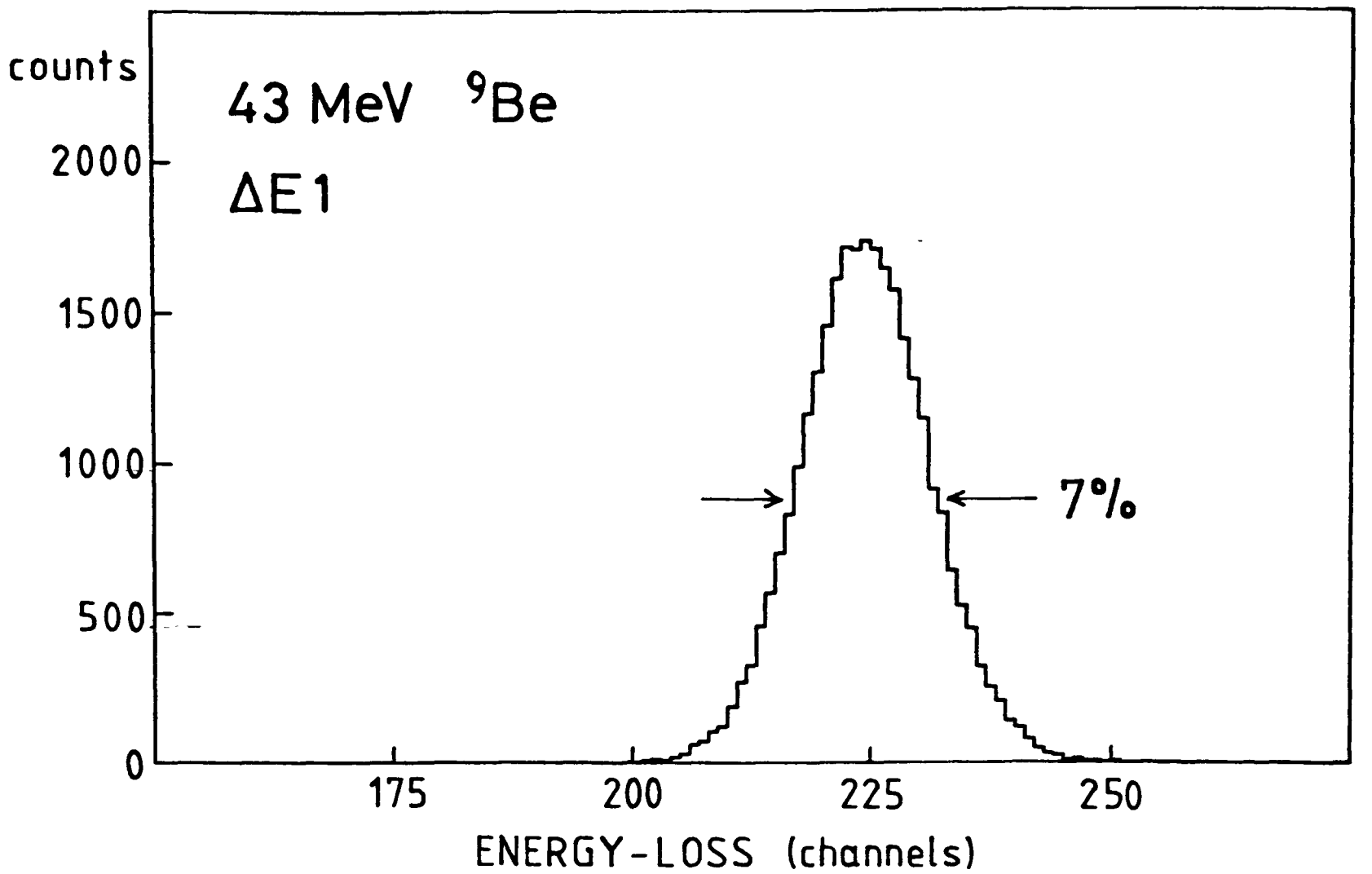


Fig. 3.18 Energy-loss spectrum obtained with 43 MeV $^{9}$Be ions. Most of the observed 7% fwhm resolution is accounted for by energy-loss straggling.

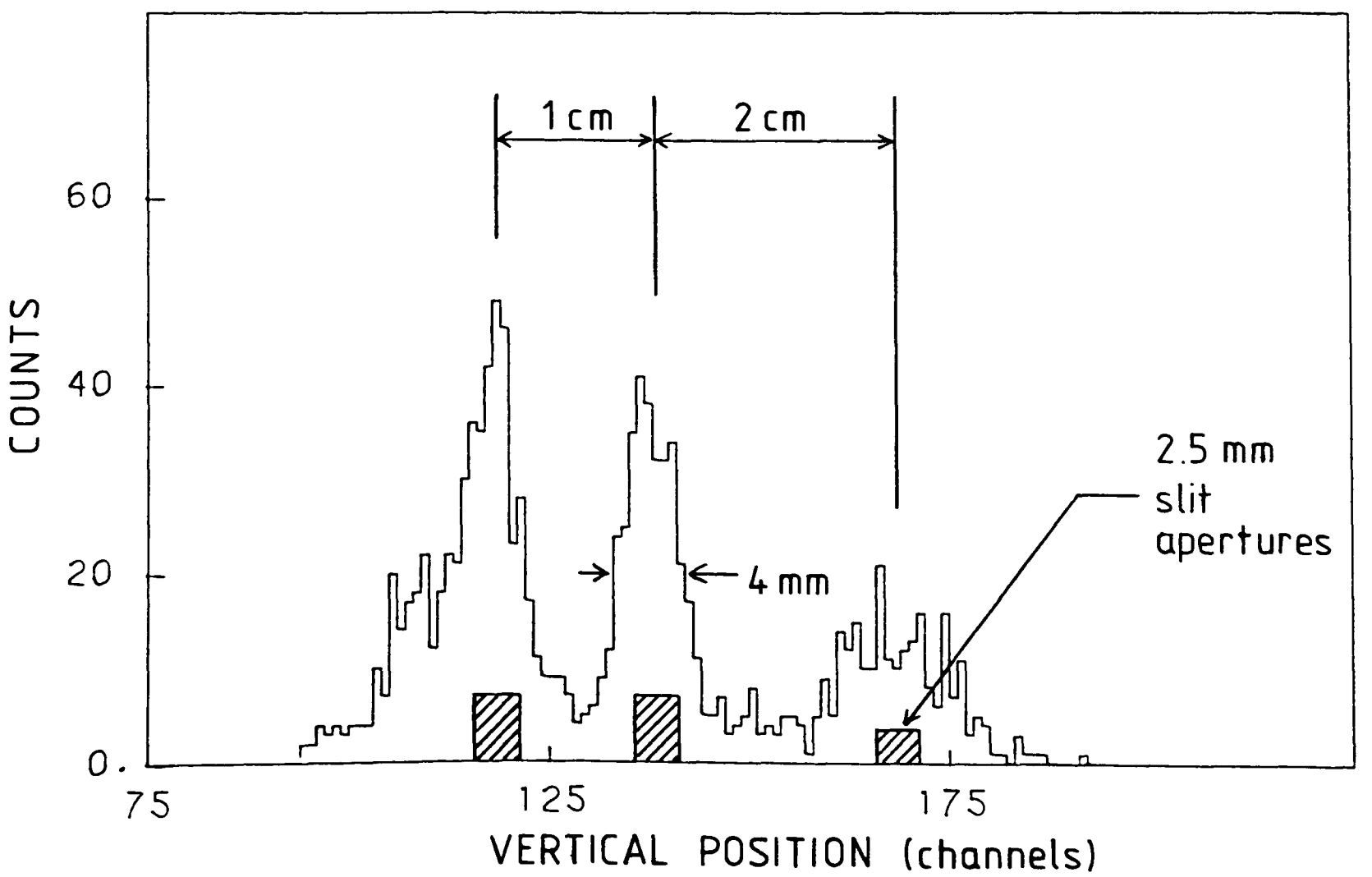


Fig. 3.19 Vertical position spectrum obtained when a 3-slit aperture was placed in front of the counter's entrance window. The relative sizes of the slits are indicated beneath the peaks.

then relatively simple: all 14 wires ought to be AC-coupled to the cathode (and large resistances inserted between the wires and the biassing chain). This has not been carried out because tests with position signals out of the median plane (as described in the next section) required separate cathode and grid signals. Also, the loss in $E_T$ resolution did not compromise any of the experiments done at that time.

### 3.6.8 Vertical Position Signals.

The position of incident ions at a right angle to the median plane of the spectrometer (the y direction) can be measured if the cathode and grid are not AC-coupled but if instead separate signals are taken from each. Then the cathode signal is proportional to the distance away from the grid (see fig. 3.3) for monoenergetic particles. To obtain a true Y signal, the cathode signal should be divided by the total energy signal. This (i.e. $E_T$) may be reconstructed by summing the grid and cathode preamplifier signals before the main amplifier. The resultant signal will only be significantly noisier than the $E_T$ signal derived in the usual way if the noise levels from grid and cathode are comparable. For the Oxford counter this was not so: the grid has a much greater stray capacitance to ground than the cathode.

A spectrum is shown in fig. 3.19 that was taken when a plate with three horizontal slots, 2.5 mm wide, had been placed over the entrance to the counter. The observed 4 mm width of the peaks can be accounted for by the multiple scattering and spread in vertical angle of the incident ions which penetrated some 20 cm into the counter.

The y-position signal was used to investigate the vertical image formed by the spectrometer (see [Pri83]). It also provided an interesting illustration of the effects of gas poisoning. Fig. 3.20a is a contour plot of $E_T$ against Y taken after the gas had been in the counter for almost 9 hours. Fig. 3.20b is the same thing taken immediately after fresh gas was flowed through the counter. In fig. 3.20a there is marked decrease in the $E_T$ signal with increasing Y, i.e. for ion tracks further from the grid. Electrons from these tracks have more chance of being captured by impurity molecules in the poisoned gas than those liberated near to the grid.

## 3.7 Summary & Discussion.

The performance of the present counter is very encouraging, especially in view of the large separation between cathode and grid. The ionization signals have shown resolution capabilities similar to a large hybrid counter built by Shapira et al. [Sha80], albeit the figures are slightly worse than the best values obtained with smaller counters, as might be expected. The proportional counters have given excellent performance, both in position resolution and linearity.

Special care was taken to keep the capacitance to ground of the $50 \times 40$ cm$^2$ cathode plate to a minimum by placing the containing vessel wall 7 cm away. For similar reasons the counter has only one full grid, although additional small sections of grid have been put underneath each proportional counter to shield the Faraday cage and $\Delta E$ plates from the positive ions generated near the anode wires. This shielding has sufficed for all experiments performed so far. From the experience with

$^{12}C + {}^{197}Au$ at 35 MeV

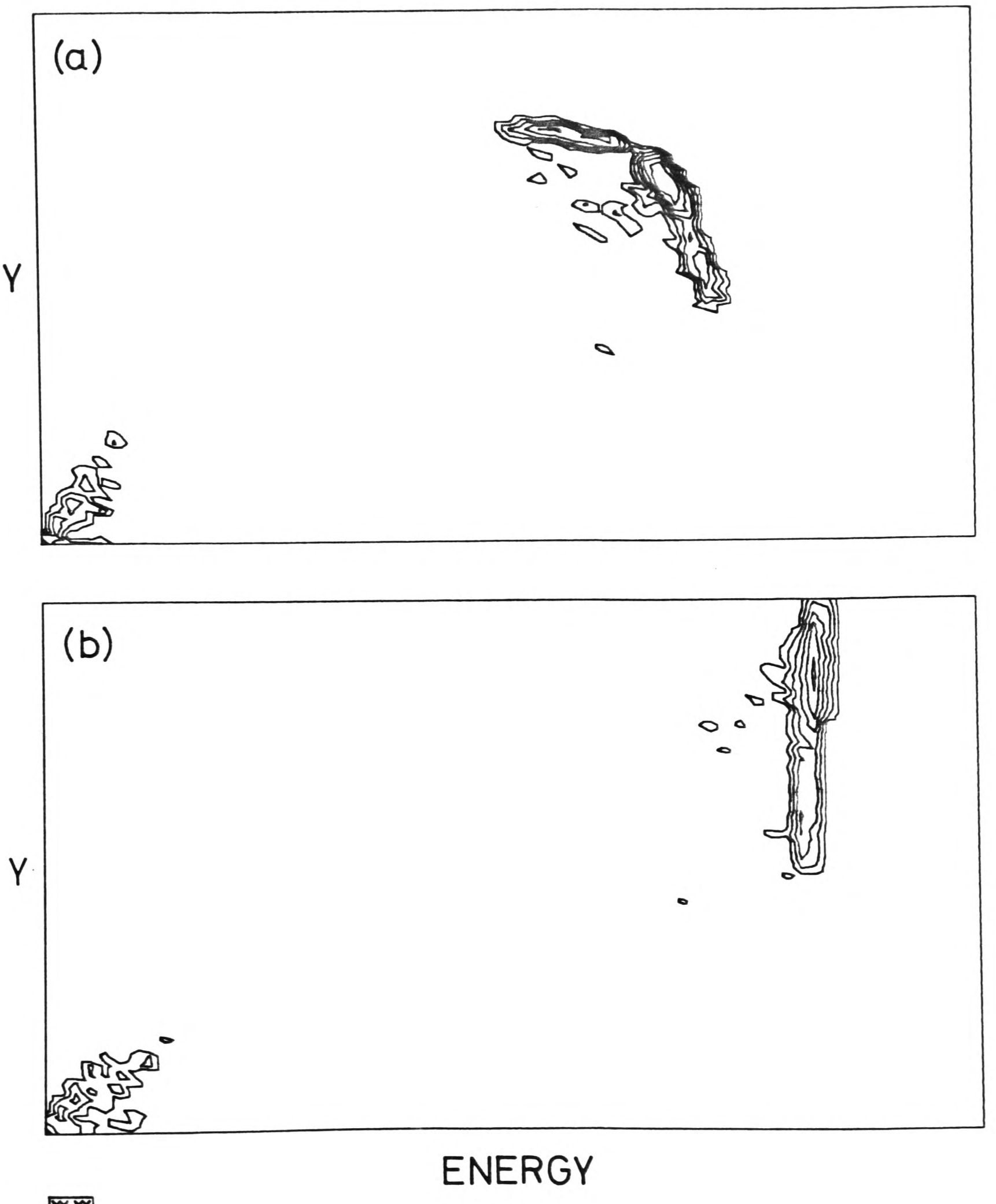


OXFORD

Fig. 3.20 Vertical position, Y, against total energy:
(a) poisoned gas,
(b) fresh gas.

the positive ion problem described in section 3.6.3, it appears that the original simpler arrangement, where the PSPCs lie on the anode plane, might have been adequate - especially if the field just above the shielding grid was made to be significantly greater than that just below the grid. This might be achieved by use of a new, shallower proportional counter design such that the field due to the wire is still strong in the critical region above the grid. Ensuring that the ratio of fields was >2:1 was seen to improve the electron collection efficiency of the PSPCs and this is particularly important in light-ion mode.

An obvious improvement to the present counter is to take signals from the potential defining wires inserted around the sides of the counter. These were necessary in order to improve the electric field uniformity at the edges of the chamber. While signals are not taken from the wires, the best $E_T$ resolution (1 to 2%) can only been seen if the centre half of the counter is used.

The wires in front of the window could be replaced by a graded-potential window in the form suggested by Naulin et al. [Nau81] if one were concerned about either the loss in effective aperture or the rare cases when ions might scatter off a wire in such a manner as to simulate another ion type (for example, an exotic nucleus).

A longer window for the counter will eventually be required if full use is to be made of the spectrometer's 60 cm focal plane. The performance of such a new counter need not be significantly worse than the present one, since the only contribution to the resolution of the ionization signals that would be unavoidably increased is the noise

resulting from the stray capacitance to ground, and this has not usually been a major factor in the observed resolutions for the present counter.

It may be desirable to take time-of-flight measurements to supplement particle identification when heavier, slower ions have to be discriminated. For this purpose a 1 or 2 ns signal would be needed. Sann et al. [San75] have derived a fast signal from the cathode of a small ionization chamber filled with methane gas and report 1.7 ns time resolution with 62.5 MeV sulphur ions. Such low figures cannot be achieved with isobutane-filled chambers, however, since the maximum electron drift velocity is only one half that in pure methane. Erskine et al. [Ers76] obtained 5 ns resolution with their isobutane-filled counter.

Another possible timing signal might be obtained from the scintillation light radiated by gas atoms or molecules that are excited or ionized by the incident particle. Isobutane again is not a good medium for this, since the amount of useful light available is probably small [Bir64]. This problem may be avoided if the counter is divided into two sections by a thin foil. The front part, containing the PSPCs, would then be filled with isobutane so that multiple scattering is kept to a minimum, whilst the back part would contain a gas more suitable for scintillation such as pure argon or xenon. The gas cell for the Oxford counter has in fact been constructed with this in mind: at present the two sections are simply joined by an O-ring seal.

A third way to derive a timing signal is to place a parallel plate avalanche counter (PPAC) just inside the entrance window. These counters can easily provide sub-nanosecond time resolution (see, for

example, Breskin and Zwang [Bre77]). The main disadvantage would be in the additional thickness of material to be penetrated by the ion before the position measurement is taken, resulting in greater scatter and fluctuation in the energy loss. Tassan-Got et al. [Tas82] have used a PPAC just outside the entrance window to a hybrid counter.

In summary, the detector described in this chapter has been found to work reliably and very satisfactorily. There are several ways in which the performance might be upgraded or extended, as the need arises. The present detector is now in routine use for all experiments performed on the Oxford spectrometer.

# CHAPTER 4

# OPTICAL MODEL ANALYSIS OF THE ELASTIC SCATTERING

## 4.1 Introduction.

Optical model potentials to be used in the DWBA analysis of the ($^{9}$Be,$^{10}$B) reaction were obtained by fitting parameters to elastic scattering data which represented entrance or exit channels in the reaction. Potentials of the usual Woods-Saxon form were assumed for this purpose. These are only approximate representations for the shape of the scattering potential; for a more accurate (as well as a more physically meaningful) description of the distorting potentials in heavy-ion reactions, double-folding models might be expected to be more satisfactory [Sat74]. However, it should be borne in mind that the most common form of the double-folding model, namely that which uses the M3Y nucleon-nucleon interaction of Bertsch et al. [Ber77], does not successfully describe $^{9}$Be elastic scattering since, as remarked in Chapter 1, the predicted potentials have to be reduced by roughly one half to give a good account of the data [Sat79]. It was therefore felt that the simplicity of the conventional Woods-Saxon form was appropriate for the work described in this thesis.

The form of all the potentials used is given by

$$U(r) = - \frac{V}{1 + \exp\{(r - R_v)/a_v\}} - \frac{iW}{1 + \exp\{(r - R_w)/a_w\}} + V_c \qquad (4.1)$$

$$\text{where } V_c = \frac{Z_t Z_p e^2}{2R_c}\{3 - (r/R_c)^2\} \quad \text{for } r < R_c$$

$$= \frac{Z_t Z_p e^2}{r} \qquad \text{for } r > R_c$$

and $$R_x = r_x(A_t^{1/3} + A_p^{1/3}) \qquad x = v,w,c$$

Adequate fits to the data were obtained with this form, therefore more complicated variations were not tried. In a study of $^{9}$Be scattering Balzer et al. [Bal77] found that the quality of their fits was not improved by using Woods-Saxon-squared or surface-absorption forms.

The spins of $^{9}$Be and $^{10}$B are 3/2 and 3 respectively. In principle, this means that a spin-orbit potential, which was not considered in the following analysis, must contribute to the scattering. There is then the question of whether the neglect of the spin-orbit term leads to incorrect values of the central potential parameters. Several studies of the spin-orbit potential for the case of $^{6}$Li elastic scattering (see, for example, [Sta80], [Chu76] and references therein) have shown that the inclusion of a spin-orbit potential has very little observable effect on angular distributions (although, of course, they may be necessary to account for the asymmetry data from polarized-beam studies). The work of Amakawa and Kubo [Ama76] suggests that spin-orbit effects for $^{9}$Be and $^{10}$B would be even smaller than those for $^{6}$Li. Thus, the potentials extracted from the angular distributions are unlikely to be significantly different if the spin-orbit term is included.

A well-known feature of optical model fitting to the elastic scattering of strongly absorbed particles is that many ambiguities may arise. Many discrete sets and often continuous distributions of parameters will give equally good fits to the data. The most familiar of these ambiguities was first discussed by Igo [Igo58] and occurs

because the scattering is mostly determined by the tail of the potential. At large radii,

$$U(r) \approx -V.\exp(R_v/a_v)/\exp(r/a_v) - iW.\exp(R_w/a_w)/\exp(r/a_w)$$

so that for a fixed value of $a_v$, any pair of V, $R_v$ which keep $V.\exp(R_v/a_v)$ constant will give similar angular distributions (and likewise for the imaginary part). This happens even though the potential may be very different in the interior.

Another ambiguity arises from the fact that the data only constrains the value of the optical potential in a very limited region around the strong absorption radius, $D_{sa}$, as defined by

$$kD_{sa} = \eta + [\eta^2 + \ell_{\frac{1}{2}}(\ell_{\frac{1}{2}} + 1)]^{\frac{1}{2}} \qquad (4.2)$$

where $\ell_{\frac{1}{2}}$ is the partial wave corresponding to an absorption of $|S|^2 = \frac{1}{2}$, k is the wave number and $\eta$ the Sommerfeld parameter. Thus any potential possessing a particular strength at $D_{sa}$ and with a "reasonable" gradient is likely to give a good account of the elastic scattering ([Sat74], [Woo81]). Yet an arbitrary potential satisfying the "$D_{sa}$ criterion" may be quite unacceptable when used in calculations of inelastic scattering or transfer reactions since these reactions may, and usually do, probe different regions of the nuclear potential. Table 4.1 lists some physically significant quantities for the elastic scattering systems discussed in this chapter.

More constraints can be placed on the optical model potentials by taking data at very high energy on light targets or at very backward angles in angular steps fine enough to define the oscillations and with sufficiently good statistics to influence the fitting [Sat74]. The targets and projectile energies in the work discussed in this thesis were not, of course, primarily chosen for their desirability in

Table 4.1

Physical Quantities of the Elastic Scattering Systems.

| System | $E_{lab}$(MeV) | $E_{cm}$(MeV) | $E_{CB}$(MeV) | k($fm^{-1}$) | η | $\ell_{\frac{1}{2}}$ | $D_{sa}$(fm) |
|---|---|---|---|---|---|---|---|
| $^{9}Be+^{26}Mg$ | 43.0 | 31.93 | 9.79 | 3.20 | 3.5 | 23 | 8.5 |
| $^{9}Be+^{16}O$ | 43.0 | 27.52 | 7.15 | 2.75 | 2.3 | 19 | 8.0 |
| $^{9}Be+^{40}Ca$ | 45.0 | 36.72 | 14.96 | 3.59 | 5.6 | 25 | 8.8 |
| $^{10}B+^{25}Mg$ | 33.9 | 24.20 | 12.15 | 2.88 | 5.1 | 19 | 8.8 |
| $^{10}B+^{39}K$ | 43.96 | 34.97 | 17.62 | 3.65 | 7.1 | 26 | 9.5 |

resolving optical model potential ambiguities. As regards the angular limits of the data obtained, in most cases this was felt to be no longer profitable when the absolute cross-section had fallen much below $10^{-1}$ mb/sr. If the calculations are continued far beyond this, the effects of inelastic scattering ought to be taken into account explicitly (i.e. by a coupled-channels approach) rather than merely being included in the imaginary potential. At this point the principal virtue of the optical model, namely its simplicity, is spoilt.

The optical model potential searches were carried out with the program DWAVF, which contains the elastic scattering routines from MARS (Tamura and Low [Tam74]) together with the NAG library fitting routine E04FDF. The specific optical parameter sets used as starting parameters were taken from those found by other groups to describe scattering systems at centre-of-mass energies which resembled the experiments studied here as closely as possible. In general the procedure was to initially vary V, $a_v$, W and $a_w$ with $r_v$ and $r_w$ fixed, then vary V, $r_v$, W and $r_w$ and finally allow all parameters to be free. In common with other analyses of heavy-ion scattering (see, for example, Balzer et al. [Bal77]), the calculated cross-sections were shown to be insensitive to the Coulomb radius parameter, $r_c$, in the range $0.5\ \text{fm} < r_c < 1.5\ \text{fm}$. The value of $r_c$ was therefore either kept fixed during the searches or else varied in constant ratio to the real radius parameter.

Some test calculations were performed to determine suitable limits for the matching radii and maximum number of partial waves. During production running, integration step lengths of 0.08 fm, matching radii of 20 fm and 50 partial waves were used.

## 4.2 $^{9}Be + ^{26}Mg$ Elastic Scattering Analysis.

The elastic scattering angular distribution obtained for the case of 43 MeV $^{9}Be$ on $^{26}Mg$ is shown in fig. 4.1. The oscillations in the data are not very pronounced even at the most backward angles covered (up to 75° in the centre-of-mass frame).

Two initial sets of optical model parameters were used as input to the fitting. The first was a "universal" optical potential taken from Balzer et al. [Bal77] which fitted $^{9}Be$ scattering from a range of heavy target nuclei at incident energies of 14, 20 and 26 MeV. The second was a potential from Eck et al. [Eck80] which fitted $^{9}Be$ scattering from $^{28}Si$ at 45 MeV. The resulting searched potentials, BEM1 and BEM2 respectively, are given in table 4.2 along with the reduced chi-squared, $\chi^2$ (i.e. chi-squared divided by the number of degrees of freedom: in the following $\chi^2$ always denotes the reduced value).

Table 4.2 $^{9}Be + ^{26}Mg$ Optical Model Parameters.

| Label | V(MeV) | $a_v$(fm) | $r_v$(fm) | W(MeV) | $a_w$(fm) | $r_w$(fm) | $r_c$(fm) | $\chi^2$ |
|---|---|---|---|---|---|---|---|---|
| BEM1 | 69.8 | 0.820 | 0.9476 | 130.6 | 0.796 | 0.9065 | 0.788 | 2.4 |
| BEM2 | 17.1 | 0.693 | 1.2731 | 7.1 | 0.740 | 1.4570 | 1.351 | 2.4 |

Both potentials gave good fits to the data (see fig. 4.1) and they possess similar values of $W.\exp(R_w/a_w)$, i.e. the imaginary wells are approximately Igo-ambiguous. The potentials are plotted in fig. 4.2, where it is seen that the real wells, and to a lesser extent the imaginary wells, have equal strengths at the strong absorption radius. It is also interesting to note that the ratio of the real to imaginary well strengths at the strong absorption radius, $V(D_{sa})/W(D_{sa})$, is 0.7.

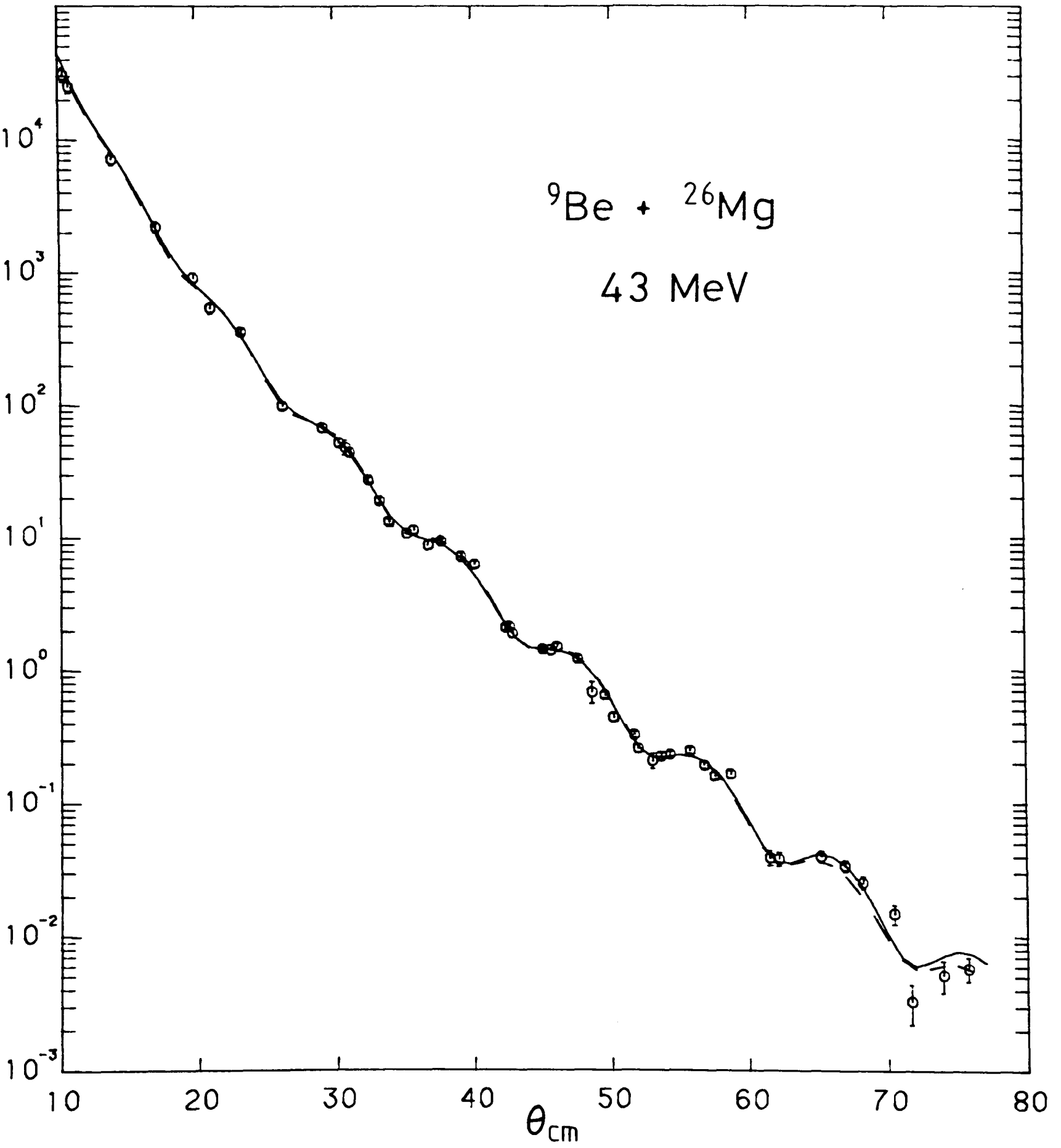


Fig. 4.1 Elastic scattering data and optical model predictions for $^{9}Be + ^{26}Mg$. Solid line: potential BEM1, dashed line: potential BEM2.

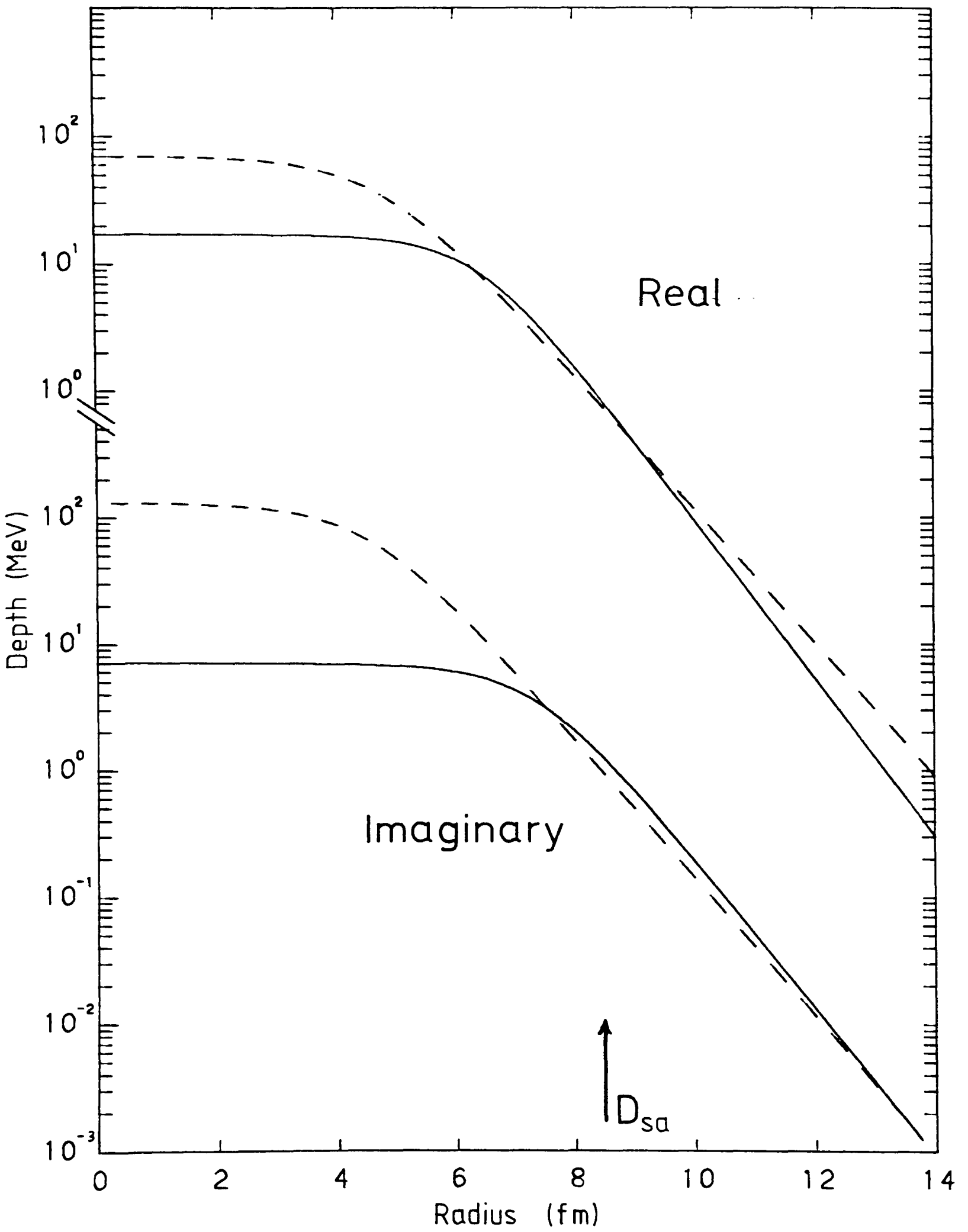


Fig. 4.2 Real and imaginary parts of potentials BEM2 (solid lines) and BEM1 (dashed lines). The strong absorption radius, $D_{sa}$, for 43 MeV $^{9}Be$ + $^{26}Mg$ is indicated.

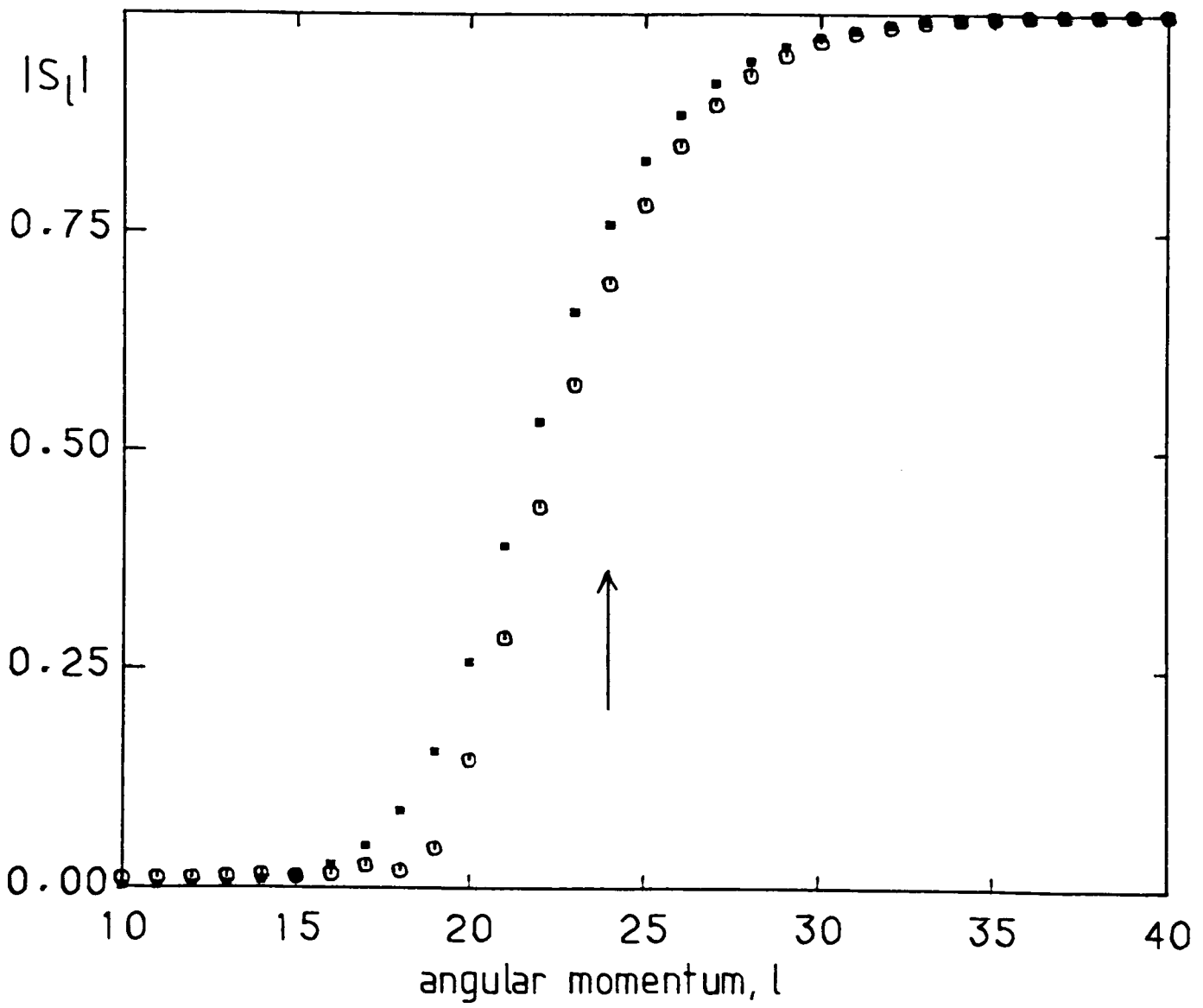


Fig. 4.3 S-matrix elements for $^{9}Be + ^{26}Mg$ elastic scattering at 43 MeV. Dots: potential BEM1, open circles: potential BEM2. $\ell_{\frac{1}{2}}$ is indicated by the arrow.

Zisman et al. [Zis80] found that this ratio for the case of $^{9}Be$ scattering from $^{28}Si$ at a wide range of incident energies was roughly constant at ~0.8.

The potentials can be seen to be strongly absorbing from the fact that the S-matrix elements (or more precisely $|S_\ell|$) fall off very quickly for partial waves lower than $\ell_{\frac{1}{2}}$ (fig. 4.3). This is to be expected from the ratio $V(D_{sa})/W(D_{sa})$ mentioned above.

## 4.3 $^{9}Be + ^{16}O$ Elastic Scattering Analysis.

It proved more difficult to obtain satisfactory fits to the strongly oscillatory data of $^{9}Be$ scattering from the lightest target nucleus studied, $^{16}O$. Two starting potentials, one from Stahel et al. [Sta77] which fitted $^{9}Be$ scattering from $^{12}C$ and the $^{26}Mg$ potential BEM1, were searched to obtain the potentials BEO1 and BEO2, whose parameters are given in table 4.3. The fits and the data are shown in fig. 4.4 and resemble a Fraunhofer diffraction pattern. In fact the usual semi-classical condition for Fraunhofer diffraction, $\ell_c \sin\theta_c < 1$ [Hod78], is just exceeded here: if $\ell_c$, the "critical" angular momentum is taken as $\ell_{\frac{1}{2}}$ and $\sin\theta_c$ is calculated from

$$\sin\frac{\theta_c}{2} = \frac{\eta}{k.D_{sa} - \eta},$$

we find $\ell_c \sin\theta_c = 1.1$.

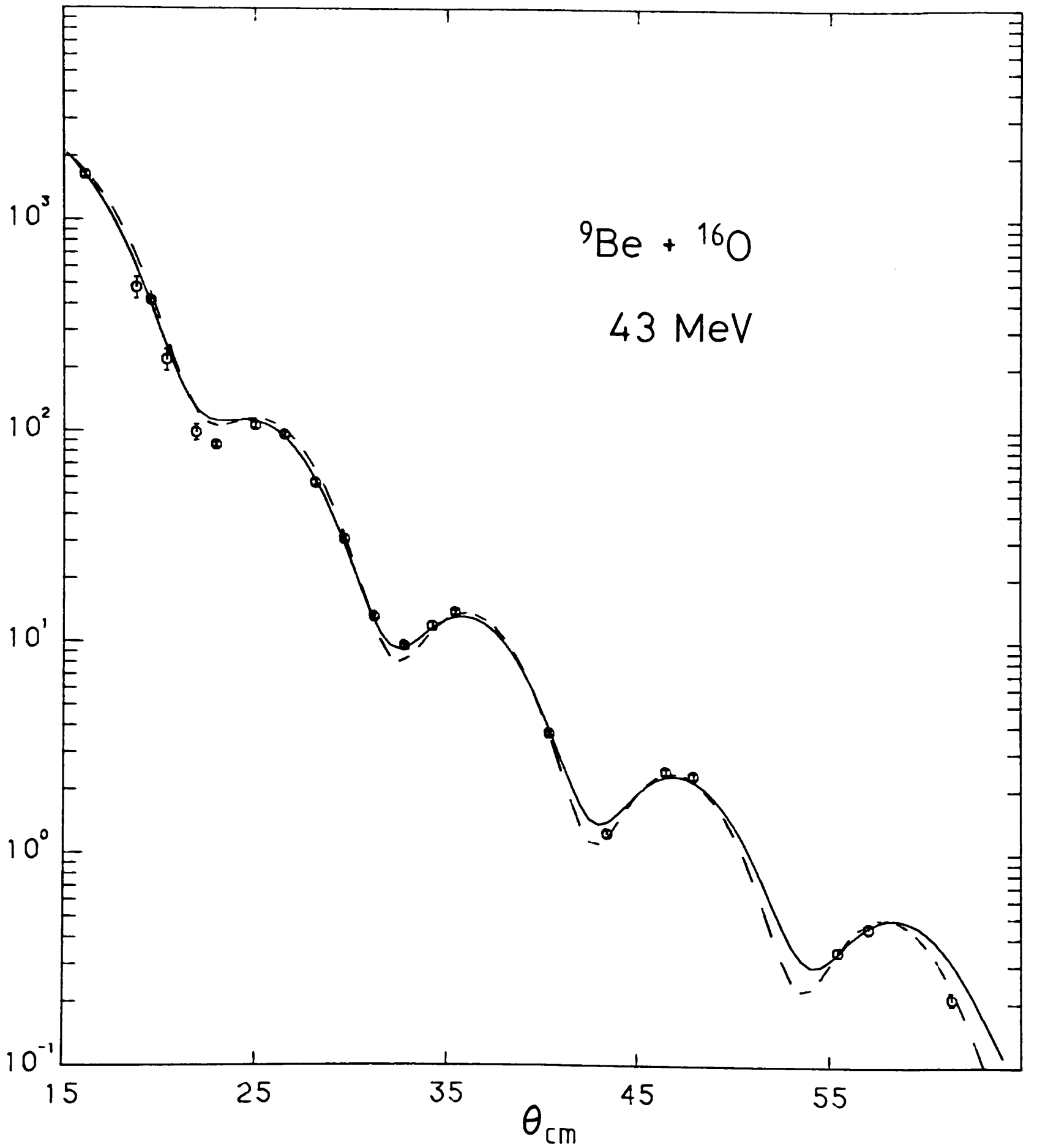


Fig. 4.4 Elastic scattering data and optical model predictions for $^{9}Be + ^{16}O$. Solid line: potential BE01, dashed line: potential BE02.

Table 4.3 $^{9}Be + ^{16}O$ Optical Model Parameters.

| Label | V(MeV) | $a_v$(fm) | $r_v$(fm) | W(MeV) | $a_w$(fm) | $r_w$(fm) | $r_c$(fm) | $\chi^2$ |
|---|---|---|---|---|---|---|---|---|
| BE01 | 70.85 | 1.123 | 0.696 | 147.9 | 0.673 | 0.955 | 0.657 | 15.7 |
| BE02 | 9.58 | 0.899 | 1.305 | 12.4 | 0.564 | 1.377 | 1.200 | 13.6 |

The values of $\chi^2$ for these fits are significantly higher than those for the case of scattering from $^{26}Mg$, although visually the fits look reasonable. The real well of BE01 is somewhat unusual in that it has a small radius and correspondingly large diffuseness. Although the S-matrix again falls quickly to zero for partial waves lower than $\ell_{\frac{1}{2}}$, these potentials are unlike the other $^{9}Be$ ones: the V/W ratio at the strong absorption radius is greater than unity (1.5 in fact). This rather surprising result is echoed in a study of $^{6}Li$ scattering from $^{26}Mg$, $^{16}O$ and $^{12}C$ by Woods [Woo81], where again $^{16}O$ was the only target to give $V(D_{sa})/W(D_{sa})$ greater than unity, 1.3 in that case.

## 4.4 $^{9}Be + ^{40}Ca$ Elastic Scattering Analysis.

These data were taken when machine conditions allowed a slightly higher terminal voltage on the Folded Tandem, giving a beam energy of 45 MeV. The data, (plotted in fig. 4.5 as cross-section divided by Rutherford cross-section), show small evidence of diffraction oscillations and present a typical Fresnel-like pattern. This is expected, since $\ell_c \sin\theta_c = 2.7$.

Measurements for $^{9}Be + ^{40}Ca$ at this energy have already been reported by Eck et al. [Eck80]. They have derived an optical model potential which fitted their data at 45 MeV and 60 MeV simultaneously.

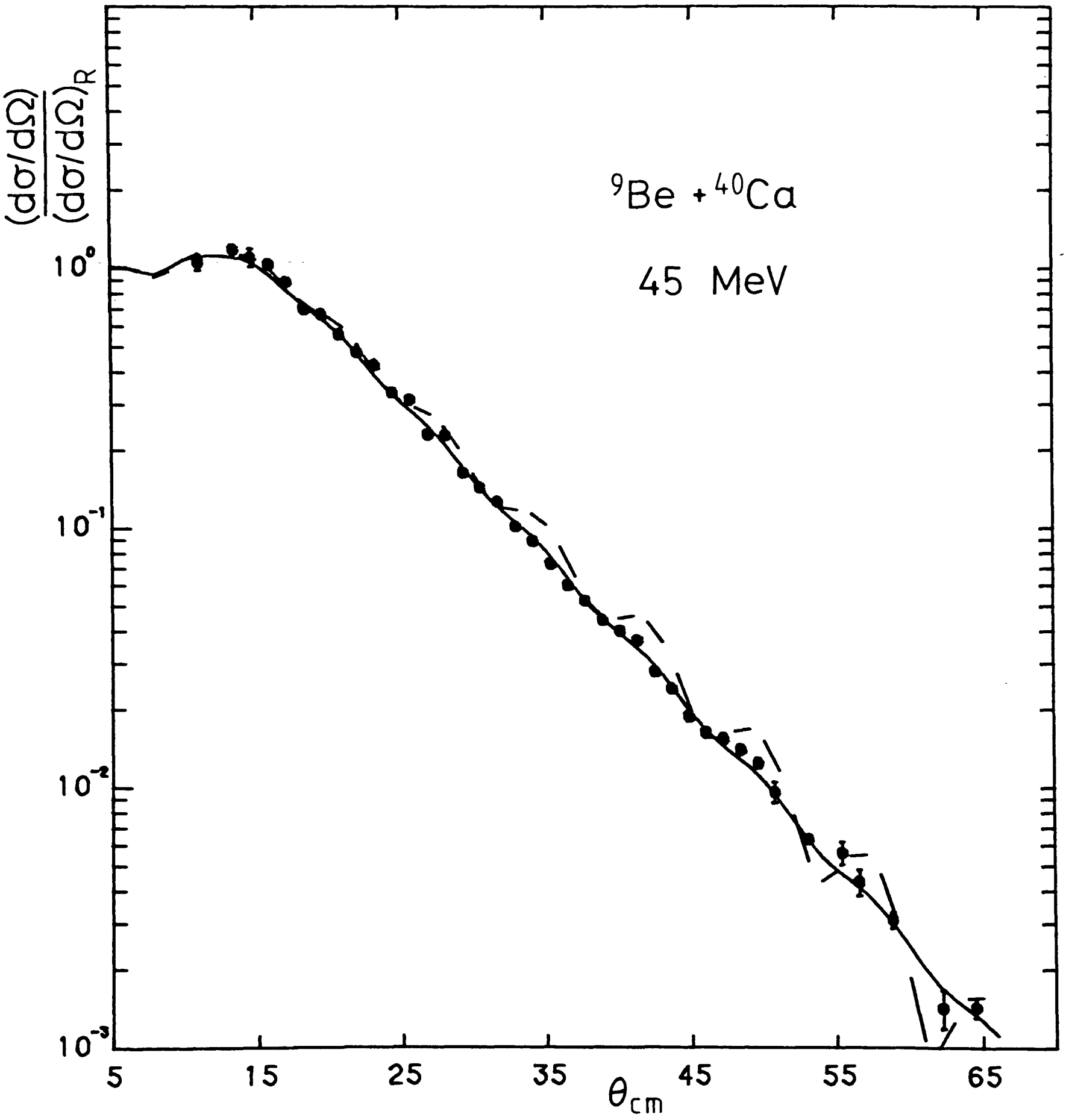


Fig. 4.5 Elastic scattering data and optical model predictions for $^{9}Be + ^{40}Ca$. Solid line: potential BECA, dashed line: potential ECK80.

This potential is listed in table 4.4 as "ECK80". The data presented here, however, is almost 30% lower than the similar energy data of Eck et al. for centre-of-mass (c.m.) angles greater than 35°, although the normalizations of the data for small angles (<25° c.m.) agree well. In view of this, a new optical potential, BECA, was found by optimising the parameters of ECK80 to fit the present data (see table 4.4).

Table 4.4 $^{9}Be + ^{40}Ca$ Optical Model Parameters.

| Label | V(MeV) | $a_v$(fm) | $r_v$(fm) | W(MeV) | $a_w$(fm) | $r_w$(fm) | $r_c$(fm) | $\chi^2$ |
|---|---|---|---|---|---|---|---|---|
| ECK80 | 10.0 | 0.5025 | 1.416 | 23.4 | 0.5011 | 1.277 | 1.35 | - |
| BECA | 9.05 | 0.760 | 1.317 | 18.3 | 0.667 | 1.272 | 1.256 | 5.3 |

Fig. 4.5 shows that the angular distribution resulting from ECK80 is too oscillatory, although it is interesting to note that it follows the normalization of this work rather than the 45 MeV data of Eck et al., and BECA is superior in accounting for the data.

The ratio of the real to imaginary wells at the strong absorption radius is 0.95 for the potential BECA.

## 4.5 $^{10}B + ^{25}Mg$ Elastic Scattering Analysis.

This experiment was performed with $E(^{10}B)$ = 33.9 MeV in order that the exit channel of the $^{26}Mg(^{9}Be,^{10}B)^{25}Na$ reaction was represented as closely as possible. The scattering was thus only 12 MeV above the Coulomb barrier in the c.m. frame and the resulting angular distribution is very structureless (fig. 4.6).

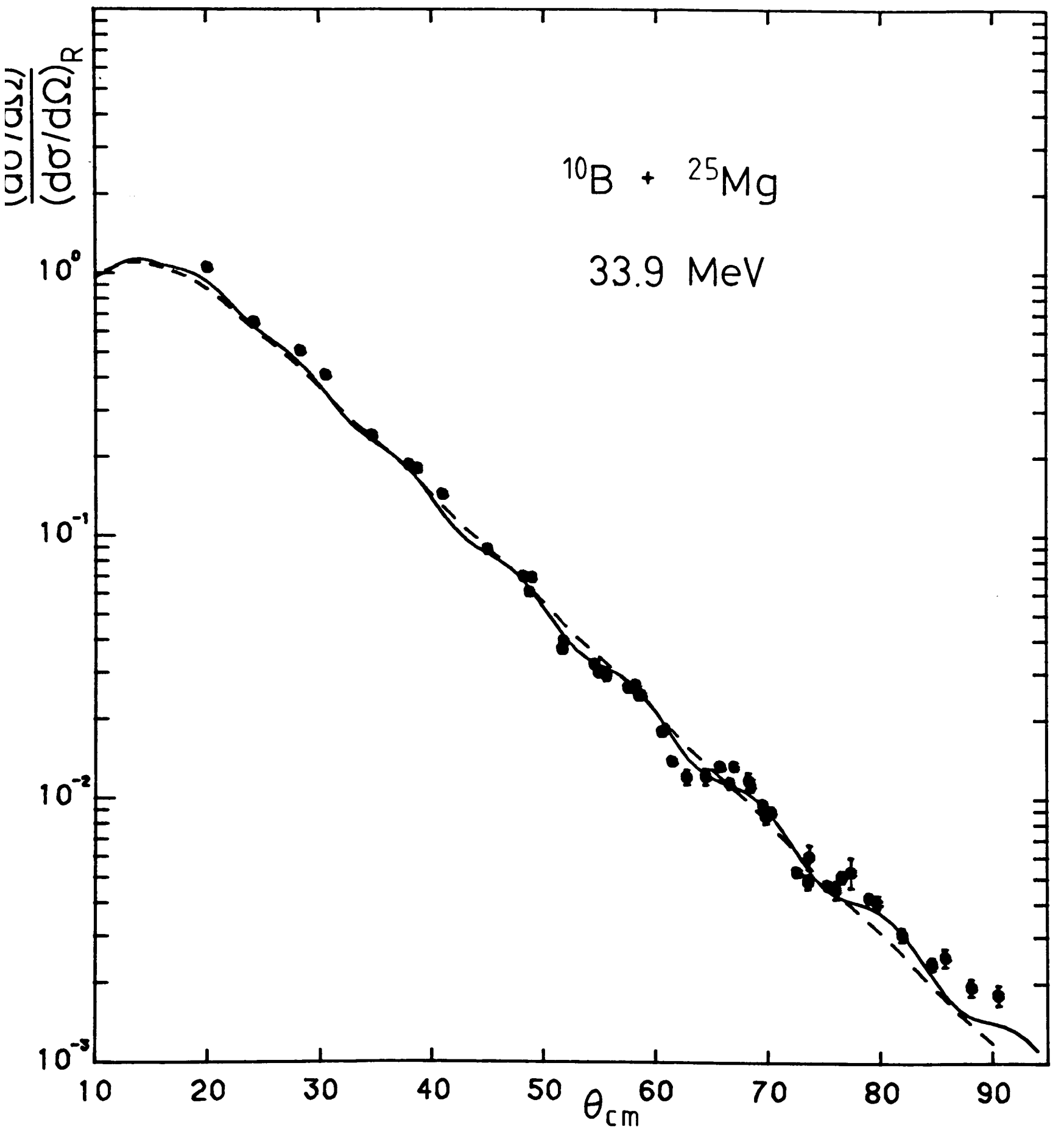


Fig. 4.6 Elastic scattering data and optical model predictions for $^{10}B + ^{25}Mg$. Solid line: potential BMG1, dashed line: potential BMG2.

Two starting potentials were taken from the literature. One was for 50 MeV $^{10}B$ scattering off $^{27}Al$ from Parks et al. [Par77]; this gave the searched potential BMG1 in table 4.5. The other was from Motobayashi et al. [Mot79] which described 65.8 MeV $^{10}B$ scattering from $^{20}Ne$ and resulted in the searched potential BMG2. The latter gave a completely structureless angular distribution while BMG1 reproduced the slight oscillations and thus gave a better fit (see fig. 4.6).

The ratio of the real to imaginary well at the strong absorption radius is about 0.8 for both potentials.

Table 4.5 $^{10}B$ + $^{25}Mg$ Optical Model Parameters.

| Label | V(MeV) | $a_v$(fm) | $r_v$(fm) | W(MeV) | $a_w$(fm) | $r_w$(fm) | $r_c$(fm) | $\chi^2$ |
|---|---|---|---|---|---|---|---|---|
| BMG1 | 76.6 | 0.705 | 1.038 | 56.9 | 0.670 | 1.082 | 1.3 | 8.6 |
| BMG2 | 16.9 | 0.726 | 1.199 | 16.6 | 0.763 | 1.269 | 1.3 | 14.1 |

Parks et al. [Par77] found that it was desirable to include quadrupole terms in the optical model description of $^{10}B$ elastic scattering from $^{27}Al$ at 50 MeV. The large ground-state quadrupole moment of $^{10}B$ (8 e.fm$^2$ [Ful69]) was put forward as the reason for the requirement of a non-spherical potential as well as the normal spherical one. The effects of the quadrupole moment on the elastic scattering angular distribution are expected [Bla59] to be a damping of the oscillations with perhaps some change in magnitude at backward angles. These effects were beneficial for $^{10}B$ +$^{27}Al$ at 50 MeV because the spherical optical model calculations alone were too strongly oscillatory. On the other hand, for the case of low energy (34 MeV) $^{10}B$ +$^{16}O$ scattering [Par80], the calculation without the quadrupole terms gave a good fit to the data and inclusion of reorientation effects

actually worsened the fit. At higher energy (50 MeV), the damping of the oscillations through the inclusion of reorientation gave an improved fit as for the $^{27}Al$ case.

It can be seen that for all the elastic scattering data presented in this thesis‡, there is no need to go further than the spherical optical model calculation, and that any damping of oscillations in the angular distributions would in general worsen the fits. We will return to this point in the discussion of the ($^{9}Be$,$^{10}B$) reaction.

## 4.6 $^{10}B$ + $^{39}K$ Elastic Scattering Analysis.

This experiment was carried out at 43.96 MeV to duplicate the exit channel of $^{40}Ca(^{9}Be,^{10}B)^{39}K$ for $E(^{9}Be)$ = 45 MeV. Two searched potentials were obtained, this time starting from potentials BMG2 and BECA described above. The data and the resulting fits are shown in fig. 4.7 and the parameters are given in table 4.6. For these potentials, $V(D_{sa})/W(D_{sa}) \simeq 0.6$. The two potentials are good examples of the Igo ambiguity.

Table 4.6 $^{10}B$ + $^{39}K$ Optical Model Parameters.

| Label | V(MeV) | $a_v$(fm) | $r_v$(fm) | W(MeV) | $a_w$(fm) | $r_w$(fm) | $r_c$(fm) | $\chi^2$ |
|---|---|---|---|---|---|---|---|---|
| BK1 | 23.7 | 0.683 | 1.233 | 52.6 | 0.843 | 1.051 | 1.3 | 3.8 |
| BK2 | 8.46 | 0.638 | 1.361 | 8.54 | 0.814 | 1.371 | 1.256 | 3.8 |

‡ $^{9}Be$ also has a large ground-state quadrupole moment (5 e.fm$^2$)

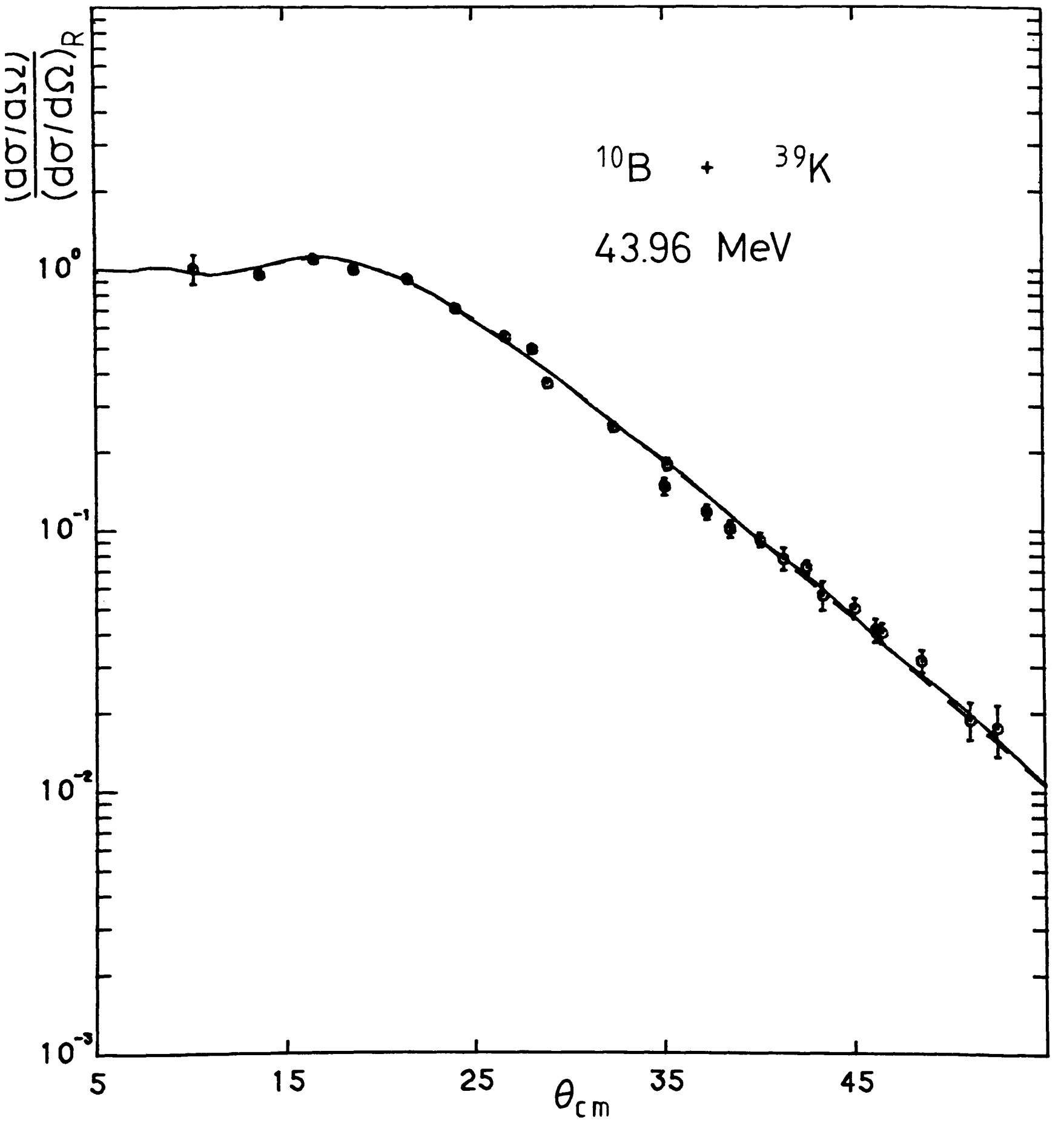


Fig. 4.7 Elastic scattering data and optical model predictions for $^{10}B + ^{39}K$. Solid line: potential BK1, dashed line: potential BK2.

## 4.7 Summary.

Optical model potentials of the Woods-Saxon form have given a good account of the elastic scattering of $^{9}Be + ^{16}O$, $^{26}Mg$, $^{40}Ca$ and of $^{10}B + ^{25}Mg$, $^{39}K$. Usually more than one potential have been found to give equally good fits to the data and, in view of the continuous nature of some of the ambiguities ([Igo58], [Sat74]), it is to be expected that these are at best but a sample of the possible ones. The potentials obtained may not be "correct" in the sense that they may not describe inelastic scattering or reaction data.

The lightest system discussed ($^{9}Be + ^{16}O$) was the only one which did not show clear evidence of strong absorption through the ratio of V/W measured at the strong absorption radius. In general, V/W has been found to be smaller for the $^{10}B$ potentials than the $^{9}Be$ ones. That is, $^{10}B$ appears to be more strongly absorbed than $^{9}Be$. Fulmer et al. [Ful82] used similar evidence to suggest that $^{10}B$ is more strongly absorbed than $^{11}B$, which in turn is more strongly absorbed than $^{16}O$. It would clearly be interesting to see a systematic study of this.

# CHAPTER 5

# DWBA ANALYSIS OF THE ($^{9}$Be,$^{10}$B) REACTION

## 5.1 Introduction.

The use of the distorted wave Born approximation (DWBA) in the study of heavy-ion reactions is by now standard procedure. A summary of the derivation of the DWBA method, with emphasis on the approximations involved, is given in Appendix A. A recent review of the theory and its application to direct reactions can be found in Satchler [Sat83]. Here we are concerned with the prediction of the ($^{9}$Be,$^{10}$B) reaction cross-sections for the targets $^{16}$O, $^{24}$Mg, $^{26}$Mg, $^{40}$Ca, $^{54}$Fe and $^{63}$Cu at energies well above the Coulomb barrier. As discussed in Chapter 1, DWBA analyses of heavy-ion single-nucleon transfer reactions which used similar mass projectiles and targets as in the present study have often proved successful in the past in accounting for experiment and given spectroscopic factors in fair agreement with those from studies of light-ion reactions.

Before discussing the reaction dynamics it is useful to write down an expression for a general single-nucleon pickup reaction. The cross-section for the reaction a + A → b + B (A=B+x, b=a+x) can be written

$$\frac{d\sigma}{d\Omega} = C^2S \sum_{j=\ell\pm\frac{1}{2}} C_b^2 S_b^j \left(\frac{d\sigma}{d\Omega}\right)^j_{DWBA} \qquad (5.1)$$

where the sum is over the possible total angular momenta of the nucleon bound in the projectile system. Two spectroscopic factors enter

equation 5.1: S for the target system and $S_b$ for the projectile system. C and $C_b$ are the usual isospin Clebsch-Gordan coefficients, thus $C_b = \langle T_b \tau_b | T_a \tau_a \; \frac{1}{2} \; \frac{1}{2} \rangle = \langle 0 \; 0 | \frac{1}{2} \; -\frac{1}{2} \; \frac{1}{2} \; \frac{1}{2} \rangle = -\sqrt{\frac{1}{2}}$, for $(^9Be, ^{10}B)$.

Use of the DWBA implies a belief that only a one-step (or "direct") process is important. In principle, multi-step processes are always possible, but their contribution to single-nucleon transfer is usually negligible unless the one-step process is inhibited in some way. This may happen, for example, if there is a large amount of momentum mismatching in the direct transfer process or if the conservation of angular momentum prohibits a certain spin transfer. These points will be discussed in the context of the $(^9Be, ^{10}B)$ reaction.

5.1.1 Reaction Dynamics.

We begin with a discussion of how the reaction dynamics will affect the cross-sections. Brink [Bri72] has derived by semi-classical considerations the following three kinematic matching conditions which should be satisfied if the transfer probability is to be large:

(1) $|\Delta k| = |k_0 - \lambda_1/R_1 - \lambda_2/R_2| \leq 2\pi/R$

(2) $\Delta L = \lambda_2 - \lambda_1 + \frac{1}{2}k_0(R_1 - R_2) + Q_{eff}R/\hbar v \approx 0$

(3) $\ell_1 + \lambda_1 = \text{even}, \; \ell_2 + \lambda_2 = \text{even}$

where $\ell_1$, $\lambda_1$ are the orbital angular momentum and component normal to the reaction plane for x bound in the target,

$\ell_2$, $\lambda_2$ as above for x bound in the ejectile,

$R_1(R_2)$ = radius of target (projectile) taken as $1.4A^{\frac{1}{3}}$ fm,

$R = R_1 + R_2$,

v = relative velocity of the two nuclei in region of transfer,

$k_0 = mv/\hbar$,

m = mass of transferred nucleon,

$$Q_{eff} = Q - (Z_b Z_B - Z_a Z_A) e^2/4\pi\varepsilon_0 R$$

(The symbol definitions above are for the case of pickup reactions).

Table 5.1 lists the best-matched values of $\frac{1}{2}R|\Delta k|$ and $|\Delta L|$ for the reactions studied here. It is seen that, with just one exception, there are always some pair of $\lambda$ values that allow the Brink conditions to be satisfied. For the case of reactions with large negative Q-values, the second Brink condition is satisfied best when $\lambda_2$ has its maximum positive value and $\lambda_1$ has its maximum negative value, so that $\Delta\lambda$ is large. Thus the $^{26}Mg(^9Be,^{10}B)^{25}Na$ reaction, which has a Q-value of -7.559 MeV, is expected to be kinematically matched when the $\ell$-transfer ($\ell_{tr}$) has its maximum value of 3. Fig. 5.1 shows that the DWBA calculated cross-section for $\ell_{tr} = 3$ is indeed dominant.

Several recent studies of heavy-ion reactions ([For74], [Sta77] and [Tam80], for example) have used a simpler form of the matching conditions: the reaction A(a,b)B will have a large transfer cross-section if

$$\Delta Q = |Q - Q_{opt}| \qquad (5.2)$$

is small. Here $Q_{opt}$ is defined as

$$Q_{opt} = (Z_b Z_B - Z_a Z_A) e^2/4\pi\varepsilon_0 R - \tfrac{1}{2}mv^2.$$

(Equation 5.2 follows from the Brink matching conditions if an "average" value of either $\lambda_1 = 0$ or $\lambda_2 = 0$ is taken.) The values of $Q_{opt}$ for the reactions under consideration are given in Table 5.2 along with the difference from the ground state Q-value. Values for an alternative expression for angular momentum matching, $|\Delta L|'$, are also listed: good grazing-$\ell$ matching is found if $|\Delta L|' \approx 0$ (this expression is physically very similar to Brink's second condition). Table 5.2 shows that none of

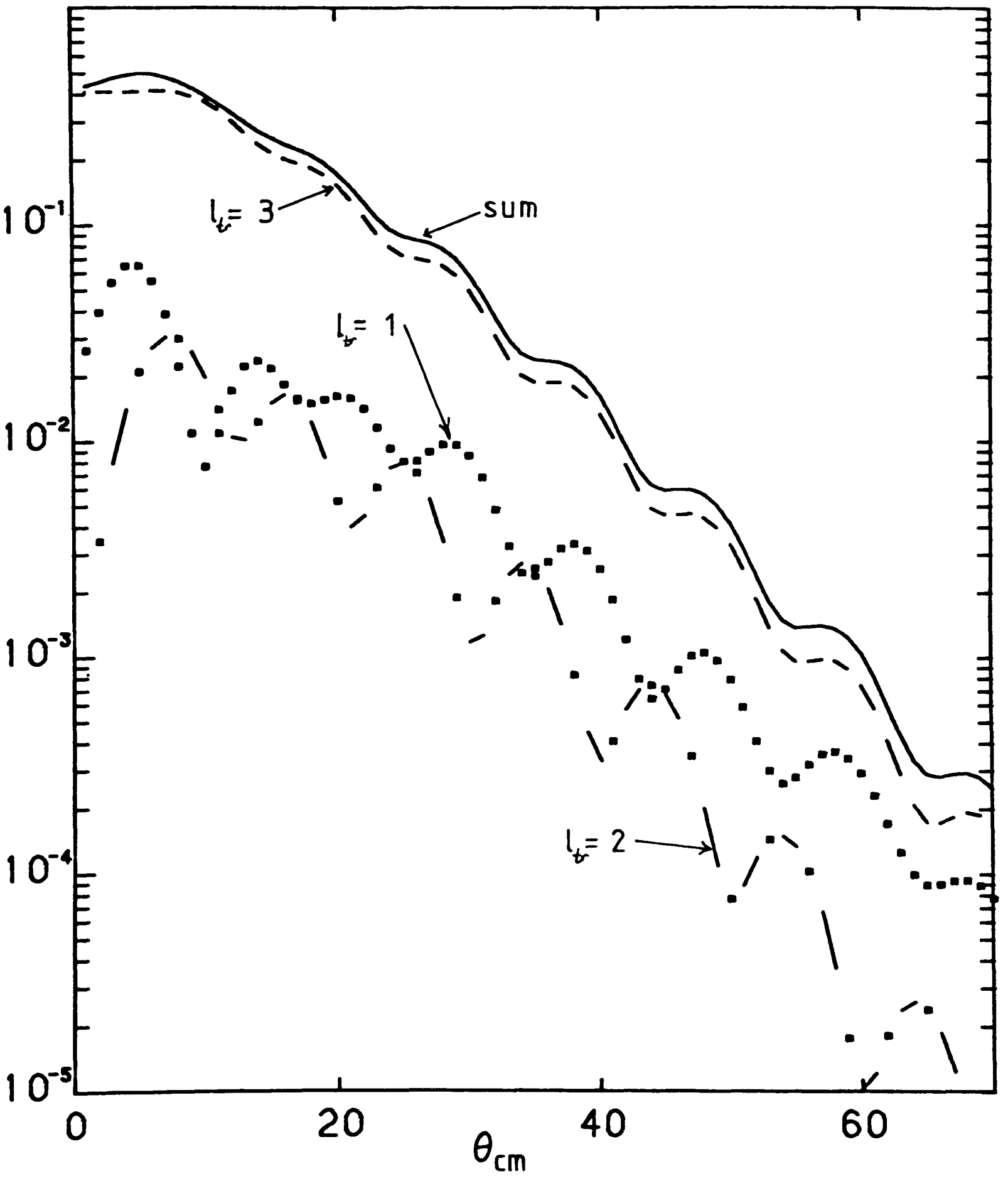


Fig. 5.1 $\ell$-transfer contributions to $^{26}Mg(^{9}Be,^{10}B)^{25}Na$.

Table 5.1

Kinematic Matching of the Reactions as given by Brink [Bri72].

| Final State | Q(MeV) | $\ell_1$ | $\lambda_1$ | $\ell_2$ | $\lambda_2$ | $\lvert\Delta L\rvert$ | $\frac{1}{2}R\lvert\Delta k\rvert$ |
|---|---|---|---|---|---|---|---|
| $^{25}$Na 5/2+ g.s. | -7.559 | 2 | -2 | 1 | 1 | 0.1 | 2.2 |
| 1/2+ 1.07 | -8.629 | 0 | 0 | 1 | 1 | 2.3 | 0.5 |
| $^{15}$N 1/2- g.s. | -5.542 | 1 | -1 | 1 | 1 | 0.1 | 1.4 |
| $^{39}$K 3/2+ g.s. | -1.744 | 2 | 0 | 1 | 1 | 0.3 | 0.6 |
| 1/2+ 2.52 | -4.264 | 0 | 0 | 1 | 1 | 1.2 | 0.6 |
| $^{62}$Ni 0+ g.s. | +0.463 | 1 | -1 | 1 | 1 | 1.1 | 1.3 |
| $^{53}$Mn 7/2- g.s. | -2.268 | 3 | -1 | 1 | 1 | 0.1 | 1.3 |
| $^{23}$Na 3/2+ g.s. | -5.105 | 2 | -2 | 1 | 1 | 1.0 | 2.2 |
| 5/2+ 0.44 | -5.545 | 2 | -2 | 1 | 1 | 0.8 | 2.2 |

Table 5.2

Matching of Q and Grazing-$\ell$ for the Reaction Ground State.

| Resid. Nucl. | $Q_{opt}$(MeV) | $\lvert\Delta Q\rvert$ | $L_{gi}$ | $L_{gf}$ | $\lvert\Delta L\rvert'$ |
|---|---|---|---|---|---|
| $^{25}$Na | 4.74 | 12.30 | 18.8 | 15.1 | 3.7 |
| $^{15}$N | 4.20 | 9.75 | 15.3 | 13.1 | 2.2 |
| $^{39}$K | 5.77 | 7.51 | 21.3 | 20.2 | 1.3 |
| $^{62}$Ni | 6.35 | 5.89 | 22.1 | 20.9 | 1.1 |
| $^{53}$Mn | 6.10 | 8.36 | 21.5 | 18.8 | 2.7 |
| $^{23}$Na | 4.71 | 9.81 | 18.0 | 15.6 | 2.4 |

where $\Delta Q = Q_{opt} - Q_{gs}$, $\quad \lvert\Delta L\rvert' = \lvert L_{gi} - L_{gf}\rvert$

$L_{gi}$ is the grazing angular momentum in the entrance channel,

$L_{gf}$ is the grazing angular momentum in the exit channel.

the actual Q-values were near optimum and from equation 5.2 it follows that the degree of mismatch was worse for transfers leading to excited states of the ejectile or residual nucleus (i.e. more negative Q). Therefore the main transition strength is expected to be to the ground states of the reaction products. This trend has already been noted in the experimental spectra shown in Chapter 2. Table 5.2 also shows that the reaction on the $^{63}Cu$ target has the smallest Q-mismatch and that on the $^{26}Mg$ target the largest. Once the target spectroscopic factors have been taken into account (0.8 for $^{63}Cu$, 2.6 for $^{26}Mg$), this is in agreement with the peak cross-sections of ~1.3 mb/sr for $^{63}Cu(^{9}Be,^{10}B)^{62}Ni$ and ~0.4 mb/sr for $^{26}Mg(^{9}Be,^{10}B)^{25}Na$ (figs. 5.5 and 5.3 respectively).

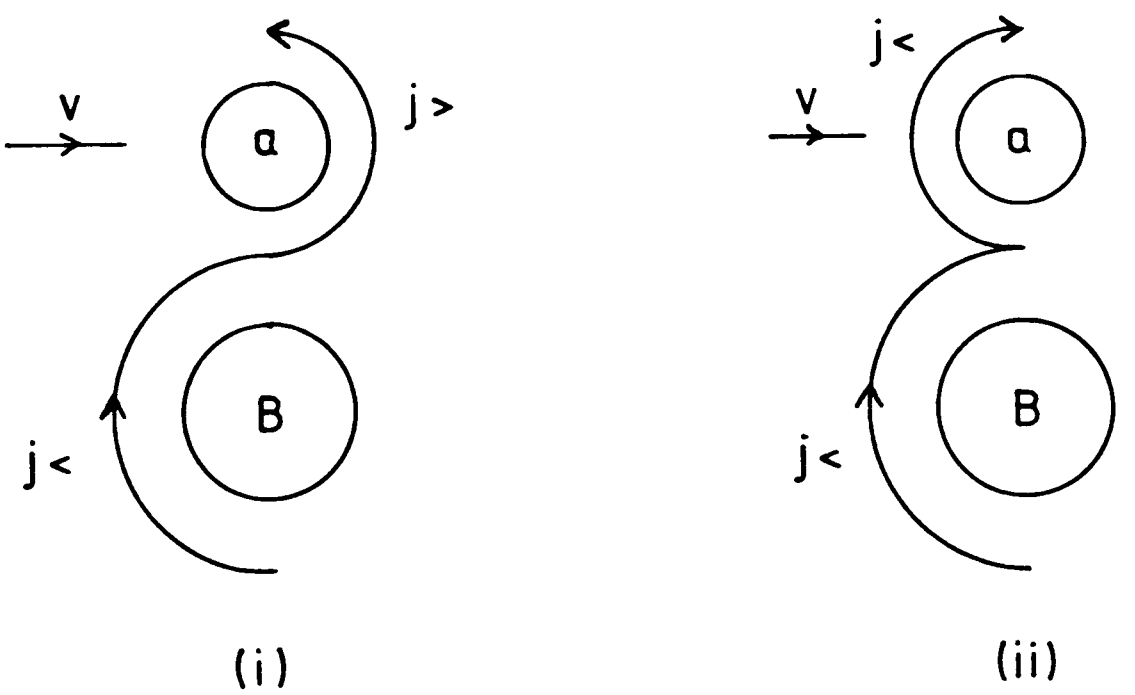


Fig. 5.2 "j-dependent effect". (i) $j_<$ to $j_>$ transition; (ii) $j_<$ to $j_>$ transition.

The total angular momentum, j, of the transferred nucleon can also affect the transition probability. Transfers from $j_>$ ($= \ell + \frac{1}{2}$) to $j_<$ ($= \ell - \frac{1}{2}$) or vice versa are generally enhanced compared to $j_>$ to $j_>$ (or

$j_<$ to $j_<$) transfers. This can be explained semi-classically [Tam74a] by considering the change in the linear momentum of the transferred nucleon in each case (see fig. 5.2). As will be seen later, this j-dependent effect on the transition probability is important in the consideration of the extracted target spectroscopic factors, S, for $^{10}B$ in its ground ($3^+$) or first excited ($1^+$) state. This is so because the transfer of a $p_{1/2}$ proton to the $3^+$ state of boron is forbidden by conservation of angular momentum ($^9Be$ has a $3/2^-$ ground state) in contrast to the situation for the $1^+$ state, where both $p_{3/2}$ and $p_{1/2}$ transfers are allowed. Furthermore, the Cohen and Kurath [Coh67] values for $S_b$ in equation 5.1 are:

$$S_b\{^9Be + 0p_{3/2}\text{proton} \rightarrow {}^{10}B(3^+)\} = 1.2004$$

$$S_b\{^9Be + 0p_{3/2}\text{proton} \rightarrow {}^{10}B(1^+)\} = 0.4690$$

$$S_b\{^9Be + 0p_{1/2}\text{proton} \rightarrow {}^{10}B(1^+)\} = 0.8764$$

This emphasizes the importance of the $p_{1/2}$ proton transfer for the $1^+$ state.

## 5.1.2 Remarks Concerning the Exact Finite Range DWBA Calculations.

The calculations were performed with the full-recoil ("exact") finite-range DWBA code SESIME, which is an extended version of Tamura and Low's SATURN-MARS-1 [Tam74]. This is expected to be slightly less accurate than the code LOLA [DeV73] because it uses a large interpolation length (typically 0.8 fm) for the numerical integration over $\underline{r}_b$, i.e. the displacement of the ejectile from the residual nucleus (a diagramatic representation of the coordinate system is given in Appendix A). The interpolation helps to make SATURN-MARS considerably faster than LOLA. However, it was important to check the accuracy of the calculations, so two test calculations were also

performed with LOLA and the results compared with those from SESIME. The differences were less than 10% throughout the range $5° < \theta_{cm} < 70°$ and were of similar sign and magnitude for the $^{10}B(3^+)$ and $^{10}B(1^+)$ cases - a point worth noting in view of the discrepancy found between these two cases which will be discussed later in this chapter.

The calculations were performed using the prior representation and only the nuclear term $V_{xa}$ was used for the interaction (this is discussed in Appendix A). Some test calculations were made with the post form of the interaction in order to obtain a rough estimate of the error introduced by the neglect of several terms in the interaction (different terms are neglected in the two representations). For the case of $^{40}Ca(^{9}Be,^{10}B)^{39}K$, the post-prior discrepancy was less than 26% in the range $8° < \theta_{cm} < 60°$. The largest differences were at the most forward and most backward angles, thus the difference in the extracted spectroscopic factor resulting from the normalization of the calculated distribution to the data was only 13%. In addition, the post-prior discrepancies were very similar whether $^{10}B$ was excited or not. Thus it is believed that the neglected terms in the form factor have little effect and certainly could not account for discrepancies between ejectile states. Similar conclusions were reached by Woods in an analysis of the $(^{6}Li,^{7}Be)$ reaction [Woo81].

The cross-sections are not especially sensitive to the optical potential parameters in the DWBA calculation. A typical test calculation showed that a 10% change in the real and imaginary diffusenesses of the exit potential produced changes of similar magnitude in the overall cross-section. The slope of the angular distribution was also slightly affected.

The radial mesh size, $\Delta r$, was chosen to be 0.1 fm. This satisfied the approximate criterion given by Tamura and Low [Tam74], $\Delta r < 0.2\pi/k$, where k is the asymptotic wavenumber in the entrance or exit channel. The form factor was calculated for a range $r_a \simeq \pm 1.4$ fm about $r_b$: the form factor had fallen to at least $10^{-4}$ of its central value at the extremes of this range. In general, 50 partial waves were used in the calculation. Comparative calculations for $^{40}Ca(^{9}Be,^{10}B)^{39}K$ with up to 65 partial waves showed negligible difference in the cross-section.

5.1.3. Form Factor Calculation.

The form factor in a single nucleon transfer reaction is the radial part of the overlap between the wavefunctions of the target and residual nucleus, $\mathcal{R}_{lj}^{AB}$ [Aus70] (for heavy-ions there is also a form factor $\mathcal{R}_{l'j'}^{ab}$ for the projectile and ejectile overlap). This is also referred to as the "bound state wavefunction" with quantum numbers $\ell$, j of a single nucleon orbit. Unless these single-particle wavefunctions have the same radial shape, at least within the nuclear interior, the normalization of the wavefunction will be incorrect (in general). Then the concept of spectroscopic factors, and hence the nuclear structure information, is lost [Aus70].

The calculation of the proper bound state wavefunctions to be used in the transition matrix element $\langle\psi_B\psi_b|V|\psi_A\psi_a\rangle$ (Appendix A, equation A.19) is a serious problem in transfer reaction analysis. The usual procedure is to generate $\mathcal{R}_{lj}^{AB}$ as an eigenfunction of a Woods-Saxon potential, the radius and diffuseness parameters of which are based upon optical model analyses of nucleon scattering and the depth of which is adjusted to give an eigenenergy equal to the separation energy of the

nucleon in the system. This is called the "well-depth" method. It gives the correct asymptotic form or tail to the wavefunction (due to the finite range of the residual nuclear interactions) but the form within the nucleus will not, except for the case of a single nucleon (or hole) outside a closed-shell core, be properly treated [Pin65]. In practice, the "well-depth" prescription has been remarkably successful and is widely used. This is because, roughly, the shape of the cross-section for a transfer process is sensitive to the form of the radial wavefunctions at the nuclear surface; the description of the interior is then important only in providing the correct normalization to the cross-section. The other extreme is to take an eigenfunction of the shell model potential without any reference to separation energies. This approach was tried by Sherr et al. [She65] after they encountered apparent inconsistencies amongst spectroscopic factors calculated using the well-depth method. In this case the asymptotic form of the wavefunction is not obtained and Pinkston and Satchler [Pin65] have shown that whilst the first method is too simple to be entirely satisfactory, the second is wrong in principle and should not be used.

Many authors have discussed possible improvements to the calculation of $\mathcal{R}_{lj}^{AB}$ (see Austern [Aus70] for a review). A prescription that is easily implemented to existing form factor codes has been suggested by Rae [Rae82] based upon the work of Austern [Aus77]). The theory behind the method is described in Appendix B; the idea is to generate a function whose shape at small radii resembles that of a shell-model basis function and whose shape at large radii is controlled by the separation energy. The method employs a fixed volume Woods-Saxon well together with a derivative (surface-peaked) potential whose depth

is varied until the eigenenergy of the wavefunction equals the experimental separation energy. In practice, the fixed potential is the shell model potential quoted by Bertsch [Ber72]:

$$U = -(51 \pm \frac{N - Z}{A} 20).f(r) + \ell^{*}16.4 \frac{1}{r}.\frac{d}{dr} f(r) \text{ MeV},$$

where the + sign is used for protons, - for neutrons, and

$$f(r) = \{1 + \exp[(r - 1.27A^{\frac{1}{3}})/0.65]\}^{-1},$$

$$\ell^{*} = -(\ell + 1) \text{ for } j = \ell - \tfrac{1}{2},$$

$$= \ell \quad \text{for } j = \ell + \tfrac{1}{2},$$

and A, N, Z refer to the composite system (i.e. p or n + core).

A modified version of SATURN has been written that has an option to include this potential together with a derivative form,

$$V_{SD} = V_{o}.\frac{d}{dr} f(r),$$

with depth $V_o$ that is searched to reproduce the input separation energy of the system.

Since it is possible to make fair comparisons of spectroscopic results with other reaction studies only if similar bound state descriptions have been used, the "well-depth" prescription has been used for most of the form factor calculations here, with the popular choices of radius parameter $r_o = 1.25$ fm (where $R = r_o A^{1/3}$) and diffuseness $a = 0.65$ fm. A spin-orbit potential with similar geometry and depth 7 MeV and also a Coulomb potential ($r_c = 1.25$ fm) were also included.

In addition, the "surface-peaked" prescription as outlined above has been tried for selected cases. The results of this are given in section 5.3.

As noted in many previous studies of heavy-ion reactions, the magnitude of the cross-section is sensitive to the bound state parameters, especially to those in the heavy* system (see, for example, [Woo80]). For $^{26}Mg(^{9}Be,^{10}B)^{25}Na$, a change in the real radius parameter, $r_o$, of 6% produced either a 29% or 11% increase in the calculated cross-section, depending on whether the change was in the heavy or light system. In neither case was there a significant alteration in the shape of the angular distribution. The normalization was relatively less sensitive to the diffuseness parameters in the bound state. It was found that a 50% decrease in the spin-orbit well depth produced only a 6% decrease in the normalization, again without changing the shape of the angular distribution.

Owing to the sensitivity of the cross-sections to the choice of bound state parameters, the extracted spectroscopic factors are rather uncertain. This provides the justification for having used the "well-depth" method with standard parameters - otherwise no comparison could have been made with other reaction values.

## 5.2 Reaction Angular Distributions and DWBA Analysis.

The angular distributions for the $(^{9}Be,^{10}B)$ reaction from the various target nuclei studied are presented in this section. The order of presentation is that in which the experiments were performed. This is done because (i) there is no apparent systematic effect with, say, target mass, and (ii) the later experiments were performed with a slightly different emphasis than the first three.

---

* i.e. target-residual system, similarly "light" system refers here to the projectile-ejectile system

In all cases, the values of $C^2S$ have been extracted by normalizing the theoretical curves to the data via

$$C^2S \sum_{j=l\pm\frac{1}{2}} C_b^2 S_b^j = \frac{\sum_i \sigma_{th}^i \cdot \sigma_{exp}^i / \Delta^2(\sigma_{exp}^i)}{\sum_i \sigma_{th}^{i2} / \Delta^2(\sigma_{exp}^i)}$$

where $\Delta(\sigma_{exp})$ is the experimental error on the cross-section. The values of $S_b^j$ have been taken from the p-shell compilation of Cohen and Kurath [Coh67] unless otherwise stated.

### 5.2.1 $^{26}Mg(^9Be,^{10}B)^{25}Na$ at 43 MeV.

Three angular distributions have been obtained from different states in the spectra. These are shown in fig. 5.3 and arise from transitions to (i) the unresolved $^{25}Na$ ground and first excited states ($^{25}Na_{0+1}$) with $^{10}B$ in its ground state, (ii) $^{25}Na_{0+1}$ with $^{10}B$ in its first excited state, (iii) $^{25}Na$ second excited state with $^{10}B$ in its ground state. No other transitions were strong enough or sufficiently clear from neighbouring peaks in the spectrum for reliable analysis. The bombarding energy of the $^9Be$ projectile is too low to give any pronounced oscillations in the cross-sections (compare the results of Bond et al. [Bon73], which show that the onset of oscillations in the $^{40}Ca(^{13}C,^{12}C)^{41}Ca$ reaction is at ~60 MeV).

Also shown in fig. 5.3 are the results of DWBA calculations with Woods-Saxon potentials from table 4.2 in the entrance channel and table 4.5 in the exit channel. Default bound state parameters as given in section 5.1.3 were used. Although at forward angles the quality of the fit to the data is good, for $\theta_{cm} > 50°$ the DWBA predicted distributions for $^{25}Na_{0+1}$ fall off too rapidly. Changes to the bound state radius or

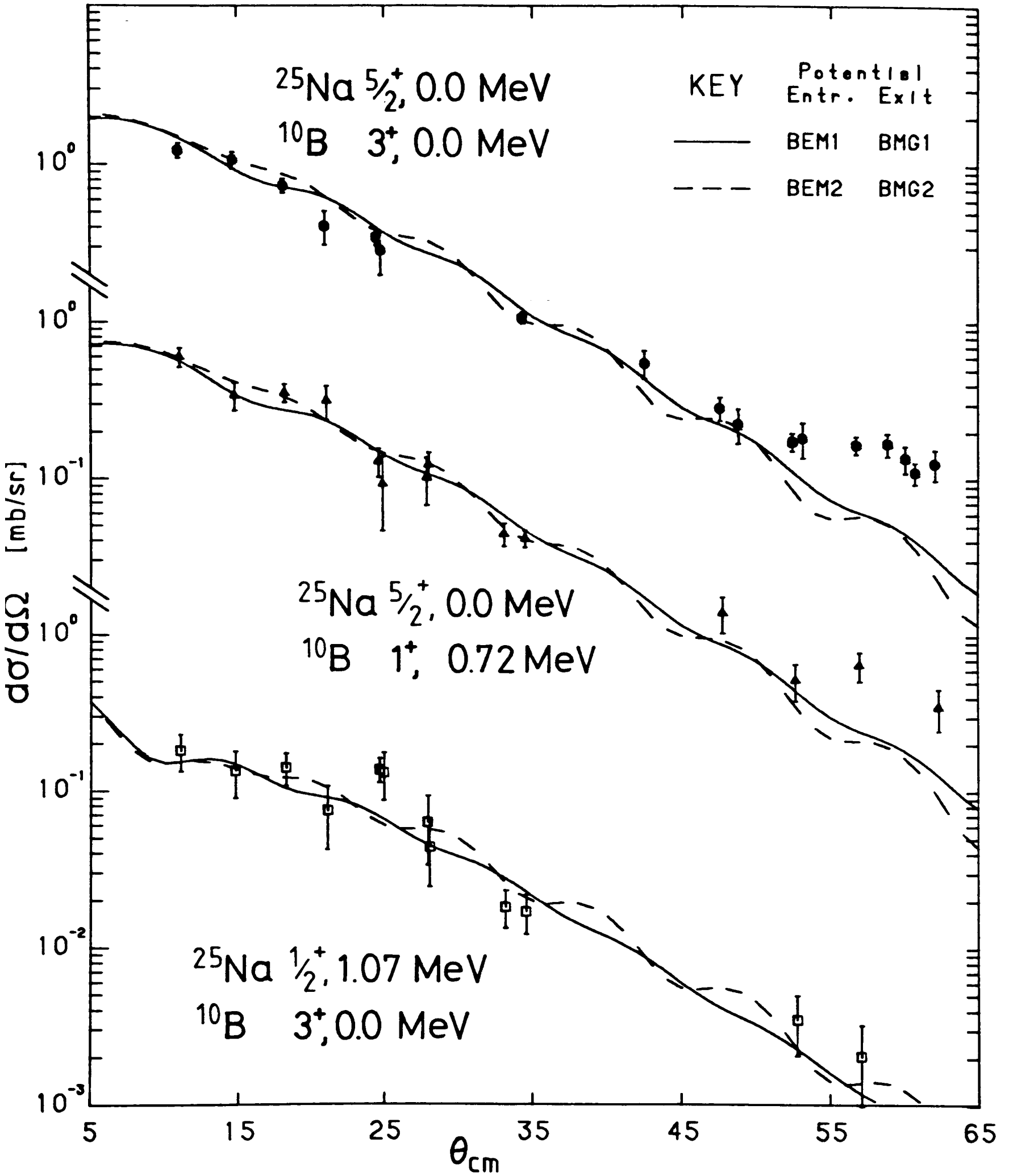


Fig. 5.3 Angular distributions for states in $^{10}$B and $^{25}$Na from the reaction $^{26}$Mg($^{9}$Be,$^{10}$B)$^{25}$Na at 43 MeV. (The top two distributions include a small contribution from $^{25}$Na $3/2^+$, 0.09 MeV.)

diffuseness by 10% made no effect on the shape of the angular distribution, although the normalization was sensitive to this as remarked earlier. Changes to the optical model potential geometry parameters by 10% made slight changes to the slope of the whole angular distribution. Better overall agreement could not be achieved by adjusting these parameters. The fact that this disagreement occurs at backward angles where the direct transfer cross-section is predicted to be low ( < 0.1 mb/sr) suggests that second order effects are no longer negligible in this region.

Despite the problem with the fits at backward angles, spectroscopic factors have been extracted from the normalization which gives the minimum $\chi^2$ for all the data (these are presented in table 5.3). In fact, because of the relatively large error bars on the backward angle data, the values of $C^2S$ for $^{25}Na_{0+1}$ would differ by only 8% if the normalization were restricted to data for $\theta_{cm} < 50°$ (for $^{25}Na_2$ there would be little difference).

Spectroscopic factors obtained through other reaction studies are also listed in table 5.3. It can be seen that the use of potentials BEM2 and BMG2 for ($^9Be$,$^{10}B$) produces values of $C^2S$ that are much higher than these. When potentials BEM1 and BMG1 are used, the value for $C^2S$($^{25}Na_{0+1}$) obtained via the $^{10}B$ first excited state (2.6±0.3) is in good agreement with both light-ion experiment results and the shell model value of 2.63 [Bro80], but the values obtained via the $^{10}B$ ground state are again rather high. Analysis of the ($^{11}B$,$^{12}C$) reaction by Paschopoulos et al. [Pas75] also gave a large spectroscopic factor (table 5.3). It is not uncommon for heavy-ion reactions to give poor absolute values of $C^2S$, mainly because of ambiguities in the optical

Table 5.3 Spectroscopic Factors for $^{26}Mg \rightarrow {}^{25}Na + p$

(i) $^{25}Na_{0,1}$ {Ex = 0.0 $5/2^+$, Ex = 90 keV $3/2^+$}

Configuration assumed: $(0d_{5/2})^{-1}$

| Reaction | $(^9Be,^{10}B_0)$ | $(^9Be,^{10}B_1)$ | $(^6Li,^7Be_0)$ | $(^6Li,^7Be_1)$ | $(d,^3He)$ | $(^{11}B,^{12}C)$ |
|---|---|---|---|---|---|---|
| Reference | * | * | [Woo80] | [Woo80] | [Jän73] | [Pas75] |
| $C^2S$ | $4.1^{\alpha}$ | $2.6^{\alpha}$ | 3.2 | 2.7 | $2.94^{\gamma}$ | 4.60 |
| | $6.8^{\beta}$ | $4.5^{\beta}$ | | | | |

(ii) $^{25}Na_2$ {Ex = 1.07 MeV $1/2^+$}

Configuration assumed: $(1s_{1/2})^{-1}$

| Reaction | $(^9Be,^{10}B_0)$ | $(d,^3He)$ | $(^{11}B,^{12}C)$ |
|---|---|---|---|
| Reference | * | [Jän73] | [Pas75] |
| $C^2S$ | $0.49^{\alpha}$ | 0.35 | 0.43 |
| | $0.95^{\beta}$ | | |

Notes: *) this work;

α) OM potentials BEM1 (entr.) and BMG1 (exit);

β) OM potentials BEM2 (entr.) and BMG2 (exit);

γ) $2.61(0d_{5/2})^{-1} + 0.33(0d_{3/2})^{-1}$

potentials or different parameterizations of the bound state well, although the relative values are usually quite acceptable: often the spectroscopic factors for excited states are normalized through the ground state values (see, for example, [Sta77]).

The discrepancy observed here between the spectroscopic factors extracted when $^{10}B$ is in its ground or first excited state is difficult to explain. This is more serious than the poor absolute values of $C^2S$ because the calculations are less sensitive to the bound state parameters in the light system, which may at first be thought to be at fault. The relative errors on the normalization of the DWBA cross-sections to the data are mainly due to the statistical fluctuations in the data: these are less than 2%. The larger systematic errors (8%) arising from uncertainties in the target thickness, collimator sizes, etc., are not relevant to the consideration of differences between $^{10}B_0$ and $^{10}B_1$ results. Since the excitation energy of $^{10}B_1$ is small (718 keV) compared to the kinetic energy (~33 MeV), one can rule out some electronic or detector discrimination. It would also seem unlikely that a poor software PI gate could produce a large effect. Nevertheless this was checked by replaying the data with both broad and narrow $^{10}B$ windows: no significant difference resulted in the $^{10}B_0$ to $^{10}B_1$ ratio.

There is also the possibility that this discrepancy has arisen because the calculation has been done for $^{25}Na_0(5/2^+)$ alone, whereas the experimental data is known to include a contribution from $^{25}Na_1(3/2^+)$. An experiment performed with the spectrometer showed that at $15^\circ_{lab}$ the ratio of $^{25}Na_0$ to $^{25}Na_1$ is 6:1 when $^{10}B$ is detected in its ground state (section 2.6). Nothing could be deduced about this ratio when $^{10}B$ is in

its excited state, but considerations of j-dependent effects suggest that it will be greater than 6:1, since the dominant transfer of the $0p_{1/2}$ proton ($j_<$) to $^{10}B_1$ will be suppressed for the $d_{3/2}$ state ($j_<$) but enhanced for the $d_{5/2}$ state ($j_>$). Suppose we take as an extreme case the population of the $d_{3/2}$ state to be negligible when $^{10}B$ is left in its excited state. Then the spectroscopic factor for $^{25}Na_0$ when $^{10}B$ is left excited is unchanged from the value given in table 5.3 (namely $C^2S=2.6$ if potentials BEM1 and BMG1 are used), but the value for $^{10}B_0$ should be decreased by $1/6^{th}$ to $C^2S=3.4$ - assuming that the $^{25}Na_0$:$^{25}Na_1$ ratio measured at 15° is a fair indication for the whole angular range†. Thus even this extreme hypothesis has left a sizeable discrepancy between $^{10}B_0$ and $^{10}B_1$.

We are forced then to admit that the theoretical treatment must be inadequate in some way. This is surprising in view of the success of the ($^6Li$,$^7Be$) reaction from the same target nucleus (see table 5.3: $C^2S$ for ($^6Li$,$^7Be_0$) is larger than that for ($^6Li$,$^7Be_1$) but the size of the discrepancy is only 17% compared with 43% for ($^9Be$,$^{10}B$)).

In summary, the DWBA analysis of $^{26}Mg(^9Be,^{10}B)^{25}Na$ has been found unsatisfactory on three counts:

(i) the deduced spectroscopic factors are too high in general (this is probably a reflection on the optical model potentials used rather than the DWBA),

---

† DWBA calculations have shown identical slopes for the reaction leading to $^{25}Na(5/2^+)$ and $^{25}Na(3/2^+)$, other things being equal.

(ii) the backward angle data are not accounted for,

(iii) there is a discrepancy between the spectroscopic factors extracted when $^{10}B$ is in its ground or first excited state.

### 5.2.2 $^{16}O(^{9}Be,^{10}B)^{15}N$ at 43 MeV.

The experimental cross-sections and DWBA predictions for the reaction to the $1/2^-$ ground state of $^{15}N$ for $^{10}B$ in its ground and first excited state are shown in fig. 5.4. There are clear oscillations in the angular distribution because this reaction is higher above the Coulomb barrier than was the case for the $^{26}Mg$ target. It is seen that calculated angular distributions have too steep a slope compared with the $^{10}B_0$ data. No better agreement could be found amongst various combinations of entrance and exit potentials, including a potential from Nair et al. [Nai74] which was successfully used in the analysis of $^{12}C(^{10}B,^{9}Be)^{13}N$ at 100 MeV and one from Woods [Woo81], with a small real radius, which descibed $^{7}Li + ^{15}N$ elastic scattering at 29 MeV. The calculations discussed here used either potential BE01 or BE02 in the entrance channel, and in the exit channel a potential from Motobayashi et al. [Mot79] which fitted $^{10}B + ^{16}O$ elastic scattering at 65.8 MeV. The latter is listed in table 5.4.

Table 5.4 Additional Optical Model Potential Parameters.

| Label | V(MeV) | $a_v$(fm) | $r_v$(fm) | W(MeV) | $a_w$(fm) | $r_w$(fm) | $r_c$(fm) |
|---|---|---|---|---|---|---|---|
| [Mot79] | 82. | 0.77 | 0.92 | 27. | 0.354 | 1.29 | 1.3 |

The poor quality of the fits to the data make the extracted spectroscopic factors for $^{10}B_0$ inaccurate. The values obtained from a least-squares fit to the whole angular range are given in table 5.5. A

$^{16}O(^{9}Be, ^{10}B)^{15}N$ at 43 MeV

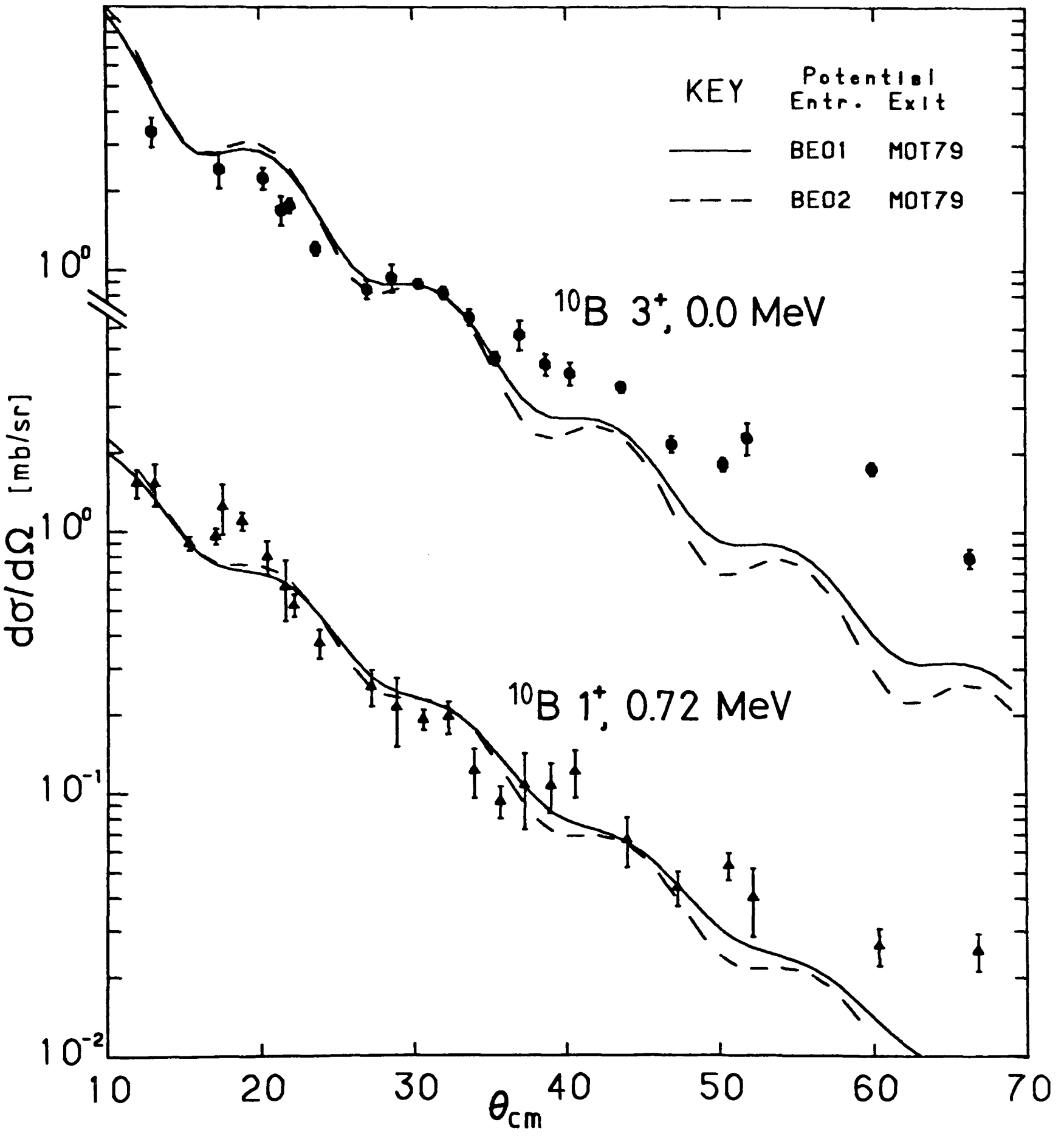


Fig. 5.4 Angular distributions for $^{15}N_0$ with $^{10}B_0$ and $^{10}B_1$.

measure of the uncertainty may be seen by normalizing the theoretical curve to only the last 10 data points (i.e. for $\theta_{cm} > 35°$). For the distribution calculated using potential BE01, this increased the value of $C^2S$ from 1.9 to 2.8 - a change much bigger than the estimated systematic error on the data. This must be taken into account in the comparison of spectroscopic factors with those from other work.

Table 5.5 Spectroscopic Factors for $^{16}O \rightarrow {}^{15}N(1/2^-) + p$

Configuration assumed: $(0p_{1/2})^{-1}$

| Reaction | $(^9Be,{}^{10}B_0)$ | $(^9Be,{}^{10}B_1)$ | $(d,{}^3He)$ | $(^{10}B,{}^{11}C)$ |
|---|---|---|---|---|
| Reference | * | * | [Hie67] | [Nai75] |
| $C^2S$ | $1.9^{\alpha **}$ | $2.3^{\alpha}$ | 2.14 | 1.51 |
| | $1.9^{\beta **}$ | $2.4^{\beta}$ | | |

Notes: *) this work;
α) OM potentials BE01 (entr.) and MOT79 (exit);
β) OM potentials BE02 (entr.) and MOT79 (exit);
**) errors on these values >> 8% (see text).

The reason behind the failure of the DWBA to account for the data is not known. Certainly the major part of the $^{15}N$ ground state is a $p_{1/2}$ hole coupled to the $^{16}O$ ground state [Hie67]. $^{16}O$ is not, however, a perfect double-closed shell nucleus (if it were, one would expect $C^2S=2.0$ instead of the value of 1.5 found from a shell model calculation that included configuration mixing [Mil71]). It is interesting to note that Woods [Woo81] found that the DWBA calculations for the $^{16}O(^6Li,{}^7Be)^{15}N$ also gave poor fits to the data; this was not the case for the $(^{10}B,{}^{11}C)$ reaction studied by Nair [Nai75], however.

With respect to the $^{10}B_0/^{10}B_1$ anomaly apparent for the $^{26}Mg$ target, little has been gained from this experiment because of the uncertainty in $C^2S$ when $^{10}B$ is in its ground state. The values of $C^2S$ obtained when $^{10}B$ is excited are slightly high compared with those obtained in other reaction analyses.

### 5.2.3 $^{40}Ca(^{9}Be,^{10}B)^{39}K$ at 45 MeV.

The data and results of the DWBA calculations using potential BECA in the entrance channel and either potential BK2 or ECK80 in the exit channel are shown in fig. 5.5. It is seen that both exit potential choices give good fits to the data, but that with ECK80 is slightly superior. This probably indicates that potential BK2 has the wrong slope around the strong absorption radius, because potential ECK80 does not give a good account of the $^{10}B + ^{39}K$ elastic scattering data (the $\chi^2$ is about ten times worse than that for BK2). The spectroscopic factors are given in table 5.6 where it is seen that those obtained when potential BK2 is used are in general much higher than both the values found by light-ion work and the weak-coupling limit of 4.0. The overall values extracted when potential ECK80 is used in the exit channel are more reasonable but the most striking feature of table 5.6 is once again the discrepancy between values of $C^2S$ for $^{10}B$ in its ground or first excited state (in future, this will be referred to as "the $^{10}B_0/^{10}B_1$ anomaly" or simply "the anomaly"). The discrepancy here is even larger than that for the $^{26}Mg$ target and, what is more, is <u>reversed</u> (i.e. the value of $C^2S$ for $^{10}B_0$ is smaller than that for $^{10}B_1$ whereas the opposite is true for $^{26}Mg(^{9}Be,^{10}B)^{25}Na$). Again it was found that the relative size of the anomaly is independent of the optical potentials used. This is more general than shown by table 5.6: various other combinations of

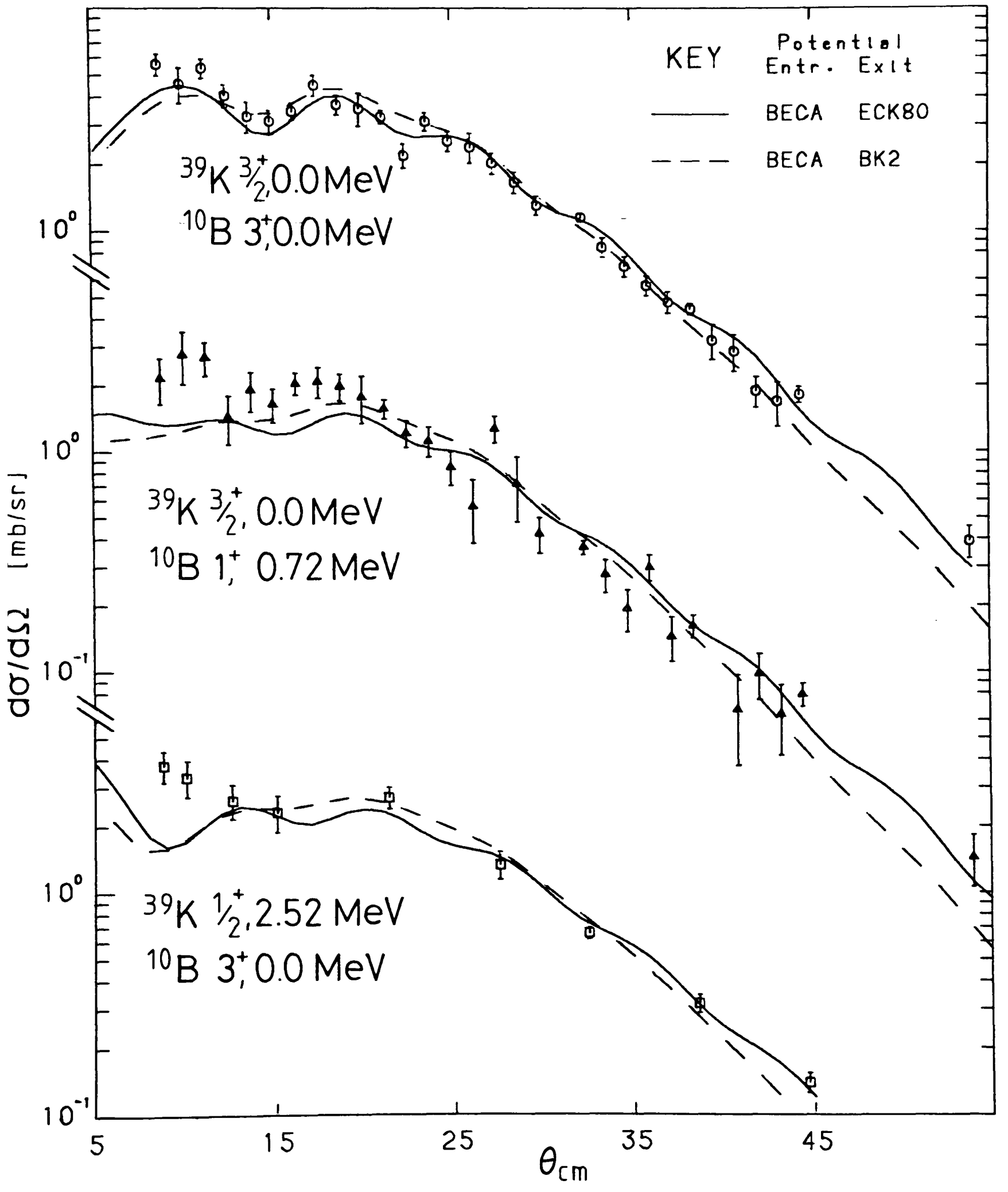


Fig. 5.5 $^{40}$Ca($^{9}$Be,$^{10}$B)$^{39}$K reaction angular distributions.

Table 5.6 Spectroscopic Factors for $^{40}Ca \rightarrow {}^{39}K + p$

(i) $^{39}K_0$ {Ex = 0.0 $3/2^+$}

Configuration assumed: $(0d_{3/2})^{-1}$

| Reaction | $(^9Be,{}^{10}B_0)$ | $(^9Be,{}^{10}B_1)$ | $(d,{}^3He)$ | $(^7Li,{}^8Be)$ |
|---|---|---|---|---|
| Reference | * | * | [Hie67] | [Hur79] |
| $C^2S$ | $4.8^{\alpha}$ | $7.8^{\alpha}$ | 4.2 | 3.9 |
| | $3.5^{\beta}$ | $5.4^{\beta}$ | | |

(ii) $^{39}K_1$ {Ex = 2.52 MeV $1/2^+$}

Configuration assumed: $(1s_{1/2})^{-1}$

| Reaction | $(^9Be,{}^{10}B_0)$ | $(d,{}^3He)$ | $(^7Li,{}^8Be)$ |
|---|---|---|---|
| Reference | * | [Hie67] | [Hur79] |
| $C^2S$ | $2.6^{\alpha}$ | 1.62 | 0.71 |
| | $1.9^{\beta}$ | | |

Notes: *) this work;

α) OM potentials BECA (entr.) and BK2 (exit);

β) OM potentials BECA (entr.) and ECK80 (exit).

entrance and exit potentials have been tried with similar results.

- - - - - - - - - - - - - -

In the light of the results from the DWBA analysis of the ($^{9}$Be,$^{10}$B) reaction on the $^{26}$Mg and $^{40}$Ca targets, it was decided to investigate the $^{10}B_0/^{10}B_1$ anomaly in more detail. Two approaches were carried out concurrently: the data were extended to other target nuclei and more sophisticated calculations were attempted. These are reported later.

The emphasis in the second series of experiments was therefore placed on the relative spectroscopic factors extracted, and previous results had shown that these were insensitive to the DWBA optical model potentials. Thus it was not important to find new optical model potentials that accurately described the entrance and exit channels in the later experiments. Instead they were taken from the results of the earlier analyses or from the literature: the policy was to try "reasonable" potentials until a good fit to the reaction data was obtained. The implications of this are that the absolute spectroscopic factors derived might be expected to be less reliable than those for the earlier series of experiments.

### 5.2.4 $^{63}$Cu($^{9}$Be,$^{10}$B)$^{62}$Ni at 43 MeV.

This target was chosen partly because Hudson et al. [Hud75] had carried out a DWBA analysis of the $^{63}$Cu($^{6}$Li,$^{7}Be_{0,1}$)$^{62}Ni_{0,1}$ reaction at $E(^{6}Li)$ = 34 MeV and found excellent agreement between spectroscopic factors obtained with $^{7}Be_0$ and $^{7}Be_1$.

The angular distributions for the $^{63}Cu(^{9}Be,^{10}B_{0,1})^{62}Ni_{0}$ and $^{63}Cu(^{9}Be,^{10}B_{0})^{62}Ni_{1}$ reactions are presented in fig. 5.6. A roughly "bell-shaped" distribution is seen, as is often the case for transfer reactions on heavy target nuclei [Kov74], peaked at $\sim 25^{\circ}_{cm}$.

Various combinations of entrance and exit potentials were tried, using BECA, BK1, BK2 and ECK80 of tables 4.4 and 4.6. The best fit to the $^{63}Cu(^{9}Be,^{10}B_{0})^{62}Ni$ data was obtained with potential ECK80 in both entrance and exit channels - other potentials gave poorer fits for $\theta_{cm} < 20^{\circ}$. The results of the calculations with this potential are shown normalized to the data in fig. 5.6 and the spectroscopic factors for $^{62}Ni_{0}$ are given in table 5.7.

Table 5.7 Spectroscopic Factors for $^{63}Cu \rightarrow {}^{62}Ni(0^{+}) + p$

Target configuration assumed: $(1p_{3/2})^{-1}$

| Reaction | $(^{9}Be,^{10}B_{0})$ | $(^{9}Be,^{10}B_{1})$ | $(^{6}Li,^{7}Be_{0})$ | $(^{6}Li,^{7}Be_{1})$ | $(d,^{3}He)$ |
|---|---|---|---|---|---|
| Reference | * | * | [Hud75] | [Hud75] | [Hie68] |
| $C^2S$ | 0.39 | 0.48 | 0.79 | 0.81 | 0.68 |

Note: *) this work.

It is seen that the values of $C^2S$ for the present work are in poor agreement with those for other reactions. The use of other potentials gave slightly higher values but worse fits. Again a discrepancy is present for $^{10}B_{0}/^{10}B_{1}$, although not to the same extent as for the previous target nuclei.

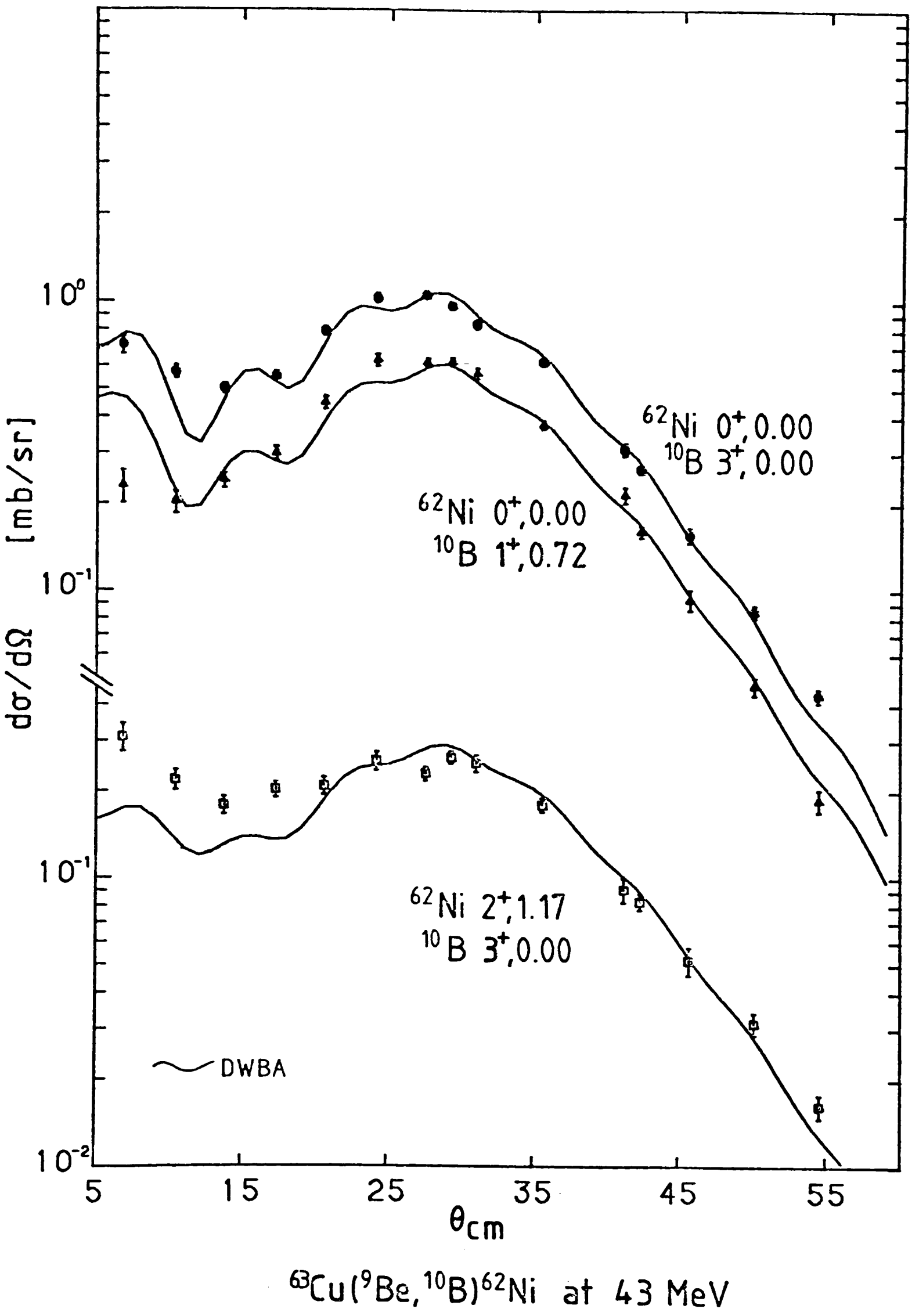


Fig. 5.6 Angular distributions for transitions to $^{62}$Ni and $^{10}$B ground and first excited states. The curves are the DWBA predictions with the optical potential ECK80.

The cross-section for the transfer to the $2^+$ (1.17 MeV) state in $^{62}Ni$ was also calculated with the potential ECK80, assuming a component in the ground state of $^{63}Cu$ corresponding to $^{62}Ni(2^+)\otimes 1p_{3/2}$ as done by Hudson et al. (the fit for this also is shown in fig. 5.6). The deduced spectroscopic factor was 0.102, but if this is scaled by the same amount required to make the spectroscopic factor for $^{62}Ni_0$ equal to Hudson et al.'s value, the result is in good agreement with the corresponding one from their work (0.21 compared with 0.20 respectively).

### 5.2.5 $^{54}Fe(^{9}Be,^{10}B)^{53}Mn$ at 43 MeV.

As for the reaction on the $^{63}Cu$ target, the use of potential ECK80 in both entrance and exit channels of the DWBA calculation results in a satisfactory fit to the data (fig. 5.7). The angular distribution for the reaction shows a bell-shaped peak around the grazing angle of about $30^\circ_{cm}$ with an additional rise in cross-section towards more forward angles.

The deduced spectroscopic factors are given in table 5.8. It should be remembered that the absolute values of these are subject to some uncertainty because of the way the enrichment of $^{54}Fe$ in this target was measured (Chapter 2). Even so, the values deduced in this work are in significant disagreement with the light-ion ones and the shell model limit of 6.0, and this is probably a reflection on the inadequacy of the optical model potentials. What is more important in the context of the previous ($^{9}Be,^{10}B$) results is the remarkably consistent values of $C^2S$ for $^{10}B_0$ and $^{10}B_1$.

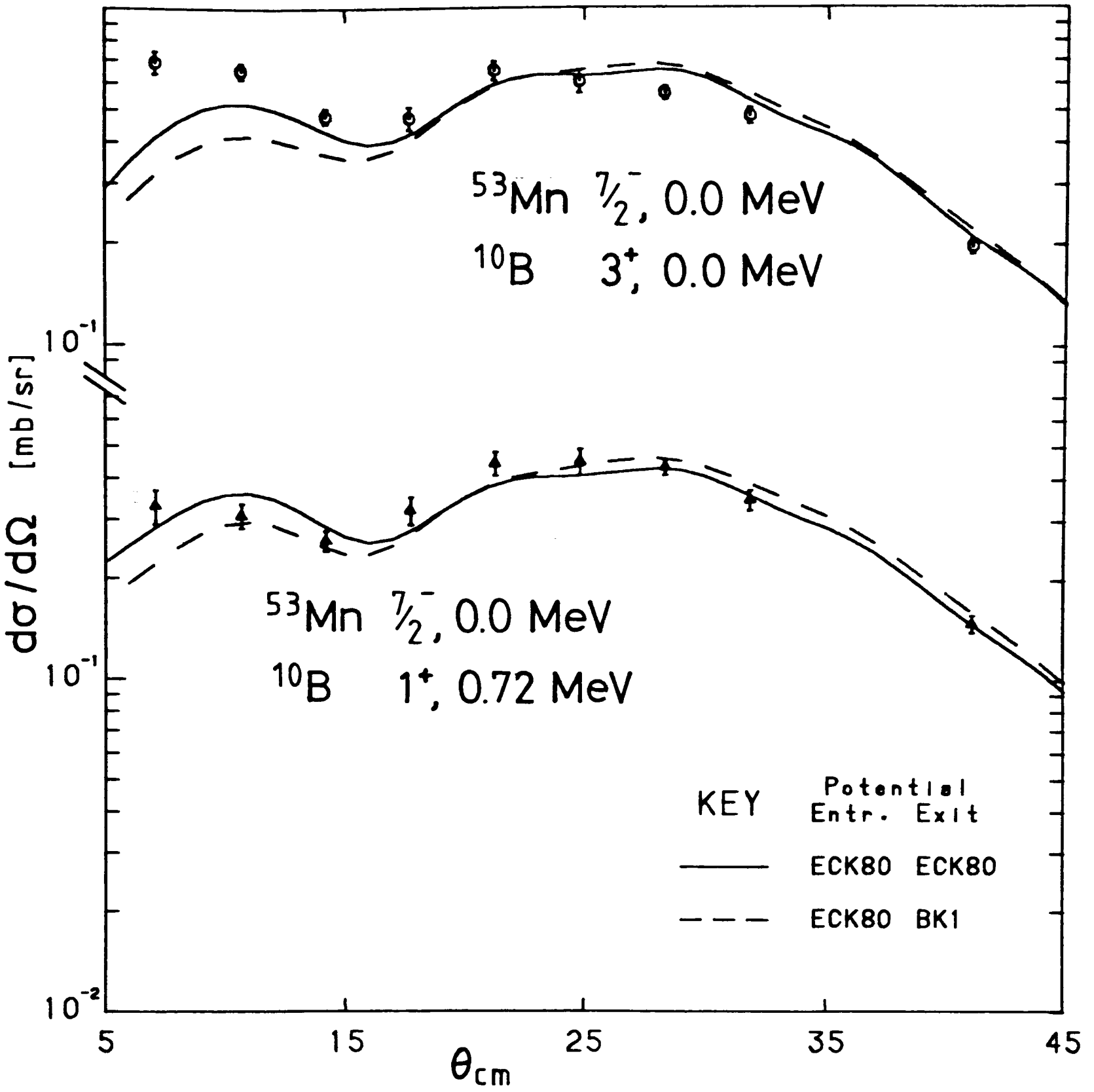


Fig. 5.7 Angular distributions for $^{54}Fe(^{9}Be,^{10}B)^{53}Mn$.

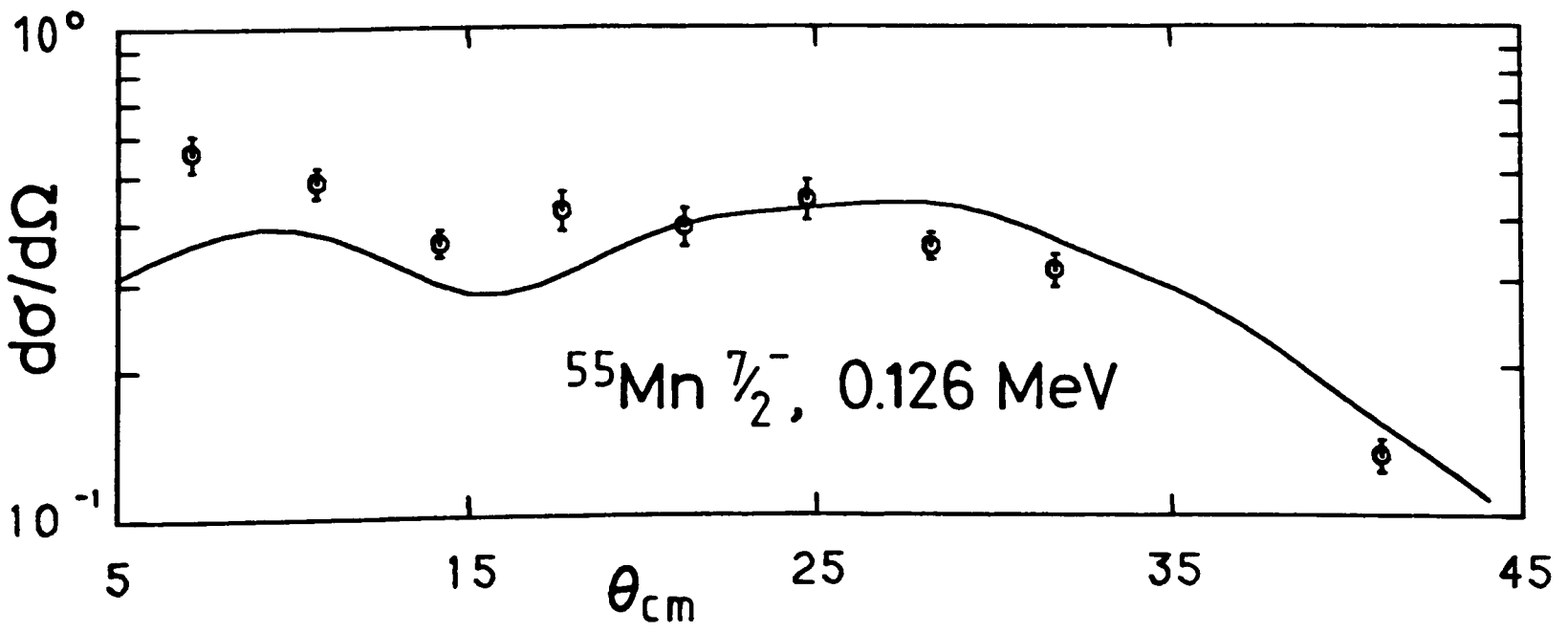


Fig. 5.8 Angular distribution for $^{56}Fe(^{9}Be,^{10}B)^{55}Mn$.
The curve is the DWBA prediction with potential ECK80.

Table 5.8 Spectroscopic Factors for $^{54}Fe \rightarrow {}^{53}Mn(7/2^-) + p$

Configuration assumed: $(0f_{7/2})^{-1}$

| Reaction | $(^9Be,{}^{10}B_0)$ | $(^9Be,{}^{10}B_1)$ | $(d,{}^3He)$ | $(d,{}^3He)$ |
|---|---|---|---|---|
| Reference | * | * | [New68] | [Mai69] |
| $C^2S$ | $2.9^{\alpha}$ | $2.7^{\alpha}$ | 5.9 | 4.4 |
| | $3.9^{\beta}$ | $3.8^{\beta}$ | | |

Notes: *) this work;
α) OM potentials ECK80 (entr. and exit);
β) OM potentials ECK80 (entr.) and BK1 (exit).

Fig. 5.8 shows the DWBA fit to the $^{56}Fe(^9Be,{}^{10}B){}^{55}Mn_1$ reaction, assuming a $0f_{7/2}$ pickup. This calculation was carried out in order to ascertain the $^{56}Fe$:$^{54}Fe$ ratio (equal spectroscopic factors for $^{56}Fe$ and $^{54}Fe$ were assumed). The absolute spectroscopic factor for $^{54}Fe$ was then calculated.

### 5.2.6 $^{24}Mg(^9Be,{}^{10}B){}^{23}Na$ at 43 MeV.

The convenient spacing of ground and first excited states of $^{23}Na$ (440 keV) allowed $^{10}B_0$ and $^{10}B_1$ angular distributions for each of them to be obtained (fig. 5.9). The effect of $j_< j_>$ enhancement in $^{23}Na_0{}^{10}B_0$ and $j_>j_>$ inhibition in $^{23}Na_1{}^{10}B_0$ (as mentioned in section 5.1.1) is dramatically illustrated by the difference in observed cross-sections in fig. 5.9.

The optical model potential set that gave the more reasonable values of $C^2S$ for $^{26}Mg(^9Be,{}^{10}B){}^{25}Na$, namely BEM1 in the entrance and BMG1 in the exit channel, was used in the DWBA analysis. The resulting fits to the data and spectroscopic factors are shown in fig. 5.9 and

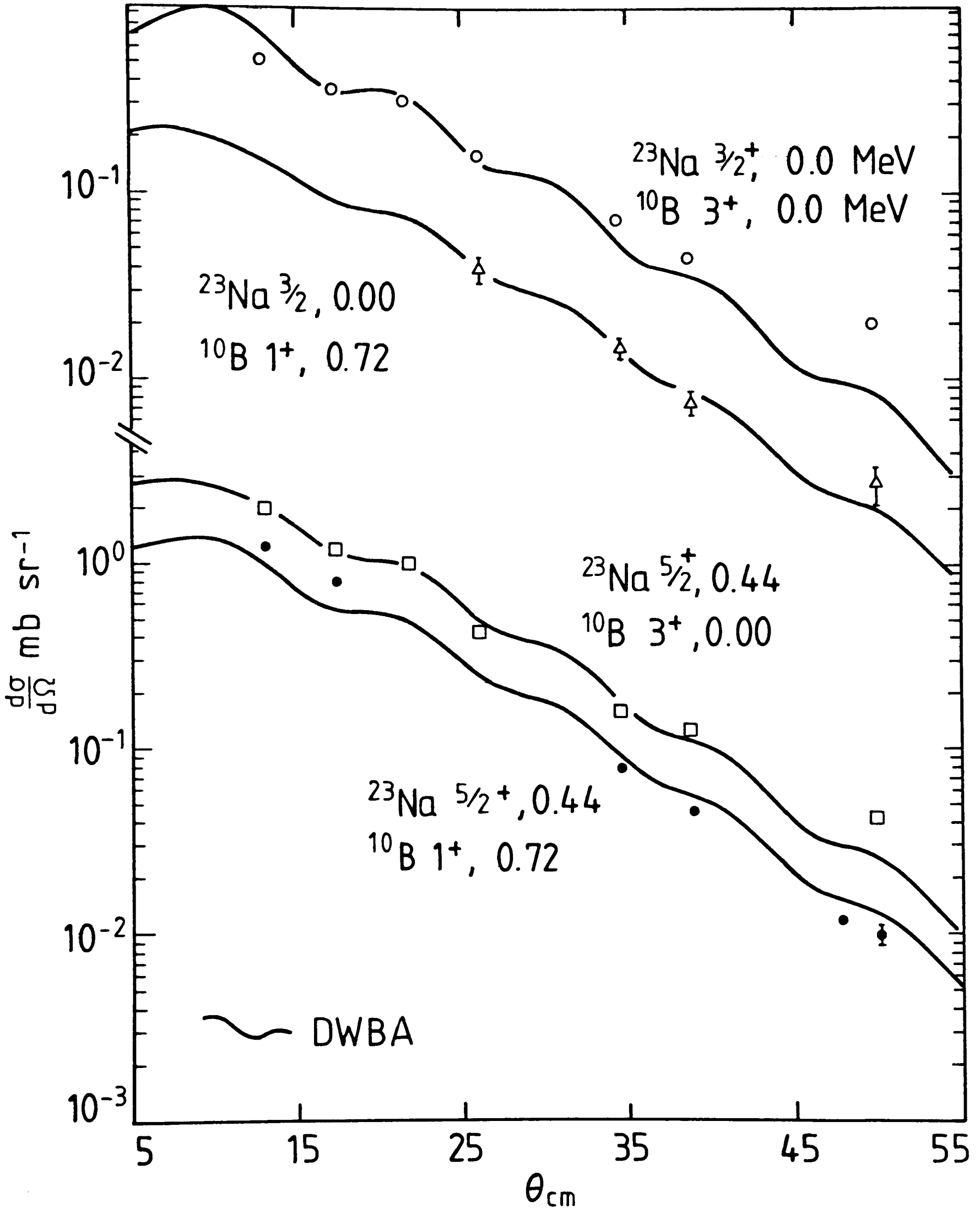


Fig. 5.9 Angular distributions for states in $^{10}$B and $^{23}$Na from the reaction $^{24}$Mg($^{9}$Be,$^{10}$B)$^{23}$Na. The curves are the DWBA predictions with the optical potentials BEM1 (entr.) and BEM2 (exit).

Table 5.9 Spectroscopic Factors for $^{24}Mg \rightarrow {}^{23}Na + p$

(i) $^{23}Na_0$ {Ex = 0.0 $3/2^+$}

Configuration assumed: $(0d_{3/2})^{-1}$

| Reaction | ($^9$Be,$^{10}B_0$) | ($^9$Be,$^{10}B_1$) | (d,$^3$He) | (p,d) |
|---|---|---|---|---|
| Reference | * | * | [Krä71] | [Koz68] |
| $C^2S$ | 0.59 | 0.36 | 0.24 | 0.36 |

(ii) $^{23}Na_1$ {Ex = 0.44 MeV $5/2^+$}

Configuration assumed: $(0d_{5/2})^{-1}$

| Reaction | ($^9$Be,$^{10}B_0$) | ($^9$Be,$^{10}B_1$) | (d,$^3$He) | (p,d) |
|---|---|---|---|---|
| Reference | * | * | [Krä71] | [Koz68] |
| $C^2S$ | 2.83 | 2.25 | 3.78 | 2.83 |

Note: *) this work: OM potentials BEM1 (entr.) and BMG1 (exit).

table 5.9. The calculated cross-sections are seen to fit the data well. It should be noted, however, that the data do not extend as far back in angle as those for $^{26}Mg(^{9}Be,^{10}B)^{25}Na$, so one cannot say whether the same problems observed there exist or not. Reasonable agreement is seen between the absolute values of the spectroscopic factors and the light-ion work. The $^{10}B_0/^{10}B_1$ anomaly is again evident - no more so than for the $^{25}Na$ ground state.

## 5.2.6 $^{40}Ca(^{9}Be,^{10}B)^{39}K$ at 30 MeV.

It was decided to repeat the $^{40}Ca(^{9}Be,^{10}B)^{39}K$ reaction, which had given a large anomaly at 45 MeV, at an energy closer to the Coulomb barrier[†]. This was undertaken in the light of the smallest values of the anomaly being for the two heaviest target nuclei studied, $^{63}Cu$ and $^{54}Fe$. An interesting question then was: will the DWBA analysis give a better account of the data when the transfer takes place further from the nuclear interior, where Coulomb effects are relatively more important?

Fig. 5.10 shows the data and the results of the DWBA calculatiuons with potential BECA in the entrance channel and ECK80 in the exit channel (i.e. the same combination of potentials that successfully fitted the reaction at 45 MeV). A rather poor representation of the 30 MeV reaction data for $^{10}B_1$ is produced at forward angles. The $^{10}B_0$ cross-section reaches a peak of 0.9 mb/sr at $\sim 35^\circ_{cm}$ compared with 6 mb/sr at $10^\circ_{cm}$ for the 45 MeV data (fig. 5.5).

---

[†] 15.0 MeV (c.m.) corresponding to a lab. energy of 18.3 MeV.

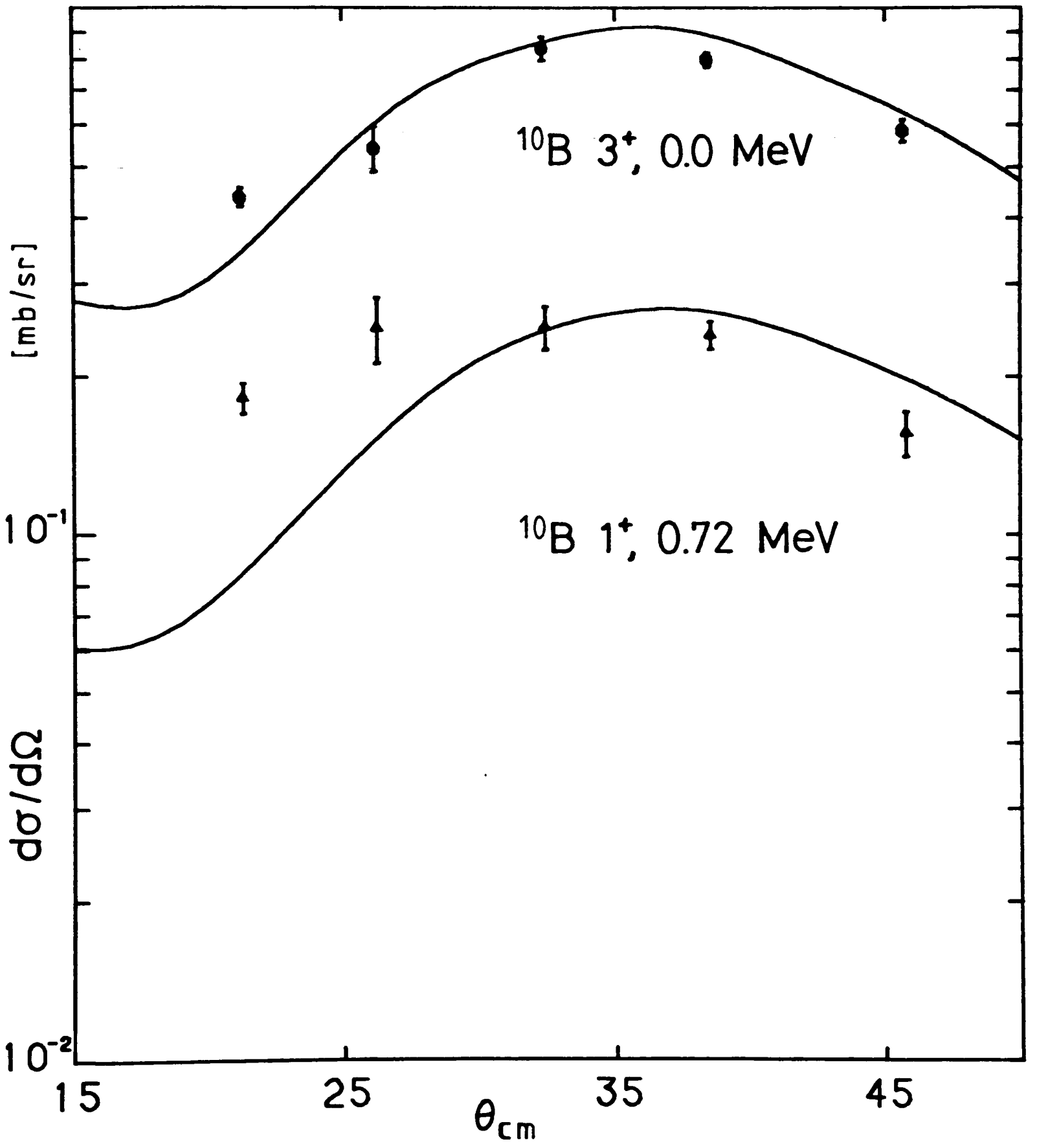


Fig. 5.10 Angular distributions for the reaction $^{40}Ca(^{9}Be,^{10}B)^{39}K$ at 30 MeV. The curves are DWBA predictions with the optical potentials BECA (entr.) and ECK80 (exit).

The spectroscopic factor, $C^2S$, extracted for $^{10}B_0$ was 2.2; that for $^{10}B_1$ was 3.8. Clearly, the anomaly is no smaller for the $^{40}Ca(^{9}Be,^{10}B)^{39}K$ reaction at 30 MeV than it was at 45 MeV.

### 5.2.7 Summary of the $^{10}B_0/^{10}B_1$ Anomaly.

The remainder of this chapter concentrates on the anomaly found between the spectroscopic factors extracted when $^{10}B$ is in its ground ($3^+$) or first excited ($1^+$) state. It is convenient now to define an "anomaly factor", AF, as

$$AF = \frac{S(3^+) - S(1^+)}{\frac{1}{2}[S(3^+) + S(1^+)]},$$

where $S(J^+)$ is the spectroscopic factor extracted when $^{10}B$ is in its $J^+$ state. AF is thus the difference in S divided by the mean, which is independent of the choice of optical potential as we have seen. The values of AF for all the cases considered in sections 5.2.1 to 5.2.6 (with the exception of the $^{16}O$ target) are tabulated in table 5.10.

A few words should be said about the size of the discrepancies in the spectroscopic factors. In a review of heavy-ion reactions, Tamura et al. [Tam80] comment that "the theory always predicts cross-sections within a factor of two". This statement concerns the general accuracy of the DWBA cross-section magnitude; the relative spectroscopic factors are always found to be much more accurate than this. Obviously, it is also interesting to see if anomalous spectroscopic factors between projectile excited states have been found in other cases. Ford et al. [For74] report such a discrepancy between cross-sections for $^{10}Be_0$ and $^{10}Be_1$ in the $^{208}Pb(^{11}B,^{10}Be)^{209}Bi$ reaction at 72.2 MeV. This

Table 5.10

Summary of the Anomaly Found in ($^{9}Be$,$^{10}B$).

| Target | Residual State† | E($^{9}Be$) (MeV) | AF (see text) |
|---|---|---|---|
| $^{26}Mg$ | $^{25}Na_0$ (+$^{25}Na_1$) | 43 | 43% |
| $^{40}Ca$ | $^{39}K_0$ | 45 | -47% |
| $^{63}Cu$ | $^{62}Ni_0$ | 43 | -22% |
| $^{54}Fe$ | $^{53}Mn_0$ | 43 | 5% |
| $^{24}Mg$ | $^{23}Na_0$ | 43 | 50% |
| $^{24}Mg$ | $^{23}Na_1$ | 43 | 23% |
| $^{40}Ca$ | $^{39}K_0$ | 30 | -58% |

† the subscript 0 or 1 denotes the residual nucleus ground or first excited state respectively.

reaction has Q and grazing-$\ell$ values close to optimum. The DWBA calculations when $^{10}Be$ is emitted in its $2^+$, 3.37 MeV state underestimate the cross-sections for the $1f_{7/2}$ and $(1f_{5/2}+2p_{3/2})$ residual nucleus configurations and overestimate them for the $0i_{13/2}$ group. In terms of an equivalent "anomaly factor" to the one defined above, the magnitude of this discrepancy is only about 30%. Amongst a study of various single-nucleon transfers on $^{12}C$, Rae [Rae76] found that the $^{12}C(^{12}C,^{11}C_1)^{13}C$ reaction gave spectroscopic factors which were about one half the values when $^{11}C$ was detected in its ground state.

There are probably other such isolated cases in the literature, but no systematic study. The survey of the $(^{9}Be,^{10}B)$ reaction presented here has shown that this anomaly is present over a range of target nuclei and Q-matching.

## 5.3 Alternative Description of the Bound State.

The value of AF has been found to be independent of changes in the bound state parameters provided the same changes are made to the description of $^{10}B_0(0p_{3/2})$, $^{10}B_1(0p_{3/2})$ and $^{10}B_1(0p_{1/2})$. This will not be so if different adjustments are made in each case. Therefore it is to be expected that the alternative description of the bound state outlined in section 5.1.3 will affect the values of AF.

The "well-depth" prescription may be criticised in that it produces different wavefunctions within the nuclear interior for different binding energies of the transferred proton, whereas in the shell model these wavefunctions are the same, and it is the shell model framework

that spectroscopic factors are defined. It is interesting to see if the alternative description of the bound state, which has a fixed shell model potential in the interior, can account for the $^{10}B_0/^{10}B_1$ anomaly. Calculations were performed for the reaction on the $^{26}Mg$, $^{40}Ca$ and $^{63}Cu$ targets. The results are given below in table 5.11 (the angular distributions were not significantly different to the ones previously shown).

Table 5.11 also compares the mean square radii for the proton in $^{10}B$ for the different bound state calculations. The most substantial difference between the two prescriptions is in the calculation of the $0p_{1/2}$ wavefunction, which explains why AF is very little different for $^{40}Ca$ (pickup of a $j_<$ proton). On the other hand, for $^{26}Mg$ and $^{63}Cu$ (pickup of $j_>$ protons) the $^{10}B_0$ cross-section is increased relative to $^{10}B_1$ when the "surface-peaked" bound state prescription is used. This has the effect of reducing AF for $^{26}Mg$ but making it worse for $^{63}Cu$.

In general, AF will be little changed for $j_<$ target pickup, i.e. for $^{40}Ca$, and $^{24}Mg$ leading to $^{23}Na_0$, and made more negative for $j_>$ pickup, ($^{26}Mg$, $^{63}Cu$, $^{54}Fe$ and $^{24}Mg$ leading to $^{23}Na_1$). The latter effect is not always desirable, so one concludes that the use of the "surface-peaked" bound state description has not solved the problem.

There is some evidence from table 5.11 that the absolute values of the spectroscopic factors are more reasonable (in the sense of being closer to shell model expectations) when calculated in this manner. In particular, the values extracted for $^{40}Ca(^{9}Be,^{10}B)^{39}K_0$ using the optical model parameters that described the appropriate elastic scattering are in much better agreement with the shell model limit than the

Table 5.11

(i) Values of $C^2S$ and AF for the "Alternative" Bound State Calculation.

| Target | Ejectile state | $C^2S$ | AF | Potential used Entr. | Exit |
|---|---|---|---|---|---|
| $^{26}Mg$ | $^{10}B_0$ | 2.2 | 16% | BEM1 | BMG1 |
| $^{26}Mg$ | $^{10}B_1$ | 1.9 | | | |
| $^{40}Ca$ | $^{10}B_0$ | 3.3 | -52% | BECA | BK2 |
| $^{40}Ca$ | $^{10}B_1$ | 5.5 | | | |
| $^{63}Cu$ | $^{10}B_0$ | 0.32 | -45% | ECK80 | BK1 |
| $^{63}Cu$ | $^{10}B_1$ | 0.50 | | | |

(ii) Mean Square Radii of the Bound State Orbitals.

| | "well-depth" | "alternative" |
|---|---|---|
| $^{10}B_0(0p_{3/2})$ | 2.925 fm | 2.932 fm |
| $^{10}B_1(0p_{3/2})$ | 2.981 fm | 2.964 fm |
| $^{10}B_1(0p_{1/2})$ | 2.910 fm | 3.062 fm |

corresponding values from table 5.6.

Finally, it is interesting to compare the mean square radii of the bound state orbitals with values calculated by the shell model where the total radius of the proton density distribution is normalized to the experimental RMS charge radius. This method has been used in the past to help determine bound state parameters for transfer reactions [Woo80]. It still does not necessarily describe the whole wavefunction correctly, but it does reduce the arbitrariness of the "standard" bound-state parameters. The values for $^{10}$B(0.0 MeV) calculated by a nuclear density code [Bro81] which extrapolates from fits to the A=16-40 mass region are:

$$0p_{3/2}\langle r^2\rangle^{\frac{1}{2}} = 2.713 \text{ fm},$$

$$0p_{1/2}\langle r^2\rangle^{\frac{1}{2}} = 2.823 \text{ fm},$$

which, although lower than the values in table 5.11, are approximately in the same ratio.

## 5.4 The Projectile Spectroscopic Factors, $S_b^j$.

Throughout the above analysis, the values of $S_b^j$ in equation 5.1 have been taken from Cohen and Kurath's compilation (see end of section 5.1.1). It is clear that if different values of $S_b^j$ were used, AF would in general be changed. Furthermore, the value of AF for a given target might be either increased or decreased depending on the relative importance of $^{10}$B($0p_{3/2}$) or $^{10}$B($0p_{1/2}$).

Since the work of Cohen and Kurath has been the standard p-shell interaction for many years and has been tested on many occasions (see, eg. [Hud75]) it seems unlikely that the results for ($^{9}$Be,$^{10}$B) could be much in error. However, $^{9}$Be may be regarded as a cluster of 2$\alpha$ + n, by analogy with $^{6}$Li which is also loosely bound and known to be composed of clusters [Roo76]. Unfortunately the various experimental determinations of S($^{10}$B → $^{9}$Be + p) do not distinguish between transfer to the $p_{3/2}$ or transfer to the $p_{1/2}$ orbit of $^{10}$B($1^{+}$). The values listed in table 5.12 assume either one or the other and are therefore only approximate. This may account for the rather high deduced ratio of S($^{10}$B$_0$)/S($^{10}$B$_1$) compared to the theory.

Table 5.12 Spectroscopic Factors for $^{10}$B → $^{9}$Be + p.

(note that the isospin Clebsch-Gordan term, $C_b^2 = \frac{1}{2}$, has not been included.)

| | | | - - - $S_b^j$(expt) - - - | | | $S_b^j$(theory) |
|---|---|---|---|---|---|---|
| $E_x$ | $J^\pi$ | $j_{tr}$ | [Kar76] | [Par73] | [Art68] | [Coh67] |
| 0.0 | $3^+$ | 3/2 | 0.68 | 1.33 | 0.92 | 1.20 |
| 0.72 | $1^+$ | 1/2 | 1.15 | 2.42* | 1.78 | 1.35 |

(*) assumed $j_{tr}$ = 3/2

The values of $S_b^j$ in ref. [Coh67] use the (A=8-16)POT interaction [Coh65] for $^{10}$B and heavier nuclei, while the (A=6-16)2BME interaction is preferred for A < 9. The 2BME-type effective interactions generally

give slightly better fits to the experimental energy levels of the p-shell nuclei, but they are fitted with more free parameters than the POT-type. Shell model calculations for the above spectroscopic factors were performed on the OEG PDP-10 with the alternative (6-16)2BME and (8-16)2BME interactions and compared with the (8-16)POT results. Those with the (8-16)2BME interaction differed by less than 10% from the (8-16)POT ones, but the (6-16)2BME interaction produced a value for $S^{p3/2}\{^{9}Be + p \rightarrow {}^{10}B(1^{+})\}$ that was 40% higher than the corresponding (8-16)POT value (0.669 and 0.469 respectively). This is presumably the result of the additional fits to A=6 and A=7 in the (6-16)2BME interaction.

In view of the above points, it was felt that there was some justification for trying different spectroscopic factors in the projectile system to see if the $^{10}B_0/^{10}B_1$ anomaly could be accounted for. At the time when this was done, the data for the $^{63}Cu$, $^{54}Fe$ and $^{24}Mg$ targets had not been obtained. The values of $S_b^j$ that remove the anomaly for the $^{26}Mg$ and $^{40}Ca$ targets are:

| | "adjusted" | (8-16)POT |
|---|---|---|
| $S^{p3/2}$ | 1.122 | 0.469 |
| $S^{p1/2}$ | 0.150 | 0.876 |

Two criticisms of this may be made: (i) it seems improbable that the Cohen and Kurath values should be so much in error, (ii) the "adjusted" values have made negligible the $p_{1/2}$ component in $^{10}B(1^{+})$, which is certainly not borne out by experiment (see Karban et al. [Kar76]). In addition, the anomaly is made worse for the $^{63}Cu$, $^{54}Fe$ and $^{24}Mg$ targets. This is not, then, the answer.

## 5.5 Projectile Spin Effects.

In Chapter 4 it was argued that the neglect of the spin-orbit potential was a quite reasonable approximation for the analysis of the elastic scattering. Even fewer studies have been made with the spin-orbit potential in heavy-ion transfer work than in elastic scattering. Wust et al. found better fits to the $^{88}Sr(^{16}O,^{15}N)^{89}Y$ reaction at 96 MeV if a small spin-orbit potential were included [Wus79]. Their reaction, however, was selected to enhance the effects of spin through a high grazing-$\ell$ value of 50 and a large angular momentum mismatch (~6). For ($^{9}Be,^{10}B$) at 43-45 MeV, the grazing-$\ell$ value is less than 25 for the targets studied here, and table 5.2 shows that the $\ell$-mismatch is small. Therefore it seems very unlikely that spin-orbit terms in the optical potential could have any significant effect.

It was also mentioned in Chapter 4 that the non-zero spins of $^{9}Be$ and $^{10}B$ allow these nuclei to possess large ground-state quadrupole moments. Other analyses of $^{10}B$ elastic scattering have sometimes required a non-spherical potential in addition to the usual optical potential in order to give a successful account of the data. Although this was not the case for the analysis presented in Chapter 4, it is worth some further consideration here, particularly because shell model calculations have shown that $^{10}B(1^{+})$ has a very small quadrupole moment (0.7 e.fm$^{2}$). Can this difference between the $^{10}B$ ground and first excited states explain the anomalous spectroscopic factors? A crude test of this is to use a more diffuse optical potential for $^{10}B(3^{+})$ in the reaction, since this represents a spatial average of a non-spherical potential. But, as mentioned in section 5.1.2, the DWBA cross-sections

are not especially sensitive to this parameter. Furthermore, the effect on the values of AF would be in the same sense for all targets considered. It is also noted that in the case of $(^{11}B,^{10}Be_{0,1})$, where Ford et al. found a projectile excitation anomaly, the quadrupole moments are all zero or very small.

## 5.6 Conclusions.

The one-step DWBA calculations have succeeded in reproducing the shape of the $(^{9}Be,^{10}B)$ data for all targets except $^{16}O$ and the very backward angle data of $^{26}Mg$. The latter problem may be due to the rather strong coupling to the first $2^+$ state of $^{26}Mg$. The cause of the poor fit in $^{16}O(^{9}Be,^{10}B)^{15}N$ is not understood, although failure to find a correct exit channel potential cannot be ruled out.

In general, the absolute values of the spectroscopic factors extracted have agreed to within 25% of other experimental values and theoretical calculations. An exception to this was the value for $^{40}Ca(^{9}Be,^{10}B_1)^{39}K_0$ which was too high by a factor of 1.5, despite the use of optical potentials that described the elastic scattering. This may be caused by incorrect optical potential values away from the strong absorption radius (see discussion in Chapter 4) but may also be caused by the true bound state description being rather different from the "standard" one that has been successful for other nuclei. The DWBA analysis of the $^{26}Mg(^{6}Li,^{7}Be)^{25}Na$ reaction has encountered similar problems: several different optical potentials were found which gave equally good fits to elastic scattering data, but only one combination of these in the reaction calculation yielded reasonable spectroscopic

factors. The other choices gave values that were roughly 50% too low [Woo80].

The most surprising failure of the DWBA analysis has been the inconsistency of the spectroscopic factors extracted when $^{10}B$ is detected in its ground or first excited state. This anomaly has been found to be insensitive to optical model parameters. Comparison of spectroscopic factors obtained through different excited states of the ejectile is a better test of the theory than a study of different residual nucleus states, since the relative cross-sections are less sensitive to the description of the bound state, which is always a source of some uncertainty.

A novel method for the computation of form factors has been described. This method is more satisfying than the usual "well-depth" prescription from the nuclear structure viewpoint. DWBA calculations with the form factor generated in this way have given better agreement with light-ion results and different relative values of $C^2S$ for $^{10}B(3^+)$ and $^{10}B(1^+)$ compared to the "well-depth" method. However, there has not been an overall improvement in the $^{10}B_0/^{10}B_1$ anomaly and it is concluded that incorrect form factors are unlikely to be the source of the problem.

The use of projectile spectroscopic factors different to the ones given by Cohen and Kurath has also been unsuccessful in removing the anomaly for <u>all</u> the reaction data. Partial success can be achieved for certain targets, but only at the expense of values of $S_b^j$ that seem physically unjustifiable and by making the anomaly worse for other cases.

It appears that the direct transfer DWBA calculation has failed. This is despite the quite reasonable magnitude of the cross-sections observed in the ($^{9}$Be,$^{10}$B) reaction and the generally good agreement for the shape of the angular distributions; discrepancies in the fits to the data have in the past often been accounted for by the explicit inclusion of coupling to excited states. In the next chapter we consider possible explanations for the failure of the DWBA, in particular some calculations of indirect processes in the reaction mechanism.

# CHAPTER 6

# INVESTIGATION OF INDIRECT PROCESSES

## 6.1 Introduction

This chapter concerns some inquiries into whether indirect processes not described by the DWBA analysis in Chapter 5 might account for the $^{10}B_0/^{10}B_1$ anomaly and if so, which channels might be expected to be important. Since the number of possible channel couplings is infinite, (if couplings to states in the continuum are included), one always has to truncate in practice and limit the considerations to those excited states or routes with large coupling parameters or spectroscopic factors. In the following, two cases are considered separately, although there is no reason why they should not act concurrently. These are excitation of the target system and excitation of the projectile system.

All three target nuclei showing large anomalies in table 5.10, $^{26}Mg$, $^{40}Ca$ and $^{24}Mg$, have strongly excited rotational or vibrational states: the first $2^+$ states in $^{24,26}Mg$ and the $3^-$, 3.74 MeV state in $^{40}Ca$. DWBA analyses of some transfer reactions involving such targets have failed in the past and explicit inclusion of the coupling to the excited states has often removed the discrepancies (see [Kov74], [Tam80] or [Hod78] for reviews). However, one should note that most of the problems with DWBA calculations in such cases have taken the form of failure to describe the true shape of the angular distributions rather than failure to predict consistent cross-section magnitudes.

Nevertheless, it was felt important to seek evidence for any inadequacy of the DWBA through a Coupled Channels Born Approximation (CCBA) analysis of $^{26}Mg(^{9}Be,^{9}Be')^{26}Mg^{*}$. A comparison of the results of DW and CC analyses ought to indicate whether the excitation of the $2^{+}$ state was weak enough to be treated as a perturbation, as required by DWBA theory.

A second reason for studying inelastic excitation is to test the optical potentials found in Chapter 4 over a greater radial extent. In this context, a DWBA analysis of $^{40}Ca(^{9}Be,^{9}Be')^{40}Ca^{*}$ has been performed.

Some quantitative calculations have been performed to estimate the effects of inelastic excitation followed by transfer. The magnitude of a two-step process cross-section will be roughly proportional to the product of the cross-sections for each individual step. The contribution of sequential particle transfer, ie. a "coupled reaction channels" process, to the $(^{9}Be,^{10}B)$ reaction can be neglected, since this would involve a two or more particle transfer at some stage. If one of the transitions is a strong inelastic excitation, however, the two-step contribution may be significant. Such effects have been shown to be important for certain heavy-ion transfer reactions. In a study of the $^{26}Mg(^{13}C,^{12}C)$ and $^{26}Mg(^{13}C,^{14}C)$ reactions at low bombarding energies, Sinclair et al. demonstrated that for transitions from $j_{<}$ ($j = \ell - \frac{1}{2}$) to $j_{>}$ ($j = \ell + \frac{1}{2}$), or vice versa, inelastic effects are negligible, but for transitions of the form $j_{<}$ to $j_{<}$, inelastic excitation followed by a $j_{<}$ to $j_{>}$ transition makes a significant contribution to the cross-sections ([Sin76], [Cha76]).

A proper treatment of this problem for the ($^{9}$Be,$^{10}$B) reaction would involve an exact finite-range CCBA analysis. A no-recoil CCBA analysis, which was carried out by Sinclair et al., was not feasible here since the no-recoil approximation is known to give inaccurate cross-section magnitude estimates for heavy-ion transfer [Tam80] and this is the very thing that we are concerned with. Although exact finite-range CCBA computer codes do exist and have on a few occasions been applied to heavy-ion transfer studies, (see [Tam80] for a review), there is the difficulty that the optical potentials found from DWBA analyses of elastic scattering are no longer valid, and have to be be researched. Instead, a finite-range two-step code has been used here to estimate the effects of inelastic excitation followed by transfer, i.e. only one-way coupling has been considered. This is a better approximation than one might think at first, since the complex optical potential that fits the elastic scattering data must already take into account some of the coupling to inelastic channels. More specifically, this "effective" potential implicitly includes (albeit in an approximate manner) all the processes illustrated in fig. 6.1a when a DWBA calculation is performed. The routes omitted are shown schematically in fig. 6.1b. These routes may be approximately taken into account by the two-step calculation represented in fig. 6.1c, where the omitted routes are calculated explicitly but the coupling is one-way only. Such calculations have been performed by Rae [Rae76] for various single-nucleon transfer reactions on $^{12}$C, with some degree of success. The anomalous $^{11}$C*(2.00 MeV) results previously mentioned in Chapter 5 (section 5.2.7) were covered in this treatment, but the inclusion of the two-step inelastic excitation failed to resolve the discrepancies in spectroscopic factors.

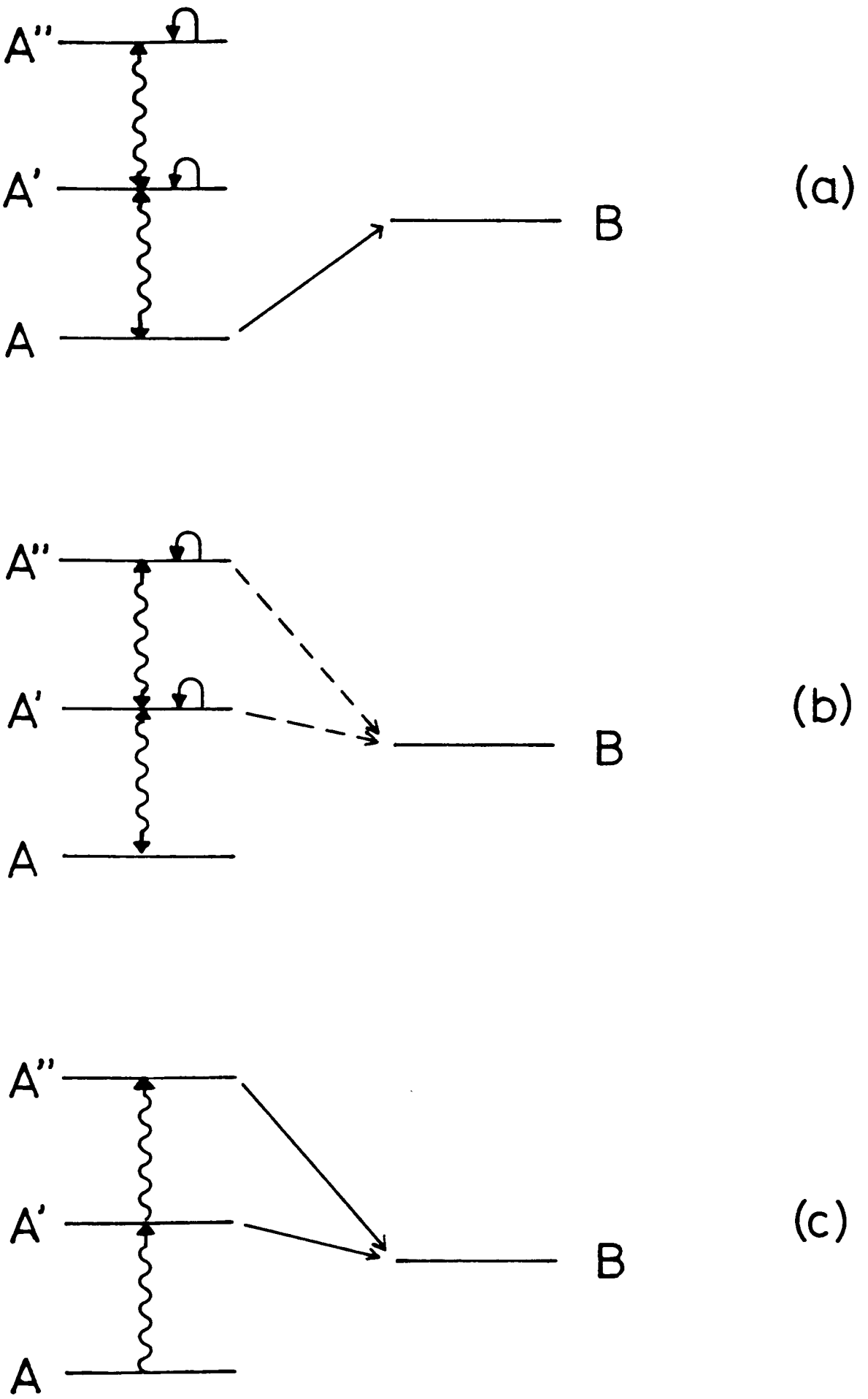


Fig. 6.1 (a) routes implicitly included,

(b) routes omitted,

(c) approximate calculation of omitted routes.

## 6.2 Inelastic Scattering Analysis.

The inelastic scattering data for $^{26}Mg$ and $^{40}Ca$ are shown in figs. 6.2 and 6.3 respectively. The oscillations in the angular distribution for the $2^+$, 1.81 MeV state in $^{26}Mg$ are roughly in antiphase to those in the elastic scattering distribution, as expected from the Blair phase rule [Bla60].

The DWBA analysis was performed with the computer code DWUCK [Kun68]. A complex, derivative, collective form factor was used. This was:

$$F_L(r) = F_L^N(r) + F_L^C(r),$$

$$F_L^N(r) = \beta_L^N\left(V.\frac{R_V}{a_V}.\frac{df}{dr} + iW.\frac{R_W}{a_W}.\frac{dg}{dr}\right)$$

$$F_L^C(r) = \frac{eZ_A 4\pi\sqrt{B(EL)}}{2L+1}.r^{-(L+1)} \qquad r > R_C$$

$$= 0, \qquad r < R_C$$

where f and g are Woods-Saxon potentials with geometries defined in the usual way by V, $R_V$, $a_V$, etc., as for equation 4.1. This is applicable to both rotational excitation of deformed nuclei and vibrational excitation of spherical nuclei. In the above, $\beta_L^N$ is the deformation parameter (or "coupling" parameter if a CC analysis is being performed). If the Coulomb excitation is negligible, $\beta_L^N$ is determined by normalizing the calculated cross-section to the data via

$$\left(\frac{d\sigma}{d\Omega}\right)^L = (\beta_L^N)^2 |\langle J_A L K0 | J_B K\rangle|^2 \sigma_{DW}^L. \qquad (6.1)$$

For $^9Be$ scattering, Coulomb excitation is small but not entirely

negligible (this is shown later by comparing calculations with and without the Coulomb term included). The normalization is then obtained through the fact that the deformation length $\beta^N R$ of the matter distribution is similar to that of the charge distribution, $\beta_C R_C$, [Hod78] which in turn may be related to the reduced transition probability

$$B(EL)\uparrow = \left(\frac{3}{4\pi}.Ze\right)^2 (R_C^L \beta_L)^2. \qquad (6.2)$$

Then, with the appropriate normalizing factor for Coulomb excitation, equation 6.1 may still be used to find $\beta_L^N$.

The results of the DWBA analysis for the $^{26}Mg$ $2^+$ excitation are given in fig. 6.2 and table 6.1. Potentials BEM1 and BEM2 of table 4.2 have been used (in both the form factor and the distorted wave calculation). It is seen that the use of potential BEM1 gives a better fit to the data than BEM2 and also gives a value of $\beta_2$ in close agreement with the values of 0.29 found by Blair and Naqib [Bla70] in a DWBA analysis of $^{26}Mg(\alpha,\alpha')^{26}Mg$ and $0.28 \pm 0.01$ found by Rebel et al. [Reb72] in a CC analysis of the same reaction at 104 MeV.

Table 6.1 $^{26}Mg$ DWBA Inelastic Scattering Results.

| | Including Coulomb Ex. | | Without Coulomb Ex. | |
|---|---|---|---|---|
| Potential | $\beta_2$ | $\chi^2$ | $\beta_2$ | $\chi^2$ |
| BEM1 | 0.30 | 2.9 | 0.33 | 3.4 |
| BEM2 | 0.17 | 11.1 | 0.20 | 4.6 |

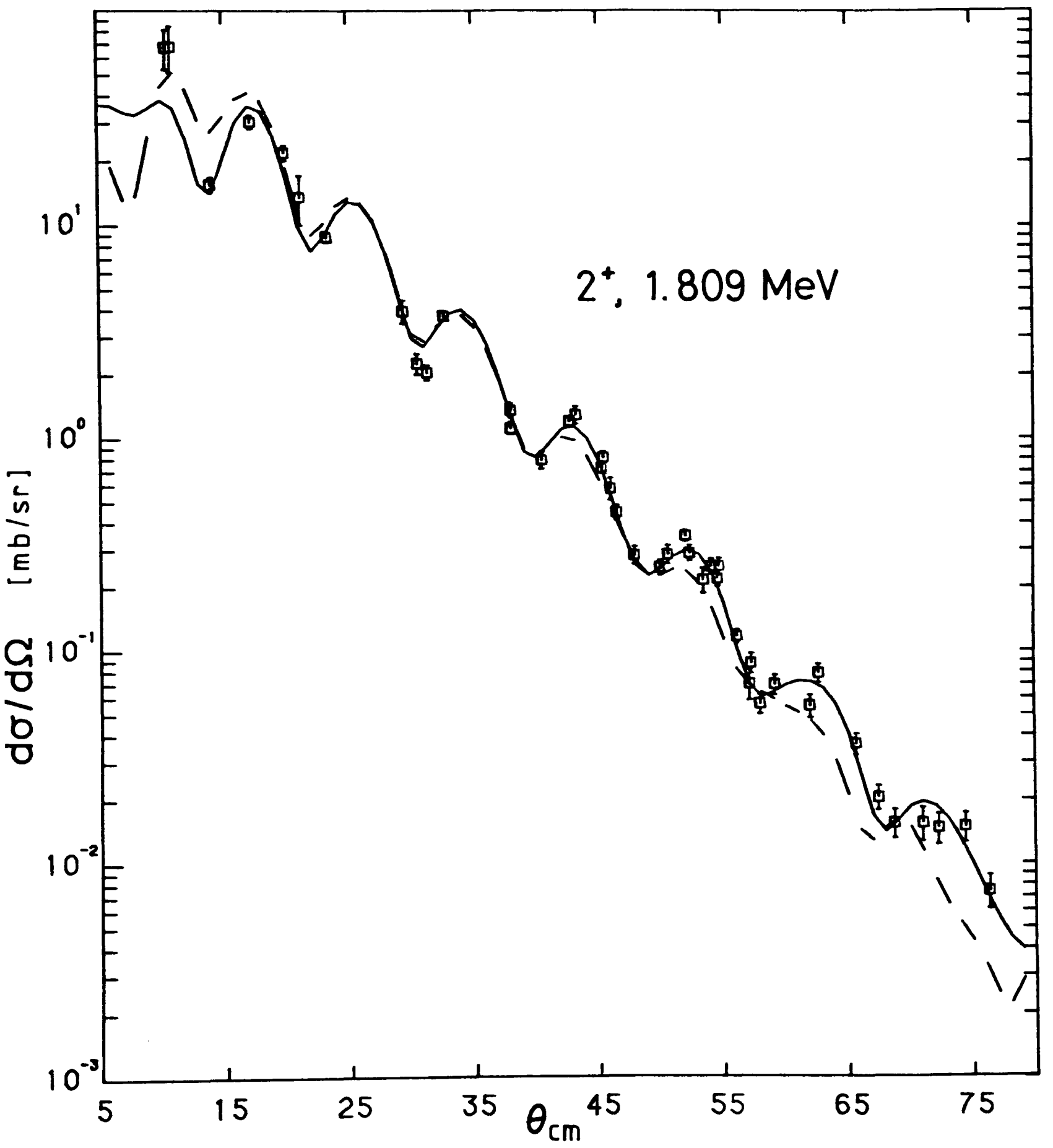


Fig. 6.2 Data and DWBA angular distribution for the inelastic excitation of $^{26}$Mg. Solid curve: potential BEM1, dashed curve: potential BEM2.

Results obtained with other projectiles, however, differ significantly from these values: for example, 0.4 found for $^{26}Mg(p,p')^{26}Mg$ [Her76]. This is because the size of the projectile contributes to the value of $\beta$ [Tho77] and should really be unfolded before comparisons are made. Potential BEM2 has a very large Coulomb radius parameter ($R_c$ = 6.81 fm$^{\dagger}$) which appears to be responsible for the poor quality of the fit to the data (compare values of $\chi^2$ with and without Coulomb excitation). Even without Coulomb excitation, the value of $\beta_2$ with this potential is low, and we conclude that BEM2 is unreliable (which agrees with the findings of section 5.2.1).

The angular distributions from the DWBA analysis of the $^{40}Ca$ octupole excitation are displayed in fig. 6.3. Clearly, potential BECA gives a better account of the data: potential ECK80 produces a distribution which is too oscillatory although the overall gradient is correct. Similar results were found for the elastic scattering analysis in section 4.4. The derived values of $\beta_3$ are presented in table 6.2. The deformation parameters and lengths are rather low compared to light-ion values, especially those for ECK80; representative light-ion results are $\beta_3$ = 0.24, $\delta_3$ = 1.36 fm obtained for $^{40}Ca(\alpha,\alpha')^{40}Ca$ by Lippincott and Bernstein [Lip67].

---

$^{\dagger}$ Note that the elastic scattering analysis was not sensitive to the choice of this parameter.

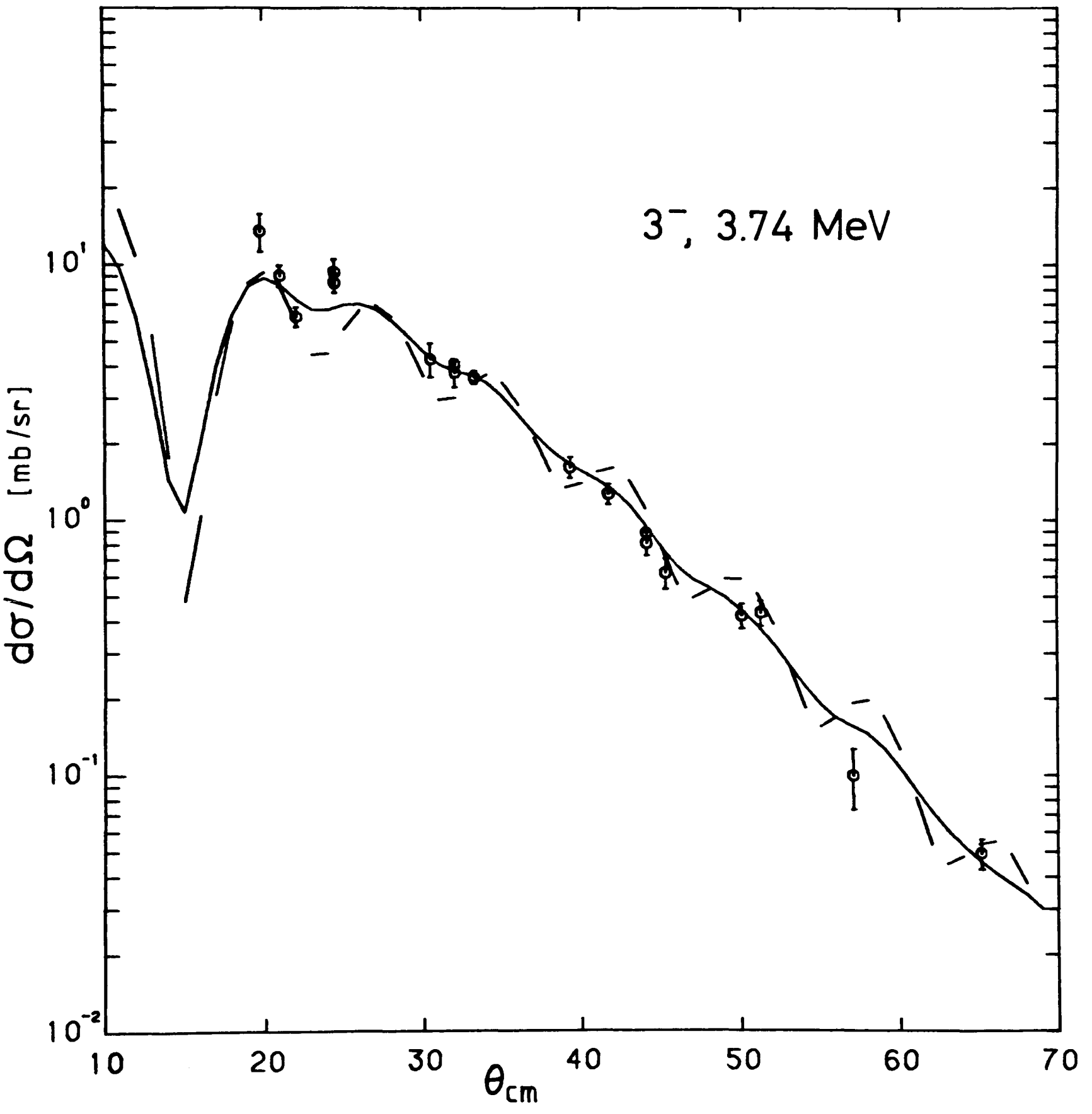


Fig. 6.3 Data and DWBA angular distribution for the inelastic excitation of $^{40}Ca$. Solid curve: potential BECA, dashed curve: potential ECK80.

Table 6.2 $^{40}$Ca DWBA Inelastic Scattering Results.

(Coulomb Ex. included)

| Potential | $\beta_3$ | $\chi^2$ | $\delta_3 = R\beta_3$ (fm) |
|---|---|---|---|
| BECA | 0.15 | 2.3 | 1.07 |
| ECK80 | 0.12 | 12.1 | 0.86 |

We now turn to the CCBA analysis of $^{26}$Mg($^{9}$Be,$^{9}$Be)$^{26}$Mg. The calculations were performed with the code CHUCK [Kun68]. Couplings between the $0^+$ and $2^+$ states were the only ones considered. The lack of strength to the $4^+$ state (fig. 2.2) suggests that explicit inclusion of this state would not significantly alter the results, also, it is noted that Woods [Woo81] has successfully analysed $^{26}$Mg($^{6}$Li,$^{6}$Li)$^{26}$Mg by including only $0^+$-$2^+$ coupling. Reorientation terms for the $2^+$ state were included as was Coulomb excitation.

Calculations were commenced with the DWBA potential BEM1. As expected from the discussion in section 6.1, the potential parameters needed to be adjusted in order to give a reasonable fit to both the elastic and inelastic data once the coupling was explicitly included. A version of CHUCK was used that minimized the $\chi^2$ of the fit to both $0^+$ and $2^+$ states simultaneously. The results are plotted in fig. 6.4 and the final potential is given in table 6.3, where the DWBA potential is repeated for ease of comparison. The deformation parameter (or coupling constant) was initially 0.30. This too was allowed to vary, but it remained stable at 0.29. It is seen that the CCBA potential has a smaller real diffuseness but extends out to a larger radius. The final fits to both elastic and inelastic scattering data are worse by a factor

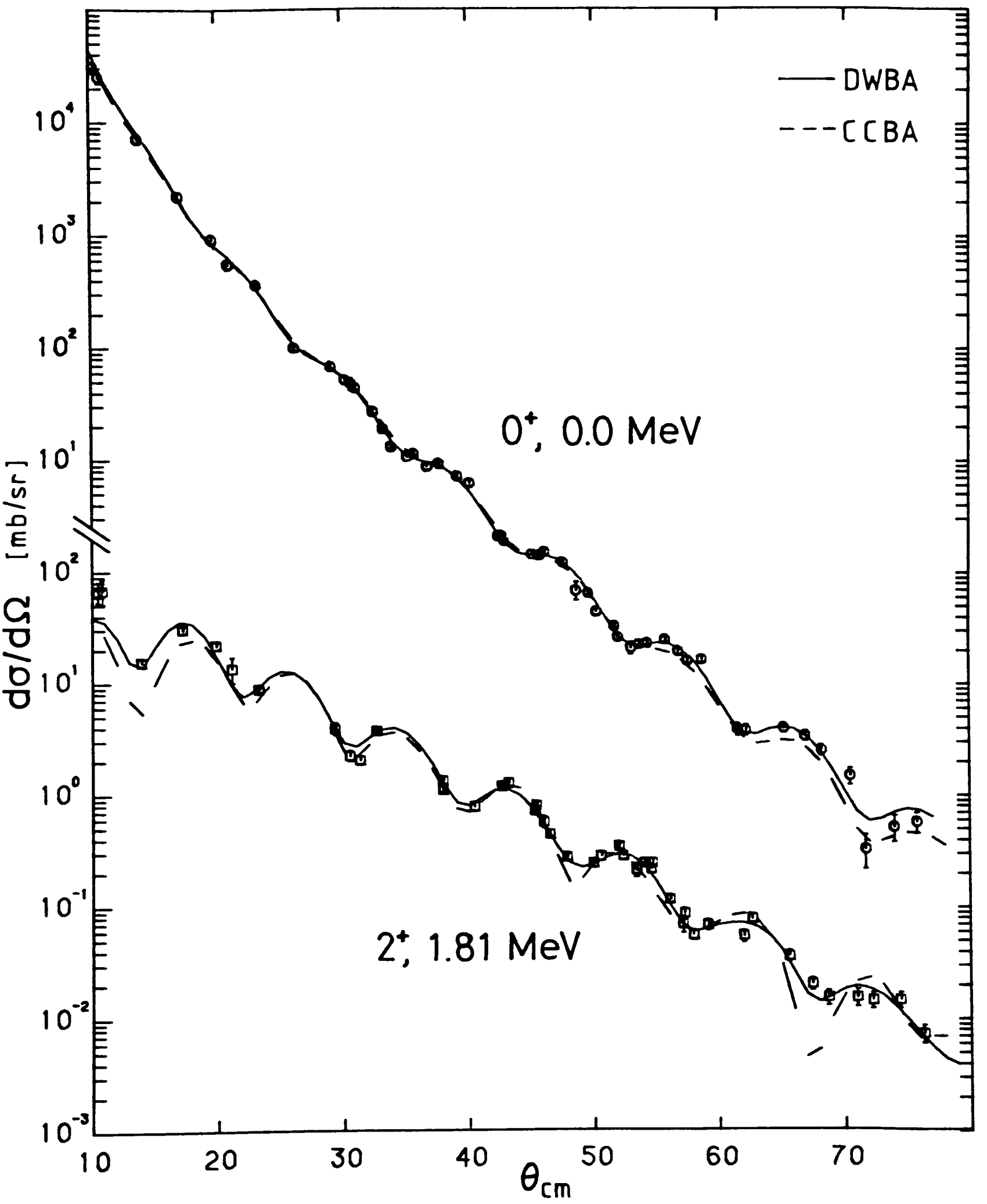


Fig. 6.4 Comparison of DWBA and CCBA analyses of $^{9}$Be elastic and inelastic scattering from $^{26}$Mg.

Table 6.3

(i) CCBA & DWBA Searched Potentials for $^{26}Mg(^{9}Be,^{9}Be)^{26}Mg$.

| Label | V(MeV) | $a_v$(fm) | $r_v$(fm) | W(MeV) | $a_w$(fm) | $r_w$(fm) | $r_c$(fm) |
|---|---|---|---|---|---|---|---|
| BEM1 | 69.8 | 0.820 | 0.9476 | 130.6 | 0.796 | 0.9065 | 0.788† |
| (CC) | 74.9 | 0.616 | 1.0616 | 131.5 | 0.880 | 0.8049 | 0.731 |
| Difference | 7% | -33% | 11% | 1% | 10% | -13% | -8% |

†) parameter not searched.

(ii) Values of Reduced Chi-squared for above potentials.

| Label | $\chi^2_{el}$ | $\chi^2_{inel}$ |
|---|---|---|
| BEM1 | 2.4 | 2.9 |
| (CC) | 4.6 | 7.0 |

of two in $\chi^2$ compared to the DWBA results, which may be because the searching routine finished in a local minimum. Some arbitrary adjustments were made to the final potential parameters and searching recommenced but no better fit could be found. Since the DWBA fits to the data were very good in any case, one would have been surprised to find improvement.

If all the optical parameters had changed by small amounts, ( < 10%, say), it would suggest that a DWBA treatment of the reaction was adequate. However, the real diffuseness parameter, $a_v$, did change by 33%. On the other hand, this alone is probably not sufficient evidence to say that the coupling is too strong for a DWBA analysis. Hence the result of this analysis is inconclusive. A more satisfactory way to decide whether such coupling effects are important is to perform calculations like the one described below for $^{9}Be^{*}$.

## 6.3 Two-step Calculation for Projectile Excitation.

One of the reasons that attention was concentrated on the projectile-ejectile system was that many other heavy-ion reactions on the same target nuclei as used in the present experiments had shown no similar anomaly to $^{10}B_0/^{10}B_1$. Examples of $(^{6}Li,^{7}Be_{0,1})$ have been given in Chapter 5. At the time that work on the two-step calculations began, values of AF for only the $^{26}Mg$ and $^{40}Ca$ targets were known. The sign of AF for these targets suggested a j-dependent effect such that the anomaly could be removed if the relative $p_{1/2}$ or $p_{3/2}$ transfer contributions to $(^{9}Be,^{10}B_1)$ were altered.

An inspection of the tabulated experimental values of B(E2) transition strengths in $^{9}$Be and $^{10}$B [End79] singled out the $3/2^{-}$, 0.0 MeV to $5/2^{-}$, 2.43 MeV transition in $^{9}$Be as the most likely to produce a significant effect on the direct-transfer cross-section (see table 6.4). The specific routes considered are discussed later.

The calculations were performed after modifications to allow for inelastic scattering were made to the exact finite-range code SESIME which is normally used for sequential particle transfer. These modifications involved: (i) writing an inelastic scattering form factor code with output compatible with the DWBA program MARS in no-recoil mode; (ii) amending the transition amplitude normalization as appropriate for inelastic excitation; (iii) changes to the DWBA "overlap" integral calculation such that the finite-range form factor is made radially in step with the preceding inelastic excitation integrals. This was carried out in the spirit of maintaining standard input files for the code.

The modified code was tested as follows. Firstly, one-step inelastic scattering calculations were compared with those from DWUCK and found to agree. Secondly, double inelastic excitation calculations were compared with those from CHUCK. Here there was a discrepancy of about 15% between the magnitudes of the cross-sections although the shapes were identical; the actual value of the discrepancy varied slightly with projectile energy. This point is not pursued here because it is small compared with the magnitude of cross-section required to give an appreciable final effect.

Table 6.4

Some B(E2)↑ Values for $^{9}Be$ & $^{10}B$.

All values are in $e^2fm^4$, and are either taken from [End79] or calculated by the Oxford Shell Model Code.

(i) From $^{9}Be$ $3/2^-$ ground state

| $J^\pi$, Ex(MeV) | [End79] | OSMC |
|---|---|---|
| → $5/2^-$, 2.43 | 40.4 | 32.1 |
| → $1/2^-$, 2.8 | - | <0.01 |
| → $7/2^-$, 6.76 | 17.4 | |

(ii) From $^{10}B$ $3^+$ ground state

| | | |
|---|---|---|
| → $1^+$, 0.72 | 1.8 | 3.0 |
| → $1^+$, 2.15 | 0.6 | |
| → $2^+$, 3.59 | 0.6 | |

Finally, three test calculations for

$$^{3}He + ^{19}F \rightarrow d + ^{20}Ne(3^{+},10.9\ MeV) \rightarrow d + ^{20}Ne(2^{+},9.5\ MeV)$$

were compared. These were performed using SESIME where the transfer was calculated both with exact and no-recoil finite-range options and CHUCK (which is a zero-range form factor code). The two-step cross-section for the no-recoil calculation was ~25% lower than the zero-range one, but the discrepancy between the zero-range and exact finite range was less than half of this - presumably because of a fortuitous cancellation of errors. Again, a detailed analysis of this was not attempted.

Calculations were performed for $^{26}Mg(^{9}Be,^{10}B)^{25}Na$ and $^{40}Ca(^{9}Be,^{10}B)^{39}K$. For each target nucleus, six routes were considered: these are illustrated schematically in fig. 6.5.

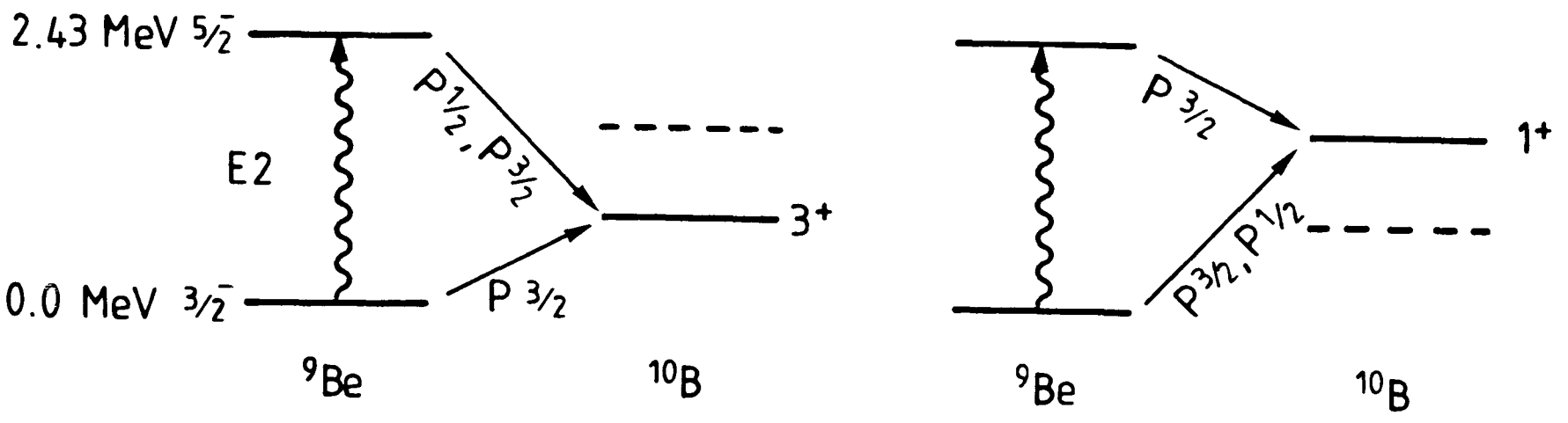


Fig. 6.5 Projectile excitation routes considered in the two-step calculation.

At the end of the calculations, the transition amplitudes for these were

added together after multiplication by the light system spectroscopic factors, and also by $\beta_2$ for the inelastic transition, where appropriate. The total cross-section was then calculated. The values of $\sqrt{S_b}$, obtained through the Oxford Shell Model Code with the (8-16)POT interaction, were:

$$S_b^{\frac{1}{2}}\{^9Be(5/2^-) + 0p_{3/2} \rightarrow {}^{10}B(3^+)\} = 0.92,$$
$$S_b^{\frac{1}{2}}\{^9Be(5/2^-) + 0p_{1/2} \rightarrow {}^{10}B(1^+)\} = -0.24,$$
$$S_b^{\frac{1}{2}}\{^9Be(5/2^-) + 0p_{3/2} \rightarrow {}^{10}B(1^+)\} = 0.12$$

The coupling parameter, $\beta_2$, was determined from equation 6.2 to be 0.9, after insertion of the B(E2) value from Endt (table 6.4). This is a remarkably high value of $\beta_2$, which would, strictly speaking, require a more sophisticated treatment of the inelastic scattering form factor than the one described in section 6.2. We are here concerned more with its use as a coupling parameter and not with any measure of deformation. In the absence of any other value for this parameter, it was felt that a reasonable estimation of the size of second-order processes could still be made (see also discussion below regarding the incoherent addition of amplitudes).

The partial and total cross-sections, multiplied by $C_b^2 S_b$ and $\beta_2^2$, are shown in figs. 6.6 ($^{26}Mg$) and 6.7 ($^{40}Ca$). The shapes of the angular distributions are unaffected by the inclusion of the two-step processes. Although the total cross-sections were found by adding transition amplitudes, it can be seen from the figures that virtually the same result would follow if the contributing cross-sections were incoherently added. In fact, the amplitude of a two-step process involving inelastic excitation can be shown to be approximately 90° out of phase with the direct amplitude [Mad80]. Thus there is little interference between

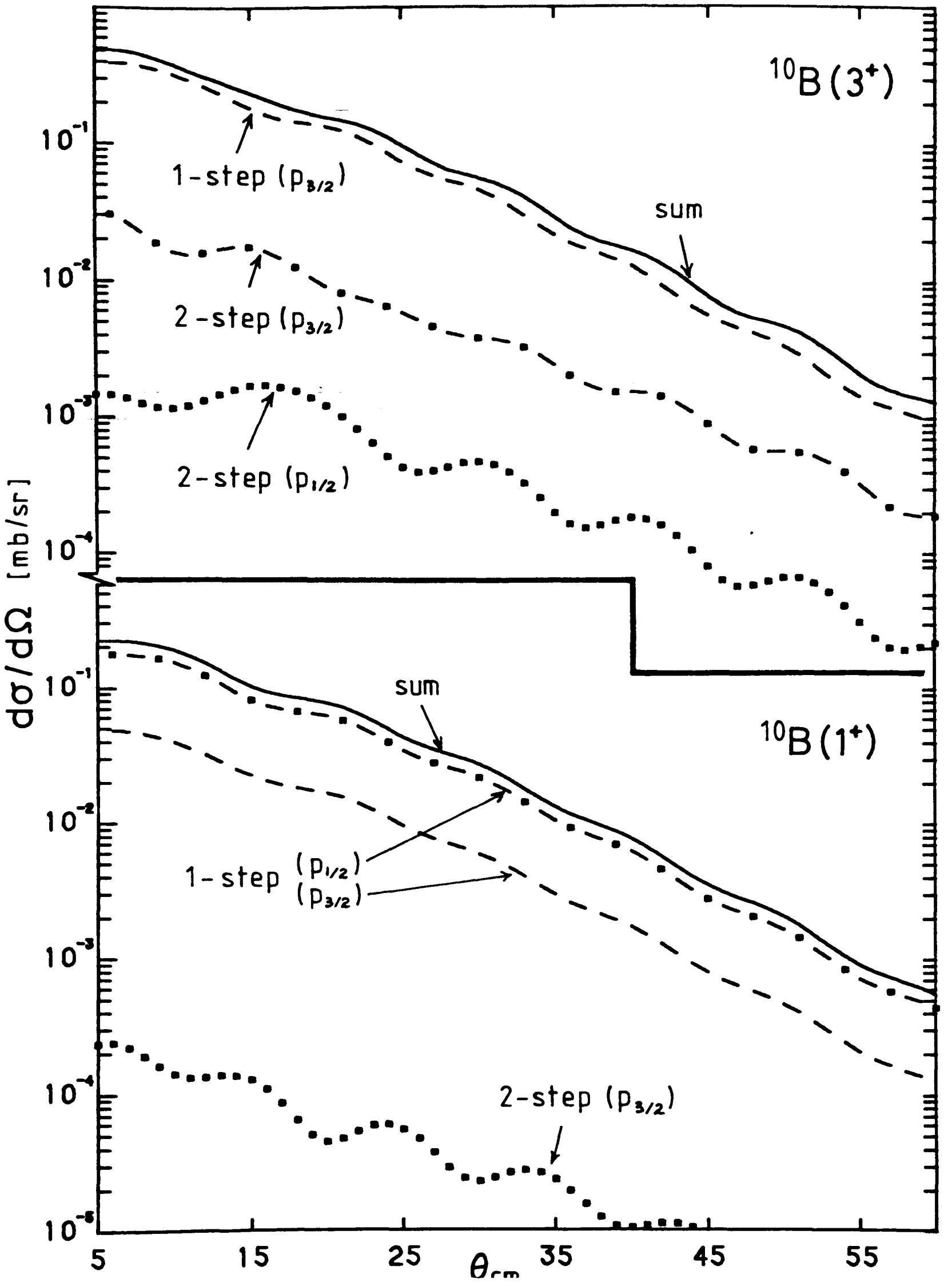


Fig. 6.6 Direct and two-step contributions to $^{26}Mg(^{9}Be,^{10}B_{0,1})^{25}Na$.

these processes. Figs. 6.6 and 6.7 also show that the only significant contribution from the two-step process is from the $p_{3/2}$ transfer to $^{10}B(3^+)$, which is mostly a consequence of the values of $S_b$ given above.

Normalization of the total cross-section to the data gave values for the target system spectroscopic factor in the usual way. The net effect of the points made above is that the $^{10}B_0/^{10}B_1$ anomaly is reduced from AF = 43% to AF = 17% when $^{26}Mg$ is the target, but made worse when $^{40}Ca$ is the target (AF changed from -47% to -61%). The magnitude of the changes is encouragingly large; the problem is that it acts in the same direction for both targets. This is not necessarily so for all such two-step routes: a route that gave more emphasis to the transfer of a $p_{1/2}$ proton to the ground state of $^{10}B$ would affect the $^{40}Ca$ case less than the $^{26}Mg$ one, owing to the $j_>-j_<$ factor. Whilst no $^9Be$ or $^{10}B$ ground state transition exists with as large a B(E2) value as large as the one considered, effects comparable in magnitude to the quantitative result here may still be obtained, since interference can occur between different two-step route amplitudes. It is also possible that a route with a more moderate value for $\beta$ may be compensated by a larger value of $C_b^2S_b$ in the particle transfer. Thus the conclusions drawn from this calculation are by no means negative.

## 6.4 Summary of Attempts to Account for the $^{10}B_0/^{10}B_1$ Anomaly and Conclusions.

Three approaches have been made in an effort to understand the anomaly shown in table 5.10.

(i) The bound state description for $^{10}B(3^+)$ and $^{10}B(1^+)$ has been changed

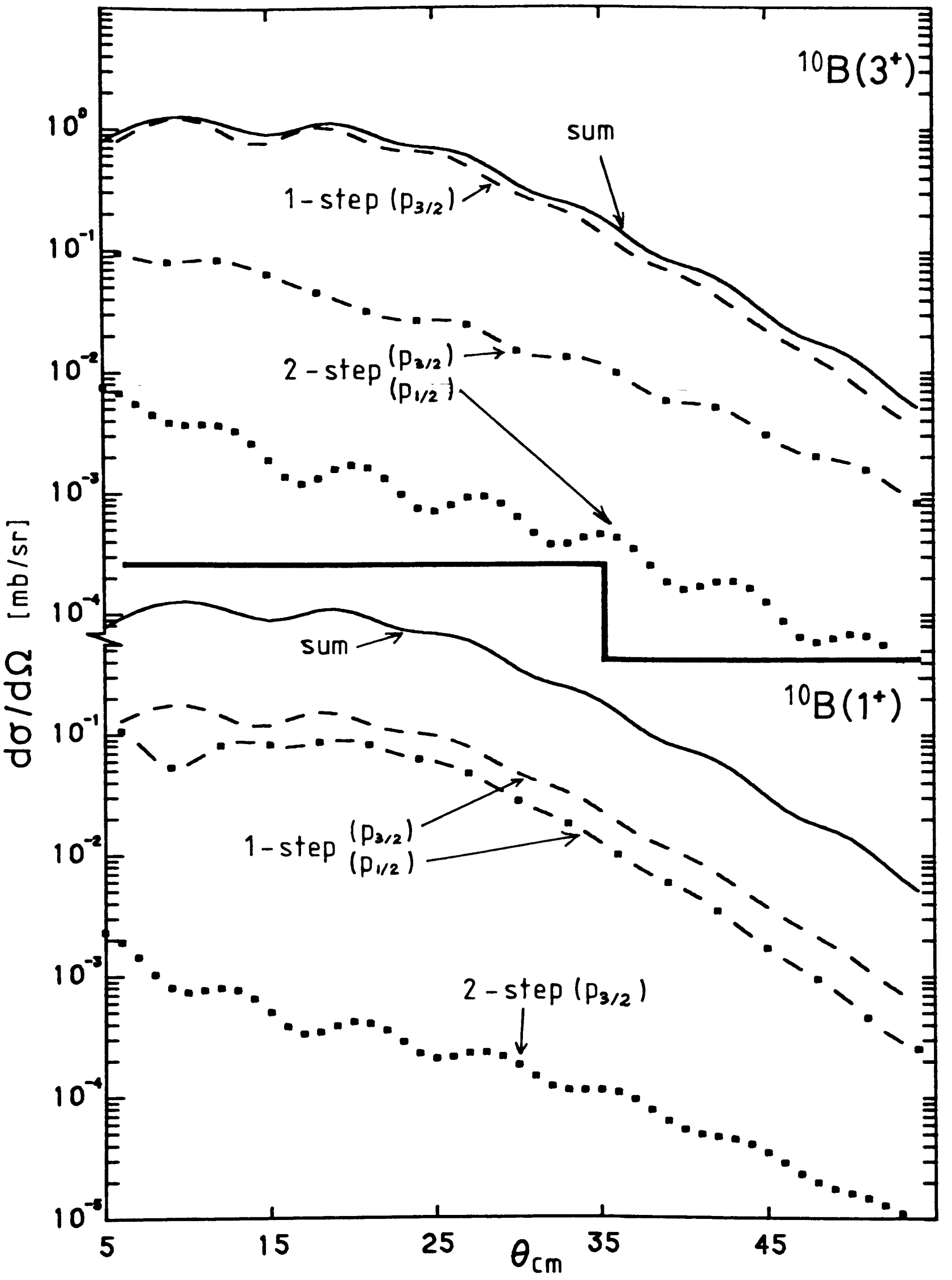


Fig. 6.7 Direct and two-step contributions to $^{40}Ca(^{9}Be,^{10}B_{0,1})^{39}K$.

both together and separately. This has made a difference to the values of AF, but one which has the same sign for all targets. Similar results were obtained for alterations to the optical potential parameters in the distorted wave calculation - these were intended to simulate different deformations of $^{10}B$.

(ii) Alternative spectroscopic factors in the description of $^{9}Be + p \rightarrow {}^{10}B$ have been tried in place of the standard Cohen and Kurath values (although no strong justification for this was found). The anomaly for $^{26}Mg$ and $^{40}Ca$ could be made less severe, but only at the expense of making it worse for other targets.

(iii) Consideration of a two-step route through inelastic excitation of $^{9}Be$ showed a sizeable (~20%) effect, but again it had the same sign for both $^{26}Mg$ and $^{40}Ca$.

Satchler warns of "the danger of merely invoking multistep processes in an ad hoc fashion in order to explain away some inconvenient experimental results" [Sat80]. Yet for the anomaly under consideration, a thorough discussion about other phenomena within the one-step framework has been carried out. It is emphasized that only the comprehensive nature of the data presented here, covering many different target nuclei, has lead to the rejection of some hypotheses.

In this chapter, some indirect processes have been considered. Since the largest anomalies occur for $^{24,26}Mg$ and $^{40}Ca$, it is natural to suspect that coupling to excited states in these targets must be included explicitly here, either through a full CCBA calculation or through a two-step process of inelastic excitation followed by transfer. The amount by which such processes might affect the spectroscopic factors extracted from different states in $^{10}B$ cannot be discussed

adequately without some quantitative results, but one can suggest a $j_<-j_>$ mechanism for such routes as illustrated schematically in fig. 6.8.

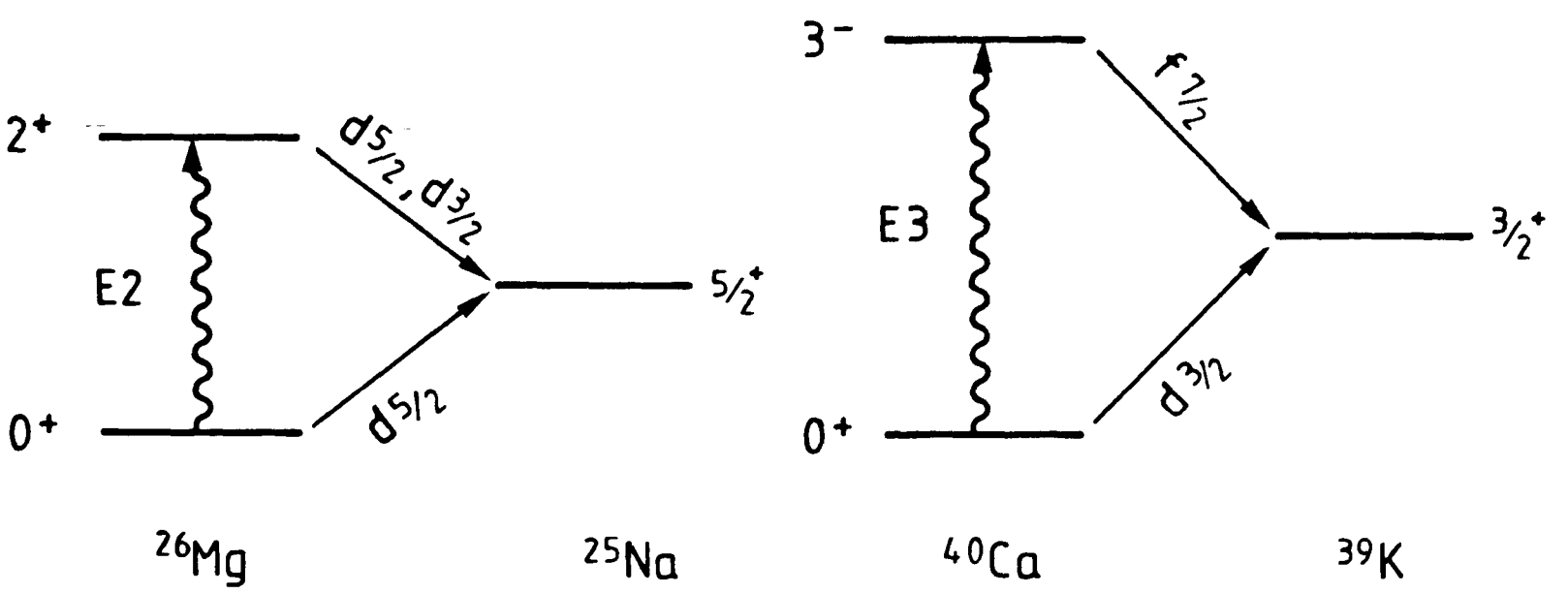


Fig. 6.8 Two-step routes through target excitation.

A two-step calculation was not attempted for these cases because no spectroscopic information for transfer from the excited states was available. It is noted, however, that the coupling parameters for these states are considerably weaker than the one used in the $^{9}$Be calculation and it is the square of this that multiplies the inelastic excitation cross-section. Thus it would be surprising if the anomaly could be accounted for by these two-step routes alone.

Another reason to believe that the projectile system is important in the understanding of the anomaly is the large breakup cross-section of $^{9}$Be, which has been mentioned in Chapter 1 as the probable cause behind the failure of the double-folding model's description of $^{9}$Be

scattering. This is very pertinent, since it indicates strong coupling to states in the projectile and may therefore render inadequate the DWBA treatment of the reaction. In a study of ($^{9}$Be,$^{8}$Be) at E($^{9}$Be) = 50 MeV, Stahel et al. measured the peak breakup cross-section of $^{9}$Be on $^{28}$Si to be greater than 30 mb/sr, and that for $^{40}$Ca and $^{208}$Pb to be roughly 60 and 10 mb/sr respectively [Sta77]. These are not only substantial cross-sections, but ones that depend on the target nucleus in an interesting way. The ($^{9}$Be,$^{10}$B) experiments reported here showed a slightly greater anomaly for lower projectile energy, and hence for interactions further from the nuclear field, but it is difficult to draw any conclusions from this in view of the additional fact that the target which gave the most consistent DWBA results was the heaviest, $^{54}$Fe. Werle et al. [Wer73] have investigated the sequential breakup of $^{9}$Be at energies below the Coulomb barrier, and have found that three intermediate states were important: $1/2^{+}$, $5/2^{-}$ and $5/2^{+}$. The E2 transition to the $5/2^{-}$ state is the one which was considered in section 6.3. We can speculate that in the scattering off different target nuclei, these "breakup channels" are populated by differing amounts.

This is argued in the following manner: the $^{9}$Be projectile will be distorted as it approaches the target nucleus and the extent of distortion will depend on the nuclear charge of the target (if the Coulomb field is important) or the diffuseness of the nuclear field. The deformation may be considered to be an excitation of various vibrational states in the projectile. Then the transfer probability is governed by the spectroscopic amplitude between the excited $^{9}$Be state and the $^{10}$B state in question. This amplitude depends on the nuclear structure of $^{9}$Be and $^{10}$B and is therefore not dependent in a simple

manner on the degree of deformation. This provides a mechanism that would account for an anomaly which seems to vary with target nucleus in a far from obvious way. Unfortunately, this has to remain a speculation (at least as far as the present work is concerned) because the $1/2^+$ and $5/2^+$ states in $^{9}$Be cannot be described in the p-shell basis and hence the spectroscopic amplitudes necessary for an estimation of the effect are not readily obtainable. Although the above provides an explanation of the anomaly, the data from $^{24,26}$Mg and $^{40}$Ca suggest that a complete description should also include target as well as projectile excitation.

Finally, it should be said that although the extent of the present data is wide-ranging, it would still be interesting to study other mass regions or perhaps the sd-shell in more detail. Further mass or energy systematics may help to shed light on the anomaly. $^{208}$Pb is often considered a good choice for spectroscopic study since it is a doubly-magic nucleus. The ($^{9}$Be,$^{10}$B) reaction on this target would need rather higher beam energies than are currently available at Oxford if the Coulomb barrier is to be surmounted, but it remains an attractive proposition for the future.

# APPENDIX A

## Application of DWBA Theory to Single-Nucleon Transfer

### A.1 Distorted Wave T-Matrix for Direct Reactions.

In this section the formulae for the transition amplitude in a non-relativistic nuclear reaction are derived. In the interests of simplification, Coulomb forces have been neglected. The notation follows that of Austern [Aus70], where the detailed derivation may be found.

Consider a beam of particles, denoted by "a", impinging on a target "A" with momentum $\underline{k}_\alpha$. The system a + A is the incident channel $\alpha$, and we are concerned with final channels $\beta$ that are also two-particle systems. We begin by writing the Schrödinger equation for the stationary state wavefunction, $\Psi^+$, that describes the nuclei in the asymptotic region (i.e. a large distance away from the interaction):

$$H\,\Psi^+(\underline{k}_\alpha) = E\,\Psi^+(\underline{k}_\alpha) \qquad (A.1)$$

(the superscript "+" indicates that the wavefunction has been chosen with all the scattered waves radially outgoing). The asymptotic form of the wavefunction is

$$\Psi^+(\underline{k}_\alpha) = \psi_\alpha \exp(i\underline{k}_\alpha.\underline{r}_\alpha) + \sum_\beta \psi_\beta f(\underline{k}_\alpha,\hat{\underline{r}}_\beta) r_\beta^{-1} \exp(ik_\beta r_\beta) \qquad (A.2)$$

The coefficient $f(\underline{k}_\alpha,\hat{\underline{r}}_\beta)$ is the scattering amplitude for channel $\beta$. It is a function of the scattering angle, as indicated by the unit vector.

The differential cross-section for the reaction $\alpha \to \beta$ is the ratio of the outgoing flux in channel $\beta$ to the ingoing flux in channel $\alpha$ and is given by basic scattering theory as

$$\frac{v_\alpha}{v_\beta} |f(\underline{k}_\alpha, \hat{\underline{r}}_\beta)|^2$$

where the velocity $v$ is defined by $v = \hbar k/\mu$ ($\mu$ is the reduced mass of the system).

To calculate the asymptotic wavefunction in channel $\beta$, equation A.1 is projected thus:

$$(\psi_\beta, H\Psi^+) = E(\psi_\beta, \Psi^+) \qquad (A.3)$$

where the scalar product notation indicates integration over the internal variables of $\psi_\beta$ only. Now a kinetic energy operator, $T_\beta$, and potential energy operator, $V_\beta$, are defined in terms of the "channel-radius" variable $\underline{r}_\beta$ which is the displacement between the centres of mass of b and B (see fig. A.1):

$$\underline{r}_\beta = \frac{1}{n_b} \sum_{i=1}^{n_b} \underline{r}_i - \frac{1}{n_B} \sum_{i=n_b+1}^{n_b+n_B} \underline{r}_i, \qquad (A.4)$$

($n_b$ denotes the number of nucleons in b, etc.),

$$T_\beta = \frac{-\hbar^2}{2\mu_\beta} \nabla^2_{\underline{r}_\beta}, \qquad (A.5)$$

and

$$V_\beta = \sum_{\substack{i=1,2,\ldots,n_b \\ j=n_b+1,\ldots,n_b+n_B}} V(i,j) \qquad (A.6)$$

(i.e. the sum of all the interactions which are not internal to b or B).

Then, after substituting $H = T_\beta + V_\beta$, equation A.3 can be reduced to

$$\{T_\beta - E\}(\psi_\beta, \Psi^+) = -(\psi_\beta, V_\beta \Psi^+) \qquad (A.7)$$
$$= \{T_\beta - E\}\xi_\beta(\underline{r}_\beta).$$

We now introduce the distorting potential, $U_\beta(r_\beta)$ into equation A.7:

$$\{T_\beta + U_\beta - E\}\xi_\beta = -(\psi_\beta, [V_\beta - U_\beta]\Psi^+). \qquad (A.8)$$

$U_\beta$ is a function of the magnitude of the channel-radius variable only. A suitable choice of $U_\beta$ greatly simplifies the computation of the transition amplitude as we will see later.

The stationary state eigenfunctions of the LHS of A.8 are defined as:

$$\{T_\beta + U_\beta - E\}\chi_\beta^+(\underline{k}_\beta, \underline{r}_\beta) = 0, \qquad (A.9)$$

such that, asymptotically,

$$\chi_\beta^+ \rightarrow \exp(i\underline{k}_\beta . \underline{r}_\beta) + \text{outgoing scattered waves.} \qquad (A.10)$$

A solution for $\xi_\beta$ may be found from equation A.8 using Green's functions techniques [Aus70]. This leads to a generalized expression for the transition amplitude, $T_{\alpha\beta}$:

$$T_{\alpha\beta} = T^0_{\alpha\alpha}\delta_{\alpha\beta} + (\chi^-_\beta \psi_\beta, [V_\beta - U_\beta]\Psi^+). \qquad (A.11)$$

Apart from the use of the stationary state wavefunction, which has not been justified, no approximations are made in the derivation of this T-matrix. The use of the stationary state wavefunction is discussed by Austern [Aus70] who shows that this is a very reasonable assumption when the dimensions of a typical scattering experiment are considered.

We are now ready to take the particular case of direct reactions (DI) of the form

$$a + A \rightarrow b + B.$$

The stationary state wavefunction may be expanded so:

$$\Psi^{+}_{DI} = \sum_{\gamma} \psi_c \psi_C \xi_\gamma (\underline{r}_\gamma), \qquad (A.12)$$

where the sum is over all channels $\gamma = c + C$. Substitution in A.11 yields

$$T^{DI}_{\alpha\beta} = (\psi_b \psi_B \chi_\beta^{-}, [V_\beta - U_\beta] . \sum_{\gamma} \psi_c \psi_C \xi (\underline{r}_\gamma)), \qquad (A.13)$$

(the term that describes elastic scattering has been omitted). Equation A.13 is known as the post form of the reaction amplitude because it is based on the interaction in the exit channel ($\beta$). Alternative expressions are obtained if the wavefunction of the time-reversed reaction is projected on the entrance channel:

$$T^{DI}_{\alpha\beta} = (\sum_{\gamma} \psi_c \psi_C \xi^{-} (\underline{r}_\gamma), [V_\alpha - U_\alpha] \psi_a \psi_A \chi_\alpha^{+}). \qquad (A.14)$$

This form of the transition amplitude is known as the prior form.

A.2 The Distorted Wave Born Approximation.

For practical purposes it is necessary to use approximations in the calculation of A.13 or A.14. The most general approximate method used to obtain $T_{\alpha\beta}$ is that of the "distorted wave Born approximation". This method emphasises the role played by the entrance channel. We refer here to the post form of the interaction - a parallel derivation follows for the prior form.

First, A.13 is rewritten in two parts, splitting off the term with $\gamma = \alpha$:

$$T^{DI}_{\alpha\beta} = (\psi_b \psi_B \chi_\beta^{-}, [V_\beta - U_\beta] \psi_a \psi_A \xi (\underline{r}_\alpha)) + (\psi_b \psi_B \chi_\beta^{-}, [V_\beta - U_\beta] . \sum_{\gamma \neq \alpha} \psi_c \psi_C \xi (\underline{r}_\gamma)), \qquad (A.15)$$

A.15 is still invariant to the choice of distorting potential, $U_\beta$.

Now the approximations are made: the second line of A.15 is dropped, (hence the expansion of $T_{\alpha\beta}$ is apparently first order or "Born"), and in the first line, $\xi_\alpha$ is approximated by $\chi_\alpha^+(\underline{r}_\alpha)$ - hence "distorted wave approximation". We are left with

$$T_{\alpha\beta}^{DWBA} = (\psi_b\psi_B\chi_\beta^-,\ [V_\beta - U_\beta]\psi_a\psi_A\chi_\alpha^+). \qquad (A.16)$$

$T_{\alpha\beta}^{DWBA}$ is <u>not</u> invariant to the choice of $U_\beta$; therefore it only yields accurate results if $U_\beta$ is chosen correctly.

The second of the above approximations, namely

$$\xi_\alpha(\underline{r}_\alpha) \approx \chi_\alpha^+(\underline{r}_\alpha) \qquad (A.17)$$

is probably rather accurate. Both these functions predict the same elastic scattering in channel $\alpha$ (compare equations A.2 and A.10), so they must be identical outside the nucleus. This is not necessarily true inside the nucleus because of exchange contributions to the elastic scattering which are neglected in $\chi_\alpha^+$, and because of uncertainties in the optical potential form from which $\chi_\alpha^+$ is calculated [Aus70]. However, neither of these effects are likely to be large owing to strong absorption in the nuclear interior.

The omission of the second line of A.15 is a more difficult approximation to justify. Even if the contributions of the excited channels are significantly weaker than the elastic channel, we can ignore them only if the resultant error is minimized by judicious choice of $U_\beta$. The optical potential that fits the elastic scattering in channel $\beta$ is almost always selected. To see why, we note that one of the largest contributors to the second line of A.15 is probably the term with $\gamma = \beta$. This contribution is

$$(\psi_b\psi_B\chi_\beta^-,\ [V_\beta - U_\beta]\psi_b\psi_B\xi_\beta) = \int d^3r_\beta \chi_\beta^{-*}\{\langle bB|V_\beta|bB\rangle - U_\beta\}\xi_\beta \qquad (A.18)$$

where the bra-ket notation indicates integration over only the internal

coordinates of $\psi_b$ and $\psi_B$ (inside the bracket, these wavefunctions have been abbreviated to 'b' and 'B' respectively). If $U_\beta$ in A.18 is the optical potential that describes elastic scattering in channel $\beta$, $\langle bB|V_\beta|bB\rangle$ is approximately cancelled in the integrand. This choice of $U_\beta$ also has the practical advantage that it can be determined from experiment.

It is important to realise, however, that the expression in A.16 is still only an approximation to A.13: the optical potential for channel $\beta$ is not quite identical to $\langle bB|V_\beta|bB\rangle$ since it is affected by the coupling to other channels, and besides, it is not clear how the use of $U_\beta$ would affect the terms of A.15 that have $\gamma \neq \beta$ (eg. channels coupled to the initial or final states by inelastic excitation).

The accuracy of the approximation is improved if the excitation of other channels is small - in other words, if the Born approximation is valid. It seems clear, though, that this method is better than first order if the optical potential used is $U_\beta$, since it implicitly contains a rough account of these additional couplings in its imaginary part. For this reason, some authors prefer to call the method simply "the Distorted Wave Approximation".

We should also comment upon the validity of using a potential that is a simple function of the separation of the colliding pair's centres. This concept might seem unreasonable, especially for heavy-ion reactions where the true overlapping wavefunctions represent a many-body problem. However, due to strong absorption and Coulomb repulsion, these reactions tend to be peripheral and thus take place where the two nuclear densities overlap very little. Therefore we have good reason to believe

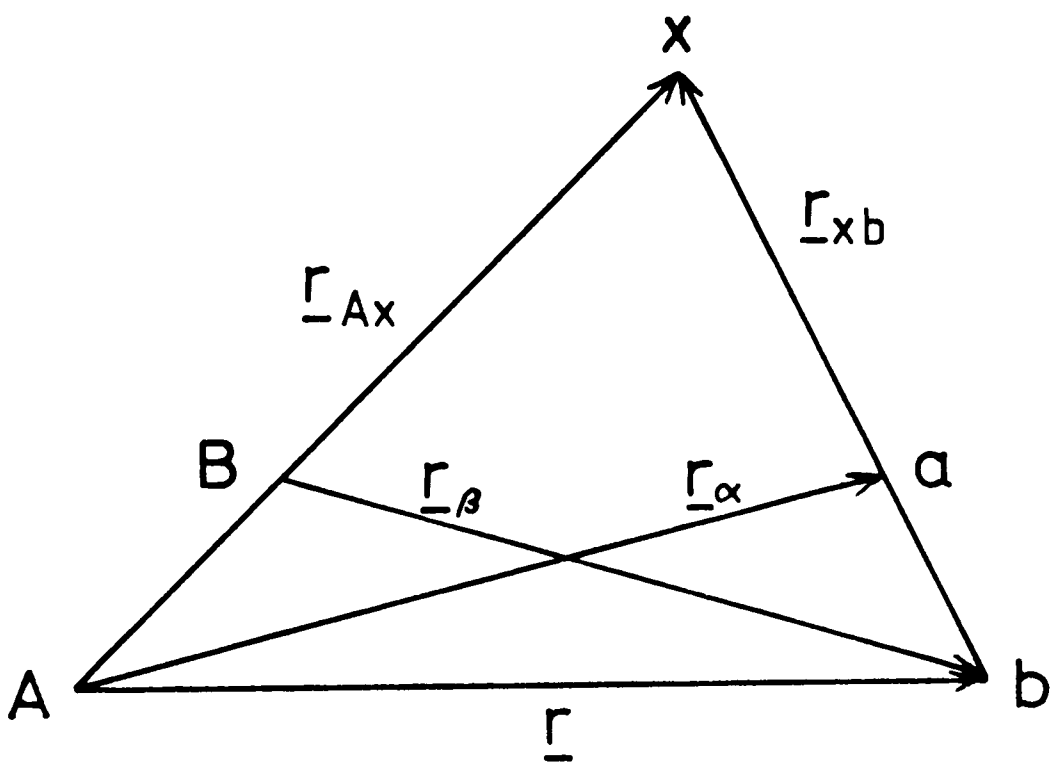


Stripping

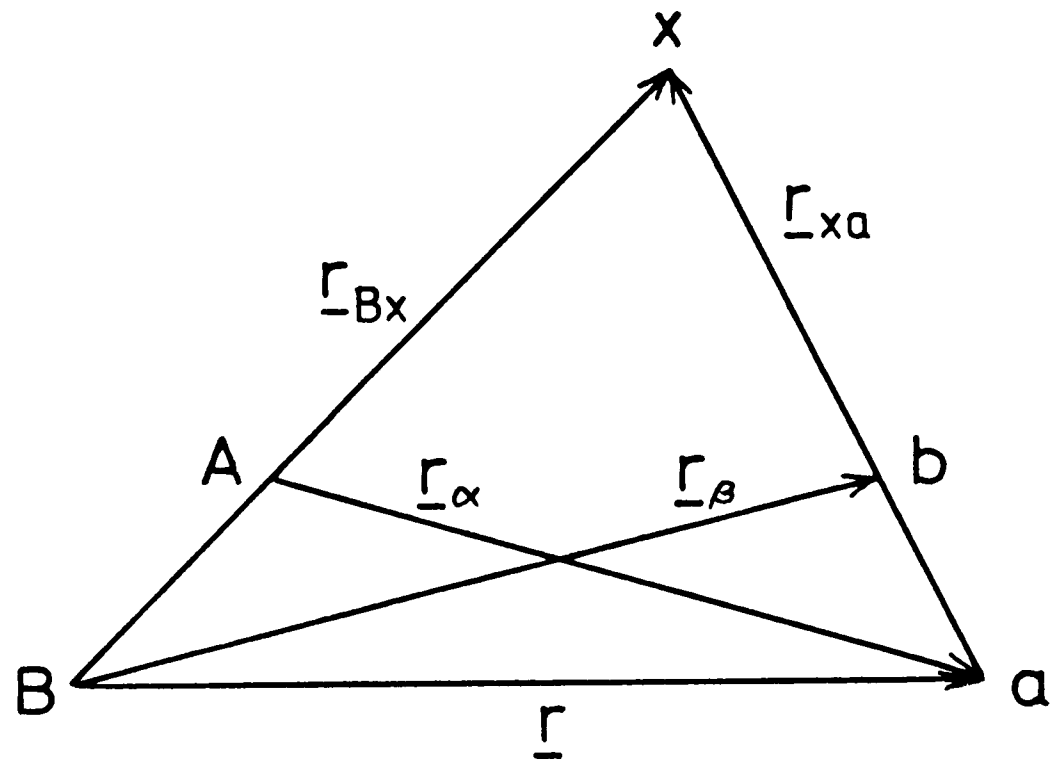


Pickup

Fig. A.1 Coordinate system for single nucleon transfer.

that a simple potential concept will work [Sat74].

The DWBA transition amplitude may be rewritten with the integration over the spatial coordinates displayed as:

$$T_{\alpha\beta}^{DWBA} = J\int d^3\underline{r}_\alpha \int d^3\underline{r}_\beta \; \chi_\beta^{-*}(\underline{k}_\beta,\underline{r}_\beta)\langle Bb|V|Aa\rangle\chi_\alpha^{+}(\underline{k}_\alpha,\underline{r}_\alpha) \qquad (A.19)$$

where J is the Jacobian of the transformation from the natural coordinates $(\underline{r}_{Ax},\underline{r}_\beta)$ to $(\underline{r}_\alpha,\underline{r}_\beta)$ where $\underline{r}_{Ax}$ is the coordinate of the transferred particle with respect to A (fig. A.1). The matrix element in A.19 is taken between the internal states of the particles:

$$\langle Bb|V|Aa\rangle = \langle\psi_B\psi_b|V_\beta - U_\beta|\psi_A\psi_a\rangle.$$

This matrix element contains all the nuclear structure information while the distorted waves treat the reaction dynamics.

The prior form of A.19 is derived from A.14 and differs from A.19 only in that $(V_\beta - U_\beta)$ is replaced by $(V_\alpha - U_\alpha)$.

## A.3 Explicit Form of the Interaction Matrix.

We now concentrate on single-nucleon pickup reactions, i.e. those of the form A(a,b)B where A = B + x, b = a + x. The interaction V in equation A.19 contains three nuclear terms:

$$V_N(post) = V_{aB} + V_{xB} - U_{bB}$$

$$V_N(prior) = V_{aB} + V_{xa} - U_{aA},$$

where U is an optical potential. There are also three corresponding Coulomb terms in the complete interaction, which are usually neglected because of their smallness (as was done for the work described in this thesis). DeVries et al. have shown that this neglect can lead to

significant post-prior discrepancies for heavy-ion reactions on targets with high atomic numbers (they investigated $^{88}Sr(^{16}O,^{15}N)$ and $^{208}Pb(^{11}B,^{10}Be)$) and have also shown that the spectroscopic factors deduced from heavy-ion reactions at low energy (less than about 1.5 times the Coulomb barrier) may begin to differ from light-ion ones unless the Coulomb terms are included [DeV74]. It is noted in Chapter 5 that the post-prior discrepancy in $^{40}Ca(^{9}Be,^{10}B)^{39}K$ was less than 26% and the effect of the Coulomb terms have been shown to be unimportant for the $^{16}O(^{6}Li,^{7}Be)$ reaction at 36 MeV [Woo81].

If the prior representation is adopted, the nuclear interaction $V_{aB}$ is assumed to cancel with $U_{aA}$, leaving only the interaction $V_{xa}$ between the transferred nucleon and the smaller of the two cores. Similarly, in the post representation the term $V_{xB}$ only is kept in the transition matrix element. The prior representation is usually chosen for pickup reactions because the interaction $V_{xa}$ is considered to be better known than $V_{xB}$ and because $V_{aB}$ and $U_{aA}$ cancel more exactly than $V_{aB}$ and $U_{bB}$. Parallel arguments are used to show that the post representation is better for stripping reactions. However, the difference between potentials describing the interactions of a or b with the residual nucleus decreases as the projectile mass increases. Therefore the advantages of the prior compared to the post form are less pronounced for heavy-ion pickup reactions.

Since the optical potential is assumed to cancel with an interaction term, it does not explicitly occur in the calculation of the transition amplitude. It affects the T-matrix elements by determining the distorted waves, $\chi$.

# APPENDIX B

## Improved Form Factor Calculation

An improvement on both the popular "well-depth" method of form factor calculation and the simple use of a shell-model wavefunction [She65] has been suggested by Rae [Rae82] as a development of the procedure discussed by Austern [Aus77]. The purpose of this appendix is not a rigorous derivation of the method but an attempt to show why it is physically "reasonable".

In the "well depth" prescription, the radial part of the bound state wavefunction, $\mathcal{R}_{lj}^{AB}$, for a particle with quantum numbers $l$, j transferred from nucleus A to nucleus B is calculated by solving the Schrödinger equation

$$[E_B - E_A - T - V(r)]\mathcal{R}_{lj}^{AB}(r) = 0. \qquad (B.1)$$

Here $E_B$ and $E_A$ are the binding energies of nuclei B and A, T is the radial kinetic energy operator and V(r) is a potential whose depth is adjusted independently for each form factor. The problem with form factors generated through equation B.1 is that residual interactions between particles outside the core have been neglected (we can see that this would be a too simple description of a nucleon incident upon the core at energies <u>above</u> threshold). The exact form factor equation is

$$[E_B - E_A - T - U_l(r)]\mathcal{R}_{lj}^{AB}(r) = P^{AB}(r)$$

[Aus77] where $U_l(r)$ is the single-particle shell model potential and $P^{AB}$, the inhomogeneous or "source" term, accounts for residual interactions.

By analogy with the coupled-equations form of the Schrödinger equation for scattering by a potential, this can be written

$$[E_B - E_A - T - U_\ell(r)]\mathcal{R}^{AB}_{l_j}(r) = \sum_\alpha P'_\alpha(r)\mathcal{R}^\alpha(r). \qquad (B.2)$$

Pinkston and Satchler [Pin65] propose the solution of this equation by iteration after assuming that, to zero order in the coupling, $P'_\alpha(r)$ can be taken as a multiple of shell model basis functions with undetermined coefficients. A more convenient approach for the purposes of calculation is described here.

First we assume that $P'_\alpha(r)$ is proportional to dU/dr with strength $\beta_\alpha$ - the form of this seems reasonable by analogy with a first order inelastic scattering expansion. This gives

$$[E_B - E_A - T - U_\ell(r)]\mathcal{R}^{AB}_{l_j}(r) = \sum_\alpha \beta_\alpha \frac{dU}{dr}\mathcal{R}^\alpha(r) \qquad (B.3)$$

In order to evaluate this, we must further assume that all the radial functions on the right hand side are proportional to $\mathcal{R}^{AB}_{l_j}(r)$, that is

$$\mathcal{R}^\alpha(r) \approx \mathcal{R}^{AB}_{l_j}(r)\times c(\alpha)/c(AB),$$

where the c's are coefficients of fractional parentage (compare equation (19) of [Pin65]). Then equation B.3 is uncoupled:

$$[E_B - E_A - T - U_\ell(r) - N.\frac{dU}{dr}]\mathcal{R}^{AB}_{l_j}(r) = 0 \qquad (B.4)$$

(N is an arbitrary normalization factor).

Comparing this with equation B.1, we see that the "well depth" method's potential V has become the shell model potential $U_\ell$ and an additional, surface-peaked potential has been introduced. This is important because in practice it allows us to keep $U_\ell(r)$ <u>fixed</u> whilst the depth of the surface-peaked potential is varied until the correct eigenenergy, $E_B - E_A$, is obtained. At small r, this has no effect and

the nuclear interior is properly described. At large r, where $U_\ell$ and N.dU/dr are negligible, equations B.4 and B.1 reduce to

$$[E_B - E_A - T]\mathcal{R}^{AB}_{lj}(r) = 0,$$

with the required asymptotic solution

$$\mathcal{R}^{AB}_{lj}(r) \underset{r\to\infty}{\sim} \exp(-kr)$$

where $k^2 = 2m(E_B - E_A)/\hbar^2$. Coulomb effects have been ignored here, but the same conclusion follows if they are included.

The remaining task is the proper normalization of $\mathcal{R}^{AB}_{lj}(r)$. This may be achieved by requiring the overlap of $\mathcal{R}^{AB}_{lj}(r)$ with the pure shell-model wavefunction to be the spectroscopic factor [Aus70], but it is more convenient to divide $\mathcal{R}^{AB}_{lj}(r)$ by $C^2S$ and normalize to unity. Then the spectroscopic factor appears as a multiplying factor to the theoretical cross-section (see equation 5.1 in Chapter 5). The requirement is

$$\int \Psi(r)\,\mathcal{R}^{AB}_{lj}(r)\,r^2dr = 1, \qquad \text{(B.5)}$$

for a correctly normalized $\mathcal{R}^{AB}_{lj}(r)$, where $\Psi(r)$ is a solution of

$$[\varepsilon - T - U_\ell]\Psi(r) = 0.$$

The implementation of this procedure in the existing form factor code SATURN has already been mentioned in section 5.1.3. The calculation proceeds as follows. The user inputs the geometry of the derivative potential and an initial value for the depth, together with the experimental separation energy for the transferred particle. The program contains the fixed, shell-model potential parameters - the ones from ref. [Ber72] quoted in section 5.1.3. The searching routine in the code that serves the "well depth" prescription has been adapted to vary the depth of the derivative potential until the eigenenergy is equal to the input separation energy, whilst the depth of the volume potential is

kept fixed. One can view the sum of the derivative and volume potential as another well of approximately Woods-Saxon shape but with a new well radius (see fig. B.1).

The wavefunction (not yet normalized) is then temporarily stored and a further calculation is performed to find $\Psi(r)$, the shell-model wavefunction. This is done by using the fixed Bertsch parameters in the volume Woods-Saxon well, but without a derivative potential. This time the eigenenergy is varied to finish at some energy $\varepsilon \neq (E_B - E_A)$. The normalization of $\mathcal{R}_{ij}^{\alpha\beta}(r)$ is then found through equation B.5, where the numerical integration is carried out by the NAG library routine D01GAF.

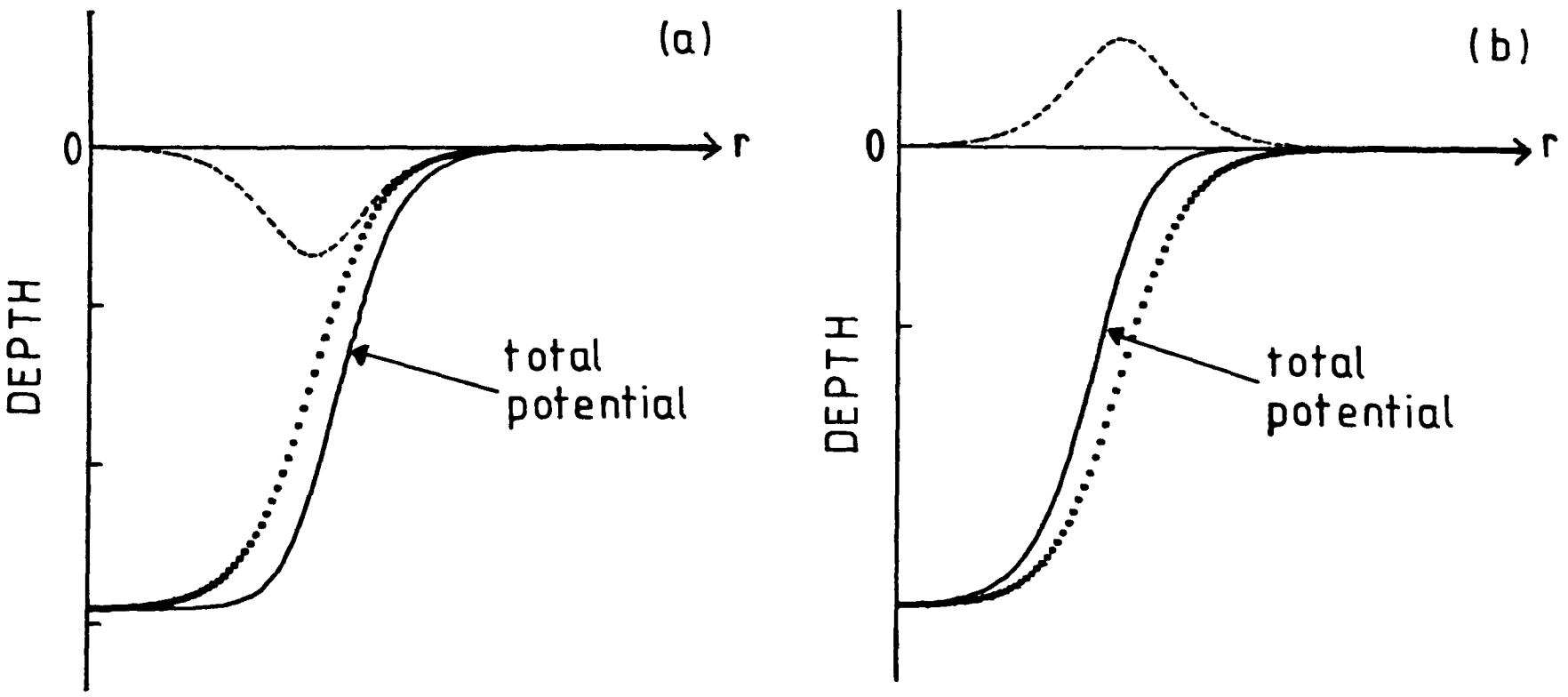


Fig. B.1 Result of adding (a) an attractive, and (b) a repulsive, surface-peaked potential to a volume Woods-Saxon well. The relative magnitudes of the volume and surface-peaked potentials are representative of those found in the ($^{10}B$,$^{9}Be$) calculations described in Chapter 5, section 5.3.

# APPENDIX C

## Energy Resolution of Beams from the Accelerator

A discussion of the energy resolution of the beams received from the Oxford Folded Tandem follows. When analysing resolution tests of the spectrometer's focal plane detector it is important to know what contribution to the observed width of the peaks arises from the beam quality and, in general, to be assured that this contribution is small.

The object and entrance slits to the 90° analysing magnet at the base of the accelerator are often regarded as the elements that define the spread in momentum (or energy) of the extracted beam. This is indeed so if the entrance slits to the magnet are illuminated by a wide beam (i.e. one that extends beyond the slit aperture) containing a broad spectrum of particle momenta. The Oxford Folded Tandem analysing magnet, in common with most other designs, is double-focussing with object and image at twice the radius. In this case the energy resolution geometrically imposed by the slits is [Eng67]

$$\frac{\delta E}{E} = \frac{s_1 + s_2}{2r}, \qquad (C.1)$$

where $s_1$ and $s_2$ are the apertures of the object and image slits and r is the radius of the bending magnet (r = 183 cm for the Oxford Folded Tandem).

The assumptions above, however, do not hold for the experiments described in this thesis. This is made clear when numbers are inserted for the beam used in the position resolution tests of the spectrometer and its detector: putting $s_1$ = 8 mm, $s_2$ = 2.5 mm and E = 27 MeV in equation C.1 gives $\delta E$ = 77.5 keV. The observed resolution of the scattered beam at the focal plane of the spectrometer was under 9 keV (section 3.6.4).

The magnet slits do not usually define the beam: most of the beam is contained within an envelope smaller than the slit apertures. Only the "tails" of the beam profile strike the slits (the slit readings can then be used to stabilize the accelerator's terminal voltage). The beam quality (i.e. by how much it varies in energy) is partly determined by fluctuations in the accelerating voltage and partly by energy-loss differences and straggling in the carbon stripper foil near the positive terminal of the tandem. Terminal voltage fluctuations have been observed to be less than about 1 kV [Hyd83]. Energy-loss straggling and differences can be calculated in a similar manner to that used in section 2.4 (the non-uniformity of the stripper foils is difficult to estimate but may be taken as great as 20% without significantly affecting the total energy spread).

The method of production of the beryllium beam introduces an additional factor which turns out to dominate the other contributions mentioned above. Beryllium is injected into the accelerator in the form of $BeH^-$. This molecular-ion is accelerated up to the positive terminal of the tandem and enters the stripper foil, whereupon its electrons are very rapidly removed. The stripping process occurs so quickly that the $Be^{4+}$ and $H^+$ ions momentarily remain placed apart at the original bond

length, $a_0$. The electrostatic repulsion of these ions causes them to fly apart with a release of potential energy in the c.m. frame equal to $Q.q.e^2/a_0$, where Q and q are the charges on the ions. This is known as a "Coulomb Explosion" [Gro82]. The resulting change in energy of the $^9Be^{4+}$ ion depends on the direction of the proton's motion in the c.m. frame. The spread in energy is, to first order,

$$\delta E_{max} \simeq 2\sqrt{\{E_i(\mu/m)Q.q.(e^2/a_0)\}} \qquad (C.2)$$

[Gro82] where $E_i$ is the initial kinetic energy of the molecular-ion, $\mu$ is the reduced mass and m is the mass of the final fragment. Insertion of values for 9 MeV $^9BeH^-$ ions, and taking an estimate of 1 Å for $a_0$ as a typical length of a bond between hydrogen and a light element, gives $\delta E_{max} \simeq 13$ keV. This is much larger than the bond energy, $Q.q.e^2/a_0 \simeq 50$ eV, showing that the accelerator acts as a kind of amplifier in this context.

Estimates of the energy spread contributions to some beams used in experiments are now given. A nominal stripper foil thickness of 5 $\mu g/cm^2$ is assumed.

27 MeV $^4$He beam

| | |
|---|---|
| Terminal voltage instabilities | 3 keV |
| Energy-loss straggling in stripper | 0.4 keV |
| Stripper foil non-uniformity (20%) | 0.6 keV |
| added in quadrature | 3.1 keV |

43 MeV $^{9}$Be beam

| | |
|---|---|
| Terminal voltage instabilities | 5 keV |
| Energy-loss straggling in stripper | 3 keV |
| Stripper foil non-uniformity (20%) | 4 keV |
| Coulomb Explosion (equation C.2) | 13 keV |
| added in quadrature | 15 keV |

The result of adding all the contributions in quadrature is also given. Strictly speaking, this is not a valid procedure since the shape of the individual energy-spread distributions are not likely to be Gaussian. The number merely serves as a rough guide for comparisons with other sources of resolution broadening in the experiments.

## References.


[All80] W.W.M.Allison and P.A.Le Bas, computer program FISH (unpublished).

[Ama76] H.Amakawa and K.-I.Kubo, Nucl. Phys. A266 (1976) 521.

[Art68] K.P.Artemov, V.Z.Gol'berg, V.P.Rudakov and I.N.Serikov, Sov. J. Nucl. Phys. 7 (1968) 314.

[Aus70] N.Austin, "Direct Nuclear Reaction Theories" (Wiley, New York, 1970).

[Aus77] N.Austin, Nucl. Phys. A292 (1977) 190.

[Bal77] R.Balzer et al., Nucl. Phys. A293 (1977) 518.

[Ber72] G.F.Bertsch, "The Practitioner's Shell Model" (North-Holland, Amsterdam, 1972).

[Ber77] G.F.Bertsch, J.Borysowicz and H.McManus, Nucl. Phys. A284 (1977) 399.

[Bho82] R.K.Bhowmik, J.S.Winfield and D.G.Lewis, computer program HYBRID (unpublished).

[Bir64] J.B.Birks, "The Theory and Practice of Scintillation Counting" (MacMillan, New York, 1964).

[Bla59] J.S.Blair, Phys. Rev. 115 (1959) 928.

[Bla60] J.S.Blair, G.W.Farwell and D.K.McDaniels, Nucl. Phys. 17 (1960) 641.

[Bla70] J.S.Blair and I.M.Naqib, Phys. Rev. C1 (1970) 569.

[Boh74] S.Bohrmann et al., Jahrbuch, Max Planck Institute, Heidelberg (1974) p102.

[Bon73] P.D.Bond, J.D.Garret, O.Hansen, S.Kahana, M.J.Levine and A.J.Schwartzschild, Phys. Lett. 47B (1973) 231.

[Bor68] C.J.Borkowski and M.K.Kopp, Rev. Sci. Instr. 39 (1968) 1515; IEEE Trans. Nucl. Sci. NS-17 (1970) 340; Rev. Sci. Instr. 46 (1975) 951.

[Bre77] A.Breskin and N.Zwang, Nucl. Instr. Meth. 144 (1977) 609.

[Bri72] D.M.Brink, Phys. Lett. 40B (1972) 37.

[Bro80] B.A.Brown, private communication.

[Bro81] B.A.Brown, computer code DENS (unpublished).

[Bun49] O.Bunemann, T.E.Cranshaw and J.A.Harvey, Can. J. Res. A27 (1949) 191.

[Cha76] B.T.Chait, D.Phil. Thesis, Oxford, 1976.

[Chu76] L.T.Chua, F.D.Becchetti, J.Jänecke and F.D.Milder, Nucl. Phys. A273 (1976) 243.

[Cla71] R.G.Clarkson and N.Jarmie, Comp. Phys. Comm. 2 (1971) 433.

[Coh65] S.Cohen and D.Kurath, Nucl. Phys. A73 (1965) 1.

[Coh67] S.Cohen and D.Kurath, Nucl. Phys. A101 (1967) 1.

[Cur58] S.C.Curran in "Handbuch der Physik" (ed. S.Flugge, Springer-Verlach, Berlin, 1958) Vol. 45.

[DeV73] R.M.DeVries, computer code LOLA (unpublished). A short description is given by DeVries in Phys. Rev. C8 (1973) 951.

[DeV74] R.M.DeVries, G.R.Satchler and J.G.Cramer, Phys. Rev. Lett. 32 (1974) 1377.

[Eck80] J.S.Eck, T.R.Ophel, P.D.Clark and D.C.Weisser, Nucl. Phys. A334 (1980) 519.

[End77] P.M.Endt, Atomic Data and Nucl. Data Tables 19 (1977) 23.

[End79] P.M.Endt, Atomic Data and Nucl. Data Tables 23 (1979) 3.

[Eng67] H.A.Enge, in "Focusing of Charged Particles, Vol.II" (ed. A.Septier, Academic Press, London, 1967).

[Eng79] H.A.Enge, Nucl. Instr. Meth. 162 (1979) 161.

[Ers76] J.R.Erskine, T.H.Braid and J.C.Stoltzfus, Nucl. Instr. Meth. 135 (1976) 67.

[Ers79] J.R.Erskine, Nucl. Instr. Meth. 162 (1979) 371.

[For74] J.L.C.Ford et al., Phys. Rev. C10 (1974) 1429.

[For79] J.L.C.Ford, Nucl. Instr. Meth. 162 (1979) 227.

[Ful58] H.W.Fulbright in "Handbuch der Physik" (ed. S.Flugge, Springer-Verlach, Berlin, 1958) Vol. 45.

[Ful69] G.H.Fuller and V.W.Cohen, Nuclear Data A5 (1969) 433.

[Ful79a] H.W.Fulbright and J.R.Erskine, Nucl. Instr. Meth. 162 (1979) 355.

[Ful79b] H.W.Fulbright, Nucl. Instr. Meth. 162 (1979) 21.

[Ful82] C.B.Fulmer, S.Mukhopadhyay, G.R.Satchler, R.L.Auble, J.B.Ball, F.E.Bertrand, E.E.Gross and D.L.Hensley, Nucl. Phys. A385 (1982) 103.

[Gro82] K.O.Groeneveld, in "Proc. Int. Seminar on High-Energy Ion-Atom Collision Processes, Debrecen" (ed. D.Berenyi and G.Hock; Elsevier Scientific, Amsterdam, 1982).

[Hen74] D.L.Hendrie, in "Nuclear Spectroscopy and reactions" (ed. J.Cerny; Academic Press, New York, 1974). Also D.L.Hendrie, J.R.Meriwether, F.Selph, D.Morris and C.Glasshauser, Bull. Am. Phys. Soc. 15 (1970) 650; and UCRL Annual Report, Univ. of Cal. (1970) 280.

[Her76] M.Herman, A.Marcinkowski, B.Zwieglinski, W.Augustyniak, J.Bielwioz and W.Zych, J. Phys. G 2 (1976) 831.

[Hie67] J.C.Hiebert, E.Newman and R.H.Bassel, Phys. Rev. 154 (1967) 898.

[Hie68] J.C.Hiebert and E.Newman, Nucl. Phys. A113 (1968) 176.

[Hod78] P.E.Hodgson, "Nuclear Heavy-Ion reactions" (Oxford University Press, 1978).

[Hud75] G.M.Hudson, K.W.Kemper, G.E.Moore and M.E.Williams, Phys. Rev. C12 (1975) 474.

[Hur79] J.R.Hurd, D.R.James, J.J.Bevelacqua and L.R.Medsker, Phys. Rev. C20 (1979) 1208.

[Hyd83] H.R.McK.Hyder, private communication.

[Igo58] G.Igo, Phys. Rev. Lett. 1 (1958) 72.

[Jän73] J.Jänecke, Nucl. Phys. A204 (1973) 497.

[Kar76] O.Karban, A.K.Basak, J.B.A.England, G.C.Morrison, J.M.Nelson, S.Roman and G.G.Shute, Nucl. Phys. A269 (1976) 312.

[Kov74] D.G.Kovar, Proc. Int. Conf. on Reactions between Complex Nuclei, Nashville, 1974 (North-Holland, Amsterdam) Vol. 2, p.235.

[Koz68] R.L.Kozub, Phys. Rev. 172 (1968) 1078.

[Krä71] E.Krämer, G.Mairle and G.Kaschl, Nucl. Phys. A165 (1971) 353.

[Kun68] P.D.Kunz, computer codes DWUCK and CHUCK, 1968 (unpublished).

[Lan77] L.D.Landau and E.M.Lifshitz, "Quantum Mechanics", 3rd edn. (Pergamon Press, Oxford, 1977).

[Led78] C.M.Lederer and V.S.Shirley (editors), "Table of Isotopes", 7th edn. (Wiley, New York, 1978).

[Lip67] E.P.Lippincott and A.M.Bernstein, Phys. Rev. 163 (1967) 1170.

[Mac82] D.S.MacMillan and E.F.Redish, Phys. Rev. Lett. 48 (1982) 391.

[Mad80] V.A.Madsen and V.R.Brown, in "The (p,n) Reaction and the Nucleon-Nucleon Force" (ed. C.D.Goodman, S.M.Austin, S.D.Bloom, J.Rapaport and G.R.Satchler; Plenum, New York, 1980).

[Mai69] G.Mairle, G.T.Kaschl, H.Link, H.Mackh, U.Schmidt-Rohr, G.J.Wagner and P.Turek, Nucl. Phys. A134 (1969) 180.

[Mar68] J.B.Marion and F.C.Young, "Nuclear Reaction Analysis, Graphs and Tables" (North-Holland, Amsterdam, 1968).

[Mil71] D.Miljanic and V.Valkovic, Nucl. Phys. A176 (1971) 110.

[Mot79] T.Motobayashi, I.Kohno, T.Ooi and S.Nakajina, Nucl. Phys. A331 (1979) 193.

[Nai74] K.G.Nair, H.Voit, M.Hamm, C.Towsley and K.Nagatani, Phys. Rev. Lett. 33 (1974) 1588.

[Nai75] K.G.Nair, H.Voit, C.Towsley, M.Hamm, J.D.Bronson and K.Nagatani, Phys. Rev. C12 (1975) 1575.

[Nau81] F.Naulin, M.Roy-Stephan and E.Kashy, Nucl. Instr. Meth. 180 (1981) 647.

[New68] E.Newman and J.C.Hiebert, Nucl. Phys. A110 (1968) 366.

[Nor70] L.C.Northcliffe and R.F.Schilling, Nuclear Data A7 (1970) 233.

[Oed83] A.Oed, P.Geltenbort, F.Gonnenwein, T.Manning and D.Souque, Nucl. Instr. Meth. 205 (1983) 455.

[Oph78] T.R.Ophel and A.Johnston, Nucl. Instr. Meth. 157 (1978) 461.

[Oph82] T.R.Ophel, Australian National Univ. Report ANU-P/848, (1982).

[Par73] Y.S.Park, A.Niiler and R.A.Lindgren, Phys. Rev. C8 (1973) 1557.

[Par77] L.A.Parks, K.W.Kemper, A.H.Lumpkin, R.I.Cutler, L.H.Harwood, D.Stanley, P.Nagel and F.Petrovich, Phys. Lett. 70B (1977) 27.

[Par80] L.A.Parks, D.P.Stanley, L.H.Courtney and K.W.Kemper, Phys. Rev. C21 (1980) 217.

[Pas75] I.R.Paschopoulos, P.S.Fisher, N.A.Jelley, S.Kahana, A.A.Pilt, W.D.M.Rae and D.Sinclair, Nucl. Phys. A252 (1975) 173.

[Pin65] W.T.Pinkston and G.R.Satchler, Nucl. Phys. A72 (1965) 641.

[Pri83] D.M.Pringle, D.Phil. Thesis, Oxford, 1983.

[Püh79] F.Pühlhofer, Contribution to Study Weekend on Use of Magnetic Spectrometers in Nuclear Physics, Daresbury, March 1979.

[Rad74] V.Radeka, IEEE Trans. Nucl. Sci. NS-21 (1974) 51.

[Rae76] W.D.M.Rae, D.Phil. Thesis, Oxford, 1976.

[Rae82] W.D.M.Rae, private communication.

[Reb72] H.Rebel, W.G.Schweimer, G.Schatz, J.Specht, R.Lohken, G.Hauser, D.Habs and H.Klewe-Nebenius, Nucl. Phys. A182 (1972) 145.

[Ric74] P.Rice-Evans, "Spark, Streamer, Proportional and Drift Chambers" (Richelieu Press, London, 1974).

[Roo76] P.G.Roos, D.A.Goldberg, N.S.Chant and R.Woody, Nucl. Phys. A257 (1976) 317.

[San75] H.Sann et al., Nucl. Instr. Meth. 124 (1975) 509.

[Sat74] G.R.Satchler, Proc. Int. Conf. on Reactions between Complex Nuclei, Nashville, 1974 (North-Holland, Amsterdam) Vol. 2.

[Sat79] G.R.Satchler and W.G.Love, Phys. Rep. 55 (1979) 183.

[Sat80] G.R.Satchler, "Introduction to Nuclear Reactions" (MacMillan, London, 1980).

[Sat83] G.R.Satchler, "Direct Nuclear Reactions" (Oxford University Press, 1983).

[Seg65] E.Segre, "Nuclei and Particles", 1st Edn. (Benjamin, New York, 1965).

[Sha75] D.Shapira, R.M.DeVries, H.W.Fulbright, J.Toke and M.R.Clover, Nucl. Instr. Meth. 129 (1975) 123.

[Sha80] D.Shapira, G.L.Bomar, J.L.C.Ford, J.Gomez del Campo and L.C.Dennis, Nucl. Instr. Meth. 169 (1980) 77.

[She65] R.Sherr, B.F.Bayman, E.Rost, M.E.Rickey and C.G.Hoot, Phys. Rev. 139 (1965) B1272.

[Sin76] D.Sinclair, B.T.Chait, S.Kahana and B.S.Nilsson, Phys. Rev. C14 (1976) 1033.

[Sin80] D.Sinclair, L.K.Fifield and D.M.Pringle, Annual Report Nucl. Phys. Lab., Univ. Oxford 1979-80, p32.

[Sta77] D.P.Stahel, G.J.Wozniak, M.S.Zisman, B.D.Jeltma and J.Cerny, Phys. Rev. C16 (1977) 1456.

[Sta80] D.P.Stanley, F.Petrovich and P.Schwandt, Phys. Rev. C22 (1980) 1357.

[Tam74] T.Tamura and K.S.Low, Comp. Phys. Comm. 8 (1974) 349.

[Tam74a] T.Tamura, Phys. Rep. 14C (1974) 59.

[Tam80] T.Tamura, T.Udagawa and M.C.Mermaz, Phys. Rep. 65 (1980) 345.

[Tas82] L.Tassan-Got, C.Stephan, G.Bizard, J.Duchon, J.L.Laville, M.L'Haridon and M.Louvel, Nucl. Instr. Meth. 200 (1982) 271.

[Tho77] W.J.Thompson and J.S.Eck, Phys. Lett. 67B (1977) 151.

[Wer73] H.Werle, L.Van der Zwan and K.W.Geiger, Z.Physik 259 (1973) 275.

[Wil50] D.H.Wilkinson, "Ionization Chambers and Counters" (Cambridge, 1950).

[Woo80] C.L.Woods, N.A.Jelley, A.A.Pilt and J.S.Winfield, J. Phys. G 6 (1980) L187.

[Woo81] C.L.Woods, D.Phil. Thesis, Oxford, 1981.

[Wus79] P.Wust, W.von Oertzen, H.Ossenbrink, H.Lettau, H.G.Bohlen, W.Saathoff and C.A.Wiedner, Z.Physik A291 (1979) 151.

[Zis80] M.S.Zisman, J.G.Cramer, D.A.Goldberg, J.W.Watson and R.M.DeVries, Phys. Rev. C21 (1980) 2398.

# Errata.

p.54 The reference to Shapira et al. (line 17) is [Sha75].

p.110 Last line should read "..., and it is within the shell model...".

p.129 Comment on value of $\beta_2$ for $3/2^-$,0.0 → $5/2^-$,2.43 E2 transition in $^9$Be:

Experimental determinations of this deformation parameter support the value deduced here from B(E2). For example, Peterson has obtained a value of $\beta = 0.9 \pm 0.14$ from the analysis of $^9$Be($\alpha,\alpha'$) at 35.5 MeV.

[Nucl. Phys. A377 (1982) 41.]